

学位論文

Design and Analysis of Optics in Terahertz Receivers for Radio Astronomy

電波天文用テラヘルツ受信機における光学系の設計と解析

平成 25 年 10 月博士（理学）申請

東京大学大学院理学系研究科
物理学専攻

Alvaro Gonzalez Garcia

Abstract

Radio astronomy at Terahertz frequencies (0.1 – 10 THz) is a relatively new branch of astronomy powered by the development of receiver technologies at these traditionally unexplored wavelengths which lie between radio frequencies and the far infrared. The difficulty in applying radio or optical techniques in this range has postponed astronomical observations until recently. A rapid technological development powered by a renewed interest in applications in this band has allowed the development of THz receivers to be used for astronomy and astrophysics.

Astronomical observations at these frequencies are critical to understand star and planet formation in our Galaxy and extragalaxies, interstellar chemistry, and magnetic fields in space, among others. Black body radiation from the cold interstellar gas peaks at these frequencies, which makes them very important for continuum observations. The THz range is also especially rich in rotational spectral lines of fundamental molecules present in the interstellar medium. The careful study of detected lines allows characterizing the composition, red-shift and chemical and physical characteristics of astronomical objects. The detection of the polarization of radiation coming from astronomical sources is also critical to improve our understanding on magnetic fields in space and its possible influence in star formation processes.

The development of very sensitive receivers at frequencies around 1 THz is very recent, which makes this spectral region very interesting for astronomy. Improvements in receiver technology directly impact on our capabilities to study astronomical objects. Improvements in sensitivities allow detecting fainter objects. Improvements in optical efficiencies allow shorter acquisition times and deeper observations with a given time. Improvements in polarization discrimination allow better characterization of magnetic fields.

Receiver radio-frequency (RF) input optics is one of the key elements of receivers for radio astronomy at THz frequencies. It couples the energy collected by the usually large telescope antenna into the tiny ultra-sensitive detectors required by radio astronomy. At THz frequencies, optics also provides an efficient solution for local oscillator (LO) injection in heterodyne receivers. Quasi-optics provide an elegant and simple theory for the analysis of this kind of optics. In radio astronomy applications, optics is usually located completely or partly within the confined space of a cryostat, since detectors are usually cooled down at temperatures near 0 K in order to improve sensitivity.

This thesis describes the design, analysis, and optimization of optics for several receivers to be used for radio astronomy research in the ALMA (Atacama Large Millimeter/sub-millimeter Array) and ASTE (Atacama Sub-millimeter Telescope Experiment) telescopes. The focus of this thesis is the analysis of some recently discovered receiver performance degradations due to fabrication and alignment tolerances of optical components, which are comparable to their small size, and due to the effect of the operating environment. The understanding of these degradations becomes critical to improve performance as detector performance is currently approaching physical limits. The receiver cross-polarization performance, basic for observations of magnetic fields in space, is also studied in detail.

LO injection optics aims at providing a stable LO signal to the mixing device. The more stable the signal, the more stable the operation of the receiver is. This translates into more repeatable astronomical measurements and the possibility to extend single-observation times. In this thesis, a horn-to-horn power transmission system has been proposed and useful design equations have been derived. The concept has been proven by careful measurements and used for the ALMA band 10

receiver (787-950 GHz). A similar system has been successfully used in the measurement of the beam patterns of a 900-GHz receiver based on HEB mixers developed at the University of Tokyo. Additionally, simple quasi-optical attenuators based on beam truncation have been designed, fabricated and used on ALMA band 10 receivers. These attenuators have been useful to increase the sensitivity of the receiver by reducing its noise temperature.

In the case of RF optics, the optical systems of the two previous receivers have been carefully analyzed theoretically and characterized in the laboratory. A new tolerance analysis method has been proposed to consider the effect of fabrication and alignment tolerances in optics at THz frequencies. The application to ALMA band 10 has been useful to determine the expected performance variations for each one of the 66 cartridges (+7 spares) to be used in ALMA. The analysis results show good agreement with the measurement results of the 60 cartridges manufactured and tested so far. The application to the HEB-mixer receiver has been useful to identify a defective component, which will be replaced in the future. The receiver performance is expected to be enhanced after this replacement, with the consequent improvement in astronomical observation capabilities.

When the ALMA band 10 optics was first used within a cryostat, optical performance was greatly degraded with respect to room-temperature operation. Reflections on the cryostat infrared filters and window have been identified as the cause of this degradation and solutions have been proposed. This has allowed an average aperture efficiency improvement as large as 2.5 % at some frequencies.

A new method to estimate the total cross-polar performance of a receiver has been developed and successfully applied to the analysis of ALMA band 4 (125-163 GHz) and band 10 optics. This method is based on the modeling by Gaussian modes of the cross-polarization contributions generated by the different components in a receiver. It aims at obtaining the phases with which different components combine. It provides clear indications on how to design robust optics in terms of cross-polarization.

Finally, the frequency dependence of the ALMA band 4 cross-polarization performance has been analyzed by careful electromagnetic analysis. The dielectric loading of the horn antenna has been identified as the most likely cause of the cross-polarization degradation measured at some frequencies.

The new analysis methods and solutions proposed along this thesis are of interest for most astronomical receivers for observations at millimeter and sub-millimeter wavelengths. The results presented in this thesis have been applied to the ALMA band 10 receiver and to the University of Tokyo HEB receiver and have contributed and/or are expected to contribute to improve the performance of both receivers. In particular, this work contributed the unprecedented receiver performance of the ALMA band 10 receiver. In turn, this means enhanced observation capabilities and the possibility of performing more and better astronomical observations in the relatively unexplored 900-GHz region.

Additionally, the careful research on cross-polarization has allowed understanding the limitations of the ALMA band 4 receiver in terms of polarization discrimination. An improvement of the polarization discrimination capability of this receiver is difficult due to different constraints. However, the results of this thesis should be helpful to improve our understanding on cross-polarization generation in receivers and to not making the same mistakes in future receivers. Therefore, these results will be useful to understand how to design receivers which can measure the polarization of the incoming signal with high accuracy. Such a performance will open a new field in astronomy and astrophysics by allowing us to measure the magnetic field and its distribution in space with unprecedented sensitivity. The role of magnetic fields in space is still poorly understood and an outstanding problem which requires new receiver developments. Polarization discrimination performance such as that of the ALMA band 10 receiver is useful to tackle this problem properly.

Contents

1. Introduction	1
1.1. Terahertz Radio Astronomy	1
1.2. Receivers for THz Astronomy	4
1.2.1. Direct detectors.....	5
1.2.2. Heterodyne detectors	6
1.3. ALMA and ASTE	10
1.3.1. Atacama Large Mm /sub-mm Array (ALMA).....	11
1.3.2. Atacama Sub-millimeter Telescope Experiment (ASTE).....	12
1.4. Optical Systems	13
1.4.1. Importance of optics in THz receivers.....	13
1.4.2. Optical components	14
1.4.3. Performance degradation in optics.....	15
1.5. Background and Aims of this Study.....	16
1.6. Outline of the Thesis	18
2. Analysis Techniques	21
2.1. Introduction.....	21
2.2. Quasi-Optical Analysis	21
2.3. Physical Optics.....	25
2.4. Near-Field Measurements.....	25
2.5. Far-Field Calculations from Near-Field Data	28
2.6. Performance Definitions	31
3. LO Injection using Optics	37
3.1. Introduction.....	37
3.2. Limits of LO Waveguide Feeding	38
3.3. Quasi-Optical Injection.....	40
3.4. LO Injection for University of Tokyo HEB Receiver Experiment	43
3.4.1. Background.....	43
3.4.2. Quasi-optical analysis.....	44
3.5. LO Injection for ALMA Band 10	46
3.5.1. Design	46
3.5.2. Coupling efficiency	48
3.5.3. Measurements	51
3.5.4. Application to ALMA band 10 cartridges	55

3.6. Side-Band Noise and LO Injection	56
3.6.1. Explanation of the problem.....	56
3.6.2. Design of quasi-optical attenuators	57
4. Radio Frequency Input Optics.....	63
4.1. Introduction.....	63
4.2. HEB Receiver 900-GHz RF Optics.....	63
4.2.1. Optics design	63
4.2.2. Measurement characterization.....	67
4.3. ALMA Band 10 Tertiary Optics	72
4.3.1. Optical design	72
4.3.2. Measurement characterization.....	78
4.3.2.1. Room temperature setup	78
4.3.2.2. Cryogenic temperature setup.....	79
4.3.2.3. Design verification by measurements	79
4.3.2.4. ALMA band 10 prototype optical performance.....	81
5. Tolerance Analysis using Physical Optics and Monte Carlo Techniques.....	85
5.1. Introduction.....	85
5.2. ALMA Band 10 Tolerance Analysis	87
5.2.1. Corrugated horn tolerance analysis	87
5.2.2. Optics tolerance analysis.....	89
5.2.2.1. With nominal-dimensions corrugated horns.....	91
5.2.2.2. Corrugated horns with 5- μm corrugation tolerance	92
5.2.2.3. Corrugated horns with 10- μm corrugation tolerance	92
5.2.2.4. Histograms	93
5.2.2.5. Analysis of results	96
5.2.3. Measurement results	97
5.2.4. Statistics of the first 60 ALMA band 10 cartridges.....	99
5.3. 900-GHz HEB Receiver Tolerance Analysis.....	100
6. Effect of IR Filters on ALMA Band 10 Optics	107
6.1. Introduction.....	107
6.2. ALMA Band 10 Optical Performance using IR Filters in the Cryostat.....	108
6.3. Reasons for Degraded Optics Performance	111
6.4. Proposed Solution	114
6.5. Validation through Measurements	115
7. Study on Cross-Polarization Performance	125
7.1. Introduction.....	125
7.2. Cross-Polarization in Optical Components.....	126
7.2.1. Cross-polarization in metallic mirrors	126
7.2.2. Cross-polarization in dielectric surfaces.....	127
7.2.3. Cross-polarization in horns.....	129
7.2.4. Cross-polarization in OMTs	130

7.3. Cross-Polarization of a Quasi-Optical System	130
7.4. ALMA Band 10 Optics Cross-Polarization	133
7.5. ALMA Band 4 Optics Cross-Polarization	135
7.5.1. Analysis of the total system cross-polarization.....	135
7.5.2. Research on the frequency dependence of system cross-polarization	144
7.5.2.1. Connection between horn and OMT	145
7.5.2.2. OMT analysis.....	148
7.5.2.3. Infrared filters analysis	149
7.5.3. Influence of IR filters on the corrugated horn.....	153
7.5.3.1. Electromagnetic fields in terms of input admittance	154
7.5.3.2. Changes in input admittance	158
7.5.3.3. Conclusions of this analysis	164
8. Summary and Conclusions.....	165
8.1. Summary	165
8.2. Conclusions.....	169
Acknowledgments.....	171
Appendix A. Probe Horn compensation	173
Appendix B. Joint Paper	183
Bibliography	197

Chapter 1

Introduction

1.1. Terahertz Radio Astronomy

Since Galileo pointed a small home-made telescope to the skies in 1610 until around the 1930s, astronomical observations were mostly limited to the visible part of the spectrum. In the 1860s, James Clerk Maxwell proved that light was electromagnetic radiation and with the aid of his famous equations, he determined that “light” can exist at any wavelength [1]. This constitutes a theoretical base for astronomy at any frequency. However, the lack of receivers to detect radiation at frequencies other than visible or the near ultraviolet (UV) made that observations at other frequencies had to wait for a while. In a happy accident, Karl Jansky from Bell Laboratories, pointed a radio antenna to the sky and got some unexpected extraterrestrial radiation at a wavelength of 14.6 m (20.5 MHz) which was not coming from the Sun. That was the beginning of radio astronomy [2]. We now know it is radiation from plasma in the interstellar medium in the Galactic Center region. After that, powered by the huge development of microwave technology motivated by World War II, observations at radio frequencies multiplied and many discoveries were done [3]. For example, different molecules such as OH, NH₃, H₂CO, HCN or CO were found in interstellar clouds in the next decades [4]. Radio observations also paved the discovery of new objects such as pulsars, quasars or radio galaxies [5]. In 1965, Wilson and Penzias detected the microwave cosmic background (CMB) spectrum, which corresponds to a black body radiation at around 3 K [6]. After radio astronomy was established as a branch of astronomy, other frequency bands such as high energy X-rays and gamma rays or the near and far infrared have since been used for observations after appropriate receivers became available [7-8]. Observations in different parts of the spectrum provide information about different physical processes. Therefore, the combination of results of observations in different frequency bands helps to achieve a comprehensive understanding of astronomical sources. Figure 1.1 shows a comparison of images of the Orion Nebula in visible and IR frequencies. The IR image shows the cold gas between stars, whereas the visible image highlights the stars.

Today, we know that the universe is mostly composed of very cold dust and molecular gas (10 - 50K) with hotter denser regions (100-200K). The blackbody radiation associated to these temperatures peaks at frequencies in the far infrared and the sub-millimeter regions of the spectrum [9]. Therefore, the THz region (0.1-10 THz) is a very interesting spectral region for

continuum observations of dust broadband thermal radiation. At these frequencies, gases at temperatures between 10 and 200 K present strong atomic and molecular emission lines. As an example, figure 1.2 shows the spectral lines in a sample spectrum around 151.5 GHz and the molecules associated to each spectral line. The study of these spectral lines provides information about the chemical composition and physical conditions in interstellar clouds and it is thus important to understand the nature and evolution of the interstellar medium. The study of the chemical composition of regions where stars are formed is also very important for a better understanding of star formation processes [10].

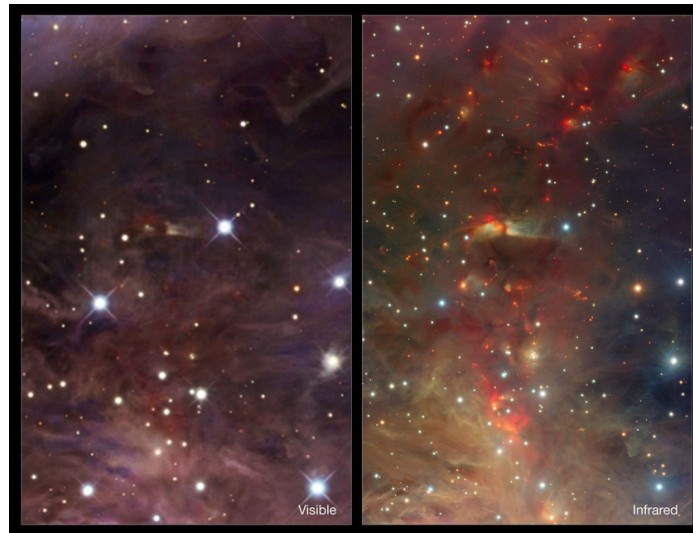


Figure 1.1. Comparison of visible (left) and infrared (right) images of the Orion Nebula. Different features are observable at different spectral ranges. (SOURCE: <http://www.eso.org/public/images/eso1006d>)

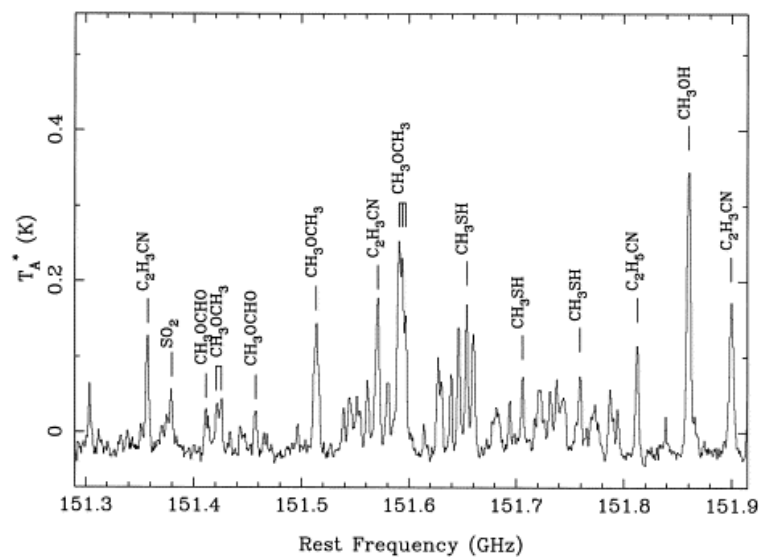


Figure 1.2. A sample spectrum in the 2-mm wavelength region for source G327.3-0.6 (SOURCE: [11])

Due to the expansion of the universe and according to Hubble's law (1929), the recessional velocity of galaxies is proportional to their distance to the Earth [12]. In turn, this means that spectral lines are shifted by Doppler Effect to lower frequencies, e.g. red-shifted, and distant galaxies are more red-shifted than nearby galaxies. Many interesting spectral lines of far away galaxies are shifted into the THz range. In particular, red-shifts of 2-4 correspond to an age when galaxy formation was especially active, and this can be readily observed at THz frequencies. Finally, the THz range is also interesting to investigate young star regions which strongly emit in the UV or visible range but are covered by dust clouds. The size of dust particles is very close to the radiation wavelength. Dust is therefore a very efficient scatterer of UV, visible and even Near Infrared radiation. This absorbed radiation is re-emitted in the THz region [13].

In order to give some clear examples of astronomical observations in the THz range, it is convenient to focus on a specific frequency interval for observations, so-called radio-frequency (RF) bandwidth. Much of the work in this thesis is done in the frequencies corresponding to band 10 of the ALMA (Atacama Large Millimeter/sub-millimeter Array) telescope [14], which extends from 787 GHz to 950 GHz. The most interesting scientific opportunities at this band are summarized next:

1. This frequency band contains many unique lines which are key tracers of the interstellar medium:

-The upper transition of C I (neutral atomic carbon) at 809 GHz provides information about the physical and chemical conditions at the interfaces between dense and more diffuse molecular clouds. This line corresponds to a temperature of 62 K and complements the information which can be obtained at 492 GHz, which corresponds to a temperature of 24 K [15-16].

-The HDO (deuterated water molecule) transitions at 849 and 894 GHz are useful to derive the water vapor abundance and physical conditions of the environment around molecular clouds. It also probes the H/D enrichment with respect to the interstellar medium [17].

-Lines of CO 7-6, HCN 9-8 and 10-9 and HCO⁺ 9-8 and 10-9 near 800 GHz are very good indicators of physical conditions in hot and dense parts of molecular clouds.

-Observations of CH⁺, 13CH⁺ transitions at 835 and 831 GHz [18] will be used to investigate physical conditions of diffuse envelopes of molecular clouds, which will provide us with an important clue to understanding the formation processes of molecular clouds.

2. There are also many red-shifted lines in this frequency band, such as the 1.899 THz line of C II, which is a key tracer of the cooling processes of gas in the interstellar medium, and can be observed with red-shifts in the range $z = 1$ to 1.4.

3. The continuum emission from dust peaks at around this band. Observations with high angular resolutions at this band are useful to study proto-planetary disks.

Traditionally, the main inconvenient for the development of THz astronomy has been the non-existence of receivers. THz frequencies are too high for radio techniques and too low for optical receivers. In recent years, there has been a strong technological development in this frequency range powered by many interesting applications in the fields of astronomy, medical science,

spectroscopy, atmospheric science or security, among others. In the case of astronomy, large diameter antennas and very sensitive receivers are required to collect and detect the faint radiation coming from astronomical sources. In the last three decades, several ultra-low-noise superconducting detector technologies have been established [19]. Examples of heterodyne receivers are Superconductor-Insulator-Superconductor (SIS) mixers [20] and Hot Electron Bolometer (HEB) mixers [21]. Examples of direct detectors are Kinetic Inductance Detectors (KIDs) [22] and Transition Edge Sensors (TES) [23]. The development of these superconducting technologies has been mostly driven by the need of high sensitivity detectors for astronomy.

The Earth atmosphere also poses a challenge to THz astronomical observations. The atmosphere absorbs much of the THz radiation coming from space. However, there are some frequency bands or windows at which the atmosphere does not completely absorb THz radiation [24]. Therefore, these atmospheric windows determine the frequencies at which THz astronomy is possible from the Earth surface. One of the main factors of atmospheric attenuation is water vapor content. This explains that most planned or already existing THz telescopes are located at very high elevation and in very dry places, such as the Atacama Desert in Chile [25] or in high-elevation sites in Antarctica [26]. The other possibility is to use space telescopes located far away from the Earth atmosphere, such as ESA Herschel [27], located on an orbit around the Lagrangian point L2.

1.2. Receivers for THz Astronomy

Astronomical receivers can be divided in two different categories: direct detectors and heterodyne detectors. The first are based on directly detecting the amount of incoming radiation, without considering the phase at which it arrives. When photons arrive at a direct detector, the temperature of the receiver changes and that can be detected through some change in some other physical parameters, such as resistance or inductance. The main advantage of direct detection is that it is extremely broadband, which makes these detectors appropriate for continuum observations. However, they require some kind of spectrometer at the receiver input when spectroscopic observations are performed. Unfortunately, the spectral resolution of spectrometers is around some GHz at frequencies in the THz range, which translates in velocity resolutions in the order of 100 km/s, which is not enough for most applications. Velocity resolutions in the order of 0.01 km/s are necessary to observe fine velocity structures of spectral lines. Currently, this kind of resolutions can only be obtained with heterodyne detectors. In heterodyne detectors, the incoming astronomical (RF) signal is down-converted to a lower intermediate frequency (IF) in the order of GHz by means of a local oscillator (LO) signal of well-known phase. Therefore, the phase difference between the incoming RF signal and the LO signal can be readily obtained at GHz frequencies. In other words, a full region of the RF spectrum, whose bandwidth is the same as the IF bandwidth, is brought down to lower frequencies at which fast electronics can analyze the information with great detail and efficiency. The inconvenient of heterodyne receivers is that the observational bandwidth is limited to the IF bandwidth, which is normally limited by technology. In the case of SIS mixer receivers, the limit is due to the IF low noise amplifiers, whereas in the case of HEB receivers, it is due to the HEB mixers. Therefore, each kind of receivers (direct or heterodyne) is appropriate for different applications, depending on whether our observations require large bandwidth or good spectral

resolution. For example, direct detectors are useful for microwave background studies, imaging or continuum observations. Heterodyne detectors are necessary for spectroscopy or interferometry. A brief description of the main kinds of astronomical receivers follows.

1.2.1. Direct detectors

Transition Edge Sensors (TES)

A TES is a cryogenically-cooled particle detector based on the strong temperature dependence of the normal conductor – superconductor phase transition. A TES is normally composed of a superconductor, normally tungsten, titanium or aluminum, on a constant temperature bath, whose temperature is slightly below the superconductor critical temperature, T_c . The superconductor is biased at constant voltage. When an incoming photon hits on the sensor, it is absorbed and the temperature of the sensor increases slightly with respect to the bath. Due to negative electro-thermal feedback, the sensor resistance increases causing the current through the sensor to drop in order to reduce the Joule dissipated power. After the photon is absorbed, the temperature equals the bath temperature again and the resistance comes back to nominal. Changes in the bias currents of sensors can be detected by the sensor read-out, which usually uses SQUIDs (Superconducting QUantum Interference Device).

The magnitude of the resistance change per absorbed photon is inversely proportional to the sensor heat capacity. Therefore, small heat capacities are preferable, which means small sensor size. The design of the thermal link between the superconducting material and the thermal bath is also critical. If the thermal conductivity is too low, it is difficult to cool the sensor back to the bath temperature. However, if the thermal conductivity is too high, the change in temperature due to incident photons is directly absorbed by the bath itself and there are no changes in sensor resistance.

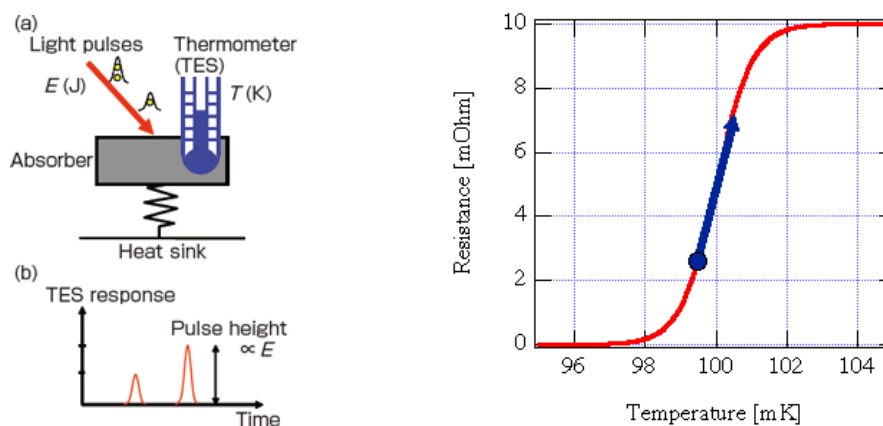


Figure 1.3: Working principles of a TES detector (SOURCES: left: AIST Today, No.34, p.21, Apr. 2009; right: http://web.mit.edu/figueroagroup/ucal/ucal_tes/)

The main advantage of TES is their extreme sensitivity. For example, they will be used in the SAFARI instrument [28] of the future JAXA mission SPICA [29], for which NEP (noise equivalent

power) in the order of $1e-19$ W/√Hz are required. TES have already been successfully applied in a number of astronomical projects, e.g. SCUBA-2 [30], ACT (Atacama Cosmology Telescope) [31] and South Pole Telescope [32].

Kinetic Inductance Detectors (KIDs)

KIDs are cryogenically-cooled particle detectors based on the change of kinetic inductance which occurs when incoming photons break Cooper pairs and generate excess quasi-particles. The kinetic inductance is inversely proportional to the density of Cooper pairs. Therefore, it increases when Cooper pairs are broken. This inductance is combined with a capacitor to create a resonance at microwave frequencies. When photons reach the detector and the kinetic inductance changes, so does the resonance frequency. An electronic readout is used to detect the changes in the resonances. Multiple detectors can be read out using a single common transmission line, such as a coplanar waveguide. Typical superconducting materials for KIDs are Al, Ti or Nb. Operating temperatures are usually in the 100 mK range.

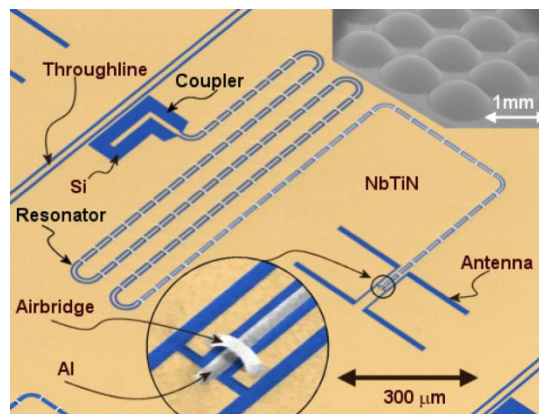


Figure 1.4. Photograph of a MKID camera pixel (SOURCE: [34])

The possibility of frequency multiplexing in the read-out allows using a high number of sensors per read-out channel and is one of the strengths of this kind of direct detectors. KIDs are the most promising current technology for large cameras for sub-mm astronomy. Cameras for THz astronomy using KIDs have already been used in the Caltech Southern Observatory (CSO) [33], in the Atacama Path Finder Experiment (APEX) [34] or in the IRAM 30-m Pico Veleta telescope [35].

1.2.2. Heterodyne detectors

As explained before, heterodyne receivers are required for applications in which very high spectral resolutions are needed. Additionally, they are also used for applications for which phase information is important. For example, they are necessary for phase interferometry. Phase interferometry [36] is a very popular technique for radio-astronomy based on the combinations of signals from different single-dish telescopes to recreate observations with an equivalent dish whose diameter would be the distance between antennas. This technique allows synthesizing large

apertures with modest aperture antennas. ALMA [37] is probably the most famous operative phase interferometer at the moment and it will be described in more detail in section 1.3.

Heterodyne receivers were originally developed at radio and microwave frequencies, and then, used at higher and higher frequencies well into the THz band. At lower frequencies, at which amplifiers are readily available, the down-conversion of RF signals is preceded by pre-amplification in order to improve the noise performance of the whole receiver according to Friis formula (1.1) [38]. Friis formula relates the system total noise temperature T_{total} to the noise temperature T_i and gain G_i of each component.

$$T_{\text{total}} = T_1 + \sum_i \frac{T_i}{\prod_{j=1}^{i-1} G_j} = T_1 + \frac{T_2}{G_1} + \frac{T_3}{G_1 G_2} + \dots \quad (1.1)$$

The use of pre-amplification also simplifies the noise requirements for the mixing device, since the noise temperature of the mixer is divided by the pre-amplifier gain. However, at THz frequencies, there are no amplifiers available. Therefore, the first element in the receiver chain just after the optics will be the mixer. This means that extremely low noise and low conversion loss mixers are required at THz frequencies. Consequently, THz mixers for astronomy are usually based on superconductors and cooled down to cryogenic temperatures. Mixers down-convert a small bandwidth at astronomical observation frequencies (RF) to microwave intermediate (IF) frequencies by using a local oscillator (LO) signal. The mixing is performed by exploiting some physical non-linearity, for example, the non-linearity in the I-V (current-voltage) curve of a SIS junction. Therefore, the resulting signal contains a copy of the RF bandwidth at IF frequencies, but also a series of harmonics of all the signals involved. As a first order approximation, which is valid for a good mixer design, the frequency down-conversion can be expressed as stated in (1.2):

$$f_{\text{IF}} = |f_{\text{RF}} - f_{\text{LO}}| \quad (1.2)$$

Equation (1.2) indicates that RF frequencies below and above the LO frequencies by the same amount will end up at the same IF frequency. The use of frequency discrimination schemes introduces a possible classification of heterodyne receivers:

1. SSB (Single Side-Band) receivers use an additional filtering scheme to detect only the Lower Side-Band (LSB), $f_{\text{IF}} = f_{\text{LO}} - f_{\text{RF}} > 0$, or the Upper Side-Band (USB), $f_{\text{IF}} = f_{\text{RF}} - f_{\text{LO}} > 0$
2. DSB (Double Side-Band) receivers do not add any additional frequency discrimination
3. 2SB receivers detect the LSB and USB simultaneously

After the corresponding IF signal is generated, it can be amplified by a LNA (Low Noise Amplifier). The LNA is the first amplifying element in the receiver chain and, therefore, it must present a moderate gain and very good noise performance in order to keep the system noise as low as possible. Often used LNAs for THz receivers are InP HEMT (Hot Electron Mobility Transistor) amplifiers and SiGe HBT (Heterojunction Bipolar transistor) amplifiers. Once the IF signal is amplified in the LNA, noise contributions of other components are not critical according to (1.1). A schematic of a typical DSB heterodyne receiver is shown in figure 1.5.

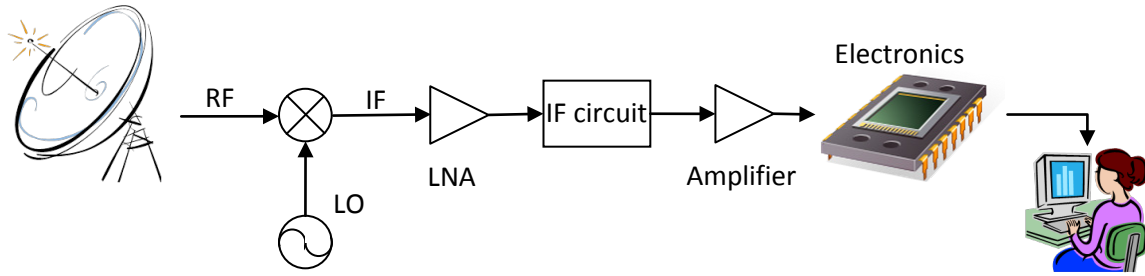


Figure 1.5. A schematic of a heterodyne receiver at THz frequencies

Superconductor-Insulator-Superconductor (SIS) mixers

SIS mixers exploit the strong non-linear behavior of Josephson junctions [39]. Josephson junctions are formed when two superconductors are separated by an insulator and their electron pair wave functions are weakly coupled. When the voltage applied to the junction exceeds the value $2\Delta/e$, where Δ is the superconductor gap voltage, Cooper pairs are broken into quasi-particles, which can tunnel through the junction. When a LO signal pumps the junction, photons break Cooper pairs and a quasi-particle tunnel junction can be established even for voltages below $2\Delta/e$, between $(2\Delta-hf)/e$ and $2\Delta/e$. This phenomenon is known as photon-assisted tunneling and can be seen in the SIS junction I-V curve (junction current I_{DC} as a function of the applied DC voltage V_{DC}) in the way of the so-called photon steps. This is shown in figure 1.6.

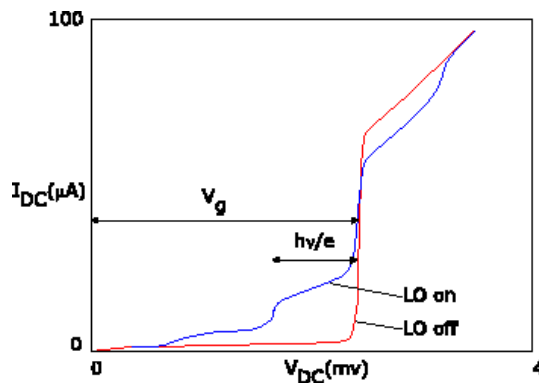


Figure 1.6. Typical SIS mixer junction current I_{DC} as a function of the applied DC voltage V_{DC}
(Source: IRAM. Available: <http://www.iram.fr/IRAMFR/ARN/jan99/node2.html>)

There can be more than one photon step, due to Cooper pair breaking by multiple photons. The voltage width of these photon steps equals hf/e too. The SIS junction is normally biased at the first photon step, near the junction strong non-linearity. The mixing theory for this kind of junction was developed by Tucker [40] and it is known as quantum mixing. In the SIS junction, Cooper pairs can tunnel from one superconductor to the other even when no voltage is applied. Additionally, due to the AC Josephson effect, the junction can oscillate at some frequency depending on the applied bias voltage. The Josephson frequency is:

$$f_j = \frac{2eV}{h} \quad (1.3)$$

where the coefficient multiplying the bias voltage V is equal to 483.6 GHz/mV. If the incoming radiation equals the Josephson frequency, the beat between the two signals creates steps in the I-V curve known as Shapiro steps. These steps cause extra noise and are undesirable. Fortunately, they can be removed by applying an appropriate magnetic field. In practice, SIS mixers include some kind of permanent or variable magnet to mitigate the AC Josephson effect.

The maximum frequency at which an SIS junction can produce mixing is given by the material gap energy. When the frequency of the incoming signal increases, the first photon step gets wider and wider, eventually reaching zero voltage. Due to the odd symmetry of the I-V curve for negative voltages, the photon step at negative voltages is at negative currents. If the frequency is increased further, the photon steps will enter voltages with the opposite sign and photon-step currents will cancel each other. Therefore, increasing the frequency beyond zero voltage translates into a narrowing of the photon step. The frequency can be increased until its value reaches $4\Delta/h$. At that frequency, the photon step would disappear. In practice, there must be some margin to $4\Delta/h$ for efficient mixing. For example, the critical temperature for Nb, the most common superconducting material in SIS junctions, is 9.2 K. According to the BCS theory, the approximate relationship between the gap energy and the critical temperature is $2\Delta=3.52k_B T_c$. This means that the maximum frequency at which Nb can be used in SIS junctions is 1.35 THz. Above this frequency, other materials such as NbN should be used. Unfortunately, the use of higher T_c materials in junctions is difficult due to the difficulty to fabricate high quality films among other problems.

The quantum mixing theory shows that SIS mixers can achieve a minimum noise temperature known as the quantum noise limit, $T_N=hf/k_B$. In practice, Nb/AlO_x/Nb junctions can achieve noise performance close to this fundamental limit. Apart from very high sensitivity, SIS junctions provide a wide instantaneous IF bandwidth. The final IF bandwidth is actually limited by the LNA bandwidth, not by the SIS mixer. A wide IF bandwidth allows the instantaneous observation of the equivalent RF bandwidth. Therefore, it decreases the time necessary for astronomical observations since several frequencies of interest can be studied simultaneously.

SIS mixers represent the state of the art in terms of heterodyne receivers and are therefore used in many receivers. SIS mixers are the key technology in most bands of ALMA [37].

Hot Electron Bolometers (HEB)

The HEB mixer is based on the absorption of radiation in a very thin (a few nm) superconducting film operated near the superconducting transition temperature, T_c . The incoming radiation breaks Cooper pairs and creates hot electrons. The temperature of some electrons is above the critical temperature and, therefore, superconductivity is broken at a local level. This introduces some resistance which is used for the mixing. The absorption mechanism is therefore not frequency dependent in the THz range. The physical layout of the mixer is a superconducting bridge between contact pads or electrodes, as shown in figure 1.7. Hot electrons must cool down quickly in order to be ready to follow the variations of the RF signal. The ability to cool down is directly related to the thickness of the superconducting film (phonon cooling) and to the electron diffusion coefficient towards the electrodes (diffusion cooling). Those are the reasons why very thin films and short

bridges are normally used for HEB mixers. Therefore, the geometry of the HEB mixers is planar and the parasitic capacitance is very small. The absorption mechanism and this practical implementation allow the use of HEB mixers at frequencies up to several THz. Therefore, HEB are the best alternative for frequencies which are too high for usual SIS mixers, nominally for frequencies above 1 THz. The sensitivity of HEB mixers is slightly worse than SIS mixers at frequencies at which both are available. Good HEB mixers at $f > 1\text{THz}$ have noise temperatures around 6-7 times the quantum limit. Another advantage of HEB mixers is the low LO power required for operation.

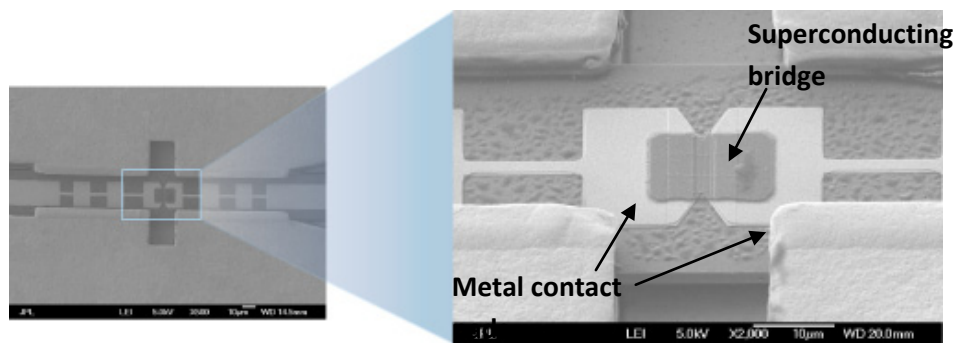


Figure 1.7. Photographs of a HEB mixer chip. The HEB geometry can be appreciated in the photograph on the right (SOURCE: NASA/JPL)

In spite of their good performance at higher THz frequencies, HEBs have a fundamental limitation in terms of IF bandwidth. The IF bandwidth of HEB mixers is limited by the thermal time constant of the hot electrons and the surrounding bath temperature. This limits practical IF bandwidths to a few GHz (between 2.5 and 5 GHz).

HEB mixers are being developed at high THz frequencies by groups all around the world. The higher frequency bands of the HIFI instrument [41] of the ESA Herschel have been implemented with HEB mixers and have been used for many important scientific findings. Other receivers using HEB mixers have been used in Earth telescopes (APEX, ASTE...), balloon observations (TELIS [42]) or airplane observations (SOFIA [43]).

1.3. ALMA and ASTE

The work in this thesis is mostly related to receivers to be used in the ALMA and ASTE telescopes. Both telescopes are located in the Atacama Desert in Chile, which is located at high elevation above sea level (5000 m) and is one of the driest places on Earth. These two points make this place one of the best places for on-ground THz astronomy. Calculated atmospheric transmissions for different precipitable water vapor (P.W.V.) contents at the ALMA/ASTE site are presented in figure 1.8 for frequencies between 200 and 1600 GHz [44]. The percentage of time below P.W.V. values of 0.25, 0.50, 1.00 and 2.00 mm is 5%, 25%, 50% and 65% respectively [45]. Figure 1.8 shows that when P.W.V. is low, there are several atmospheric windows at THz frequencies, which disappear when

P.W.V. content increases. The existence of these atmospheric windows is pretty unique and there are only a few places on Earth which show this high transmission at frequencies around 1 THz.

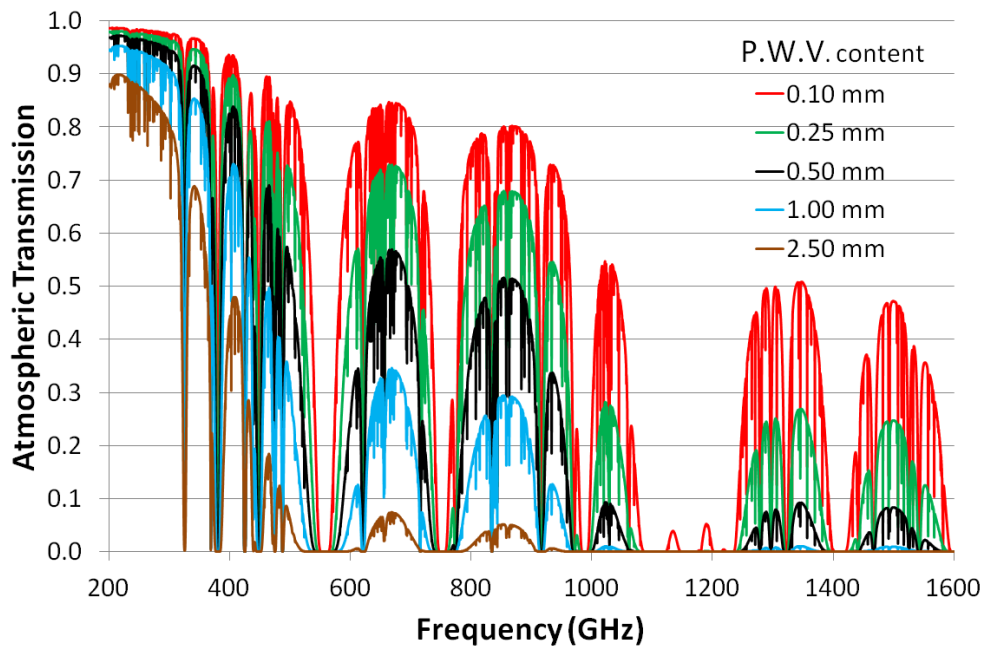


Figure 1.8. Atmospheric Transmission for different water vapor contents at Atacama Desert calculated using [44]

1.3.1. Atacama Large Mm/sub-mm Array (ALMA)

ALMA [46] is a large radio-astronomy interferometer composed of at least 54 12-m and 12 7-m diameter antennas constructed in Chile by Europe, North America and East Asia. The maximum baseline between antennas in the interferometer will be around 15 km, which will allow unprecedented resolution. ALMA has been designed for observation in all the atmospheric windows from 30 to 950 GHz. This bandwidth has been divided into 10 bands for practical implementation. The different ALMA frequency bands with their ALMA project noise specifications are indicated in table 1.1. All receivers in the THz band (0.1 – 0.95 THz in this case) are implemented using heterodyne SIS mixers. All the bands use standard Nb/AlO_x/Nb junctions. If Nb is used as metal in waveguides, the maximum operational frequency before loss and noise increase due to Cooper pair breaking is $2\Delta/h$, which is around 700 GHz. Band 10 [47] is the only band which is entirely above that frequency and uses NbTiN ($T_c = 14.5$ K, $2\Delta/h = 1065$ GHz) instead of Nb in planar waveguides. The IF bandwidth of the 2SB mixer receivers is from 4 to 8 GHz. It is from 4 to 12 GHz for bands 9 and 10 (DSB mixers). The receivers are built as cartridges and can be inserted independently in the cryostats which are installed in the secondary focus of the ALMA antennas. The operation temperature of the ALMA cryostats is 4 K.

ALMA started Cycle 0 operation in late September 2011, with only 16 antennas and bands 3, 6, 7 and 9. This limited-capability operation of the telescope has already rendered important scientific results [48-51].

Table 1.1. ALMA bands and technology used to achieve the indicated ALMA project specifications

ALMA band	Frequency (GHz)	Receiver technology	Noise temp. over 80% of band	Max. noise temp. at any freq.
1	31-45	HEMT	17	26
2	67-90	HEMT	30	47
3*	84-116	2SB SIS	37	60
4	125-163	2SB SIS	51	82
5	162-211	2SB SIS	65	105
6*	211-275	2SB SIS	83	136
7*	275-373	2SB SIS	147	219
8	385-500	2SB SIS	196	292
9*	602-720	DSB SIS	175	261
10	787-950	DSB SIS	230	344

*production of cartridges is finished



Figure 1.9. Some of the antennas of the ALMA telescope (SOURCE: [37])

1.3.2. Atacama Sub-millimeter Telescope Experiment (ASTE)

The Atacama Sub-millimeter Telescope Experiment (ASTE) 10m-aperture telescope is located in Pampa la Bola, Chile, at 4860 m above sea level, and very near the Atacama Large Millimeter/sub-millimeter Array (ALMA) site [52]. This telescope was initially conceived as a test bench for antenna and receiver technology at (sub-) millimeter wavelengths, and as a first step towards the Japanese ALMA antenna. Actually, the 10m reflector antenna was a pre-prototype of the Japanese ALMA 12m antenna [53], and the first qualification model of the ALMA band 8 receiver [54] was tested in the ASTE telescope. Therefore, the cartridge size and cryostat requirements for ASTE are similar to those for ALMA. On the other hand, several receivers implemented by different universities and institutes have been used in ASTE for astronomical observations. Examples of these receivers are the AzTEC mm-wavelength camera [55] or the CATS345 sideband separating receiver [56]. In recent years, a Hot Electron Bolometer (HEB) dual-band receiver working at 900 GHz and at 1.3 THz showing good

noise performance has been developed at University of Tokyo and successfully used for observations with ASTE [57].



Figure 1.10. The ASTE 10-m telescope (SOURCE: <http://www.ioa.s.u-tokyo.ac.jp/~kkohno/ASTE/>)

1.4. Optical Systems

1.4.1. Importance of optics in THz receivers

The target of THz receivers is to detect the electromagnetic radiation coming from astronomical sources and usually collected by a large parabolic antenna. The core of a receiver is the elements which are capable of detecting that radiation, directly or by down-conversion to electrical signals with frequencies which can be easily handled by common electronics. However, between the antenna and the detecting elements, there is another key component of a receiver: the optics. The optics is the system which makes it possible to couple the radiation coming from the antenna into the detecting elements in an efficient fashion. If the optics is not properly designed, much of the radiation collected by the antenna is lost and not detected. The ability of the optics to couple the radiation coming from the antenna into the receiver is measured by different efficiencies. Good optics will reduce observation times or improve results for a given observation time, improving the science capabilities of a telescope. Optics is also a key element to provide polarization discrimination. In some cases, it is important to observe the polarization at which electromagnetic radiation is emitted from astronomical objects. For example, the polarization of the radiation provides information about magnetic fields in space or about diffusion in molecular clouds. If the optics polarization discrimination is not properly implemented, it is not possible to distinguish between orthogonal polarizations. The polarization discrimination performance is measured by the generated cross-polarization, which is defined as the amount of one polarization when only the orthogonal polarization is incident on the optics. Common orthogonal polarizations are vertical and horizontal linear polarizations or right and left hand circular polarizations. Last but not least, optics are located in front of the mixer and the low-noise IF amplifier and are the first noise element in Friis noise formula (1.3), where T_{RX} is the total receiver noise temperature, T_{optics} , $T_{detector}$ and T_{LNA} are the noise temperature of each component, L_{optics} is the loss in the optics and $G_{detector}$ is the gain in the detector.

$$T_{RX} = T_{optics} + L_{optics} \left(T_{detector} + \frac{T_{LNA}}{G_{detector}} + \dots \right) \quad (1.3)$$

The noise temperature of the optics is directly proportional to the loss. Therefore, any loss in the optics will mean a degradation of the noise temperature in two ways: direct addition of noise, and amplification of the noise temperature of other components.

So far, all the description about the optics has been done with respect to the coupling of the RF signal into the receiver detectors (e.g. [58]). However, in the case of heterodyne receivers, optics provides a possible implementation of LO injection into the detectors (e.g. [59]). Stable LO power is necessary to provide stable operation of heterodyne receivers. Unstable LO signals will degrade the stability of observations and degrade the science capabilities of a telescope. Usually, the LO signal is generated in a different location from where it is needed. This can be due to size limitations in the receiver, to thermal loads in cryogenically cooled receivers or a number of other factors. At low frequencies in the THz range, the usual way to bring the generated LO signal into the detector is by means of metallic waveguides which present low loss at these frequencies. However, as the frequency increases, so does the metallic loss in the walls of waveguides, and optical injection of the LO signal becomes a very competitive alternative for LO injection. Basically, the generated LO signal is radiated, re-focused, re-directed and received near the RF detector by means of different optical components.

1.4.2. Optical components

Receiver optics is normally composed of some kind of antenna, focusing and redirecting elements and polarization discrimination components if required.

Antennas provide the conversion between a signal propagating in space and a guided signal in the waveguide structure where detectors are placed. Antennas can be simple planar antennas with or without lenses, such as twin-slot antennas [60] or self-complementary log-periodic antennas [61]; or high-performance horn antennas, such as diagonal or corrugated horns. The performance of antennas is measured by its gain, beam width, beam symmetry, cross-polarization or side-lobe level. Corrugated horns are usually the best antennas for high-performance receivers with polarization discrimination due to low loss, low cross-polarization, high beam symmetry, and low side-lobe levels. Additionally, corrugated horn beams are highly Gaussian (around 98% Gaussicity or 2% deviation from a Gaussian function), which allows the use of quasi-optical design techniques [62].

In terms of focusing signals, dielectric lenses and metallic ellipsoidal mirrors are often used. Mirrors are usually less lossy than lenses and are thus preferred for high-sensitivity receivers. Mirrors can also be used to change the propagation direction of signals. Flat mirrors can provide this capability without re-focusing.

Linear polarization discrimination components include orthomode transducers (OMT) and wire grids. OMTs are waveguide components with are located between the antenna and the detectors. As an example, the OMT used for ALMA band 4 receiver is presented in figure 1.11. They are the

preferred component at lower frequencies (up to 0.5 THz), at which difficult waveguide structures can be manufactured. Wire grids let one linear polarization through and reflect the other one. They are located before the antennas in the optical path. Two antennas are therefore required to detect orthogonal polarizations, one for the signal which goes through the grid and one for the signal reflected in it. Wire grids are usually used at frequencies higher than 0.5 THz, for which waveguide fabrication of OMTs becomes too difficult and costly.

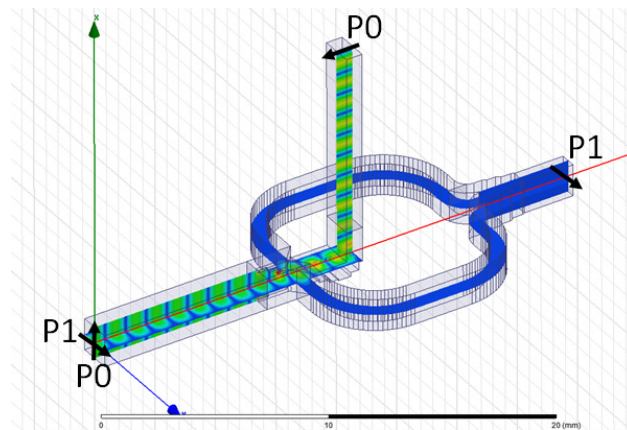


Figure 1.11. Electromagnetic simulation of the ALMA band 4 OMT. The input signal contains two orthogonal linear polarization components P0 and P1. The OMT divides that signal and provides the polarization components P0 and P1 in different outputs

1.4.3. Performance degradation in optics

Current THz receivers for radio-astronomy are approaching the technical limits of performance. Detectors provide sensitivities approaching physical limits (e.g. quantum noise limit in SIS and HEB mixers) and optics design profits from very accurate simulation and design numerical algorithms. In fact, at low frequencies at which waveguide components and optics can be manufactured accurately, fabricated components present the same performance as simulated by computer software. However, at frequencies around 1 THz, fabrication tolerances start having an important effect on performance. The impact of tolerances on performance is not new or unique at these frequencies. However, it is more noticeable when components become smaller and tolerances cannot be improved accordingly. Chapter 5 in this thesis presents a novel analysis method of the effect of tolerances on optical performance. The combination of accurate simulation tools and statistical Monte Carlo analyses allows a better characterization of different performance measures in terms of expected values, standard deviations and histograms. This translates into a better understanding of the science performance limits of a telescope when performing astronomical observations.

Receivers for radio-astronomy are usually cooled down to cryogenic temperature to improve sensitivity by using state-of-the-art superconducting detectors. The use of receivers within cryostats introduces some performance degradations which cannot be neglected as performance reaches new limits. The most clear example of these degradations are those introduced by the infrared (IR) filters used between two temperature stages in a cryostat to reduce the thermal load into the lower

temperature stage from the higher temperature stage. These filters are actually dielectric structures which are inserted in the signal path and add losses, extra reflections and cross-polarization generation. Additionally, if they are close to antennas, they can perturb their free space radiation characteristics and change antenna performance in an unexpected way. Chapters 6 and 7 of this thesis provide a detailed physical explanation of several harmful phenomena related to the influence of IR filters which degrade the science capabilities of the receiver.

1.5. Background and Aims of this Study

The work presented in this thesis has been performed by the author while working in the ALMA band 10 group at the National Astronomical Observatory of Japan (NAOJ). Part of the latest research has been done in collaboration with Professor Yamamoto's group at the University of Tokyo. The initial research in this thesis involves the design and verification of LO injection and RF optics systems. Most of the work has been performed at frequencies around 900 GHz, which correspond to ALMA band 10 (787-950 GHz) and the lower frequency band of Professor Yamamoto's HEB-mixer receiver. The LO injection optics research started from an existing preliminary design for ALMA band 10. The author then researched the physical fundamentals of quasi-optical power transmission to try to refine the design for maximum transmission efficiency and stability. After the design was finalized, a verification campaign through near-field amplitude and phase electric-field measurements was performed. Results indicated that the LO injection system works fine and overcomes some problems found in solutions using waveguides. This guarantees stable astronomical observations.

After this, the optics research focused on RF optics. During the validation of the optics designs of both receivers at 900 GHz, different performance degradations were found. In the case of ALMA band 10, total aperture efficiency was lower than measured at room temperature when the receiver was operated at cryogenic temperature. In the case of the HEB receiver, measured beam patterns were different from predictions by Physical Optics software. The author started studying the physical causes of the degradation based on two approaches. The first one was based on analyzing how expected fabrication and assembly tolerances of components affected the optics beam performance. For that, a novel approach was adopted. It was decided to exploit all the capabilities of a physically appropriate analysis method such as Physical Optics in conjunction with powerful Monte Carlo statistical methods. The second approach consisted in performing theoretical analysis and laboratory experiments to better understand why performance degradations happen. Both approaches yielded very interesting results which have been published in peer-review publications. On the one hand, the statistical analysis approach showed that tolerances had an important impact in expected performances. Larger tolerance did not only increase the performance variance, but also changed some expected average values. This was found to be critical at frequencies around 1 THz at which fabrication techniques are still not well developed [63]. Additionally, the comparison of these statistical methods and measurement proved a very powerful tool to identify the existence of defective components in the RF path [64]. On the other hand, the investigation based on measurements of ALMA Band 10 optics revealed that the reflection of the beam in cryostat IR filters was large. The reflected beam in the filters was being reflected back in the signal incoming direction

and after some diffractions, it was distorting the beam and worsening performance. Once the causes were identified, it was easy to propose a solution to mitigate this effect [65]. These two studies revealed the importance of tolerances and the operational environment of THz cryogenically-cooled receivers. In the two receivers, detector performance was state of the art, with sensitivity values approaching physical limits. However, degradations in the optical systems were hampering the use of both receivers to their full potential and limiting their science capabilities. This should highlight the importance of a good optical design and a good verification campaign.

Recently, and during the production of ALMA band 4, the cross-polarization performance of THz receivers has been investigated thoroughly. Currently, most receivers at THz frequencies are not designed for astronomical polarization measurements. Therefore, cross-polarization is not a critical performance during the design phase of a receiver and it is not properly analyzed. However, this is not the case of ALMA. For ALMA, receiver cross-polarization is a critical performance which has turned out to be very challenging for optics designers around the world. Actually, many of the ALMA receivers at different bands could not meet the original requirements for cross-polarization (XsP), $XsP < -23$ dB, or polarization efficiency of more than 99.5%. So far, when troubles were met in bands 3, 6 and 9, requests for a relaxation of specifications were issued. The justifications for these changes of specifications were normally based on cost arguments or very simple engineering reasoning. However, in the case of band 4, it was decided to look for the physical causes of the degradation from the beginning, and an exhaustive theoretical analysis of the situation together with intensive measurement campaigns were performed. Firstly, research was focused on understanding how the cross-polarization contributions from each component in the RF path add together towards a total optical system cross-polarization performance. The starting point of this research was Gaussian beams theory together with paraxial approximations of propagation equations. This research yielded a method to calculate system cross-polarization for THz systems which is physically rigorous and provides results close to measurements [66]. This method allowed determining a realistic but still stringent cross-polarization requirement for ALMA band 4. It also hints how a design must be performed in order to obtain good cross-polarization performance, which was clearly shown in the analysis of cross-polarization in the ALMA band 10 receiver optics.

After the specification change request was approved, the Band 4 team was asked to perform very precise cross-polarization measurements for several production cartridges. This consisted of cross-polarization measurements every 1 GHz in the band from 125 to 163 GHz. After this strenuous and time consuming experiment, it was found that the cross-polarization of the Band 4 receiver had very repeatable frequency dependence, with strong peaks at certain frequencies. This result was totally unexpected and, what was worse, showed that some Band 4 receivers could not meet the new ALMA specification due to some of these cross-polarization peaks. Again, a thorough investigation was performed and the physical causes of this degradation were found [67]. However, in this case, even though the situation was completely understood, it was very difficult to find a good solution for the problem within the constraints imposed by operation in the ALMA cryostats. Only some slight mitigation of the problem was possible. However, this problem highlighted the importance of considering the operational environment of the receiver from very early stages of the optical design. The lessons learned during the ALMA band 4 cross-polarization investigations should be of interest for anybody who aims at designing a dual-polarization receiver to be operated within a cryostat.

In short, the research contained in this thesis aims at understanding how optics state-of-the-art performance is affected by small fabrication and assembly errors or by the environment when operated at cryogenic temperatures. These two points become critical for THz astronomy receivers, for which component size is very small and must use superconductivity phenomena to achieve sensitivities approaching physical limits. During this research, several novel analysis methods have been developed to understand the effect of tolerances on performance or to calculate the expected system cross-polarization from the individual contributions of each optical component. The application of the research contained in this thesis has proved useful to improve the performance of ALMA band 4 and band 10 receivers and will be considered for the improvement of the HEB receiver designed by Professor Yamamoto's group.

1.6. Outline of the Thesis

This thesis consists of 8 chapters. This chapter, Chapter 1, provides the motivation for THz astronomy and describes some of the common receiver technologies at this frequency range. It provides the justification why high sensitivity receivers are required for astronomical observations and briefly introduces the most popular superconducting technologies to achieve this requirement. However important these detectors are, receiver optics also plays a critical role in the total receiver performance, including sensitivity. The importance of optics is thus stressed. The possibility of using optics for LO injection in heterodyne systems is also introduced. Finally, possible degradations in performance due to the small size of components at frequencies approaching 1 THz and due to the influence of operation at cryogenic temperatures are outlined.

Chapter 2 describes the theoretical foundations for the analysis and characterization of optical systems. It starts with an introduction to quasi-optical analysis and Physical Optics. It then describes how measurements are performed in the near-field and far-fields are calculated using Fourier transforms. Finally, it introduces the most common efficiencies used to describe the performance of optical systems.

After defining the scope of the thesis and the tools required for its understanding, chapters 3 and 4 describe the optical systems used in ALMA band 10 and Prof. Yamamoto's receivers. Chapter 3 introduces the optics necessary for LO quasi-optical injection into SIS or HEB mixers, comparing this solution with solutions using waveguide injection. The description of the LO optics in the two receivers under study follows. Finally, the need to control the power of the injected LO signal is highlighted and a simple design of LO quasi-optical attenuators is introduced. This novel design provides a very simple and cost-effective solution for LO quasi-optical attenuation. Chapter 4 deals with RF optics. It describes the optics to couple the signals coming from the Cassegrain antenna secondary mirror into the receiver. The first part of the chapter describes the analyses and measurements performed at NAOJ of the 900-GHz optics of Professor Yamamoto's HEB receiver. The second part describes ALMA band 10 optics.

Chapters 5 to 7 deal with performance degradation analyses. Chapter 5 introduces a novel tolerance analysis method using rigorous Physical Optics tools and Monte Carlo statistical methods.

This analysis is applied to the optics of the two receivers described in Chapter 4. It proves a useful tool to understanding how tolerances affect performances and to detecting defective components. Chapter 6 shows how RF power reflected in the cryostat IR filters can degrade the receiver performance and how this problem was dealt with in the case of ALMA band 10. Chapter 7 analyzes optics cross-polarization. Firstly, the most common mechanisms of cross-polarization generation are introduced. Then, a novel physically-rigorous method to estimate the total system cross-polarization performance is proposed. The application of this method to ALMA band 10 optics highlights what good design techniques are in terms of cross-polarization. The application to ALMA band 4 shows why good cross-polarization performance is hard to achieve with band 4 optics. Finally, a thorough investigation on ALMA band 4 cross-polarization frequency dependence is presented. This investigation highlights once more the importance of the operation environment on actual receiver performance.

Finally, Chapter 8 summarizes the results of this thesis and the conclusions obtained throughout this research. It also stresses how the receiver research in this thesis can actually improve the potential for novel science observations which can help to improve our understanding of our universe and its evolution.

Chapter 2

Analysis Techniques

2.1. Introduction

The target of this thesis is to improve the science capabilities of THz receivers by improving the receiver optics. Receiver optics design and analysis at THz frequencies uses well-established theories and approximations which are worth describing before starting with the core contents of this thesis. This chapter provides the tools to analyze THz optics, both theoretically and by laboratory measurements, and to quantify its performance. Performance will be presented here in terms of efficiencies, which are directly related to observational capabilities. For example, higher aperture efficiencies mean shorter observation times to obtain a result or better observations for a given time; and higher polarization efficiencies mean better polarization discrimination and the possibility to measure weaker magnetic fields in space or polarization rotation in molecular clouds.

2.2. Quasi-Optical Analysis

Quasi-optics [62] is the most useful formalism to describe beam propagation at THz frequencies. It is an intermediate case between a rigorous analysis considering diffraction and the simplified theory of geometrical optics. Geometrical optics is useful for very short wavelengths, when the wavelength is much smaller than the system dimensions and diffraction can be ignored. When the wavelength is comparable to the system dimensions, then, diffraction is the dominant mechanism of propagation and accurate electromagnetic analysis is required. Quasi-optics is useful for wavelengths between these two cases and provides a simple way to deal with diffraction without a complex mathematical formalism. It is applicable to collimated beams whose diameter is not large in terms of wavelengths. The mathematical formalism of quasi-optics is based on Gaussian beams and Gaussian beam propagation, based on the paraxial wave equation. Gaussian beams have well-defined directions of propagation and the radiation is concentrated in a few wavelengths in the transverse plane with respect to the beam propagation direction. The origin of a Gaussian beam is not a point source but a region of finite extent named beam waist. A Gaussian beam field $E(x,y,z)$ can be described mathematically similarly to a plane wave but with transverse amplitude variation $u(x,y,z)$ as stated in (2.1):

$$E(x, y, z) = u(x, y, z)e^{-jkz} \quad (2.1)$$

where z is the direction of propagation and k is the wave number.

If (2.1) is introduced in the wave equation (2.2), the result is the so-called reduced wave equation (2.3).

$$\nabla^2 E + k^2 E = 0 \quad (2.2)$$

$$\nabla^2 u(x, y, z) - 2jk \frac{\partial u}{\partial z}(x, y, z) = 0 \quad (2.3)$$

The reduced wave equation (2.3) can be further simplified if the paraxial approximation is considered. The paraxial approximation can be applied when: a) the amplitude u does not change much along the direction of propagation or $\frac{\partial u}{\partial z}$ will be small in distances of a few wavelengths; b) the variation along the direction of propagation is much smaller than the transverse variation, $\frac{\partial u}{\partial z} \ll \frac{\partial u}{\partial x}, \frac{\partial u}{\partial y}$. When the paraxial approximation is applied to (2.3), the Laplacian ∇^2 can be exchanged by the partial derivatives in x and y . Then, the paraxial wave equation (2.4) is obtained:

$$\frac{\partial^2 u}{\partial x^2} + \frac{\partial^2 u}{\partial y^2} - 2jk \frac{\partial u}{\partial z} = 0 \quad (2.4)$$

The solutions of the paraxial wave equation are Gaussian beam modes, which can be expressed in Cartesian coordinates as stated in (2.5).

$$E_{mn} = \sqrt{\frac{1}{\pi w^2 2^{m+n-1} m! n!}} H_m\left(\frac{\sqrt{2}x}{w}\right) H_n\left(\frac{\sqrt{2}y}{w}\right) \cdot \exp\left(-\frac{x^2+y^2}{w^2} - jkz - \frac{j\pi(x^2+y^2)}{\lambda R} + j(m+n+1) \operatorname{atan}\frac{\lambda z}{\pi w_0^2}\right) \quad (2.5)$$

where λ is the wavelength, w is the beam radius, w_0 is the waist size, R is the radius of curvature, H are Hermite polynomials and m, n are the order in x and y , respectively. The beam radius, beam waist and radius of curvature can be visualized in figure 2.1 (b). Figure 2.1 shows the propagation of a fundamental mode E_{00} Gaussian beam. In that case, (2.5) simplifies to the expression in (2.6):

$$E_{00} = \sqrt{\frac{2}{\pi w^2}} \cdot \exp\left(-\frac{x^2+y^2}{w^2} - jkz - \frac{j\pi(x^2+y^2)}{\lambda R} + j \operatorname{atan}\frac{\lambda z}{\pi w_0^2}\right) \quad (2.6)$$

The radius of curvature and the beam radius can be calculated as a function of distance from the waist as indicated in (2.7)-(2.8).

$$R = z + \frac{1}{z} \left(\frac{\pi w_0^2}{\lambda}\right)^2 \quad (2.7)$$

$$w = w_0 \left[1 + \left(\frac{\lambda z}{\pi w_0^2}\right)^2\right]^{1/2} \quad (2.8)$$

The radius of curvature R and the beam size w can be combined in a single parameter q , the complex beam parameter, as defined in (2.9):

$$\frac{1}{q} = \frac{1}{R} - j \frac{\lambda}{\pi w^2} \quad (2.9)$$

Equations (2.7) and (2.8) indicate that when the distance from the waist is $z \gg z_0 = \frac{\pi w_0^2}{\lambda}$, both R and w grow linearly (asymptotically) with distance. This area at which $z \gg z_0$ corresponds to the far field. The distance z_0 is known as confocal distance.

Quasi-optical theory allows expressing the radiated fields in terms of Gaussian beam propagation with just a set of simple equations. Moreover, beam transformations such as propagation or reflections in mirrors can be treated in a simple fashion using matrices. Beam transformations can be expressed as ABCD matrices which are equal to those found in transfer matrix theory in geometrical optics [68]. The matrix of a sequence of beam transformations can be expressed simply as the product of the matrices of each transformation. If the final matrix of a transformation is $\begin{bmatrix} A & B \\ C & D \end{bmatrix}$, the relationship between the initial and final beam parameters is given by the relationship of complex beam parameters given in (2.10). The most common ABCD matrices are given in table 2-1.

$$q_{\text{final}} = \frac{A \cdot q_{\text{initial}} + B}{C \cdot q_{\text{initial}} + D} \quad (2.10)$$

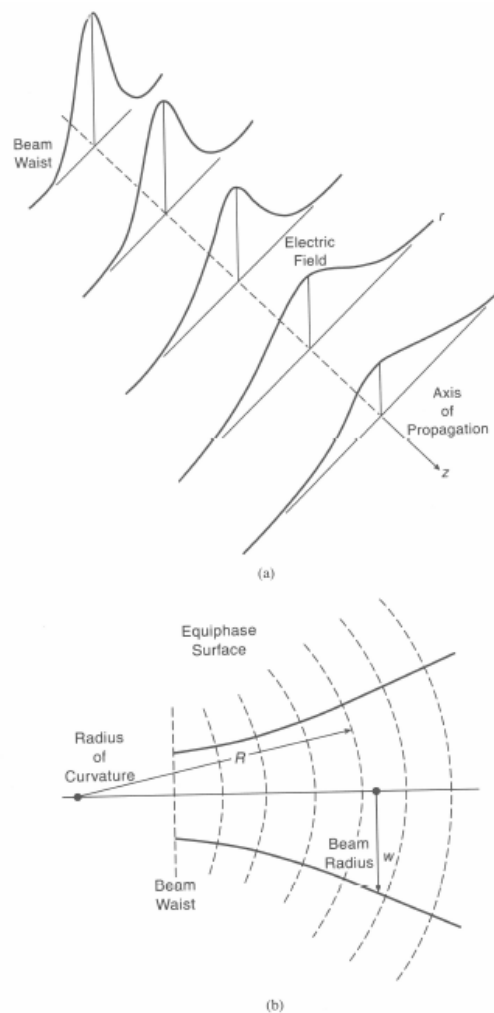


Figure 2.1. (a) Amplitude and size of a propagating Gaussian beam. (b) Beam radius and radius of curvature as function of propagated distance. (Figure 2.2 in [62])

Feeds used in receivers for radio astronomy at THz frequencies are usually horns (corrugated, diagonal, profiled...), which produce beams of high-quality (high symmetry, low side lobes, low cross-polarization level) and which can be approximated by fundamental Gaussian beams. The Gaussicity of a beam measures how well the beam fits a fundamental Gaussian mode. If beams produced or received by feeds are highly Gaussian, their propagation along an optical system can be easily modeled using equations (2.7)-(2.10). The Gaussicity of the beam generated by a corrugated horn can be easily around 98 or 99%. Therefore, these equations constitute the tools for the initial design of any optical system using good quality horns.

Equation (2.11) provides the expression to calculate how similar a given beam E matches a fundamental Gaussian beam E₀₀ described by (2.6).

$$\text{Gaussicity (\%)} = 100 \cdot \frac{|\int E^* E_{00} dx dy|^2}{\int |E|^2 dx dy \cdot \int |E_{00}|^2 dx dy} \quad (2.11)$$

Table 2-1. Common ABCD matrices

Propagation in uniform medium	$\begin{bmatrix} 1 & L \\ 0 & 1 \end{bmatrix}$, L is the propagation distance
Ellipsoidal mirror	$\begin{bmatrix} 1 & 0 \\ -\left(\frac{1}{R_{in}} + \frac{1}{R_{out}}\right) & 1 \end{bmatrix}$, R _{in} , R _{out} are radii of curvature at input and output
Thin lens	$\begin{bmatrix} 1 & 0 \\ -\frac{1}{f} & 1 \end{bmatrix}$, f is the focal distance of the lens

A fundamental Gaussian beam with given offsets x₀, y₀, and tilt angles θ_x, θ_y, can be modeled using equation (2.6) with the coordinates (x', y', z') obtained from (2.12)-(2.14):

$$x' = (x - x_0) \cos \theta_x \quad (2.12)$$

$$y' = (y - y_0) \cos \theta_y - (x - x_0) \sin \theta_x \sin \theta_y \quad (2.13)$$

$$z' = z + (x - x_0) \sin \theta_x \cos \theta_y + (y - y_0) \sin \theta_y \quad (2.14)$$

If the parameters of the Gaussian beam E₀₀ are variables, they can be optimized in order to maximize (2.11) for a given beam. The parameters derived from such an optimization are used to characterize the beam and the quality of the match is given by the final value of the Gaussicity. This technique is often used to describe beams measured in the laboratory or calculated in electromagnetic simulations.

2.3. Physical Optics

Physical Optics (PO) is an electromagnetic analysis method used in the simulation of reflectors. It is also useful to simulate mm- and sub-mm wave optics, since these systems use ellipsoidal mirrors (a special case of reflectors) in many cases.

The radiation pattern of a reflector can be calculated from the Fourier transform of the currents on the reflector surface [69]. These currents \mathbf{J}_s can be calculated from the magnetic field incident \mathbf{H}^i and reflected \mathbf{H}^r on the surface as stated in (2.15).

$$\vec{\mathbf{J}}_s = \hat{\mathbf{n}} \times (\vec{\mathbf{H}}^i + \vec{\mathbf{H}}^r) \quad (2.15)$$

where \mathbf{n} is the unitary vector perpendicular to the reflector surface.

The Physical Optics approximation [70] consists in considering $\mathbf{H}^i = \mathbf{H}^r$, which only holds true for infinite plane surfaces. In other words, the reflector surface is approximated by an infinite plane. This approximation works well when the reflector is large electrically, has large radii of curvature, and the incident field radius of curvature is large with respect to the wavelength. When the surfaces to be modeled are too curved for PO to provide an accurate solution, other methods such as the Method of Moments (MoM) [71] are required. MoM provides a numerical solution to physically correct integral equations. However, it is very time consuming for electrically large reflectors. PO provides a solution to approximate equations and this solution is usually a good approximation of the accurate solution for electrically large reflectors. The most popular simulation software implementing PO is TICRA GRASP [72].

The Physical Optics approximation does not model diffraction at reflector edges. In order to obtain better solutions, it is typical for PO software to correct the currents at reflector edges with some currents derived from another theory, the Geometrical Theory of Diffraction (GTD) [73]. GTD is based on Geometrical Optics (GO), or simple ray tracing, with some refinements to account for diffraction at edges [74]. Therefore, the combination of PO and GTD provides good electromagnetic solutions for high frequency analysis, when the wavelength is small, and reflectors are electrically large. This is the case of THz optics.

Solutions provided by PO are approximations to correct physical solutions and are closer to these than the solutions obtained by Quasi-optical techniques. Therefore, it is common to start a design of an optical system at THz frequencies using fundamental Gaussian beam theory and then, to analyze the resulting design using PO (+ GTD, if necessary). In most cases at THz frequencies, the solutions obtained by PO analysis are very close to the exact solutions.

2.4. Near-Field Measurements

After a design has been completed using quasi-optical techniques and verified and refined by PO analysis, it must be implemented and characterized in the laboratory. There are many measurement techniques for antennas and THz systems [75]. For example, electric fields can be measured in the near or in the far field regions. If near fields are measured, far fields can then be calculated by Fourier transforms. Measurements can be also performed with the system under test at the radiating or at the receiving end. Both measurements would be equivalent in virtue of the Reciprocity Theorem of antennas [76].

Basically, an electric field measurement consists of placing an antenna with a known radiation pattern in some positions with respect to the system under test. At each relative position, some constant electric power is transmitted between the two of them and amplitude and phase are measured. The electric field can be spatially reproduced in this way. In the case of a far-field measurement, the angular field distribution is constant with distance and it is therefore recommendable to choose relative positions at the same distance by changing only the relative angles. For example, a far-field pattern is measured by changing the Azimuth and Elevation angles with the probe horn and the system under test at a constant distance.

The space surrounding an antenna or an optical THz system can be divided in three zones or regions, as depicted in figure 2.2:

1) The area closest to the radiating element or the final radiating aperture is known as the *reactive near-field region*. In this region, the electric field is composed of radiating fields and reactive fields, which are strongly attenuated with distance. This region extends to a distance of about $\lambda/2\pi$ or $0.62\sqrt{D^3/\lambda}$ (depending on the author) from the radiating region, where D is the largest dimension of the antenna or radiating aperture.

2) Further from the reactive near-field region extends the *radiating near-field region* or *Fresnel region*. In this zone, the electromagnetic field is composed of only radiating fields and the angular distribution of the fields changes greatly with distance. This region extends to a distance of about $2D^2/\lambda$. In this area, there is a field component along the radial direction.

3) Finally, the *far-field region* or *Fraunhofer region* extends beyond the Fresnel region. In this area, the fields are radiating and the angular field distribution does not depend on the distance from the radiating element or aperture. In this region, fields are transverse to the direction of propagation.

In the case of the quasi-optical analysis introduced in section 2.2, the limit between the near- and the far-field regions can be described in terms of the confocal distance, $z_0 = \frac{\pi w_0^2}{\lambda}$, as explained there.

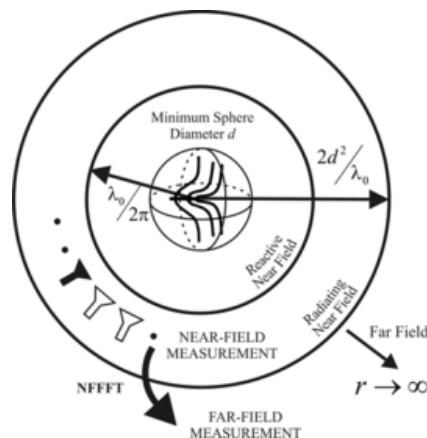


Figure 2.2. Regions around a radiating element of maximum dimension d . The regions where near- and far-field measurements are taken are also indicated (SOURCE: Prof. Dr.-Ing. Thomas Eibert, Technical University of Munich, On-line: <http://www.hft.ei.tum.de/index.php?id=98>)

Depending on the size of the antenna or the waist and the frequency, the distance $2D^2/\lambda$ or z_0 , which establishes the border between the near- and the far-field regions, can be large. In that case, far-field measurement setups would be large and would need to be within an anechoic chamber to

avoid the effects of reflections between the element under test and the probe horn in the measurement setup. In some cases, the dimensions of the test system would be unpractical. In the case of near-field measurements, setups can be compact and anechoic chambers are not necessary in many cases. It is also very typical to sample the near-field in an XY plane in front of the radiating antenna or waist, instead of measuring the fields at a constant distance from the antenna or the waist, as it is typical for far-field measurements. This also simplifies the test setup. Far fields cannot be measured directly in a near-field measurement. However, they can be easily retrieved by Fourier transformation.

In general, near-field measurements are preferred for optical systems at THz frequencies which can be approximately modeled by Gaussian beams, such as the optics in radio astronomy receivers. This is due to the small size of the measurement ranges and the ease of programming automated setups which just sample the electric field in spatial planes and not spheres.

In a near-field measurement setup, the influence of the probe horn on the measured data is important. The actual measured fields are the result of the convolution of the radiation patterns of the system under test with the radiation patterns of the probe horn. Therefore, it is critical to choose the correct probe horn and to know its radiation patterns. Probe horn characterization can be done as described in Appendix A. Once the probe horn radiation patterns are well-known, the measured patterns can be calculated by removing the probe horn contribution. This is easily done in the far-field. After applying Fourier transforms to the measured data and the probe horn radiation patterns, the convolution relationship becomes a simple multiplication. Therefore, the sought patterns can be calculated by just dividing the measured far-field patterns by the far-field patterns of the probe horn.

If the optical system implements linear polarization discrimination, co-polarization and cross-polarization patterns can be measured by just rotating the probe horn 90 degrees. The co- and cross-polarization patterns of the probe horn must be known for appropriate probe correction.

The effects of standing waves between the optical system under test and the measurement setup elements can be minimized by covering the area around the probe horn with absorbent material and by using the data of two measurements at different distances; this is at planes with different z coordinates. This procedure is only applicable if the magnitude and phase of the fields are measured. The distance between these two measurements, E_1 and E_2 , is usually a quarter of a wavelength. In that case, the fields without standing waves, E , can be retrieved by using (2.16), where the plus or minus sign depends on the measurement setup. The E-fields must be expressed as phasors, as $E = \text{Amplitude} \cdot \exp(j \cdot \text{Phase})$.

$$E = \frac{E_1 \pm j \cdot E_2}{2} \quad (2.16)$$

2.5. Far-Field Calculations from Near-Field Data

Near fields (NF) and far fields (FF) are related by means of Fourier transforms (FT). The initial space is the measurement plane XY. However, the output space is not directly expressed in geometrical dimensions, but in terms of wave number vector components, k_x , k_y , k_z . These dimensions can be expressed in spherical coordinates or in terms of Azimuth and Elevation as indicated in (2.17)-(2.19) [77]:

$$k_x = \frac{2\pi}{\lambda} \sin \theta \cos \phi = \frac{2\pi}{\lambda} \sin Az \cos El \quad (2.17)$$

$$k_y = \frac{2\pi}{\lambda} \sin \theta \sin \phi = \frac{2\pi}{\lambda} \sin El \quad (2.18)$$

$$k_z = \frac{2\pi}{\lambda} \cos \theta = \frac{2\pi}{\lambda} \cos Az \cos El \quad (2.19)$$

The number of samples taken in the XY plane is discrete, as it is the number of samples of the calculated FT. Therefore, the mathematical relationship of interest between the NF and the FF will be given by means of a Discrete Fourier Transform (DFT). The mathematical relationship between samples in the XY plane and the FF is then given by (2.20):

$$FF(k_x, k_y, k_z) = \sum_x \sum_y NF(x, y, z) e^{-j(k_x x + k_y y + k_z z)} \quad (2.20)$$

In a measurement at a plane with constant z , the term k_z only contributes a constant phase to the FF. It is customary to take $z=0$ and drop that term off (2.20). The previous DFT can be expressed in terms of Azimuth and Elevation angles as follows:

$$FF(Az, El) = \sum_x \sum_y NF(x, y, z) e^{-jk(x \sin Az \cos El + y \sin El)} \quad (2.21)$$

The previous transformation is slightly different from a common DFT and it has to be calculated slightly differently. The steps to follow are basically:

1. Define the coordinates Az, El where the FF will be calculated
2. Obtain the values of k_x and k_y for those points in the Az-El space
3. Use the transformation formula to calculate the value of the FF in the specified Az-El points

An example of NF to FF transformation for a measurement from -10 to 10 mm in X, Y with samples every 0.1 mm is presented in figure 2.3.

In order to get alias free FF it is necessary to sample the NF at the Nyquist frequency or wavelength/2. However, this condition can be relaxed if the FF area of interest is limited to small angles close to 0 degrees. According to sampling theory, the alias free spectrum of our calculated FF in the k_x - k_y space extends from $-\frac{\pi}{dx}$ to $\frac{\pi}{dx}$, where dx is the sampling distance. In the case of the Elevation angle, $El = \sin^{-1}(k_y)$, the values of the FF are alias free in the range $\pm \sin^{-1} \frac{\lambda}{2dx}$. The alias appears at values of Elevation equal to $\pm \sin^{-1} \frac{n\lambda}{dx}$, with $n \in \mathbb{N}$. If the sampling distance is $\lambda/2$, the FF is alias free from -90 to 90 degrees in Elevation. If the required angle is less than that, dx can be increased to the value $dx = \frac{\lambda}{2 \sin El}$. This consideration reduces the amount of data to be measured

and the time required for the measurement. In the case of the Azimuth, the results are more complex. The k_x dimension depends both on the Azimuth and on the Elevation. Therefore,

$$Az = \sin^{-1} \frac{k_x}{\cos El} \quad (2.22)$$

For values of Elevation close to 0 degrees, the Azimuth can be calculated as $Az \approx \sin^{-1}(k_x)$ and the same sampling considerations as for the Elevation apply. However, as Elevation increases, the argument of the arc sin function increases and so does the Azimuth. Therefore,

$$\text{Alias free } Az = \pm \sin^{-1} \frac{\lambda}{2 dx \cos El} \quad (2.23)$$

which means the alias free Azimuth range is larger or equal than for the Elevation. The sampling requirements are less restrictive than in the case of the Elevation thus. However, for large values of Elevation, the cosine function takes values close to zero and the k_x values are all around 0 for any value of Azimuth. This effect distorts the FF in the Az-El space. This is shown in figure 2.4.

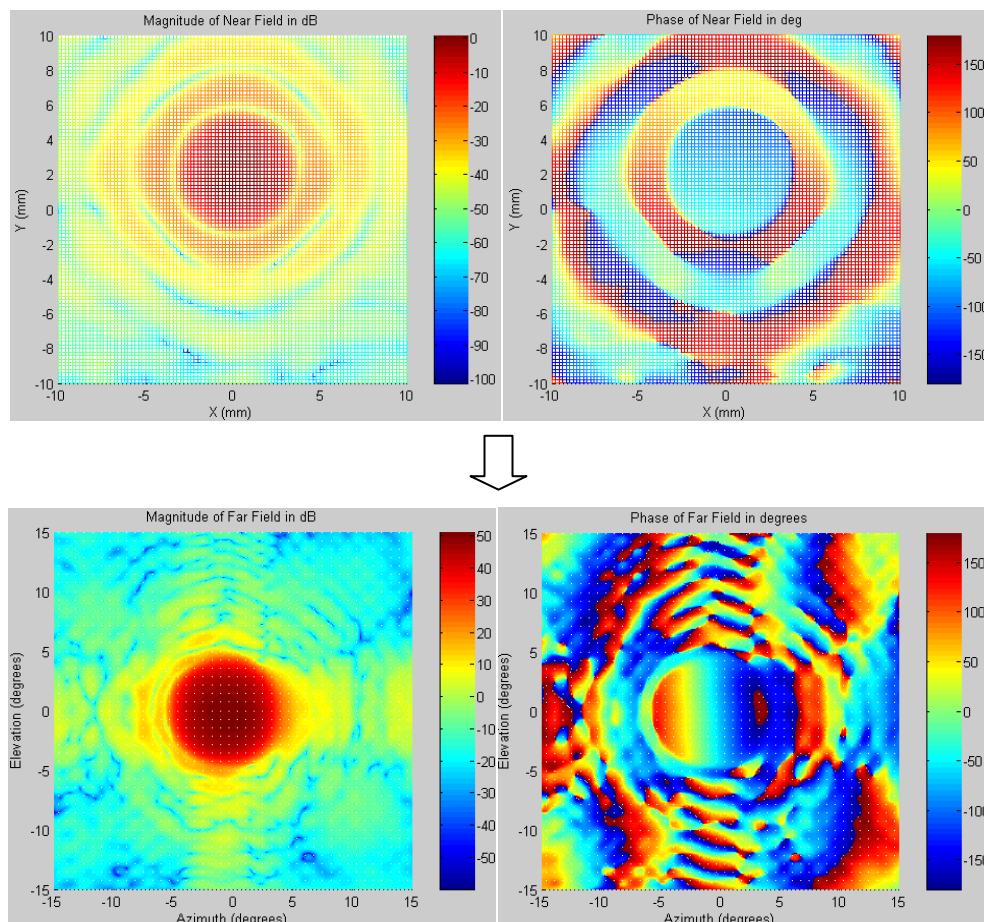


Figure 2.3. NF to FF transformation of a measurement of ALMA band 10 optics at 864 GHz

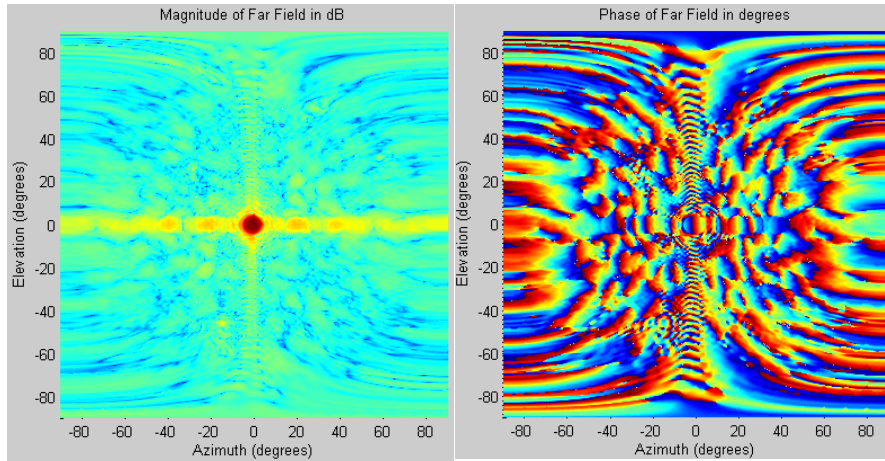


Figure 2.4. Effect of the Elevation distortion on the Azimuth for large Elevation angles

In order to appreciate the effect of aliasing, different sampling periods have been used for the same measurement at 864 GHz ($\lambda = 347.2 \mu\text{m}$). The theoretical position of the aliases in elevation, given by $\pm \sin^{-1} \frac{n\lambda}{dx}$ is ± 90 deg for $dx = 0.2$ mm, ± 60.2 deg for $dx = 0.4$ mm, and ± 25.7 deg and ± 60.2 deg for $dx = 0.8$ mm. The alias free ranges are ± 60.2 deg, ± 25.7 deg and ± 12.5 deg respectively. The results are shown in figure 2.5.

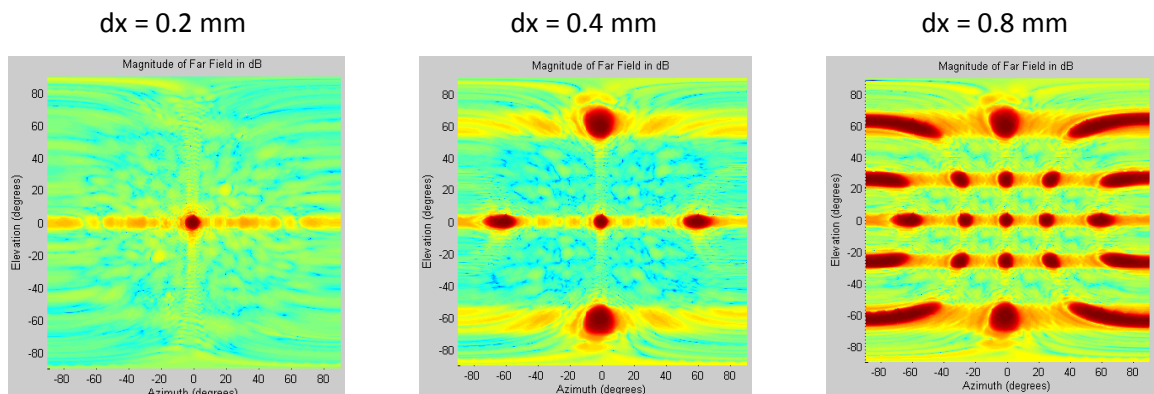


Figure 2.5. Effect of aliasing for different sampling periods in the XY plane

It is possible to use windowing on the NF data in order to reduce DFT leakage on the calculated FF [78]. In other words, it is possible to reduce the impact of the amplitude of a FF point on neighboring FF points by conditioning the NF data with some weighting functions. However, the more DFT leakage is reduced, the less spectral (angular) resolution can be achieved. Therefore, the choice of the appropriate window is a trade-off between DFT leakage and FF angular resolution. Examples of the FT of different popular windows are shown in figure 2.6. After a thorough study on ALMA band 10 optics, it was decided not to use any windows, which is equivalent to using a boxcar window, in order to not lose angular resolution.

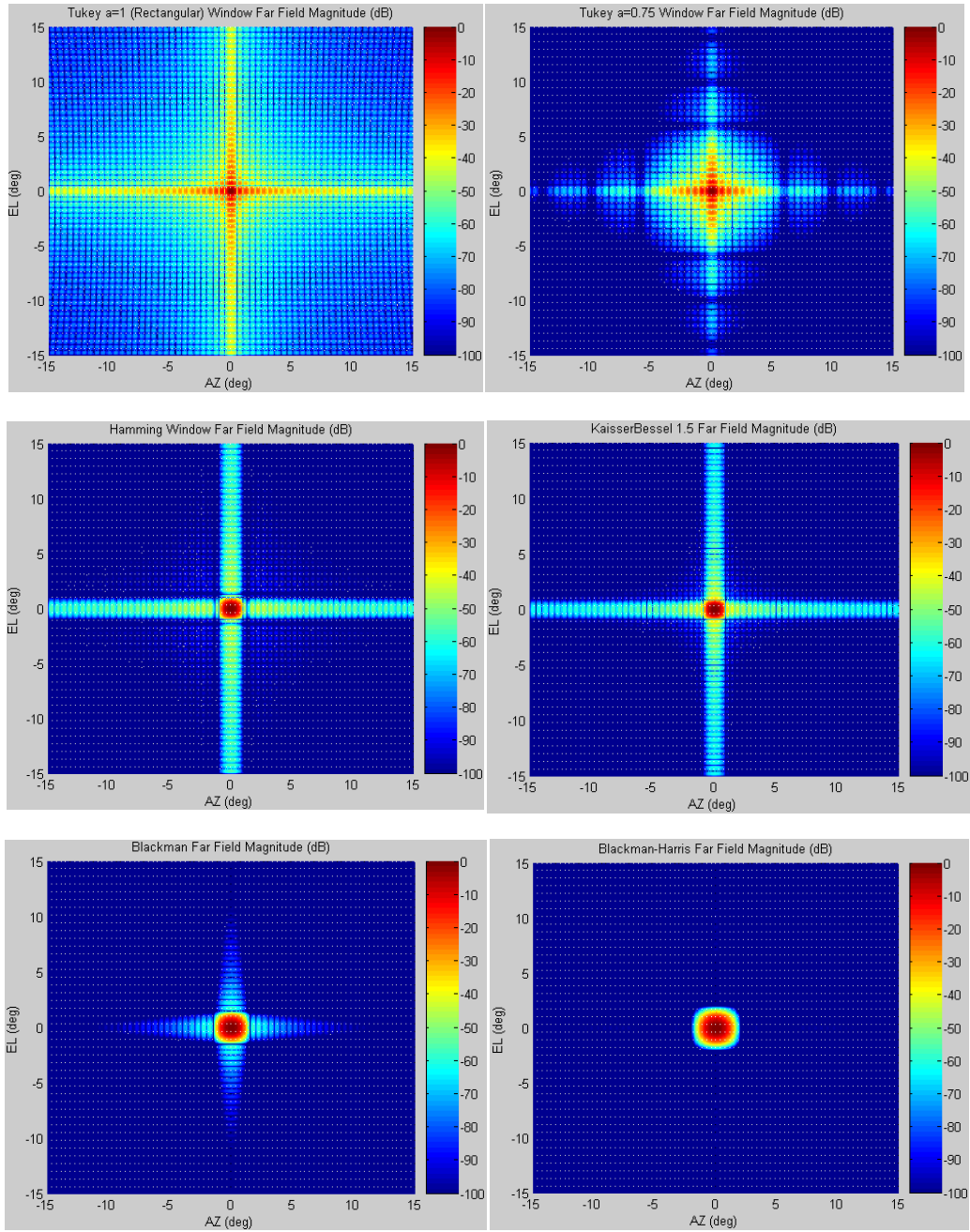


Figure 2.6. Far-Field transformation of window functions of the same size

2.6. Performance definitions

Along this thesis, the optical performance of the radio astronomy receivers under study is measured in terms of some efficiencies or some other quantities derived from offsets with respect to design values. In the case of ALMA and ASTE, telescopes are Cassegrain antennas with the receivers under study located in the focus of the secondary mirror. Additionally, in both cases, the design of the antenna is independent of the design of the receivers. Therefore, in order to make optical specifications of both systems independent, the specifications of the receiver optical

performance are referred to the secondary mirror of the Cassegrain antenna, whereas the specifications of the primary mirror are referred to an expected illumination in the secondary. Therefore, for the receivers, there is a spillover efficiency defined at the secondary mirror or a secondary mirror taper efficiency, among others. This section defines all the quantities which will be used along this thesis to describe the optical performance of receivers. In most definitions, it will be assumed that the receiver illuminates the secondary mirror to ease understanding. This is valid again in virtue of the reciprocity theorem [76].

- Spillover efficiency

The spillover efficiency indicates the fraction of electrical power reflected in the secondary mirror, and thus useful, with respect to the total power coming from the receiver. The rest of the energy will be lost. The expression to calculate spillover efficiency is given by (2.24).

$$\eta_{\text{spillover}} = \frac{\iint_{\text{sec}} |E|^2 dS}{\iint |E|^2 dS} \quad (2.24)$$

where the integration in the numerator is over the secondary mirror aperture and the integration in the denominator is everywhere in the aperture plane.

- Taper efficiency

The secondary mirror surface must be illuminated with constant electrical field amplitude and with constant phase for optimum efficiency. Therefore, the correlation of the field E at the secondary mirror and a plane wave $E_0 e^{-j\vec{k}\vec{r}}$, with E_0 constant, indicates how good the illumination is. This can be expressed mathematically as in (2.25).

$$\eta_{\text{taper}} = \frac{|\iint_{\text{sec}} E e^{j\vec{k}\vec{r}} dS|^2}{(\iint_{\text{sec}} dS) \cdot (\iint_{\text{sec}} |E|^2 dS)} \quad (2.25)$$

- Illumination efficiency

The illumination efficiency is simply the product of the spillover and taper efficiencies and indicates how well illuminated is the secondary by the radiation reaching it. It can be calculated as (2.26).

$$\eta_{\text{illumination}} = \frac{|\iint_{\text{sec}} E e^{j\vec{k}\vec{r}} dS|^2}{(\iint_{\text{sec}} dS) \cdot (\iint |E|^2 dS)} \quad (2.26)$$

- Edge Taper

The Edge Taper (usually in dB) is another amount used to characterize the illumination on the secondary mirror. It is defined as the average difference of the electrical field at the edge of the secondary with respect to the maximum value of the electrical field. For a specific kind of

illumination, and for a centered beam, certain values of Edge Taper provide optimal illumination efficiency. In the case of Gaussian beams, the optimum Edge Taper is 10.9 dB.

- Polarization efficiency

In the case of ALMA, receivers are able to detect orthogonal linear polarizations. The polarization efficiency indicates the fraction of power received at a given polarization E_{CO} when only that polarization arrives at the receiver from the secondary. The rest of the power is transferred to the orthogonal polarization E_{XS} and therefore lost. This can be expressed mathematically as (2.27)

$$\eta_{\text{Pol on secondary}} = \frac{\iint_{\text{sec}} |E_{CO}|^2 dS}{\iint_{\text{sec}} |E_{CO}|^2 dS + \iint_{\text{sec}} |E_{XS}|^2 dS} \quad (2.27)$$

Notice that both co-polar and cross-polar fields are integrated over the secondary aperture. The cross-polarization value of interest is thus the integrated power and not the peak value.

The total integrated cross-polarization power in dB is an alternative amount to describe the same efficiency and can be calculated as indicated in (2.28).

$$\text{Integrated XsP} = 10 \log_{10} \frac{\iint_{\text{sec}} |E_{XS}|^2 dS}{\iint_{\text{sec}} |E_{CO}|^2 dS} \quad (2.28)$$

In some cases, especially in near-field measurements, the peak value of the cross-polarization field with respect to the maximum value of the co-polarization field is also considered as a good indicator of the polarization purity of a receiver. This value will also be used throughout this thesis. In the case of ALMA, the polarization efficiency in the secondary must be better than 99.5 % or -23 dB.

- Defocus efficiency

The defocus efficiency indicates the loss of efficiency due to the offset of the focal point of the receiver beam with respect to the focal point of the secondary. According to [79], the defocus efficiency for a Gaussian beam whose focus is δ away from the secondary mirror focus in a Cassegrain antenna is given by (2.29), where $\alpha=0.115 \text{ EdgeTaper(dB)}$, $\beta=2k\delta/(4f_e/D_p)^2$, D_p is the diameter of the primary mirror and f_e is the equivalent focal distance of the Cassegrain antenna.

$$\eta_{\text{Defocus}} = \frac{\alpha^2}{\alpha^2 + \beta^2} \frac{1 + e^{-2\alpha} - 2e^{-\alpha} \cos \beta}{1 + e^{-2\alpha} - 2e^{-\alpha}} \quad (2.29)$$

If $\beta \ll 1$, the exact defocus efficiency equation (2.29) can be approximated by a Taylor expansion as:

$$\eta_{\text{Defocus}} = 1 - \frac{1}{\alpha^2} \left(1 - \frac{\alpha^2 e^{-\alpha}}{(1 - e^{-\alpha})^2} \right) \beta^2 = 1 - \frac{4}{\alpha^2} \left(1 - \frac{\alpha^2 e^{-\alpha}}{(1 - e^{-\alpha})^2} \right) \left(\frac{k\delta}{(4f_e/D_p)^2} \right)^2 \quad (2.30)$$

For an optimal Gaussian beam Edge Taper of 10.9 dB, $\alpha=1.254$ and $\frac{4}{\alpha^2} \left(1 - \frac{\alpha^2 e^{-\alpha}}{(1-e^{-\alpha})^2}\right)=0.309$. Therefore, (2.29) can be simplified to (2.31) in this useful particular case.

$$\eta_{\text{Defocus}} = 1 - 0.3 \cdot \left(\frac{k\delta}{(4f_e/D_p)^2} \right)^2 \quad (2.31)$$

In the case of the ALMA antenna, the secondary focus can be repositioned in order to minimize the loss of efficiency due to the defocus. When the two linear orthogonal polarizations are observed simultaneously, the secondary focus is positioned at an equal distance to the focal points of both orthogonal polarizations. In other words, the secondary mirror focus is positioned in the middle between the focal points of both polarizations. Therefore, the optimal defocus efficiency in the case of ALMA receivers is the same for both polarizations, since the absolute value of δ is the same for both polarizations. In the case of ALMA, the defocus efficiency must be better than 98 %.

- Aperture efficiency

This is the most important efficiency to describe the performance of a receiver. It is defined as the product of all previous efficiencies, as indicated in (2.32).

$$\eta_{\text{ap}} = \eta_{\text{illumination}} \cdot \eta_{\text{polarization}} \cdot \eta_{\text{defocus}} \quad (2.32)$$

In the case of ALMA, the aperture efficiency in the secondary must be better than 80 %.

- Beam squint

The beam squint in the sky is the angular separation in the sky of the beams corresponding to two orthogonal polarizations. This separation is due to the transverse offset of beam waists at the focal plane of the secondary mirror. Linear offsets Δx , Δy in the focal plane are related to angles in the sky θ by the equivalent focal distance of the telescope f_e as stated in (2.33). Units in (2.33) are m for offsets and focal distance and radians for the angle θ .

$$\theta = \frac{\sqrt{\Delta x^2 + \Delta y^2}}{f_e} \quad (2.33)$$

The equivalent focal distance of a Cassegrain telescope [80], as ALMA or ASTE, is related to the focal distance of the primary mirror f_p and the magnification factor of the secondary M . The magnification factor is related to the eccentricity e of the hyperboloidal secondary mirror as $M=(e+1)/(e-1)$. In the case of the ALMA antenna, f_p is 4.8 m and M is 20, which results in an equivalent focal distance f_e of 96 m.

It is common to express beam squint requirements as a percentage of the beam width. For example, the beam squint requirement in ALMA is 10 % of the full beam width at half maximum (FWHM). The FWHM value is proportional to the quotient of the wavelength and the largest size of the antenna D , which corresponds to the diameter of the primary mirror. The proportionality

constant depends on the specific kind of beam. For a Gaussian beam, it is $1.02 + 0.0135$ Edge Taper (dB) according to formula (6.41) in [62]. In the case of an optimum Edge Taper of 10.9 dB, it is 1.167. If the Edge Taper is 10 dB (such as for ALMA band 10), it is 1.155. Therefore, the beam squint θ in terms of the FWHM can be expressed as in (2.34), considering a 1.16 proportionality constant.

$$\frac{\theta}{\text{FWHM}} (\%) = 100 \frac{D\sqrt{\Delta x^2 + \Delta y^2}}{1.16\lambda f_e} \quad (2.34)$$

In the case of the 12 m ALMA antenna and in terms of the frequency f in GHz and focal plane offsets in mm, (2.34) can be rewritten as in (2.35):

$$\text{Beam Squint} = \frac{\theta}{\text{FWHM}} (\%) = 0.03592 \cdot f(\text{GHz})\sqrt{\Delta x^2 + \Delta y^2} \quad (2.35)$$

For example, a maximum beam squint of 10% at the highest ALMA band 10 frequency (950 GHz) means the root-mean-square (RMS) waist offset in the focal plane for orthogonal polarizations must be less than 0.29 mm or slightly less than a wavelength (0.928λ).

Chapter 3

LO Injection using Optics

3.1. Introduction

Heterodyne receivers down-convert the RF signal coming from astronomical sources to an intermediate frequency (IF) by means of a local oscillator (LO) signal. In the case of SIS/HEB mixers, the LO signal provides pumping to the superconducting devices. In other words, together with the DC bias, it provides the operating conditions at which the mixing will take place. In the absence of RF signal, the device current will be a constant determined by the DC bias voltage in the I-V curve corresponding to the existing pumping LO power. Therefore, the stability of the LO signal is critical to provide a stable operating point for astronomical observations. Unstable bias points will worsen phase and amplitude stabilities and add noise to the astronomical data. When an RF signal is injected, the RF voltage makes the device voltage fluctuate around the bias voltage, but will not change the I-V curve provided the RF power is much smaller than the LO power.

In the case of SIS/HEB mixers, the I-V curve of the superconducting devices changes when they are pumped with a LO signal. In the case of a SIS junction, photon steps due to photon assisted tunneling appear below the voltage gap in the I-V curve. In the case of an HEB, superconductivity is locally broken and the I-V curve gets closer to the normal resistance I-V curve. These phenomena are depicted in figure 3.1.

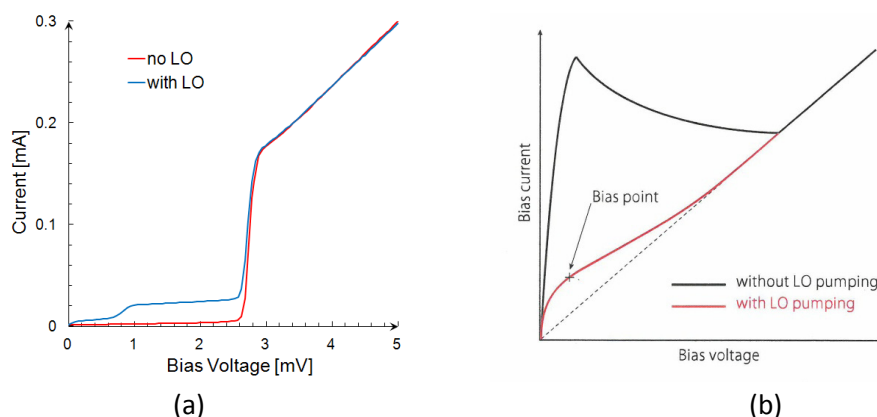


Figure 3.1. Effect of LO pumping on the I-V curves of: (a) ALMA band 10 mixer, (b) HEB mixer (SOURCE for (b): [57])

LO signals at the lower end of the THz range (frequency below ~ 1.5 THz) are usually generated by frequency multiplication of low frequency signals. Lasers are used at the higher end of the THz range. In both cases, the full LO source dissipates a considerable amount of power and in some cases, it can be bulky. However, superconducting devices must be cooled down within a cryostat to very low temperatures for their proper operation. In most cases, the cryostat power and size requirements do not allow LO sources to be near the mixers. Therefore, low-loss transmission of LO power is required between the LO source and the mixer element.

At THz frequencies, there are two existing technologies which provide LO power transmission: waveguides or quasi-optical techniques. Waveguides are preferable at low THz frequencies, due to the simplicity of the design. However, as frequency increases, so does metallic loss. As a consequence, loss around 0.5-1 THz is too high for reasonable waveguide lengths. At those frequencies, quasi-optical techniques can provide a low-loss and compact alternative transmission system. Quasi-optical waveguides are a well-known technology [81-82] and have been successfully used in receivers at mm/sub-mm wavelengths [83]. At high frequencies, the size of horns and mirrors is very compact and radiated beam sizes can be kept small. Additionally, Gaussian beam modeling simplifies the design of this kind of system. Quasi-optical beams created by common antenna horns can be modeled easily using fundamental Gaussian beams. The radiated beams can then be redirected and focused using mirrors. The lost radiated power can be minimized by correctly dimensioning mirrors. However, the performance of this kind of system is often difficult to characterize. The difficulty in the characterization lies in the difficulty to perform accurate measurements at these high frequencies, at which most measurement systems are cutting-edge technology [84].

3.2. Limits of LO Waveguide Feeding

Waveguide technology becomes very lossy at high frequencies due to the small size of waveguides and other effects like roughness or anomalous skin effect [85]. This can be explained easily considering the expression of loss in term of frequency (3.1), which can be derived from the expression for loss of the fundamental TE_{10} mode provided in [86],

$$\alpha = 8.676 \frac{1}{b} \sqrt{\frac{\pi \epsilon}{\sigma}} \frac{f^2 + \frac{2b}{a} f_c^2}{\sqrt{f} \sqrt{f^2 - f_c^2}} \text{ dB/m} \quad (3.1)$$

where a , b are the waveguide dimensions, ϵ is the medium permittivity, σ is the conductivity of the waveguide walls and f_c is the waveguide cut-off frequency. The loss is inversely proportional to the dimensions of the waveguide b and approximately proportional to the square root of frequency. Besides, the effect of roughness in the waveguide must be accounted for, and according to [87], the loss increases by a factor 1.3. Additionally, the anomalous skin effect adds an additional 13.5% increase in the case of copper at room temperature [87]. Therefore, the use of long waveguides for power transmission at THz frequencies presents heavy loss.

Additionally, there can be standing wave problems in the case of waveguide feeding due to impedance matching. In the case of waveguide feeding, the waveguide is bringing the impedances of distant elements together just by some basic impedance transformation, equivalent to rotating one of the impedances in a Smith chart. The result is often an impedance mismatch which sometimes translates in strong standing waves. Additionally, the period of the standing waves is very short, which corresponds to long distances. Standing waves can cause the available LO power to be too low at the mixing element for proper operation. Short standing wave periods translate into more points with the same behavior, this is, frequencies at which the devices are under-pumped. In the case of quasi-optical injection, the impedance of the different elements (mixer, LO source...) are matched to the free space impedance by means of radiating elements. Therefore, the matching is somehow improved between elements in both ends of the quasi-optical system. Additionally, distances between elements which could have a large mismatch (mixer/multiplier to antenna) are shortened, which increases the period of the potential standing waves and reduces the number of frequencies at which devices can be under-pumped.

In the case of ALMA band 10, the original LO injection design was done by means of overmoded waveguides and it proved to be troublesome. The initial LO signal is generated at around 16 GHz and then, it is frequency-multiplied by a factor 54 (6x3x3). The first multiplier (x6) is outside the cryostat and the other two triplers are within it. Due to thermal reasons, both triplers cannot be located in the 4K stage of the cryostat. The original proposal for the LO injection consisted in having one tripler in the 4K stage and another one in the 110K stage and connecting them by an over-dimensioned waveguide to reduce losses, as presented in figure 3.2.

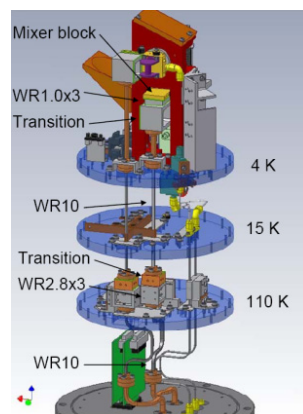


Figure 3.2. Original LO injection in ALMA band 10 by means of WR-10 waveguide and transitions

Frequency multipliers at sub-millimeter frequencies present very high return loss. This large return loss translates into a large standing wave between both triplers, as shown in the measurement in figure 3.3. Besides, waveguide technology is too lossy as explained before. All this means that apart from a strong standing wave, there were frequencies at which the SIS mixer could not be pumped properly. Therefore, it was found necessary to locate both multipliers as close together as possible. The only solution was to locate both triplers in the 110K stage. The final LO signal could be brought to the SIS mixer by waveguide technology or using quasi-optical techniques. Due to losses considerations and potential standing waves, the latter was chosen as it will be described in section 3.5.

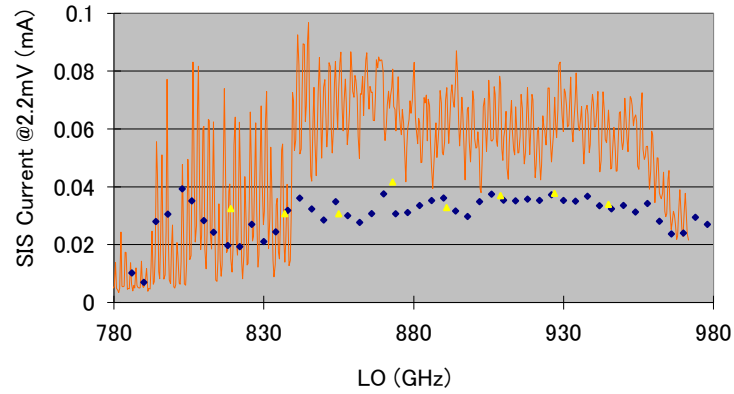


Figure 3.3. Pump current in SIS mixer. In orange, maximum available current. In blue/yellow, operating current in different conditions. Nominal minimum operating current is 0.03 mA

3.3. Quasi-Optical Injection

The schematic of a possible realization of a horn-to-horn power transmission system at THz frequencies is shown in figure 3.4. The variables involved in the design are the radii of curvature of the two ellipsoidal mirrors, R_{in} and R_{out} , the horn dimensions, and the distance between mirrors, d_2 , and between horn and mirror, d_1 . These design parameters are shown in figure 3.4. Both horns are considered identical. The horn dimensions and the distance between mirrors are usually given by the available horns and by the distance over which power must be transmitted. Then, the mirror parameters and the distance between horn and mirror have to be decided. The values of radii of curvature of mirrors (R_{in} , R_{out}) and distance (d_1) between horns and mirrors can be calculated using Gaussian optics design techniques [62]. The horn dimensions will determine the position and size of the initial waist, whereas distances d_1 , d_2 and the radii of curvature of the ellipsoidal mirrors will determine the ABCD matrices of the system.

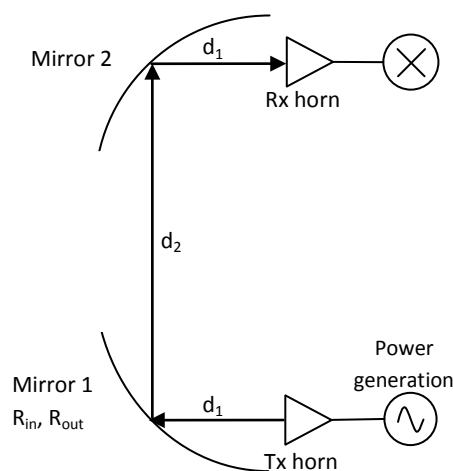


Figure 3.4. Schematic and variable names for the proposed horn-to-horn power transmission system

Distance d_1 must be such that it guarantees that the Gaussian beam reaching mirror 1 has a radius of curvature equal to the radius of curvature of mirror 1 on the transmitting side, R_{in} . This guarantees minimum beam phase distortion. Under these conditions, the output beam of mirror 1 will have radius of curvature $-R_{out}$. Identical mirrors with the same radii of curvature are preferred in order to achieve the same electric field amplitude and phase mapping in the aperture plane of the transmitting and receiving horns with a simple design. This is a condition to obtain good coupling efficiency as it will be discussed later. If the distance between the receiving horn and mirror 2 and the distance between the transmitting horn and mirror 1 had to be different, it would be necessary to use mirrors with different parameters and carefully optimize the amplitude and phase of the fields in the receiving horn aperture plane to resemble those in the transmitting horn aperture plane as much as possible. This increases the difficulty of the design process considerably. For identical mirrors, the input and output radii of curvature of mirror 2 must be R_{out} and R_{in} respectively. Then, d_2 must be such that the beam waist between mirrors 1 and 2 is exactly in the middle point between them. If the size of the waist between mirrors is appropriate, this guarantees minimum beam phase distortion in the reflection in mirror 2 and a beam waist of optimal dimensions and located in the optimal point for reception in the receiving horn. The size and position of the waist between mirrors depends on the distances d_1 and d_2 and on the initial horn waist. Using the conditions for the desired waist sizes and the conditions for non phase distortion in the mirror reflections, equations (3.2)-(3.4) were derived:

$$z_1 = \frac{z_0^2 + d_1^2 \pm \sqrt{(z_0^2 + d_1^2)^2 - z_0^2 d_2^2}}{2z_0} \quad (3.2)$$

$$R_{in} = d_1 + \frac{z_0^2}{d_1} \quad (3.3)$$

$$R_{out} = \frac{d_2}{2} + \frac{2z_1^2}{d_2} \quad (3.4)$$

where $z_0 = \pi w_0^2 / \lambda$, with λ = wavelength and w_0 = horn waist radius, $z_1 = \pi w_1^2 / \lambda$, with w_1 = waist radius between mirrors, and R_{in} , R_{out} , d_1 and d_2 are the dimensions indicated in figure 3.4. The design equations (3.2)-(3.4) have been derived using fundamental Gaussian beam theory and facilitate the design of systems as the one in figure 3.4.

Two solutions can be obtained using equation (3.2). In order to choose one of those, the amplitude distortion coefficient defined in equation (3.5) and derived from equation (5.79) in [62] must be considered:

$$U = \frac{w_m}{2\sqrt{2}} \left(\frac{1}{R_{in}} + \frac{1}{R_{out}} \right) \quad (3.5)$$

where w_m is the waist size at the ellipsoidal mirror.

The amplitude distortion coefficient is related to how asymmetrical the beam becomes after reflection and must be minimized. After using equations (3.2)-(3.4) and getting two different sets of solutions, this parameter must be calculated and the solution providing the lowest value must be chosen.

A way to further improving the initial design consists in minimizing the amplitude distortion coefficient as a function of distance d_1 only. Using all the previous conditions of waist sizes and zero phase distortion, the amplitude distortion coefficient can be described by equation (3.6):

$$U = \sqrt{\frac{\lambda}{8\pi}} \frac{\frac{d_2}{2} + \sqrt{\frac{z_1^2}{z_0}(z_1 - z_0) + \frac{z_1}{z_0} \left(\frac{d_2}{2}\right)^2}}{\sqrt{\left(\frac{d_2}{2}\right)^2 z_1 + z_1^3}} \quad (3.6)$$

The values of z_1 which maximize and minimize the amplitude distortion parameter in equation (3.6) are the roots of the polynomial $p(x)$ described in equation (3.7) which are real and for which $x \geq d_2/2$:

$$p(x) = z_0 x^7 - 9 \left(\frac{d_2}{2}\right)^2 x^6 + 7z_0 \left(\frac{d_2}{2}\right)^2 x^5 - 15 \left(\frac{d_2}{2}\right)^4 x^4 + 7z_0 \left(\frac{d_2}{2}\right)^4 x^3 - 7 \left(\frac{d_2}{2}\right)^6 x^2 + z_0 \left(\frac{d_2}{2}\right)^6 x - \left(\frac{d_2}{2}\right)^8 \quad (3.7)$$

The distance d_1 is then related to those values of z_1 by equation (3.8):

$$d_1 = \frac{z_0 z_1}{d_2/2} \frac{z_1^2 - (d_2/2)^2}{3z_1^2 + (d_2/2)^2} \quad (3.8)$$

The values of z_1 and d_1 calculated using (3.7) and (3.8) can then be used to calculate the mirror radii of curvature using equations (3.3)-(3.4). Notice that the restriction that z_1 is greater than or equal to $d_2/2$ means that the waist size between mirrors must be greater than or equal to $\sqrt{\frac{\lambda d_2}{2\pi}}$. For example, at 868 GHz, and for $d_2=200$ mm, this means the waist size between mirrors must be at least 3.32 mm. Continuing with this example, the values of waist size between mirrors can be calculated as a function of the horn waist size using equation (3.7). Results are plotted in figure 3.5 for all the values of w_0 which yield correct results. The results for the distance d_1 are quite long in all cases and require larger horns for shorter distances. The results of this example show that in some cases, the minimum amplitude distortion condition cannot be achieved in practical designs.

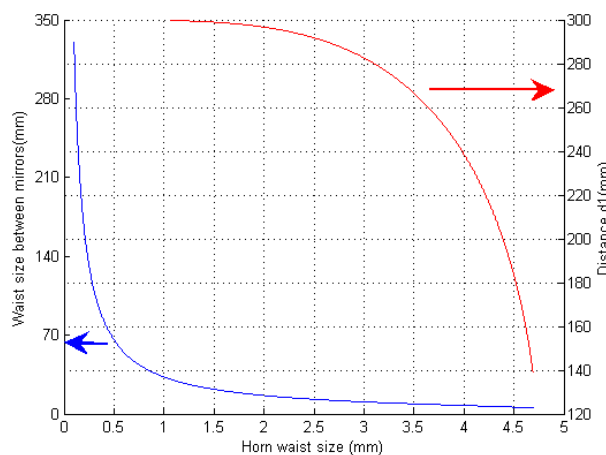


Figure 3.5. Waist size between mirrors and distance d_1 as a function of horn waist size for minimum amplitude distortion and $d_2=200$ mm

After designing the system using fundamental Gaussian beam equations, the values of the variables must be optimized to maximize the coupling efficiency between the transmitting and the receiving horns. This should be done with appropriate electromagnetic algorithms such as Physical Optics, described in section 2.3. The design is also frequency dependent, since z_0 depends on frequency. Therefore, the design parameters must be optimized over the bandwidth of interest.

3.4. LO Injection for University of Tokyo HEB Receiver Experiment

3.4.1. Background

The group at University of Tokyo led by Professor Satoshi Yamamoto has developed a dual frequency (900 GHz/1.3 THz) receiver based on HEB mixers. This receiver is described in detail in [57]. The HEB mixers are fabricated and noise tested at University of Tokyo. However, the receiver beam patterns cannot be measured in-house. Since the lower frequency band of this receiver is very close to that of ALMA band 10 (787-950 GHz) and ASTE and ALMA cryostat and cartridge sizes are the same, the beam patterns could recently be measured in the ALMA band 10 laboratory at NAOJ.

The HEB receiver uses quasi-optical LO injection for both bands. In the case of nominal operation in the ASTE telescope, the LO signal is generated outside of the cryostat and then, radiated by a diagonal horn and focused by an ellipsoidal mirror attached to this horn. This LO beam enters the cryostat through a side window and it is then reflected in a couple of flat mirrors in the receiver. Finally, the LO signal is coupled to the RF signal by means of a wire grid, located before the ellipsoidal mirror in the RF path, and both of them are received by the diagonal horn in the HEB mixer block. The schematic showing how the RF and LO are originally coupled is presented in figure 3.6. The polarization of the LO and RF beams is the same after the wire grid coupling. The LO signal provides the pumping current for the HEB mixer and must therefore be as stable as possible.

In the case of the ALMA band 10 test cryostat, there are no windows for LO injection on the side of the cryostat and the LO must be injected from the RF cryostat window. Fortunately, the total distance of the LO optical path is long enough to allow the LO signal to be coupled to the RF signal and to be input together from the cryostat window. For the beam measurements at NAOJ, the optics was slightly modified to account for this need. The RF/LO coupling wire grid in the receiver was removed from its standard position and used out of the cryostat. The modified RF-LO coupling for the measurement campaign is presented in figure 3.7. The LO optical path distance is the same in both situations, which means the quasi-optical analysis is the same in both cases.

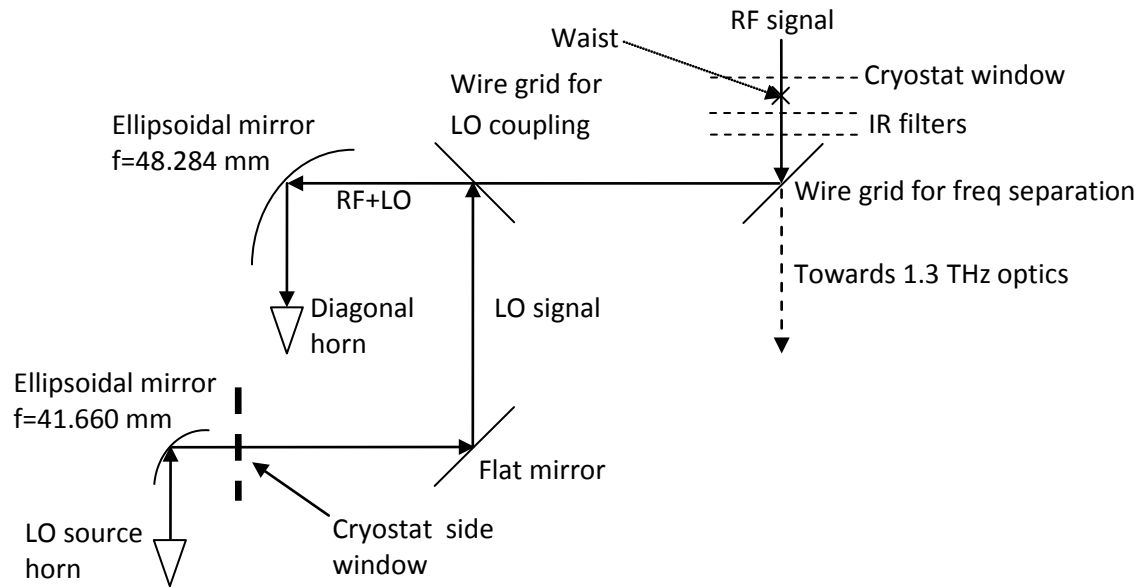


Figure 3.6. 900-GHz ASTE receiver optics

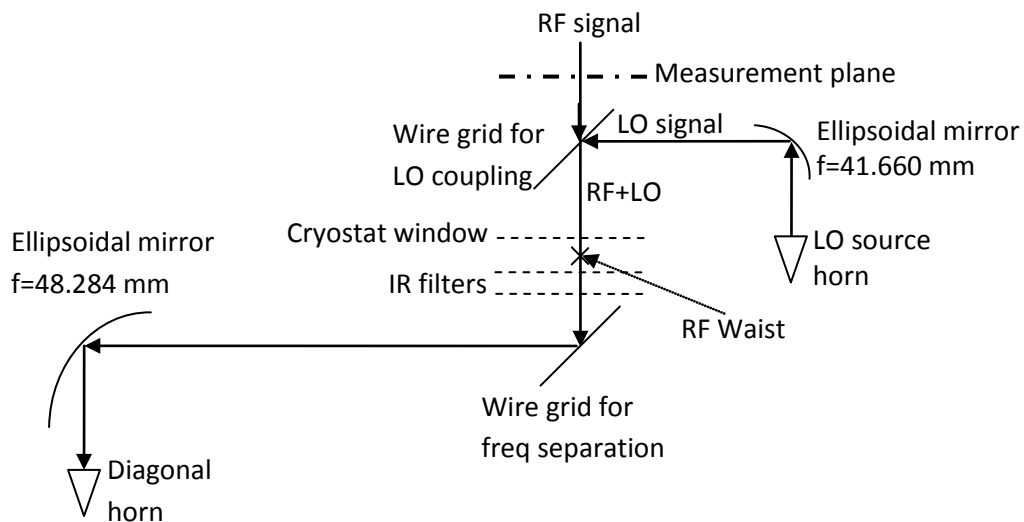


Figure. 3.7. Modification of 900-GHz ASTE receiver optics for beam pattern measurements

3.4.2. Quasi-optical analysis

The LO injection optics in figures 3.6 and 3.7 are analyzed in this section using quasi-optical analysis techniques. The LO source for the 900 GHz receiver is a 0.8-1.0 THz commercially available source fabricated by VDI [88]. It is based on a Schottky-diode multipliers chain which gets an input signal at GHz frequencies from a frequency synthesizer. The LO source output is by means of a diagonal horn whose dimensions provide a 0.691 mm waist with radius of curvature of 7.000 mm at the horn aperture (0.618 mm waist at 1.800 mm inside the horn) at 900 GHz. The LO source has an ellipsoidal mirror directly attached to it. The mirror has a focal distance $f=41.660$ mm and it is located 46.8 mm away from the horn aperture. The beam size at the mirror is 8.366 mm with radii of

curvature of 48.867 mm. Therefore, the output radius of curvature is -282.483 mm. The waist of such a source-mirror combination is located 238.712 mm from the mirror and its size is 3.293 mm. The distance between ellipsoidal mirrors in the LO optical path is 406.863 mm. Therefore, the distance from the intermediate waist to the second mirror is 168.151 mm. This means the beam size at the second mirror will be 6.340 mm with a radius of curvature of 230.289 mm. Since the second mirror focal distance is 48.284 mm, the output radius of curvature will be -61.063 mm. The output waist of the second mirror will therefore be 59.545 mm from the mirror and the size will be 1.009 mm. The distance between the second mirror and the receiving diagonal horn is 48.699 mm. Therefore, the LO beam final waist will be 10.846 mm within the horn. The receiving horn dimensions are such that the beam size at the aperture is 1.511 mm with a radius of curvature of 19 mm, which translate in a 1 mm waist at 10.676 mm within the aperture. In conclusion, the beam produced by the quasi-optical system and the beam which the receiving horn can detect are approximately the same and therefore, coupling must be good in a first order approximation. The frequency dependence of the design is presented in table 3.1.

Table 3.1. Fundamental Gaussian Beam parameters of the HEB receiver 900-GHz LO injection optics and its dependence with frequency. All values are expressed in mm

	860 GHz	900 GHz	940 GHz
Tx horn waist radius	0.623	0.618	0.613
Distance from horn waist to tx horn aperture	1.673	1.800	1.929
Beam radius at mirror 1	8.655	8.366	8.105
Beam radius of curvature at mirror 1 input	48.726	48.867	49.008
Beam radius of curvature at mirror 1 output	-287.295	-282.483	-277.839
Beam waist radius between mirrors	3.391	3.293	3.200
Beam radius at mirror 2	6.342	6.340	6.338
Beam radius of curvature at mirror 2 input	229.201	230.289	231.250
Beam radius of curvature at mirror 2 output	-61.170	-61.063	-61.026
Output waist radius	1.056	1.009	0.967
Distance from M3 to output waist	59.474	59.545	59.606
Beam radius at rx horn waist position	1.025	1.000	0.976
Beam radius of curvature at rx horn waist position	2284.769	2476.407	2675.636

In the case of the HEB receiver, the LO source and first mirror are located outside of the cryostat and their position can be modified. Therefore, before operation of the HEB receiver, it is possible to adjust the position of the source + mirror combination in order to maximize the received LO power in the HEB mixer. This can be easily done by measuring the HEB bias conditions at different LO source positions. This is a useful extra degree of flexibility to compensate for frequency dependences in the design.

In the case of the design in figure 3.7, the total length of the LO optical path was kept constant with respect to the design in figure 3.6. All elements which change the size of the LO beam are the same and are located at the same relative position in the optical path. Therefore, the quasi-optical analysis is the same for both cases. However, in figure 3.7, the size of the beam when it gets coupled to the RF beam and when it gets through the cryostat window and IR filters is different and there could be beam truncation.

The distance between the LO source mirror and the waist between mirrors is 238.712 mm. From the waist to the second mirror, it is 168.151 mm. In total, the length of the LO optical path is approximately 515 mm. The waist between mirrors is located 18.286 mm behind the ALMA band 10 test cryostat window. Therefore, the size of the beam at the window is 3.346 mm. The window radius is 10 mm. The truncation of the beam occurs at a distance $3w$ from the beam center, which means truncation at less than -77 dB from the beam maximum. Therefore, there are no truncation problems at the window. The IR filters are located at 32.714 and 64.714 mm from the waist and the diameters of the existing apertures are 25 and 30 mm, respectively. The beam sizes at those positions are 3.458 and 3.898 mm, respectively, which means truncation at less than -100 dB with respect to the beam maximum. The wire grid used to couple the RF and LO signals is located 44.5 mm from the waist, and the beam size is 3.592 mm. The wire grid diameter is 25 mm. This means the truncation occurs at $3.5w$ or at less than -100 dB. In conclusion, the change in the LO injection path does not bring about any truncation to the LO beam and the HEB mixer can be properly pumped as in figure 3.7.

For the experiment at NAOJ, the ALMA band 10 test cryostat was used to cool down the HEB receiver. The cryostat vibrates mechanically at a frequency of 1 Hz in the direction of the incoming beams. Therefore, the LO optical path changes a random distance at that frequency. A main concern at this point was if the injected LO signal would be stable enough for the HEB mixer. The first measurements proved that the HEB bias point was acceptably stable and measurements could be performed as explained in chapter 4.

3.5. LO Injection for ALMA Band 10

3.5.1. Design

ALMA band 10 receiver [89] is a cryogenically cooled heterodyne receiver working in the 787-950 GHz frequency band. The frequency down-conversion is achieved by means of a superconductor-insulator-superconductor (SIS) mixer based on NbTiN superconducting technology. This SIS mixer requires to be cooled down at 4 K for proper operation. The separation between the 4K and the 110K stages in the ALMA cryostat is more than 200 mm. After generation of the final LO signal in the 110K stage, that power must be transmitted to the SIS mixer in the 4K stage. Firstly, local oscillator power is transmitted by means of two diagonal horns and two ellipsoidal mirrors from the LO power generator to the SIS mixer block located at different cryostat levels, as indicated schematically in figure 3.4. Then, the received power is injected into the SIS mixer using a 10-dB waveguide

directional coupler. Figure 3.8 indicates the position of the LO diagonal horn in the mixer block and shows how the coupling between the RF and LO signals is performed in the mixer block.

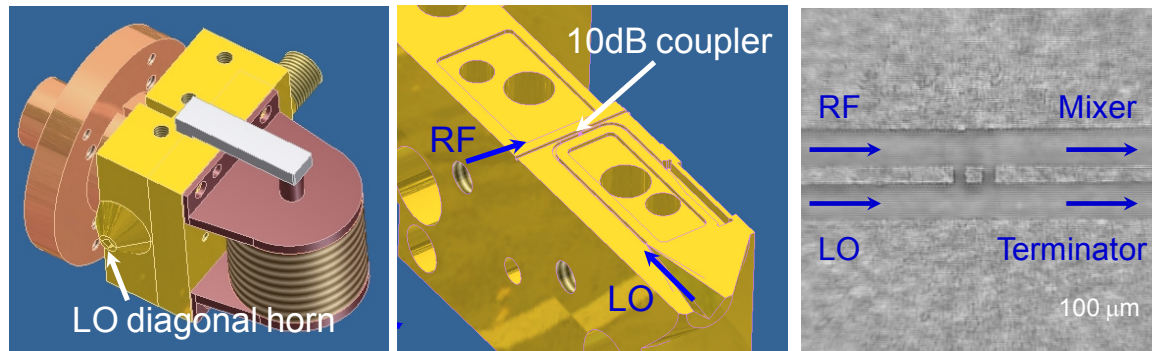


Figure 3.8. Graphical explanation of LO signal coupling to the RF signal after detection at the LO diagonal horn

The ALMA band 10 receiver works from 787 GHz to 950 GHz, with a 4-12 GHz IF bandwidth. The current SIS mixing scheme performs double side-band (DSB) down-conversion, which means the LO frequencies must range from 799 GHz to 938 GHz. Therefore, the design of the LO injection system was carried out at the center frequency of the required LO bandwidth, 868 GHz.

The horns considered for this design were rectangular and diagonal horns. Corrugated horns produce better results in terms of coupling efficiency [90], but they are much more difficult to manufacture and more expensive. Therefore, it was decided to stick to simple horns for this design. It was found that power transmission between rectangular horns is worse than for equivalent diagonal horns. Therefore, diagonal horns were chosen due to high beam symmetry, high Gaussicity and ease of fabrication. The diagonal horn aperture side and axial length are $a=1.2\text{ mm}$ and $L=5\text{ mm}$, respectively. These values are a good compromise between gain and side-lobe level. These dimensions are also easy to fabricate using standard machining techniques. Gaussian optics theory states that such a diagonal horn co-polar aperture field distribution is best fitted by a Gaussian beam with radius $0.43a$ at the horn aperture [91], 0.516 mm in this case. That yields a waist radius $w_0 = 0.464\text{ mm}$ located 0.95 mm within the horn. The distance between transmitting and receiving horns must be $d_2=226.7\text{ mm}$.

Firstly, distance d_1 for minimum distortion was calculated using equations (3.7) and (3.8). The results showed that a distance $d_1= 340\text{ mm}$ and a waist size between mirrors of 80.55 mm are required, which is not acceptable for the current design. Actually, due to size restrictions, d_1 must be kept as short as possible. Besides, a larger d_1 increases the spill-over loss for a given size of ellipsoidal mirrors. Finally, a distance of 20.5 mm was chosen between the horn and mirror 1. Therefore, the effective distance d_1 between the horn waist and the mirror is 21.45 mm at 868 GHz . The input radius of curvature of mirror 1 must be $R_{in} = 21.63\text{ mm}$ according to equation (3.3). Using equations (3.2) and (3.4), two radius of curvature were obtained: $R_2 = 176.4\text{ mm}$ or 317.1 mm for waist size between mirrors equal to 3.05 mm and 4.09 mm , respectively. The amplitude distortion

coefficient given by (3.6) was calculated for both solutions and the first one ($R_2 = 176.4$ mm, $w_1=3.05$ mm) turned out to be the best.

These values provide an optimal solution from the point of view of theoretical Gaussian optics and for the size restrictions imposed by the ALMA cryostat. The waist radius at the mirrors is 5.10 mm and 3.05 mm between them. The windows between cryostat stages through which the beam must pass were chosen big enough to guarantee no significant truncation of the beam. The size of the mirrors was taken large enough to guarantee low spill-over loss. Specifically, the major and minor semi-axes of the mirror elliptical rim are 15 and 10.5 mm. Therefore, the projected rim on the direction perpendicular to beam propagation is an approximate circumference of radius 10.5 mm. Since the beam radius at 868 GHz is 5.1 mm for both mirrors, this means an edge taper in the mirrors of around 36.8 dB or spillover loss of 0.02%. The dependence with frequency of the proposed design is presented in table 3.2.

Table 3.2. Fundamental Gaussian Beam parameters for the proposed design and their dependence with frequency. All values are expressed in mm

	799 GHz	868 GHz	938 GHz
Tx horn waist radius	0.471	0.464	0.457
Distance from horn waist to tx horn aperture	0.829	0.950	1.075
Beam radius at mirror 1	5.426	5.099	4.823
Beam radius of curvature at mirror 1 input	21.491	21.630	21.771
Beam radius of curvature at mirror 1 output	-186.174	-176.406	-167.534
Beam waist radius between mirrors	3.270	3.049	2.851
Beam radius at mirror 2	5.128	5.099	5.076
Beam radius of curvature at mirror 2 input	182.278	176.406	171.898
Beam radius of curvature at mirror 2 output	-21.544	-21.630	-21.699
Output waist radius	0.499	0.464	0.433
Distance from M3 to output waist	21.340	21.450	21.541
Beam radius at rx horn waist position	0.499	0.464	0.433
Beam radius of curvature at rx horn waist position	-398.05	Infinity	99.939

3.5.2. Coupling Efficiency

The previous design is used as a zero-th order solution for the ALMA band 10 LO injection design, since it considers only one fundamental Gaussian beam is propagating between horns. In the case of diagonal horns, the percentage of power transmitted as a fundamental Gaussian beam is 93.2% [91]. TICRA GRASP [72] was used for more accurate simulations using the Physical Optics algorithm and

for optimization of the solution, including the effects of cooling down to cryogenic temperatures. ALMA band 10 optics model is presented in figure 3.9. RF optics [58] has also been included in the model to simulate all the optical elements together. The separation between the 4K and the 110K optics is clear.

The LO injection system described must be duplicated, one system for each polarization, P0 and P1. This is due to the fact that there is one SIS mixer for each polarization. The SIS mixer blocks for these two polarizations are located perpendicularly in the 4K stage due to the implementation of the separation of polarization by means of a wire grid [58]. However, both LO horns are in the same direction. Mirror M_{3P0} is the element used to provide this direction change. Notice the different orientation of mirrors M_{3P0} and M_{3P1} with respect to the diagonal horns in the 110K stage in figure 3.9.

It is important to point out that mirrors M_4 and transmitting horns are cooled down to 110 K, whereas mirrors M_3 and receiving horns are cooled down to 4 K. An optimal solution would be to have mirrors and horns of different dimensions at each cryostat stage so that, when they are cooled down to their working temperatures, the dimensions correspond to those of the design, and similar elements at 4 and 110 K stages are the same size. However, that solution is more expensive and complex. For ALMA band 10 LO injection, it was decided to use the same manufactured mirrors and horns and optimize the solution to get the best possible power coupling when elements are cooled down. The effect of shrinkage in distances has also been taken into account in the optimization using GRASP.

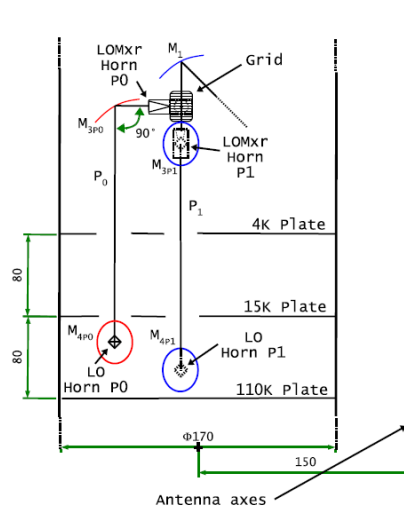


Figure 3.9. Optics model of ALMA band 10 receiver. Mirrors 1 and 2 in figure 3.4 correspond to mirrors M_3 and M_4 in this model. LO Horn P0/LO Horn P1 refers to the horns on the LO side.

LOMxr Horn P0/LOMxr Horn P1 refers to the horn on the mixer block for each polarization.

The rest of elements are the receiver tertiary optics

The electromagnetic fields arriving at the mixer horn aperture plane in the 4K stage from the LO horn in the 110K stage have been calculated for both polarizations. These fields have been used to calculate the power efficiency of the quasi-optical LO injection. Several partial efficiencies have been calculated to obtain the total efficiency η . Polarization efficiency η_{POL} has been calculated as the

power in one linear polarization divided by the total received power. Aperture efficiency η_{AP} is the power in the diagonal horn aperture divided by all the received power. Coupling efficiency η_C indicates how well the diagonal horn on the mixer end can receive the arriving power distribution. Spill-over efficiency η_{SO} , indicates the power loss by spill-over in the mirror reflections. The total efficiency has been calculated considering both co-polarization and cross-polarization received radiation, as explained in [90]. The cross-polarization part of the efficiency accounts for cross-polarization radiation which is detected by the diagonal horn cross-polarization radiation pattern. This contribution is very small in most cases. Equation (3.9) summarizes the total efficiency calculation.

$$\eta = \eta_{SO} \cdot (\eta_{POL_Co} \cdot \eta_{AP_Co} \cdot \eta_{C_Co} + \eta_{POL_Xs} \cdot \eta_{AP_Xs} \cdot \eta_{C_Xs}) \quad (3.9)$$

The optimization using GRASP consisted of maximizing the coupling efficiency in equation (3.9) over ALMA band 10 LO bandwidth. Design dimensions and efficiencies did not change much with respect to the theoretical solution, which means fundamental Gaussian beam theory was appropriate for this kind of system. The radii of curvature of mirrors after optimization are 21.6 mm and 178.8 mm at room temperature.

The resultant co-polar and cross-polar electric field distributions at the mixer horn aperture plane at 868 GHz are depicted in figure 3.10. Field distributions at other frequencies do not change much. The diagonal horn aperture is also shown in yellow for the sake of clarity. The results of the efficiency calculation at the edges and center of the ALMA band 10 LO frequency band are presented in table 3.3. The total efficiency calculated using GRASP is only around 0.2% better than the efficiency for the theoretical solution using quasi-optical theory.

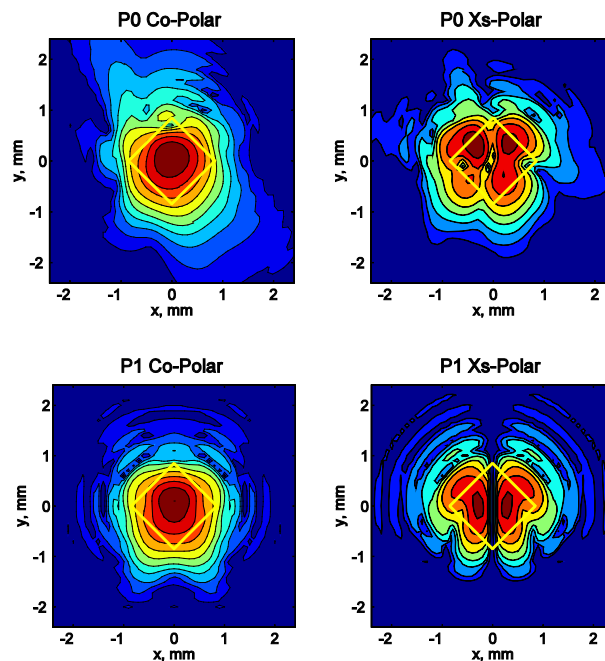


Figure 3.10. Electric field distribution at the aperture plane of the mixer horn in P0 and P1 at 868GHz. The difference between consecutive contour lines is 5 dB, the plotted values range from 0 to -60 dB

Table 3.3 shows that the efficiency is always better than 56% at all frequencies and polarizations. However, P0 is always better than P1 in terms of total efficiency; and the total efficiency degrades with increasing frequency.

Table 3.3. Partial and total efficiencies (in %) for the systems in both polarizations at 799 GHz, 868 GHz and 938 GHz

	P0			P1		
	799 GHz	868 GHz	938 GHz	799 GHz	868 GHz	938 GHz
$\eta_{\text{POL CO}}$	88.55	88.41	88.33	89.54	89.02	88.46
$\eta_{\text{POL XS}}$	9.09	9.24	9.35	7.79	8.42	9.04
$\eta_{\text{AP CO}}$	93.71	94.06	94.05	92.17	93.15	93.59
$\eta_{\text{AP XS}}$	59.54	63.42	66.90	72.46	69.74	68.57
$\eta_{\text{C CO}}$	82.62	77.87	72.03	79.19	75.57	71.05
$\eta_{\text{C XS}}$	19.79	22.87	25.43	23.41	22.33	21.18
Total η_{CO}	68.56	64.76	59.83	65.35	62.66	58.82
Total η_{XS}	1.07	1.34	1.59	1.32	1.31	01.31
η_{SO}	92.77	93.06	93.60	93.03	93.26	93.81
Total η	64.60	61.51	57.49	62.02	59.67	56.41

If a long WR-1.2 waveguide were used to transmit power 200 mm away at 868 GHz, the loss would be more than 6.3 dB. This loss can be reduced by using oversized waveguides. For example, if WR-3 is used, the theoretical loss of a straight waveguide alone would be around 2.5 dB. The price to pay is the use of waveguide section transformers and possible risks and a more difficult design due to multimode operation. Besides, extra loss must be added for any bending or transformers which are utilized; and presumably, the measured loss will be greater than the theoretical loss. Using the quasi-optical technique presented here, the total efficiency is better than 56%, which means a measured loss of 2.5 dB for the full transmission system. The disadvantage is that it is more sensitive to vibration and there is a higher risk of power leakage if the alignment between elements is lost.

3.5.3. Measurements

Two different room-temperature experiments were set up to verify the quasi-optical LO injection for ALMA band 10. The first of them consisted in mapping the co- and cross-polar field distributions near the horn aperture plane. The measured fields could then be compared to the fields in figure 3.10. The second experiment consisted in measuring the total received power after the receiving horn and using it to calculate the transmission efficiency. The position accuracy of horns and mirrors is $\pm 10 \mu\text{m}$. The machining accuracy depends on external conditions and it is difficult to assess precisely, but it is around $\pm 20 \mu\text{m}$. The roughness of the mirror surfaces expressed by means of the root-mean square profile roughness parameter R_q is $1 \mu\text{m}$.

The first measurement setup is shown in figure 3.11. The transmitter is composed of a Gunn oscillator, which transmits at around 100 GHz, followed by a chain of frequency multipliers (x9) and a

rectangular probe horn with a broad radiation pattern. The transmitter is mounted on a positioning system which allows motion on x, y and z axes and rotation around the z axis. A model with two ellipsoidal mirrors and a receiving diagonal horn reproduces the design described previously. After the diagonal horn, the received signal is down-converted to an IF frequency of 90 MHz and measured by a vector voltmeter synchronized in phase with the RF and LO signals. This system allows measuring the amplitude and the phase of the signal at any point of the measuring plane and with any linear polarization.

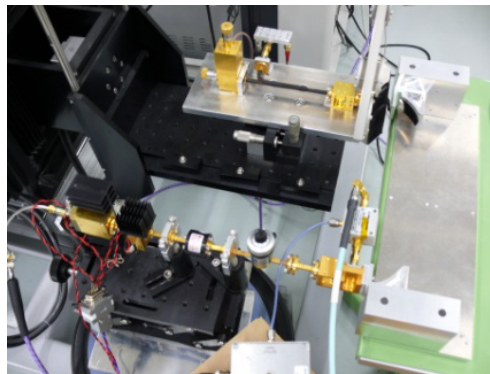


Figure 3.11. Experimental setup to measure the E-fields at the receiving horn

The actual measurement could not be performed exactly at the diagonal horn plane due to the mechanical shape of the ellipsoidal mirrors. However, it was measured as close to it as possible. The results of the measured co- and cross-polar fields are presented in figure 3.12. Fields simulated with GRASP in the same plane are also included for comparison.

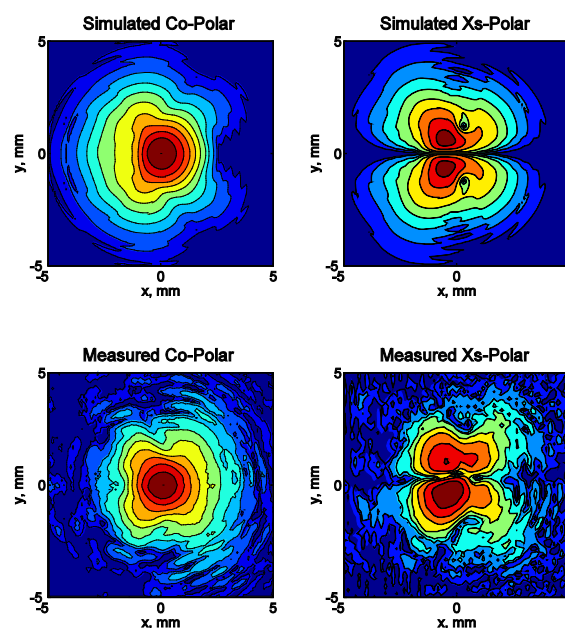


Figure 3.12. Simulated and measured electric field magnitude at a plane close to the aperture plane of the receiving horn at 868GHz. The difference between consecutive contour lines is 5 dB and the plotted values range from 0 to -60 dB

In order to compare the simulations and measurements, the co-polar fields were fitted by a fundamental Gaussian beam and the results compared. This is shown in table 3.4. The results of measurements and simulations agree quite well.

Table 3.4. Comparison of fundamental Gaussian beam fitting of simulation and measurement results.

Theoretical values included for reference

	Theoretical	Simulation	Measurement
Gaussicity	100.0 %	96.2 %	97.0%
w0x	0.464 mm	0.498 mm	0.475 mm
w0y	0.464 mm	0.468 mm	0.477 mm

The second measurement setup is shown in figure 3.13. All the design dimensions of the system under test correspond to the values designed for the ALMA band 10 receiver. Power is generated by a frequency synthesizer at around 24 GHz and multiplied to the 799-938 GHz band by means of a chain of frequency multipliers (x4, x3, x3). On the receiving side, a total power calorimeter [92] has been used to measure the total power received. This power meter is sensitive up to visible radiation. At each frequency point, two consecutive measurements have been taken with the LO source in ON and OFF states. This way, the OFF measurements can be used to calibrate the ON data in order not to account for radiation in unwanted frequencies. Then, the horns and mirrors have been removed and the transmitting and receiving end have been connected together to obtain a waveguide-to-waveguide calibration measurement.

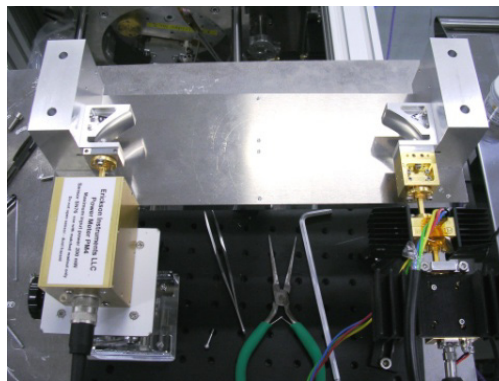


Figure 3.13. Horn-to-horn power transmission experimental setup

A significant standing wave has been found in these measurements. The lowest frequency of this standing wave, around 1.1 GHz, corresponds to a maximum distance between reflections of 13.6 cm. This distance corresponds to the dimensions between waveguide components used in the experimental setup and not to the distances between the elements composing the power transmission system.

In theory, the total power P reaching the load can be expressed as:

$$P_{\text{measured}} = P \cdot (1 - |\rho|^2) \quad (3.10)$$

where ρ is the reflection coefficient in the load [93].

Therefore, according to equation (3.10), the measured power will always be less than the power reaching the load, the power meter in this case, due to the effect of the reflection that originates the standing wave. The results of the measured power are shown in figure 3.14. The efficiency has been calculated as the ratio of the horn-to-horn measured power P_{hh} over the waveguide-to-waveguide measured power P_{ww} at each frequency. The result is presented in figure 3.15.

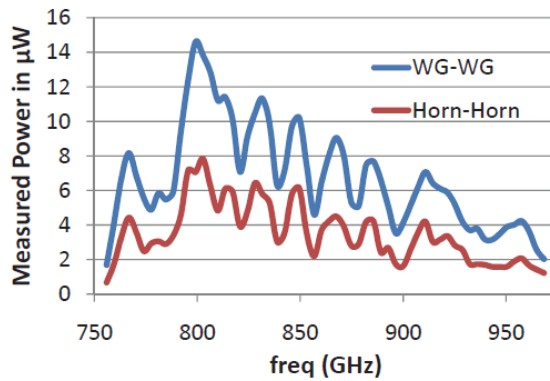


Figure 3.14. Measured power in the described experiment

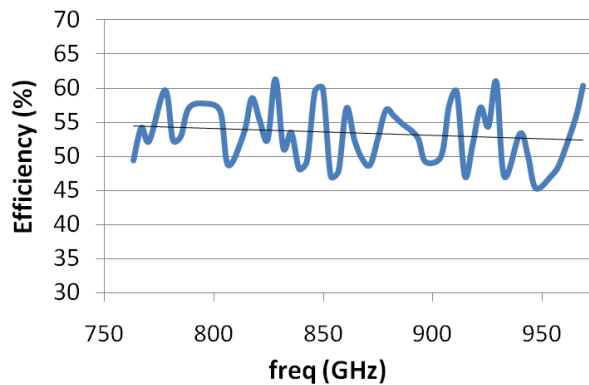


Figure 3.15. Measured efficiency of the THz horn-to-horn power transmission system

Considering equation (3.10), the calculated efficiency can be expressed as:

$$\eta_{\text{measured}} = \frac{P_{\text{hh}} - P_{\text{rh}}}{P_{\text{ww}} - P_{\text{rw}}} = \frac{\eta - P_{\text{rh}}/P_{\text{ww}}}{1 - P_{\text{rw}}/P_{\text{ww}}} \quad (3.11)$$

where η is the true efficiency, and P_{rh} , P_{rw} are the reflected power in the horn-to-horn and waveguide-to-waveguide setups.

The denominator in equation (3.11) is always less than one and will contribute to increase the measured efficiency. However, the expression in the numerator decreases the measured efficiency. After some mathematical manipulations, it is found that the measured efficiency is lower than or equal to the true efficiency when $\eta \leq P_{rh}/P_{rw}$. This condition is met approximately for all the data presented in figure 3.14. Therefore, the efficiency presented in figure 3.15 is lower than the true efficiency at almost all frequencies. The measured values of efficiency are between 50% and 60% at almost all frequencies. Therefore, the efficiency of the horn-to-horn power transmission system must be close to 55-60% at all frequencies, which means less than 2.5 dB loss. The mean value of the measured efficiency decreases with frequency, as also stated in table 3.2.

3.5.4. Application to ALMA band 10 cartridges

This power transmission system has been implemented in ALMA band 10 cartridges. It has been used to transmit the LO signal to the SIS mixers in different receiver cryostat stages. The power pumped to the SIS mixer and the power delivered from the LO have been measured for both polarizations, P0 and P1. In both cases, the power delivered to the SIS mixer is more than enough to meet operation requirements. This is shown in figure 3.16.

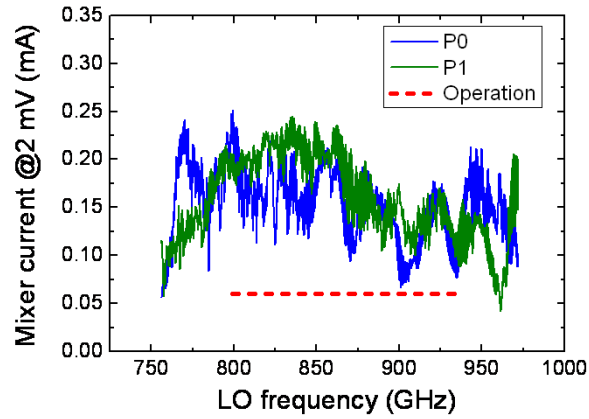


Figure 3.16. Pumped current into the SIS mixer in the receiver end of the power transmission system

The current pumped into the SIS mixer depends on the bias and LO power as described in equation (3.12),

$$I_{DC}(V_{Bias}, V_{LO}) = \sum_{n=-\infty}^{\infty} J_n^2(\alpha) I_{DC}^0 \left(V_{Bias} + \frac{n\hbar\omega}{e} \right) \quad (3.12)$$

where $\alpha = eV_{LO}/\hbar\omega$, I_{DC0} , and e are the pump strength, SIS mixer current without LO signal, and electron charge [94].

Using equation (3.12), the pump strength (or V_{LO}) and the reflection coefficient can be calculated. The calculated reflection coefficient is presented in figure 3.17. The reflection coefficient is around -20 dB.

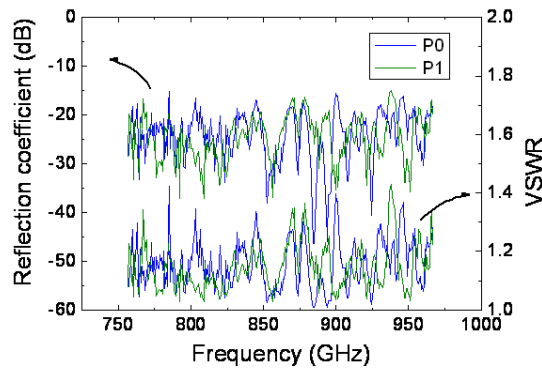


Figure 3.17. Reflection coefficient and VSWR of the power transmission system

3.6. Side-band Noise and LO Injection

3.6.1. Explanation of the problem

The output LO signal from the multipliers in the band 10 LO chain presents high side-band noise for the LO signal levels required to properly operate ALMA band 10 SIS mixers. This noise degrades the noise performance of the band 10 receiver. The current cold multipliers provide lower sideband noise when input power is high [95]. Therefore, high output power from the LO source is preferred. In that case, the total power that reaches the SIS mixer is too high for optimum operation and must be reduced. Additionally, if the LO power is reduced, the side band noise is also reduced by the same amount. Extra attenuation can be achieved by using quasi-optical attenuators in the LO injection path or by decreasing the coupling of LO signal to the SIS mixer. This second solution means a fix LO injection path design and reduces flexibility. At the moment, the output power of the LO source and multiplier chain is seldom repeatable and power conditions change for different receivers. Therefore, simple quasi-optical attenuators are preferred, since they allow choosing the appropriate attenuation for each case depending on the output power of the specific LO source and the specific performance of the components in the LO injection path for each ALMA band 10 receiver. On the other hand, the SIS junction needs a minimum pump current provided by the LO signal, and thus, a tradeoff between sideband noise and SIS pump current must be achieved. If appropriate attenuation can be provided by quasi-optical attenuators in the LO path, the cold multipliers can be over-pumped and the SIS current can be chosen to be optimum in terms of noise performance.

The radiated LO signal travels between the 110K and the 4K cryostat stages through small windows. In the original LO injection design, these windows are big enough to guarantee no truncation of the beam occurs. Quasi-optical attenuation can be carried out by making those windows smaller in size, using some metallic plates with smaller diameter. The metallic area of the window which performs truncation is painted with THz-radiation absorbent paint to ideally suppress the signal bouncing back. The used absorbent paint is composed of SiC grains (350 μm diameter), stycast epoxy 2850FT and curing agent catalyst 9 [96]. It needs curing after direct application to the attenuator. Examples of attenuators with different diameters are presented in figure 3.18.

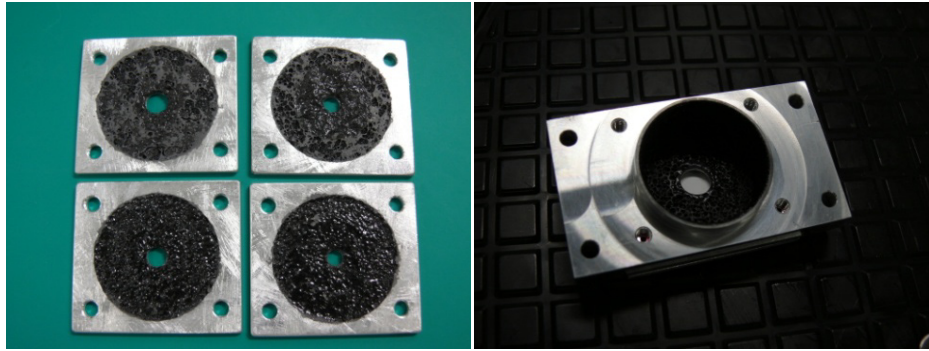


Figure 3.18. Quasi-optical attenuators for ALMA band 10 LO injection

The windows which have been covered with attenuators are the ones located between the 110K and the 15K cryostat stages. The windows between the 15K and the 4K stages keep its nominal diameter. An example of the ease of mounting of these attenuators is presented in figure 3.19. On the left of figure 3.19, the nominal IR filters at the 15K plate are presented. The attenuator on the right of figure 3.19 is mounted together with the corresponding IR filter.

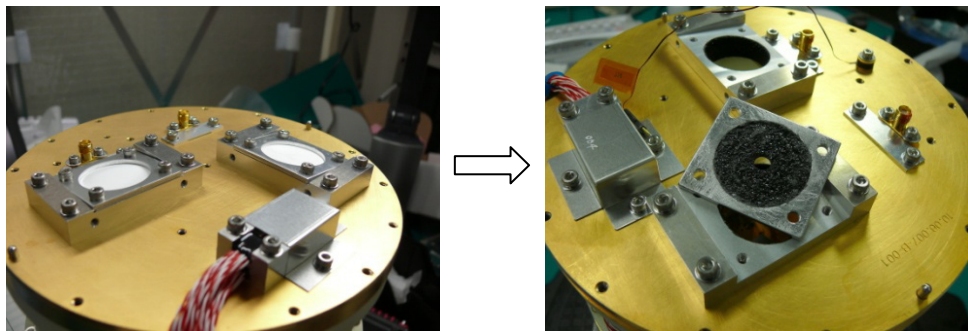


Figure 3.19. Quasi-optical attenuators in the LO injection path

3.6.2. Design of quasi-optical attenuators

The theoretical design of quasi-optical attenuators has been done by Physical Optics (PO) simulations using GRASP. Diffraction effects have been modeled using Geometrical Theory of Diffraction (GTD). The two LO windows between cryostat stages have been simulated. The size of the window closest to the SIS mixer has diameter 21.5 mm, whereas the other window is made smaller. Figure 3.20 shows the model used in GRASP to simulate the attenuation. Results of the efficiency analysis for different attenuator diameters of the LO signal for polarizations P0 and P1 are reported in tables 3.5 and 3.6. The difference in attenuation for the LO signals used for P0 and P1 is due to the fact that the distances from the mirror in the 110K stage to the respective LO window are different for them. P1 is further from the filters and therefore, the beam is smaller when it reaches the attenuator. The difference in distance for the LO signal for both polarizations is almost 34 mm.

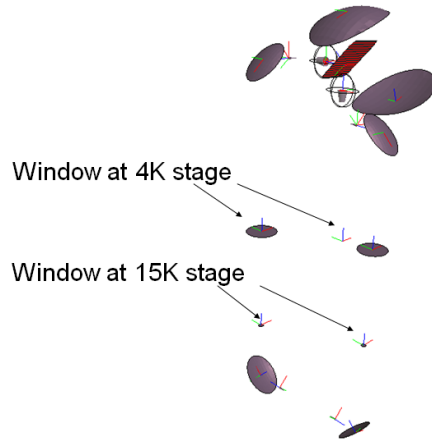


Figure 3.20. GRASP model to simulate attenuation in the LO signal path

Table 3.5. Efficiency analysis of LO transmission for P0 for different attenuators at 868 GHz

	No filter	D = 7 mm	D = 6 mm	D = 5 mm	D = 3.5 mm
η_{SO} (%)	92.39	59.61	47.65	33.78	13.52
$\eta_{POL\ COPOL}$ (%)	90.55	95.55	95.13	94.57	93.78
$\eta_{POL\ XSPOL}$ (%)	9.45	4.45	4.87	5.44	6.22
$\eta_{AP\ COPOL}$ (%)	93.28	94.23	91.89	88.86	84.11
$\eta_{AP\ XSPOL}$ (%)	60.42	81.76	78.95	75.33	70.17
$\eta_{C\ COPOL}$ (%)	83.52	62.18	54.90	47.92	39.65
$\eta_{C\ XSPOL}$ (%)	35.96	2.43	2.35	2.90	3.59
Total η_{COPOL} (%)	65.17	33.37	22.87	13.60	4.23
Total η_{XSPOL} (%)	1.90	0.05	0.04	0.04	0.02
Total η (%)	67.07	33.42	22.91	13.64	4.25
Attenuation (dB)	1.73	4.76	6.40	8.65	13.72
Extra Att (dB)	0.00	3.03	4.67	6.92	11.99

Table 3.6. Efficiency analysis of LO transmission for P1 for different attenuators at 868 GHz

	No filter	D = 7 mm	D = 6 mm	D = 5 mm	D = 3.5 mm
η_{SO} (%)	92.54	70.02	58.92	44.91	20.72
$\eta_{POL\ COPOL}$ (%)	91.38	95.26	95.14	94.77	93.84
$\eta_{POL\ XSPOL}$ (%)	8.62	4.74	4.86	5.23	6.16
$\eta_{AP\ COPOL}$ (%)	92.33	91.81	89.24	84.80	76.61
$\eta_{AP\ XSPOL}$ (%)	67.26	69.42	67.76	64.34	58.12
$\eta_{C\ COPOL}$ (%)	81.83	71.37	64.27	56.27	45.55
$\eta_{C\ XSPOL}$ (%)	32.28	0.92	0.56	1.65	2.80
Total η_{COPOL} (%)	63.88	43.70	32.15	20.31	6.78
Total η_{XSPOL} (%)	1.73	0.02	0.01	0.03	0.02
Total η (%)	65.62	43.72	32.16	20.33	6.81
Attenuation (dB)	1.83	3.59	4.94	6.92	11.67
Extra Att (dB)	0.00	1.76	3.11	5.09	9.84

The effect of truncation of the beam at the first aperture is a widening of the beam in the receiving horn, since the size of the waist between mirrors is reduced. Besides, the final beam pattern side lobes increase due to diffraction in the attenuator aperture. These two effects cause the coupling efficiency of the beam to degrade. Figure 3.21 shows the effects on the co-polar pattern of the received fields for P0 at 868 GHz in the cases without attenuation and with a 3.5 mm diameter attenuator.

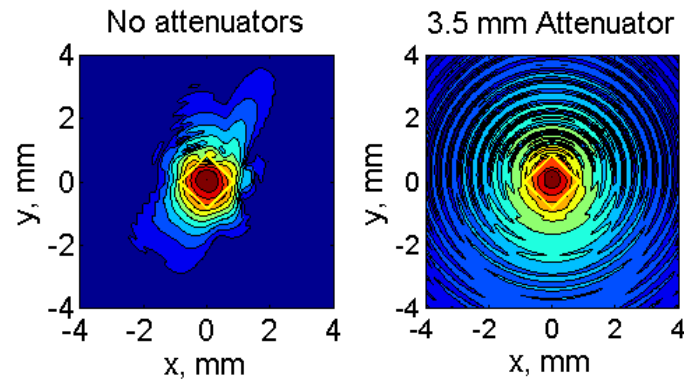


Figure 3.21. Electric field distribution at the aperture plane of the mixer horn in P0 at 868GHz. The difference between consecutive contour lines is 5 dB and values range from 0 to -60 dB

The attenuator performance is clearly frequency dependent, since the size of the beam between mirrors depends on frequency. At lower frequencies, the beam is wider and the effects of truncation will be more severe. The exact frequency dependence of attenuation will also depend on the coupling of radiation to the SIS mixer block diagonal horn and must be studied individually on a case by case basis.

Attenuators with diameter equal to 7, 6, 5 and 3.5 mm have been fabricated at NAOJ and tested with ALMA band 10 receivers. The pump current at the SIS mixer has been measured for the cases of with and without attenuators and for the mixers used for P0 and P1 polarizations. Results of pumped current are provided in figure 3.22.

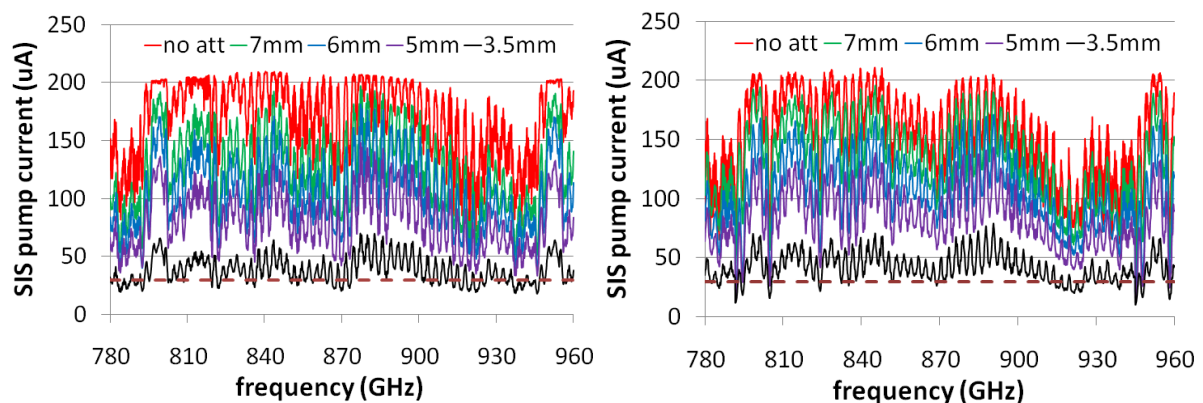


Figure 3.22. Measured SIS pump current mixer in P0 (left) and in P1 (right)

From the mixer current and using equation (3.12), the pump strength α , which is proportional to the received LO voltage, can be calculated. The values of α in the different attenuation cases are normalized by the corresponding α without attenuation and converted to dB. This is the value of attenuation. Results are presented in figure 3.23. Results present large ripples due to standing waves in the system. Therefore, it is difficult to read a unique value of attenuation at a certain frequency.

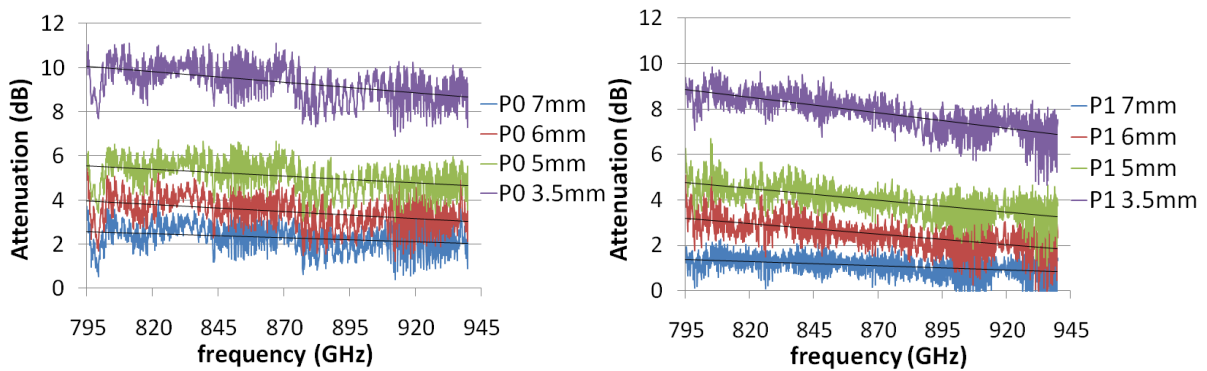


Figure 3.23. Measured attenuation for P0 LO attenuators (left) and P1 LO attenuators (right)

Table 3.7 shows a comparison of the simulated values of attenuation and the values calculated from measurement data at 868 GHz. Two values are considered for measured data, the maximum and the minimum values of attenuation around the frequency of interest. The trends in attenuation as a function of diameter and approximate values match acceptably. Measured values of attenuation are in general lower than simulations and they are more different when the attenuator aperture gets smaller. This is due to the fact that at smaller diameters diffraction effects dominate over beam truncation. Physical Optics theory is known to have some difficulties to accurately model diffracted fields, even when GTD is used [97]. Therefore, the results yielded by GRASP for small diameter attenuators are less accurate than for larger diameter values.

Table 3.7. Comparison of measured and simulated values of attenuation in dB at 868 GHz

	7mm	6mm	5mm	3.5mm
P0 Simulated	3.03	4.67	6.92	11.99
P0 Measured (max)	3.32	4.85	6.51	10.70
P0 Measured (min)	1.81	3.17	4.93	9.27
P1 Simulated	1.76	3.11	5.09	9.84
P1 Measured (max)	1.58	2.92	4.31	8.52
P1 Measured (min)	0.14	1.53	3.05	7.02

The measured uncorrected noise temperature for different attenuator diameters is presented in figure 3.24 for the mixers for both polarizations. Noise temperature clearly improves when attenuators are used. The difference between the noise temperature measured with 5 and 3.5 mm diameter attenuators does not change much, which suggests noise temperature does not improve from some value of attenuation.

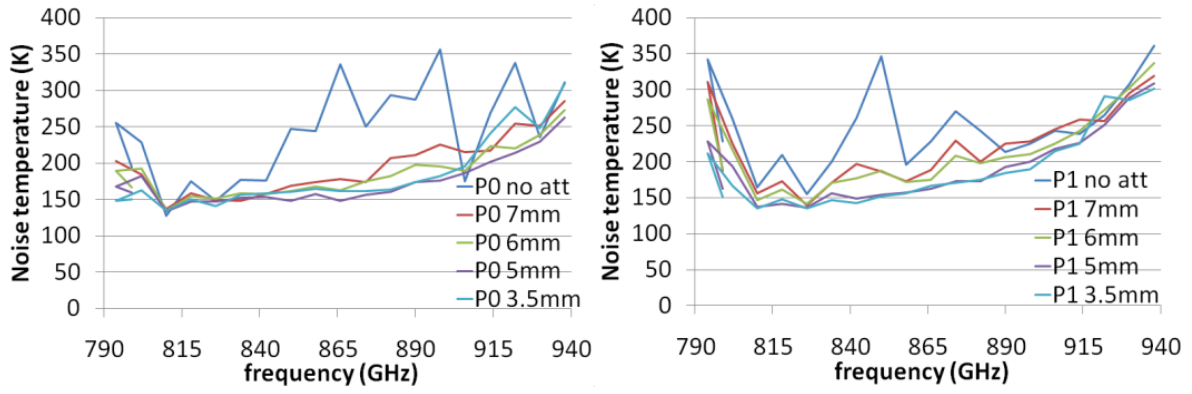


Figure 3.24. Noise temperature using different attenuators in the LO injection path

These attenuators are currently being used in the LO injection of ALMA band 10 cartridges. The appropriate value of diameter is carefully chosen for each attenuator and each cartridge in order to guarantee minimum noise and appropriate SIS mixer pumping current.

Chapter 4

Radio-Frequency Input Optics

4.1. Introduction

RF optics is the system which makes possible that the signal collected by a telescope properly reaches the detector in the astronomical receiver. The performance of RF optics will impact on the final performance of the whole telescope. The objective of the LO optics presented in chapter 3 is basically to provide stable and appropriate operational conditions for the receiver. Once the detector has been biased at a proper DC voltage/current and stably pumped by an LO signal, the RF signal can be down-converted to the IF signals which will constitute the prime matter for astronomical analyses. As explained in chapter 1, an appropriate design of the RF receiver optics makes it possible to take full advantage of the detector capabilities. Any loss or mismatches will downgrade the receiver capabilities and therefore, degrade the astronomical observations. Therefore, the performance of RF optics must be optimal. This makes RF optics one of the most important systems in astronomical receivers. Chapter 2 provided the tools necessary for the understanding of the receiver optics analysis. In chapter 4, the optics of two different astronomical receivers will be analyzed. Firstly, the 900-GHz optics in the HEB receiver developed by Professor Yamamoto's group at University of Tokyo will be studied. The original design of this optics was performed using simple quasi-optical techniques. In this chapter, that design will be validated by means of more precise Physical Optics simulations. Then, the results of the receiver experimental characterization at NAOJ already introduced in chapter 3 will be presented. Secondly, the optics in the ALMA band 10 receiver will be analyzed by quasi-optical techniques and Physical Optics software and results will be compared to measurements.

4.2. HEB receiver 900-GHz RF optics

4.2.1. Optics design

The sub-mm wavelength receiver developed at University of Tokyo uses HEB mixers [57] to detect radiation in the atmospheric windows around 900 and 1300 GHz [98]. Due to the large

difference in frequency, each band is detected by different HEB mixers located in different mixer blocks with integrated diagonal horns. The input signal is separated in the two frequency bands by means of a wire grid located just after the cryostat window, which reflects the lower band and is transparent for the upper band. Figure 4.1 shows the 4K stage of the receiver, with some modifications to have a clear view of the optics. In this study, only the 900 GHz optics is of interest and its schematic is presented in figure 4.2, which is the same as in figure 3.6 but omitting the LO injection system. This optics uses a single ellipsoidal mirror to match the beam coming from the secondary mirror of the ASTE antenna to the required beam size in the diagonal horn attached to the HEB mixer block. The local oscillator (LO) signal is injected into the HEB detector as explained in section 3.4. As explained there, the injection of the LO signal into the ALMA band 10 test cryostat requires the coupling of the RF and LO signals before the cryostat window. Therefore, the wire grid for coupling, which is normally placed just before the last ellipsoidal mirror in the optical path, is placed just in front of the cryostat window. The simplified schematic in figure 4.3 contains this little change in the optical path necessary for the experimental characterization of the optics.

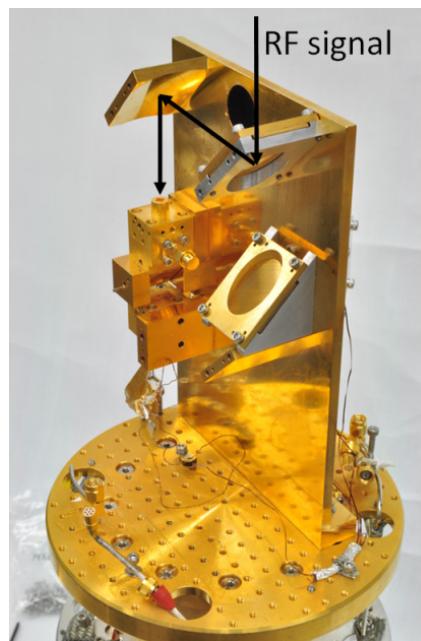


Figure 4.1. 4K stage of the HEB dual-frequency receiver, modified for a clear view of the optics

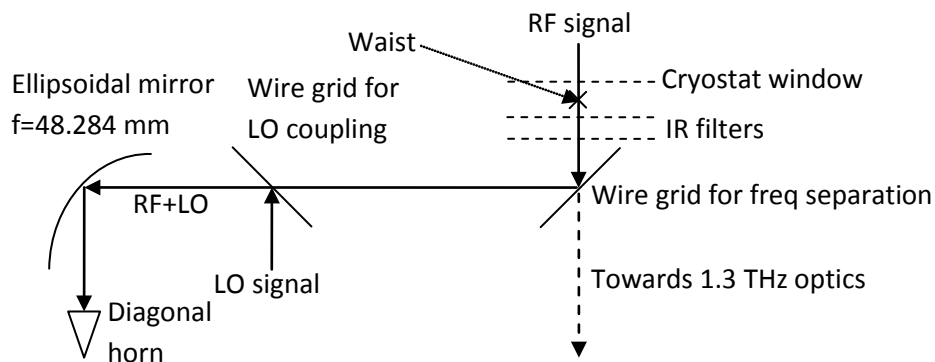


Figure 4.2. 900-GHz ASTE receiver optics

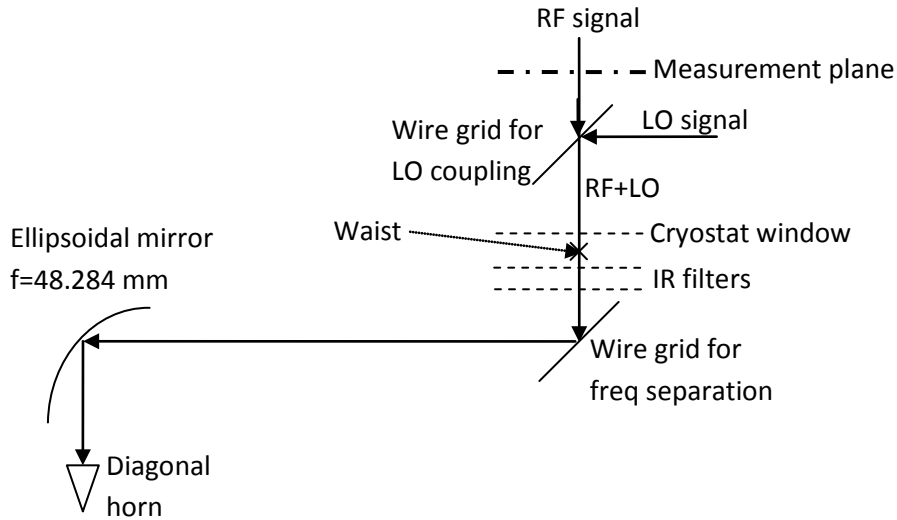


Figure 4.3. Modification of 900-GHz ASTE receiver optics for beam pattern measurements

The receiver optics has been analyzed using fundamental Gaussian beam analysis in order to obtain the sizes and radii of curvature of the ideal beams at different frequencies. The results, together with design dimensions, are presented in table 4.1. Notice that the distance mirror-waist calculated here, 172.848 mm, is slightly different from that calculated in section 3.4.2, which was 168.151 mm. This difference is due to the fact that the LO injection was not ideal. The final waist of the LO injection system did not exactly coincide in size and position with the waist of the final diagonal horn. That little difference was not important for LO injection. However, it creates that little 4.7 mm offset between the waists of the RF optics and the waist between mirrors in the LO optics.

Table 4.1. Quasi-optical analysis of ASTE 900-GHz optics (all distances in mm)

	Design	881.3 GHz	906.8 GHz	925 GHz	944 GHz
Horn side aperture	3.5				
Horn slant angle (°)	7.64°				
Horn waist radius		1.000	0.984	0.973	0.961
Distance from waist to horn aperture		10.456	10.717	10.897	11.080
Distance from horn to ellipsoidal mirror	48.699				
Beam size at ellipsoidal mirror		6.483	6.431	6.396	6.361
Beam input radius of curvature at ellipsoidal mirror		60.597	60.840	61.006	61.175
Ellipsoidal mirror focal length	48.284				
Beam output radius of curvature at ellipsoidal mirror		-237.621	-233.959	-231.525	-229.131
Final waist radius		3.385	3.290	3.225	3.160
Distance ellipsoidal mirror-waist		172.848	172.735	172.660	172.586
Distance ellipsoidal mirror-cryostat window	186.649				
Beam size at window		3.414	3.320	3.256	3.192

The optics under study has been analyzed by the Physical Optics (PO) software GRASP [72]. The beam truncation in the infrared filters and cryostat window has also been considered. Electric fields have been calculated at the theoretical beam waist location at 900 GHz (172.767 mm from ellipsoidal mirror) and at a plane at a distance of 165 mm from that waist position, which is close to the measurement plane in the performed experiments. Cross-polarization patterns have also been calculated. For the study of cross-polarization, two situations have been considered to model the frequency separation wire grid in the RF path: a perfect wire grid and a flat mirror. The actual cross-polarization of the receiver must be between those two values, depending on the quality of the wire grid. The schematic of the simulation setup in GRASP is shown in figure 4.4.

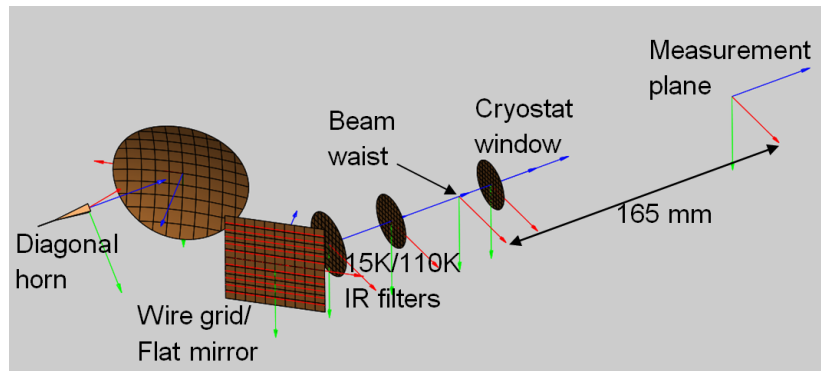


Figure 4.4. Schematic of the GRASP simulation of the optics

The results of the PO calculations have been fitted by fundamental Gaussian beams in order to be compared with the ideal quasi-optical design. Results of the fundamental Gaussian beam fitting and cross-polarization at the two planes under consideration are shown in table 4.2. These results are in good agreement with the quasi-optical analysis results in table 4.1. As expected, the shapes of the beams are similar at all frequencies. As an example, the beams at 906.8 GHz at the waist position and in the measurement plane are presented in figures 4.5 and 4.6, respectively.

Table 4.2. Gaussian beam fitting of PO results

	At waist, 172.767 mm from mirror				At meas. plane, 165 mm from waist			
Frequency (GHz)	881.3	906.8	925.0	944.0	881.3	906.8	925.0	944.0
Gaussicity (%)	94.529	94.476	94.442	94.410	94.164	94.132	94.115	94.097
Waist size in x (mm)	3.388	3.293	3.229	3.164	3.388	3.293	3.229	3.164
Waist size in y (mm)	3.382	3.286	3.221	3.156	3.382	3.286	3.221	3.156
Defocus (mm)	2.561	2.536	2.519	2.502	162.384	162.409	162.426	126.443
Offset in x (mm)	0.000	0.000	0.000	0.000	0.000	0.000	0.000	0.000
Offset in y (mm)	0.005	0.009	0.012	0.014	0.103	0.111	0.116	0.121
Tilt in x (deg)	0.000	0.000	0.000	0.000	0.000	0.000	0.000	0.000
Tilt in y (deg)	0.034	0.035	0.036	0.037	0.034	0.035	0.036	0.037
Cross-Pol wire grid (dB)	-35.22	-35.15	-35.10	-35.05	-34.86	-34.69	-34.57	-34.43
Cross-Pol flat mirror (dB)	-15.02	-15.06	-15.11	-15.17	-12.74	-12.62	-12.54	-12.46

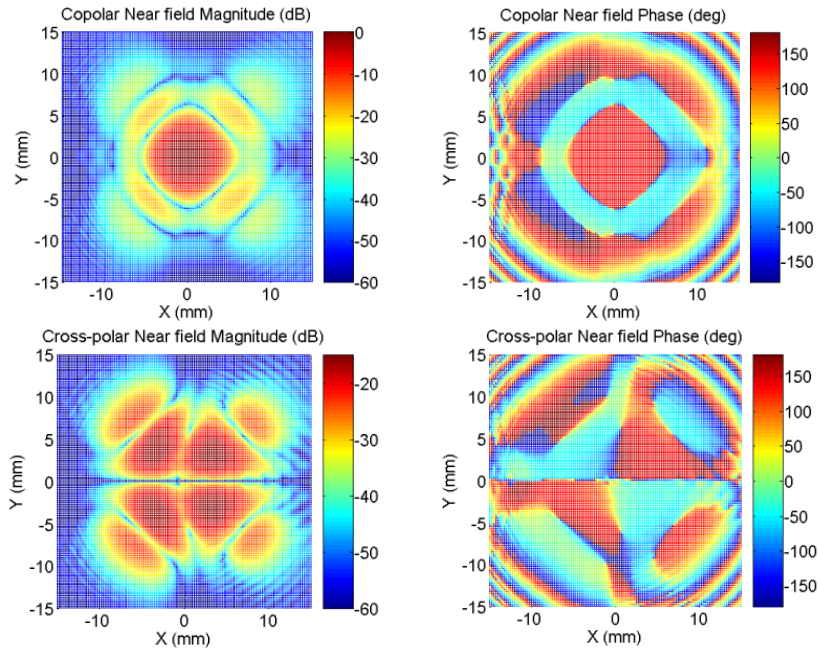


Figure 4.5. Physical optics beam pattern results at the waist plane at 906.7 GHz

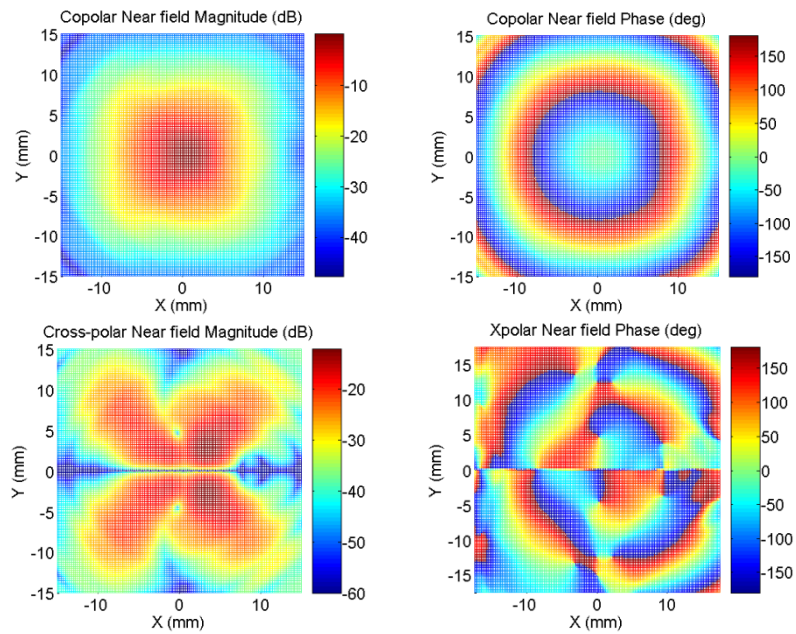


Figure 4.6. Physical optics beam pattern results at 165mm from waist plane at 906.7 GHz

4.2.2. Measurement characterization

The corrugated horn and the HEB mixer waveguide block are built together and cannot be separated. Consequently, room temperature measurements are not possible and the ASTE receiver optics must be cooled down to 4 K for its characterization using the HEB mixer to down-convert the RF signal. Mechanical 3D measurements of the cartridge were performed to guarantee that it was compatible in terms of size with the ALMA band 10 test cryostat. After size compatibility was confirmed, new cryostat beam ports and shields at the 110 K and 15 K stages were manufactured and installed in the ALMA band 10 cryostat. These parts were necessary to provide a way out of the

cryostat for the beam. These are different from the parts used for ALMA band 10, because the optical path positions of both receivers are different with respect to the cryostat axis and beams emerge from different positions [58]. ALMA band 10 Infrared filters [65] were used at the 15K and 110 K shields and a 12 micron thick Kapton film was used as cryostat window. As explained before, the coupling of the LO and RF signals was initially done by means of a wire grid. The wire grid frame was mounted on the cryostat window and it was carefully designed in order to not truncate the beam. The wires in the grid were tilted 12 degrees in order to couple both signals with the same polarization. The LO source was attached to the measurement system support structure and carefully positioned by position screws in order to provide appropriate pumping of the HEB mixer. The output power of the LO source was adjusted using an attenuator in order to provide appropriate pumping to the HEB mixer. Later on, in order to measure cross-polarization patterns, the wire grid for RF-LO coupling was changed by an 8.5 micron thick Kapton film. Both coupling methods are presented in figure 4.7. The first measurements of the receiver beam patterns probed that the LO pumping of the HEB device was stable enough for this test in spite of the 1 Hz mechanical vibration of the cold head of the cryostat. The LO coupling provided by each coupling scheme can be calculated easily using standard techniques. In the case of wire grid coupling, the grid is rotated 12 degrees with respect to the horizontal and the vertical E-field is reflected and injected into the receiver. That means the coupling in dB is:

$$\text{Wire grid Coupling} = 20\log_{10}(\sin 12^\circ) = -13.64 \text{ dB} \quad (4.1)$$

In the case of the Kapton film coupling, the coupling can be calculated using a simple lossless transmission line equivalent circuit. The coupling is just the reflection coefficient at the input of a short waveguide with characteristic impedance equal to $120\pi/\sqrt{\epsilon}$ Ohm loaded by the free space impedance, 120π Ohm. After some manipulations, the coupling can be expressed in terms of the Kapton film thickness t and relative dielectric constant ϵ as stated in equation (4.2):

$$\text{Kapton film Coupling} = 10\log_{10} \left(\frac{(1-\epsilon)^2}{\frac{4\epsilon}{\tan^2 \frac{2\pi t}{\lambda}} - (1+\epsilon)^2} \right) \quad (4.2)$$

Considering $\epsilon=3.4$ [99], the result for Kapton film thicknesses of 8.5, 12 and 25 microns is -19.72 dB, -16.81 dB and -10.95 dB. In the case of this experiment, since thinner films generate less cross-polarization, the 8.5 micron film was chosen and the attenuation of the LO source output was reduced a few dB to provide a similar LO power at the HEB mixer.

The measurement system block diagram is presented in figure 4.8. It is based on the ALMA band 10 room temperature measurement setup [58] with some important modifications to adapt it to the IF frequencies of the HEB mixer, which are around 1 GHz instead of in the 4-12 GHz frequency range for ALMA band 10. Using this setup, amplitude and phase of the signal can be measured.

By changing the position of the RF probe horn using a XYZ θ stage, the near field patterns can be measured as explained in [100]. A 10-MHz frequency reference is used as the phase reference for the generation of the LO, RF and auxiliary signals and for the vector voltmeter. The RF signal is generated by a Gunn diode locked in phase with the frequency standard and the LO signal, and a

chain of multipliers. The RF signal is then radiated by an open-ended WR-1.2 rectangular waveguide and detected by the receiver. The frequencies of the LO and RF are chosen to be 1.08 GHz apart in order to get that output frequency from the HEB mixer. This receiver output signal is further down-converted to a final IF frequency of 120 MHz. This signal is amplified and then, its magnitude and phase are measured by the vector voltmeter. The measurement set-up transmitter is located on a XYZ θ positioning stage, which allows changing the relative position between the probe horn and the cryostat. Careful alignment and planarity between the transmitter and the receiver is achieved by using a theodolite and mirrors and alignment marks in both transmitter and cryostat front plate. Afterwards, near-fields are measured with the transmitter at different positions in an XY plane in front of the optics, and the data is processed by fundamental Gaussian beam fitting and far-field calculations.

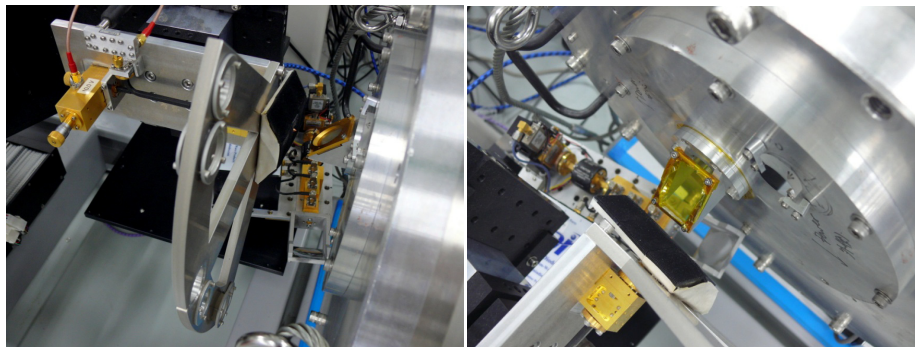


Figure 4.7. Coupling of the signals coming from the RF source (up) and the LO source (down) using a wire grid (photograph on the left) and a thin Kapton film (photograph on the right)

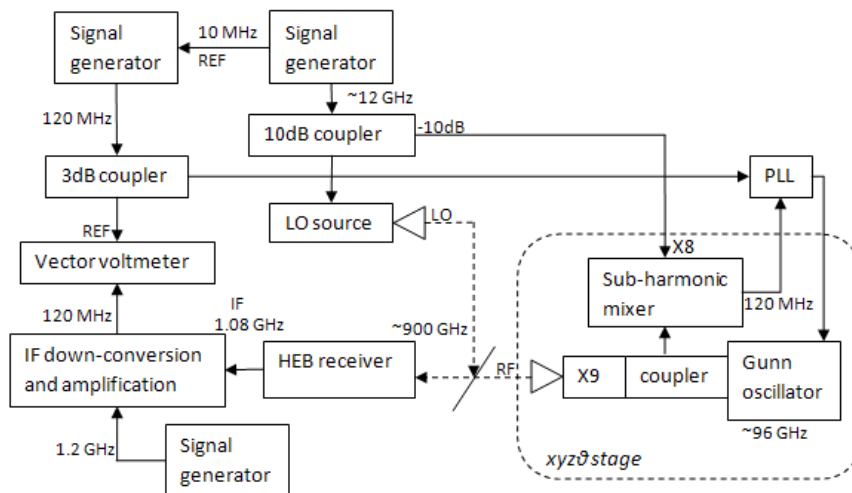


Figure 4.8. Block diagram of the measurement setup for the HEB-mixer receiver

Measurements of co- and cross-polarization beam patterns of the receiver were performed at 4 different frequencies within the RF bandwidth of the receiver. Results are shown in figure 4.9. Three of the chosen frequencies are of interest for astronomy (881.3, 906.8 and 944 GHz), whereas the other one (925 GHz) was chosen to provide a good sampling of the RF bandwidth. Co-polarization patterns using wire grid and Kapton film coupling were similar. Cross-polarization patterns using Kapton film coupling could be measured properly and cross-polarization levels with respect to the

maximum value of co-polarization could be calculated except at 906.8 GHz. At this frequency, the measured reference co-polarization pattern saturated and was unusable as a reference. Results of Gaussian beam fitting of the measured beams and cross-polarization levels are presented in table 4.3. Contrary to expectations, measured patterns are quite different from simulations. Measurements have a lower Gaussicity than expected, which is mainly due to a quite flat beam in the boresight direction. In addition, the beams are asymmetric and waist sizes are quite different from the design values at all frequencies. Beams are also tilted, with angles of almost 0.5 degrees in the X coordinate, which is the most sensitive to tolerances. Finally, the distance between the focal plane and the measurement plane changes much and has strong frequency dependence. Far-field patterns can be easily calculated from the measured data using Fourier transformation. Far-field patterns are presented in figure 4.10.

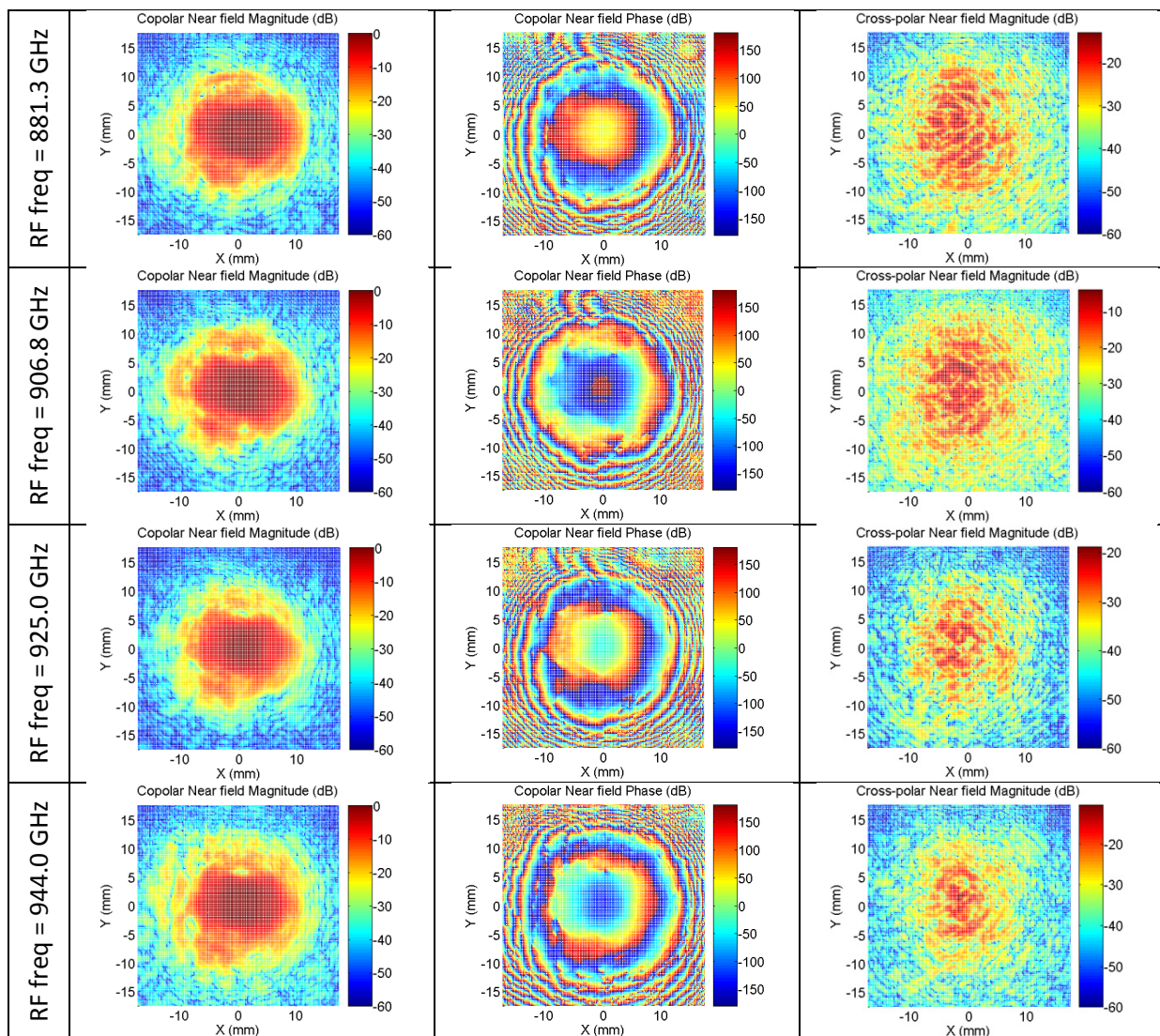


Figure 4.9. Measurements of co- and cross-polarization patterns of the 900-GHz HEB receiver

Table 4.3. Results of fundamental Gaussian beam fitting and cross-polarization levels

Frequency (GHz)	881.3	906.8	925.0	944.0
Gaussianity (%)	90.418	89.471	90.574	88.495
Waist size in x (mm)	2.755	2.650	2.591	2.405
Waist size in y (mm)	3.072	3.149	3.093	2.815
Distance to focus (mm)	145.329	142.338	123.360	134.742
Tilt in x (deg)	0.497	0.458	0.469	0.450
Tilt in y (deg)	-0.084	-0.105	-0.104	-0.120
Cross-Polarization (dB)	-13.05		-18.91	-11.24

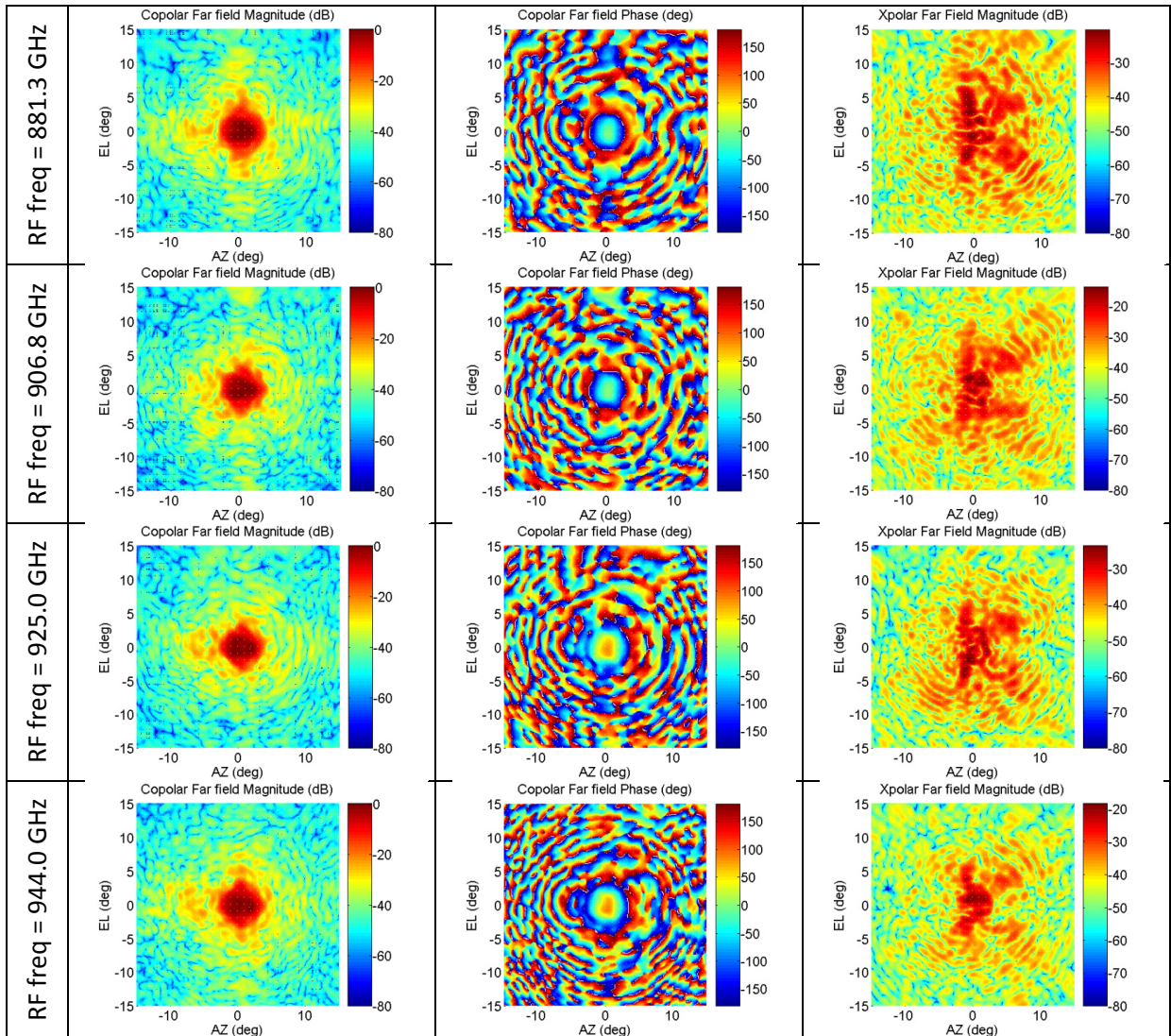


Figure 4.10. Far-field co- and cross-polarization patterns of the 900-GHz HEB receiver

The low aperture efficiency of the measured beams means that longer times are required for a certain observation quality. Besides this, the asymmetrical beam shape may produce distortion in the observations. Therefore, it is important to find the causes of these degradations in order to improve the receiver and its observation capabilities. This will be done in chapter 5.

4.3. ALMA Band 10 Tertiary Optics

4.3.1. Optical design

ALMA band 10 covers the frequency range from 787 GHz to 950 GHz, which is a 19% bandwidth at the central frequency of 868 GHz. The receiver is a dual linear polarization receiver which uses Double-Side Band (DSB) SIS mixers for down-conversion to a 4-12 GHz IF bandwidth [89]. The receiver cold optics is the element used to couple the radiation coming from the secondary mirror of the ALMA antennas into the SIS mixer blocks. All the receiver optics is located at the 4K stage of the receiver cryo-cooler and must be compact enough to fit in that limited space. ALMA band 10 tertiary optics is composed of two ellipsoidal mirrors, M1 and M2, a wire grid and two corrugated horns. The ellipsoidal mirrors have been designed to maximize antenna efficiency with independency of the frequency over the whole ALMA band 10 bandwidth. The size of the mirrors has been chosen at least 5 times the beam size to guarantee low internal spillover loss. The mirrors must also provide a pointing angle of 0.974 degrees in azimuth to point at the center of the secondary mirror from the band 10 cartridge position in the telescope cryostat [101]. The wire grid is composed of 10- μm -diameter tungsten wires separated 25 μm from each other. This separation is about $\lambda/14$ at the central frequency and smaller than $\lambda/12.5$ at the worst case frequency (950 GHz). The wire grid is used to separate both linear polarizations, P0 and P1, and it is located after the two ellipsoidal mirrors to minimize the number of optical components required. The incoming radiation is finally coupled by means of corrugated horns to the mixer blocks for down-conversion of each polarization. The use of corrugated horns guarantees a quite symmetric beam with 98% of the power coupled to a fundamental Gaussian beam. This makes it possible to use simple ABCD matrices methods for the initial design. Moreover, corrugated horns provide low levels of cross-polarization, which is helpful to meet ALMA band 10 cross-polarization requirements (-23 dB). A simple diagram of the cold optics is presented in figure 4.11.

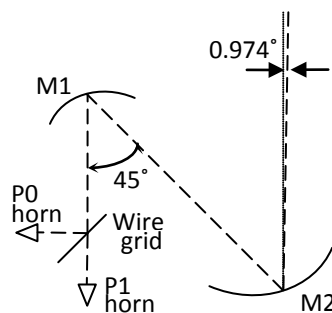


Figure 4.11. Schematic of ALMA band 10 optics

Band 10 optics has been designed using fundamental Gaussian beam techniques and ABCD matrices. Afterwards, a more rigorous analysis using the Physical Optics (PO) software GRASP has been carried out to confirm the validity of the design when higher order Gaussian modes are considered. PO also provides a good first estimation of the cross-polarization level of the optics. Finally, the optics has been characterized as part of ALMA band 10 prototype cartridges with excellent performance.

The high coupling efficiency of corrugated horns to a fundamental Gaussian beam justifies the use of quasi-optical techniques for the design of this optical system. The system performance will depend on the horn aperture diameter and slant angle, the distances between elements and the radii of curvature of ellipsoidal mirrors. The use of ABCD matrix techniques provides a good estimate for the characterization of beam size and radius of curvature at different positions of the optical system. The results of the quasi-optical design for ALMA band 10 receiver optics are presented in table 4.4. Dimensions in table 4.4 are given at room temperature, whereas the dimensions used for the analysis are those at 4 K. The quasi-optical analysis yields a theoretical Edge Taper of 12.07 dB at all band 10 frequencies, which agrees with the typical design value of 12 dB edge taper at the subreflector [102]. Therefore, the design values stated in table 4.4 provide frequency independent optics with optimal aperture efficiency at the subreflector for ALMA band 10.

Table 4.4. Results of quasi-optical design of ALMA band 10 optics in mm

	Design	787 GHz	868 GHz	950 GHz
Horn diameter	6.000			
Horn slant angle (°)	11°			
Horn waist		0.878	0.812	0.753
Distance waist to horn aperture		12.391	12.869	13.260
Distance horn to wire grid (WG)	15.000			
Beam size at WG		3.874	3.853	3.837
Distance wire grid to mirror M1	30.000			
Beam radius at M1		7.946	7.856	7.787
Beam input radius of curvature at M1		57.920	58.313	58.628
M1 Focal length	22.262			
Beam output radius of curvature at M1		-35.927	-35.777	-35.659
Distance btw mirrors	80.044			
Waist btw mirrors		0.547	0.500	0.459
Distance M1-waist		35.756	35.633	35.535
Beam radius at M2		9.763	9.714	9.677
Beam input radius of curvature at M2		44.108	44.210	44.290
M2 Focal length	35.810			
Beam output radius of curvature at M2		-186.398	-184.590	-183.210
Final waist		2.253	2.042	1.866
Distance M2-waist		176.475	176.431	176.398
Distance M2 to cryostat window	205.000			
Beam radius at window		2.726	2.557	2.222
Distance cryostat window to subreflector	5883.000			
Beam radius at subrefl.		318.187	318.187	318.187
Radius of subreflector	375.000			
Edge taper (dB)		12.07 dB	12.07 dB	12.07 dB

The corrugated horns to be used in ALMA band 10 receivers have an aperture diameter of 6 mm and a slant angle of 11 degrees at room temperature. The total length of the horn is 17.6 mm including a 3.128-mm-long impedance-matching section to a WR-1.2 rectangular waveguide. The corrugated section has a total of 134 corrugation of 54- μ m length, which is around $\lambda/6.4$ at the

design frequency of 868 GHz. The corrugation depth varies from 127 to 83 μm . The performance of such a corrugated horn has been simulated using the commercial software CHAMP [103]. The impedance-matching section was designed using the finite-elements software HFSS [104]. The simulated fields of the corrugated horn with dimensions shrunk by a factor 1.004 to simulate operation at 4 K temperature are presented in figure 4.12. The theoretical cross-polarization level is less than -40 dB for the whole frequency band and it goes down at higher frequencies. Fundamental Gaussian beam fitting has been performed for the simulated fields. The results are presented in table 4.5. The beam is almost perfectly symmetric and 98.8% of the radiated e-fields couple to a fundamental Gaussian beam, which is comparable to the theoretical 99% coupling. The corrugated horn waist size is slightly smaller than the value considered in table 4.4 at the lower frequencies but results fit perfectly at 950 GHz. The waist position is slightly deeper within the horn than in the quasi-optical analysis.

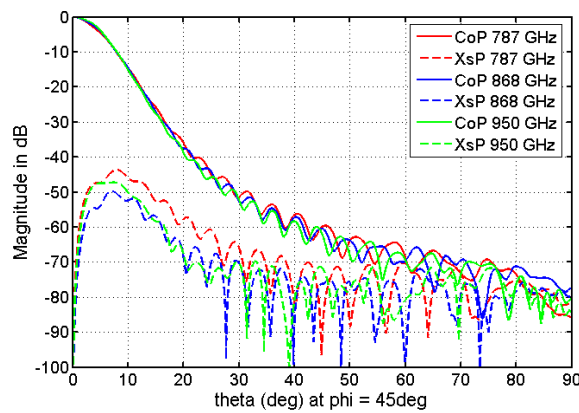


Figure 4.12. Far Field radiation patterns of corrugated horns at three ALMA band 10 frequencies

Table 4.5. Gaussian Beam fitting of the simulated fields of ALMA band 10 corrugated horns

RF frequency	787 GHz	868 GHz	950 GHz
Gaussicity (%)	98.77	98.70	98.85
w0x (mm)	0.869	0.802	0.756
w0y (mm)	0.871	0.806	0.753
Horn waist to horn aperture (mm)	12.825	13.280	13.755

The corrugated horn far fields previously calculated have been used as feed input for a physical optics model of the receiver optics with the commercial software GRASP. In this model, the effects of truncation in the windows between the different stages of the cryostat and at the cryostat top have been considered. The model used in GRASP is depicted in figure 4.13.

Using this model, the electric fields in a plane at the waist position have been calculated. An example of these results is presented in figure 4.14. The frequency dependence of the simulated fields in the optics focal plane is shown in figure 4.15. Fundamental Gaussian beam fitting has been performed on the fields simulated at the optics focal plane for both polarizations, P0 and P1. The results are presented in table 4.6. Simulated cross-polarization levels have also been included and

are always better than -34 dB. The waist sizes are slightly larger than those calculated using quasi-optical techniques, and the beam is slightly asymmetric. The waist position is slightly different too, which can be explained by the different waist position in the simulated corrugated horns.

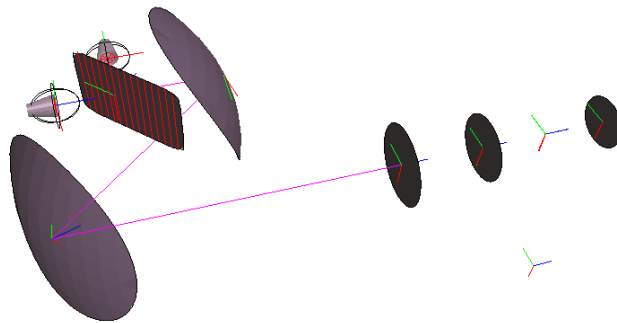


Figure 4.13. GRASP model for ALMA band 10 optics

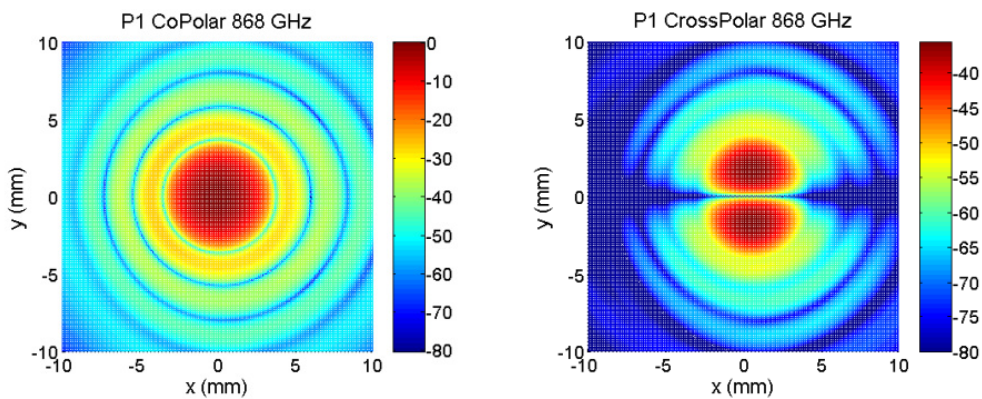


Figure 4.14. Simulated co- and cross-polar electric fields at the optics waist plane at 868 GHz

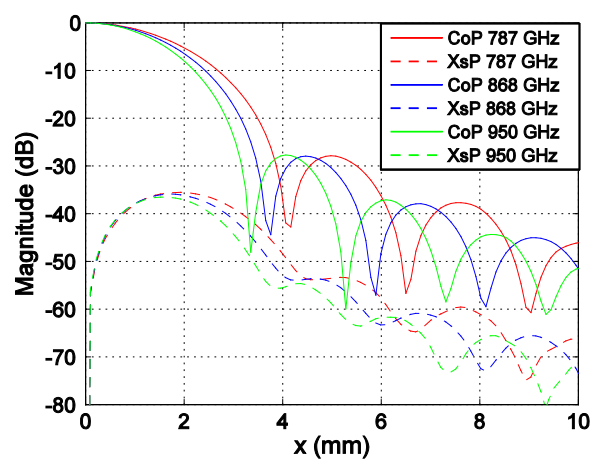


Figure 4.15. Frequency dependence of co-/cross-polarization fields at the optics focal plane for P1

Table 4.6. Fundamental Gaussian beam fitting of the fields simulated in the optics focal plane

RF Frequency	787 GHz		868 GHz		950 GHz	
Polarization	P0	P1	P0	P1	P0	P1
Gaussicity (%)	98.142	98.134	98.153	98.171	98.225	98.221
w0x (mm)	2.293	2.264	2.067	2.055	1.876	1.893
w0y (mm)	2.264	2.290	2.055	2.065	1.893	1.874
z_from_waist (mm)	-0.909	-0.862	-0.690	-0.645	0.411	0.453
X Offset (mm)	0.014	0.014	0.009	0.008	0.004	0.004
Y Offset (mm)	0.033	0.000	0.027	0.000	0.023	0.000
XTilt (deg)	0.977	0.978	0.974	0.975	0.970	0.972
YTilt (deg)	0.010	0.000	0.009	0.000	0.008	0.000
Cross-pol level (dB)	-35.77	-34.22	-36.21	-35.65	-36.38	-36.38

The fields at the secondary aperture plane, located at 5883 mm from the waist position, have also been calculated using Physical Optics simulations. The magnitude of the field at the edge of the secondary mirror (- edge taper) along the subreflector aperture for both polarizations and at several frequencies is presented in figure 4.16. The values of the edge taper for all cases are 1-2 dB smaller than the value of 12.07 dB obtained from the initial quasi-optical analysis. This is because the contribution of the higher order modes is a widening of the beam in the far field.

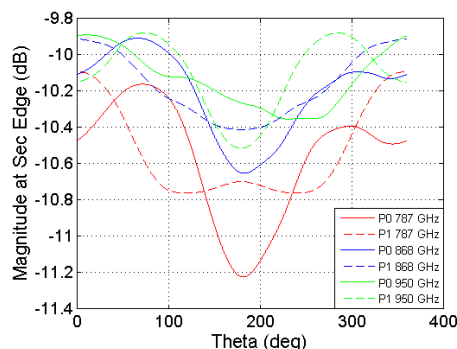


Figure 4.16. -Edge Taper in dB at the rim of the subreflector aperture

In order to calculate the exact aperture efficiency at the subreflector, the far fields of ALMA band 10 optics have been calculated from the near field results at the waist plane. Cuts of the calculated far fields at 868 GHz are shown in figure 4.17 for both polarizations. Figure 4.17 shows that the fields for P0 and P1 are very similar. All secondary lobes are below -30 dB and the cross-polarization is slightly lower than -35 dB. The frequency dependence of the far-fields for polarization P1 is shown in figure 4.18. Figure 4.18 shows that according to PO simulations, ALMA band 10 optics far fields are quite independent from frequency. Results are similar for polarization P0.

An exhaustive efficiency analysis has been carried out using the calculated far fields. The beam phase centers have also been obtained and the beam squint between polarizations has been calculated. Results are presented in table 4.7. The aperture efficiency at secondary aperture is around 87% and the beam squint is less than 1% of the full-width of the beam at half maximum

(FWHM). The average edge taper using far field calculations is around 10.2 dB, which is almost 2 dB less than in the quasi-optical analysis.

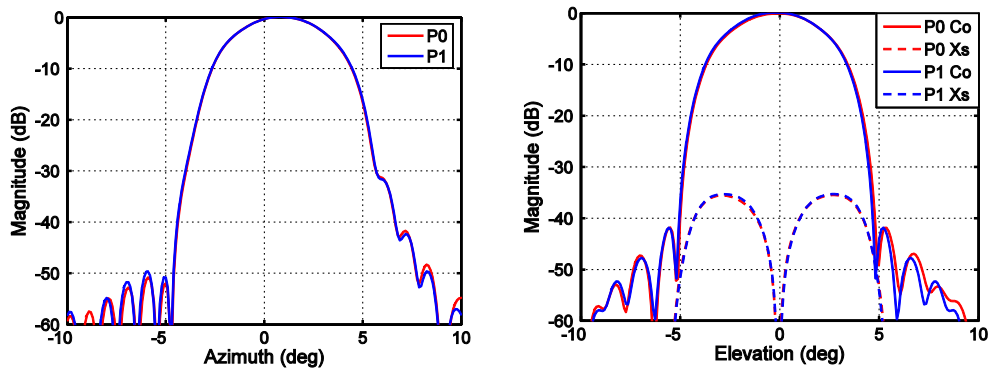


Figure 4.17. ALMA band 10 Far Fields at 868 GHz for both linear polarizations, P0 and P1

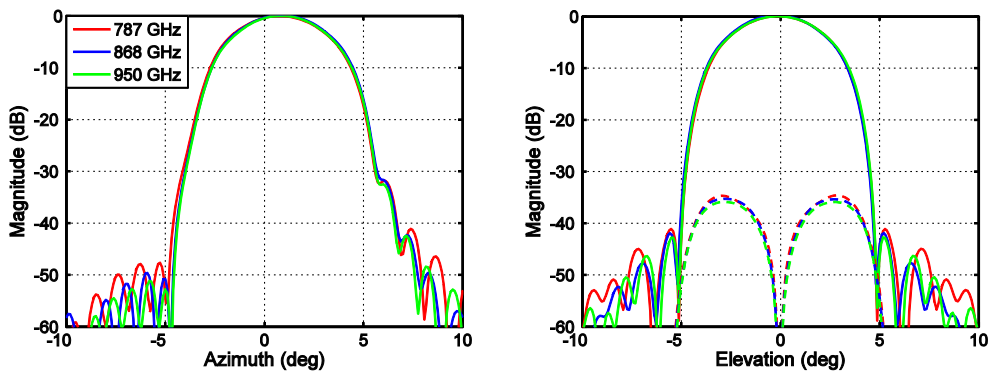


Figure 4.18. ALMA band 10 Far Fields at 787, 868 and 950 GHz for polarization P1

Table 4.7. Efficiency analysis and beam-squint of ALMA band 10 optics using PO simulations

RF Frequency	787 GHz		868 GHz		950 GHz	
Polarization	P0	P1	P0	P1	P0	P1
Edge taper (dB)	10.31	10.26	10.15	10.11	10.18	10.17
Taper eff. (%)	90.88	90.94	91.01	91.06	90.87	90.91
Spillover eff. (%)	95.70	95.69	95.59	95.57	95.51	95.50
Polarization eff. (%)	99.97	99.96	99.97	99.97	99.98	99.97
Defocus eff. (%)	100.00	100.00	100.00	100.00	100.00	100.00
Aperture eff. (%)	86.94	86.97	86.97	87.00	86.76	86.78
Offset in x (mm)	0.041	0.037	0.032	0.028	0.017	0.021
Offset in y (mm)	-0.032	0.000	-0.027	0.000	-0.024	0.000
Offset in z (mm)	1.421	1.363	1.265	1.186	-0.057	-0.259
Beam squint (% FWHM)	0.92		0.85		0.83	

4.3.2. Measurement characterization

Two measurements setups are being used for the characterization of ALMA band 10 optics: a setup at room temperature with a Schottky-diode based receiver and a setup at cryogenic temperature to characterize real band 10 cartridges. In addition, the radiation patterns of the probe horn used in these setups have been measured and utilized to provide probe compensation as explained in Appendix A. Finally, the probe horn displacement in the XY plane that occurs when the probe horn is rotated 90 degrees has been characterized in order to provide accurate beam squint results.

4.3.2.1. Room temperature setup

Measurements at room temperature are a necessary first step for characterization of individual ALMA band 10 optical components. In the case of cryogenic measurements, the focal plane of the optics is located within the cryostat and it is not possible to take planar measurements at that point. At room temperature, that measurement plane is readily accessible. Additionally, at this plane, it is where the beam is the narrowest. Therefore, the area in the near-field measurement plane which needs to be sampled is the smallest and the measurement time is reduced dramatically. ALMA band 10 SIS mixers cannot be used at room temperature and, therefore, commercially available VDI Schottky-diode receivers [88] are being used instead. The bandwidth of the utilized room-temperature receiver used for the ALMA band 10 prototype characterization ranges from 840 to 893 GHz. Therefore, three frequencies were chosen for room-temperature characterization of components: 840, 864 and 893 GHz. Currently, some new VDI receivers which cover the full ALMA band 10 bandwidth are being used in the laboratory, and therefore, the new characterization frequencies are 787, 864 and 945 GHz.

A custom sub-mm network vector analyzer was designed to perform these room-temperature measurements. This measurement system at room temperature is presented in figure 4.19 and based on [105]. The measurement system presented in 4.2.2 is based on this one. The differences between them are related to the receivers. This receiver can produce an IF frequency which can be directly measured by the volt meter. That fact simplifies the system. The IF frequency is 90 MHz in this test setup. In this case the alignment between the XYZ θ stage and the OUT (Optics Under Test) is done using a theodolite and small alignment mirrors on the support structures of the RF probe and the OUT.

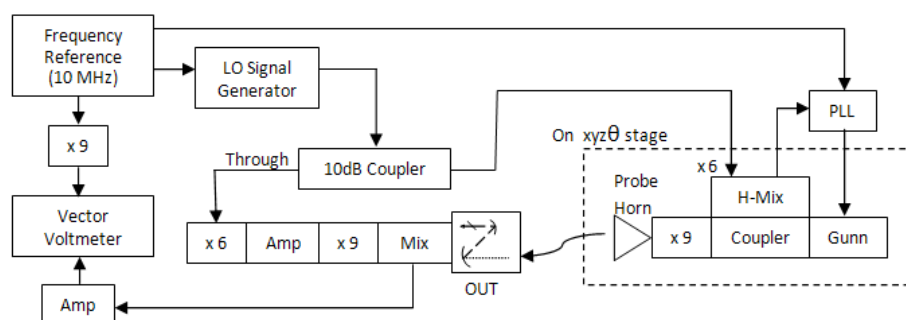


Figure 4.19. Test set-up for beam characterization of ALMA band 10 optics at room temperature

4.3.2.2. Cryogenic temperature setup

The measurement system for the characterization of ALMA band 10 tertiary optics at cryogenic operation is based on the custom network analyzer presented in figure 4.19 with slight modifications in order to use ALMA band 10 SIS mixers. Details are presented in figure 4.20. In this case, the IF frequencies produced by the receiver can only be in the range 4-12 GHz. Therefore, a second down-conversion to MHz frequencies is necessary. The final IF frequency is 50 MHz. The receiver output IF frequency is 4.95 GHz.

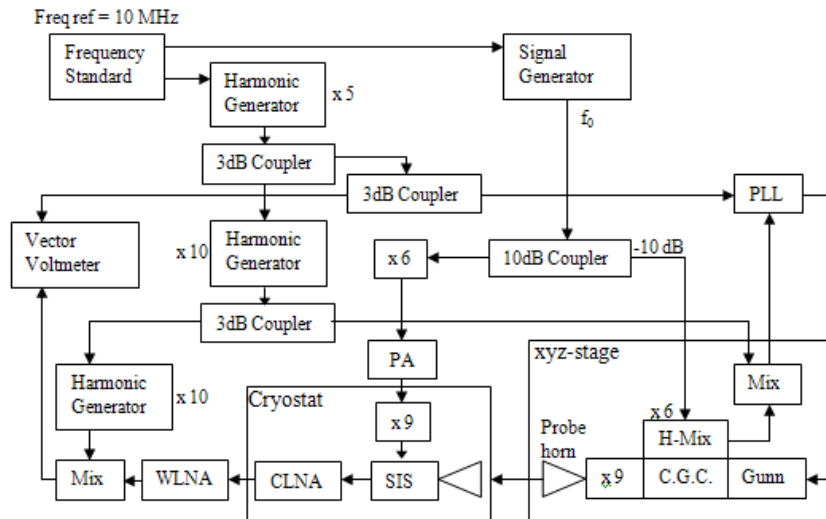


Figure 4.20. Test setup for beam characterization of ALMA band 10 cartridge in the test cryostat

4.3.2.3. Design verification by measurements

Photographs of prototype ALMA band 10 components are presented in figure 4.21. Photos of the assembled ALMA band 10 optics where the ellipsoidal mirrors, corrugated horns and wire grid are easily identifiable are shown in figure 4.22.

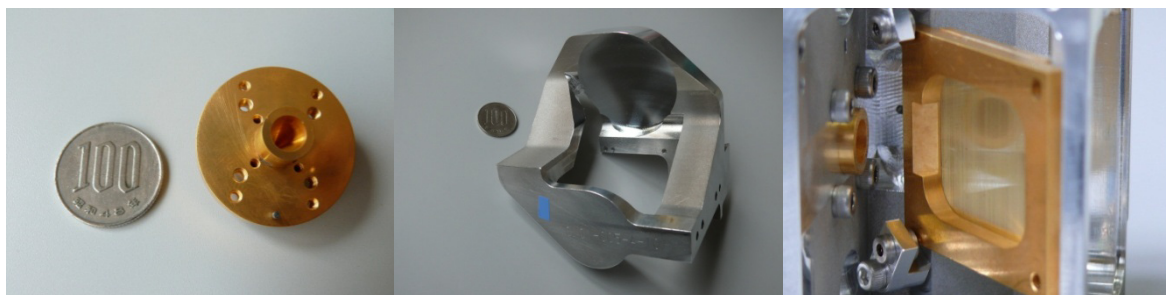


Figure 4.21. From left to right: corrugated horn, ellipsoidal mirrors and wire grid.

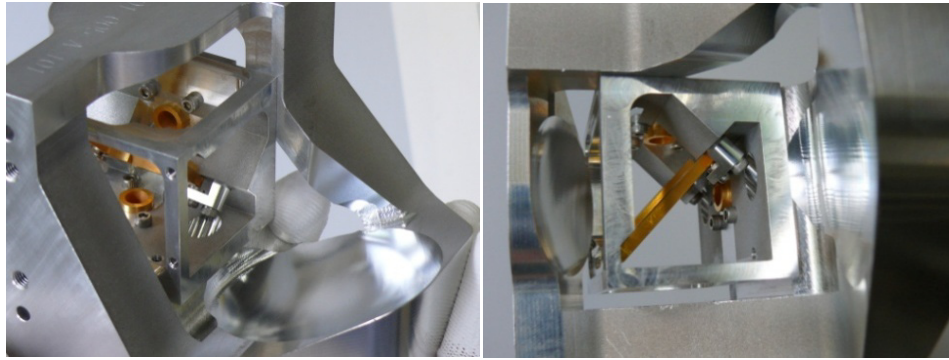


Figure 4.22. Assembled ALMA band 10 optics from different angles.

The results for an optical setup using typical ellipsoidal mirrors, wire grid and corrugated horns are presented in table 4.8 and figure 4.23. Table 4.8 shows the results of fitting the measured near-field beams with fundamental Gaussian beams. Results of Physical Optics simulations using GRASP are included for comparison. In the case of these measurements, the beams are slightly narrower than predicted by simulations. This means the actual far-field beams will be slightly wider. The rest of beam-fitting parameters are pretty similar to simulations. With respect to cross-polarization, the higher the frequency, the higher the cross-polarization level measured. Besides, values are slightly larger than for ideal simulations. Figure 4.23 shows the principal-plane cuts of the measured co- and cross-polarization near-fields at the RF frequencies of study. Physical Optics simulations have been included in the same figures for comparison. Results are very similar in all cases. Notice that simulated cross-polarization along x is 0 V/m and does not appear in figure 4.23.

Table 4.8. Gaussian beam fitting of room-temperature measurements and comparison with simulations

	840 GHz		864 GHz		893 GHz	
	Simulated	Measured	Simulated	Measured	Simulated	Measured
Gaussicity (%)	98.148	98.175	98.141	98.230	98.144	98.318
w0x (mm)	2.149	2.103	2.083	2.047	2.012	1.963
w0y (mm)	2.132	2.098	2.072	2.050	2.005	1.988
z_from_waist (mm)	1.545	1.632	1.316	1.316	1.532	1.844
XTilt (deg)	0.000	0.044	0.000	0.039	0.000	0.002
YTilt (deg)	0.977	0.986	0.976	0.972	0.975	0.966
Cross-pol level (dB)	-35.18	-34.39	-35.63	-31.70	-35.97	-30.92

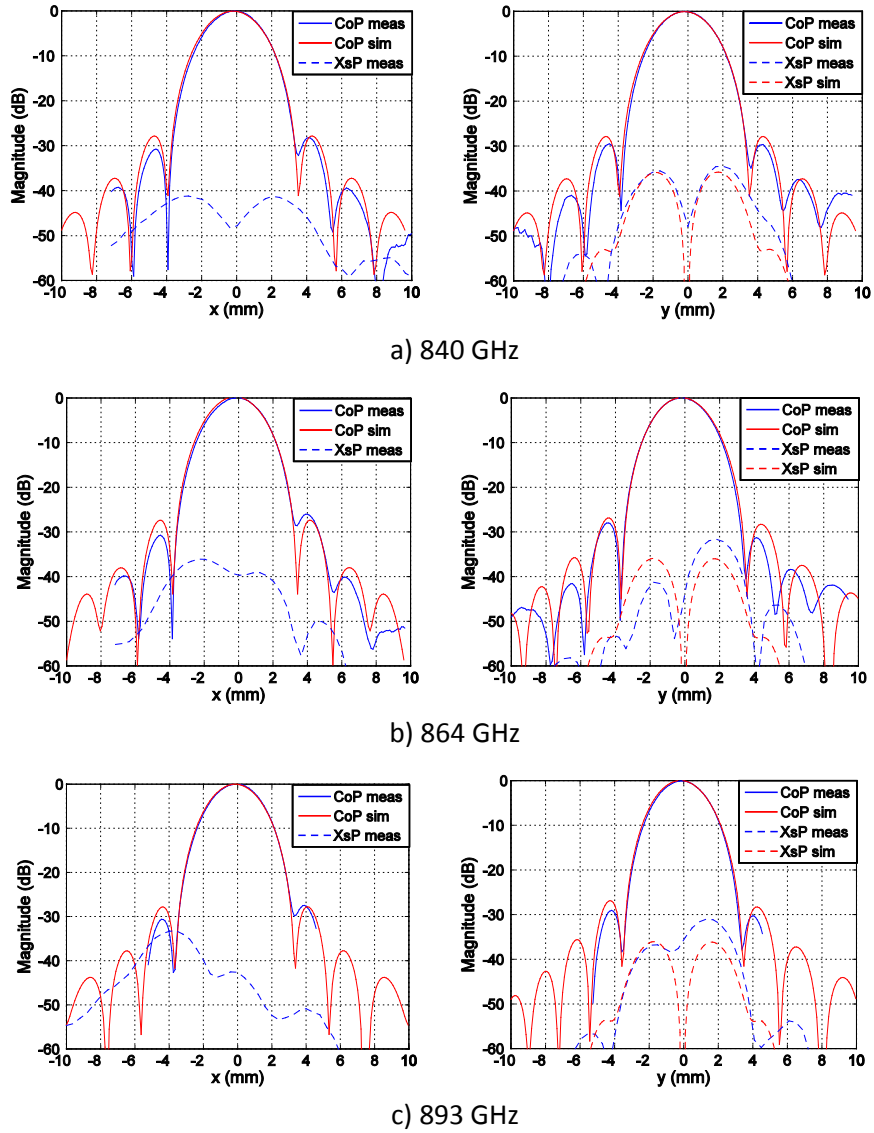


Figure 4.23. Principal-plane cuts of measured and simulated near-fields at different frequencies

4.3.2.4. ALMA band 10 prototype optical performance

Photos of ALMA band 10 tertiary optics in two different pre-production ALMA band 10 cartridges are presented in figure 4.24.

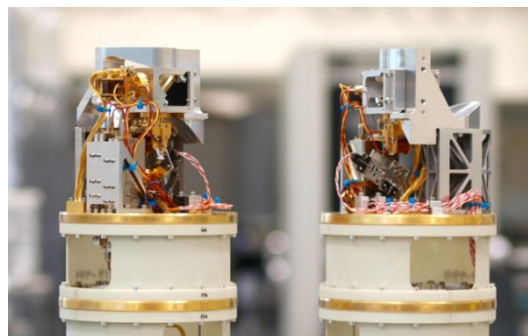


Figure 4.24. ALMA band 10 tertiary optics on two pre-production cartridges

The results of near-field measurements at ALMA band 10 lowest, middle and highest RF frequencies are presented in table 4.9. No infrared filters have been used between cryostat stages in these measurements in order to characterize the optics only. The waist sizes and tilt angles are quite close to those obtained by PO simulations. The differences are mostly due to tolerances in the fabrication and assembly of corrugated horns and ellipsoidal mirrors. Cross-polarization levels are better than -28 dB at all cases. ALMA requirement is -23 dB. Table 4.10 shows the efficiency analysis of the calculated far fields. The far-field beam is slightly narrower than predicted by simulations at 787 and 868 GHz, whereas it is slightly wider at 945 GHz. The total aperture efficiency at the secondary mirror of the telescope is better than 85.7% and in some cases, close to the simulated values of around 87%. This is much better than the 80% efficiency required for ALMA. The beam squint in the sky is better than 4.25% of the 3dB beam-width, whereas ALMA requirement is 10%.

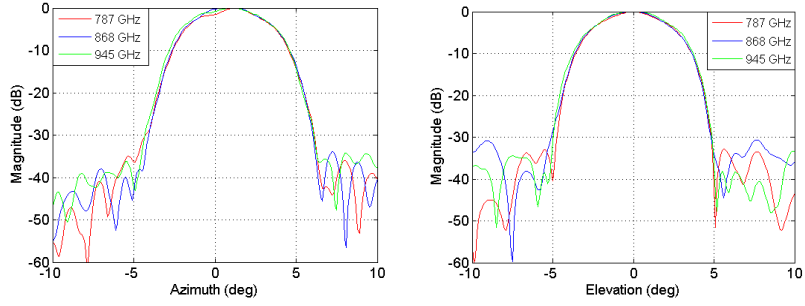
Table 4.9. Fundamental Gaussian beam fitting of measured near fields at cryogenic temperatures

RF Frequency (GHz)	787		868		945	
Polarization	P0	P1	P0	P1	P0	P1
Gaussicity (%)	97.759	98.280	98.099	98.416	97.827	97.255
w0x (mm)	2.254	2.245	2.034	2.037	1.843	1.818
w0y (mm)	2.232	2.312	2.046	2.066	1.862	1.837
z_from_waist (mm)	0.945	0.893	0.937	0.938	0.871	0.984
XTilt (deg)	-0.038	-0.074	-0.071	-0.110	-0.036	-0.055
YTilt (deg)	-29.22	-31.17	-29.57	-30.44	-30.21	-28.37

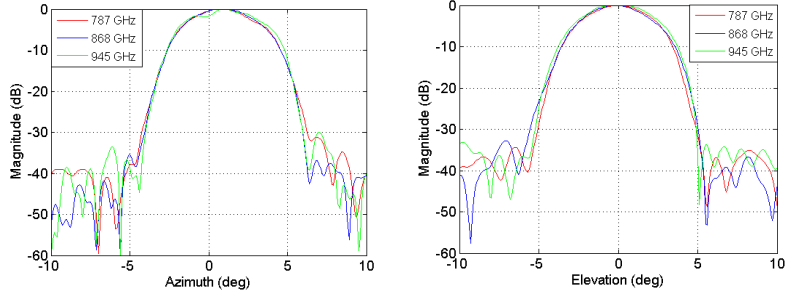
Table 4.10. Efficiency analysis and beam-squint of ALMA band 10 prototype optics measurements

RF Frequency (GHz)	787		868		945	
Polarization	P0	P1	P0	P1	P0	P1
Edge taper (dB)	10.52	11.03	10.16	10.68	9.68	9.26
Taper eff (%)	91.33	90.15	91.06	90.30	91.91	92.74
Spillover eff (%)	94.98	95.46	94.94	95.14	94.72	94.16
Polarization eff on sec (%)	99.84	99.89	99.87	99.87	99.85	99.83
Defocus Eff (%)	100.00		99.99		99.98	
Aperture eff (%)	86.34	85.78	86.14	85.70	86.82	86.96
Beam Squint (%)	4.25		2.51		2.45	

The main-plane cuts of the far-fields at different frequencies are presented in figure 4.25. The beam-patterns are mostly frequency independent in the area which illuminates the secondary mirror. It has been found that the main beam presents some minor ripples in some cases. This is due to the IR filters, as it will be explained in chapter 6. Figure 4.26 shows the agreement between the far-fields obtained by measurements and by simulations.

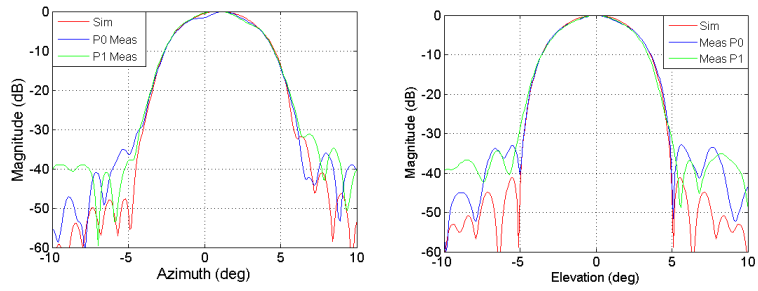


a) Polarization P0

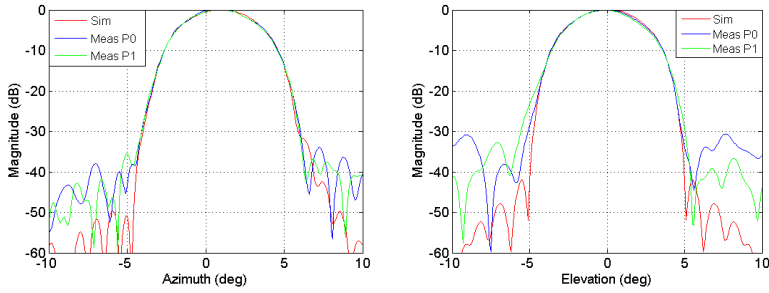


a) Polarization P1

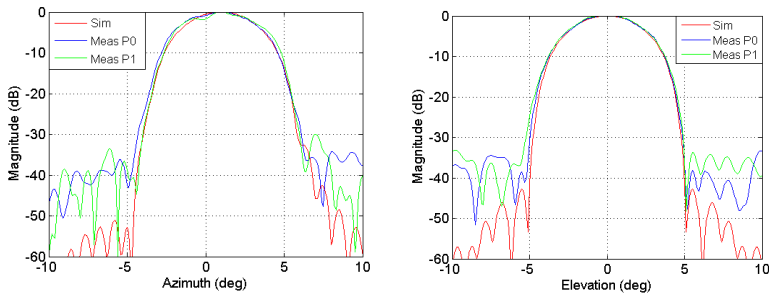
Figure 4.25. Main-plane optical beam cuts of ALMA band 10 prototype optics.



a) 787 GHz



b) 868 GHz



c) 945 GHz

Figure 4.26. Comparison of far-fields obtained by measurements and by simulations

Chapter 5

Tolerance Analysis using Physical Optics and Monte Carlo Techniques

5.1. Introduction

As frequency approaches frequencies around 1 THz, the size of horns and waveguide components is reduced. Some components base their performance on small features which become tiny at these frequencies. Corrugated horns are a good example of this. Corrugated horns are widely used as feeds at mm and sub-mm wave frequencies. Two of the main reasons for this are the low cross-polarization levels which can be achieved, and the good coupling of the radiated E-fields to a fundamental Gaussian mode, which facilitates the design of systems using quasi-optical techniques. At THz frequencies, the main technical difficulty for the use of corrugated horns is the tiny dimensions to be fabricated. In the case of ALMA band 10, the size of corrugations is as small as 54 microns. Therefore, the fabrication tolerances which can be achieved with usual milling and electroforming techniques are comparable to the dimensions to be manufactured. In addition to fabrication errors, assembly errors can also be important in the case of optical systems composed of several components. The combined effect of all these potential errors can degrade the performance significantly and impact on astronomical observations. In this case, a statistical analysis of the performance of corrugated horns or full optical systems in terms of tolerances becomes very important and can reveal unexpected results. Besides, it is useful in order to fully understand the potential and limitations of our receiver and how that translates into astronomical observation capability.

To the author's knowledge, there are not many references in the literature dealing with the analysis of tolerances in optics designs at around THz frequencies. Most of these references [106]-[107] use ray tracing techniques usually used at higher frequencies. At THz frequencies, these analyses can be a good starting point to understand the effect of tolerances on some parameters such as pointing angles, but neglect the phase and diffraction effects associated with radiation in the THz range, in which the wavelength is comparable to the components size. Careful electromagnetic characterization using Method-of-Moments analysis for the corrugated horns and Physical Optics simulations for the whole optics system can provide additional information to assess the effect of

tolerances. Once beams are calculated with these techniques, Gaussian beam fitting provides a useful tool to quantify the characteristics of the beam such as beam size, position or pointing angles. The use of this fitting analysis is justified by the high Gaussianity of beams of typical well-designed receiver optics at these frequencies.

Monte Carlo analyses [108] are a useful way to investigate the effects of tolerances on performance and to assess the robustness of designs. Monte Carlo analyses have been preferred in this study over other tolerance analyses such as worst-case (WC) or root-mean-square (RMS) analyses for several reasons. WC analyses analyze the worst possible cases, which are not usually found with real components, especially when a large number of variables are involved. Therefore, those methods are too pessimistic. RMS analyses overcome this limitation and provide results closer to expectations, but unlike Monte Carlo analyses, they cannot provide more information about the statistics of the final performances. This information, which can be provided by Monte Carlo analyses, gives more insights about the robustness of the design under study. The dimensions of each element, position and pointing angles can be modeled as Gaussian random variables with mean equal to the design value and standard deviation related to the fabrication and/or assembly tolerances. Different random sets of geometrical dimensions can be chosen for different simulations. Careful electromagnetic characterization using Method-of-Moments analysis for the corrugated horns and Physical-Optics simulations can then be used to characterize electrical performances. If the number of simulations with different random sets of dimensions is very high, the statistical performance of the system can be analyzed in terms of mean values and standard deviations.

In the case of the ALMA band 10 optics, two corrugated horns must be used for each receiver located in each of the at least 66 antennas [109]-[110] which will compose the ALMA telescope. Additionally, at least 7 spare receivers will be produced. Therefore, at least 146 corrugated horns working in the frequency band 787-950 GHz must be manufactured with state-of-the-art performance to satisfy ALMA requirements. Assembly is also critical for the ALMA band 10 tertiary optics to point exactly at the reflector antenna secondary. Despite a careful mechanical design has been performed in order to reduce the impact of assembly tolerances, it is necessary to study the effect of tolerances in corrugated horns and optics elements assemblies. Firstly, a Monte Carlo analysis of ALMA band 10 corrugated horns has been performed. Afterwards, the combined effect of tolerances on horns and other components has been characterized and results have been analyzed. Finally, measurement results have been used to verify the analyses.

After this investigation, the optics of the HEB receiver developed by Professor Yamamoto's group at the University of Tokyo has been analyzed by means of these techniques. As explained in chapter 4, measurement results significantly differed from simulation results. The disagreement between simulations and measurements has motivated an extensive campaign of Monte Carlo analyses to find out the cause of such a difference in results. Monte Carlo analyses have considered fabrication and assembly tolerances in all components in the RF chain, as well as some non-expected fabrication errors. This strategy has allowed determining what component is degrading the overall optics performance. In short, the use of all available analyses techniques together with measurements has allowed singling out an underperforming element in an astronomical receiver. The change of this component is expected to improve the optical efficiency and enhance astronomical observations. These ideas can be of interest for any quasi-optical receiver at THz frequencies.

5.2. ALMA Band 10 Tolerance Analysis

5.2.1. Corrugated horn tolerance analysis

In terms of manufacturing processes, electroforming of copper with gold plating, and direct milling on aluminum have been considered for ALMA band 10 corrugated horns. A large flange and alignment pins have been used to guarantee good alignment with respect to other optics parts, as shown in figure 5.1. The number of corrugations is 134, with 54 μm width and variable depth. A 5- μm fabrication tolerance, which is difficult to achieve in practice, means a 10% error in the corrugation width, which can potentially degrade the horn performance. The considered tolerances for the different horn dimensions are shown in table 5.1. The real fabrication tolerance which can be achieved for corrugation features is unknown. Mechanical measurements of the mandrels used for electroforming showed that this tolerance is probably between 5 and 10 μm .

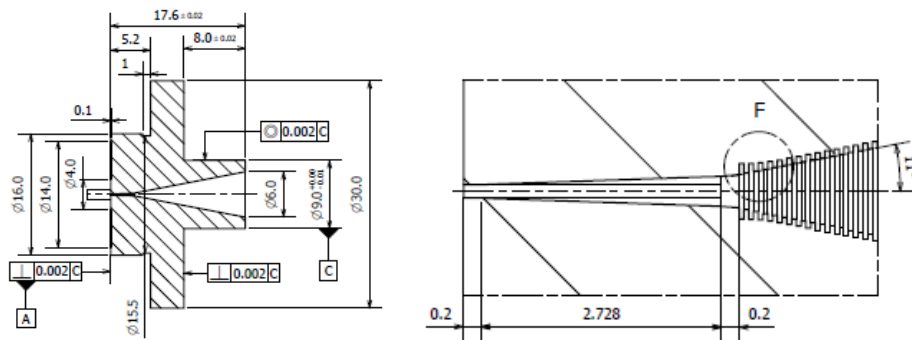


Figure 5.1. ALMA Band 10 Corrugated Horn

Table 5.1. Tolerances for Monte Carlo Analysis of corrugated horns

	Nominal Value	Manufacturing Tolerance
Number of corrugations	134	
Inner horn radius	0.187 mm	10 μm
Outer horn radius	3 mm	20 μm
Horn length	14.472 mm	20 μm
Corrugation length	0.054 mm	5-10 μm
Corrugation depth	0.127, 0.108, 0.095, 0.087, 0.083, ..., 0.083 mm	5-10 μm

Horns have been simulated using the commercial software TICRA CHAMP [103], based on Mode Matching and the Method of Moments. The analysis results provided by CHAMP can be expressed in terms of spherical wave components, which can be input to physical-optics-based software, such as TICRA GRASP [72]. GRASP is used to calculate the co-polar and cross-polar far fields of the corrugated horn under study. The results are then fitted by fundamental Gaussian beams and the cross-polarization level is calculated as the difference between the maximum of the co-polar and cross-polar field patterns. All these steps must be repeated for each set of corrugated horn random

geometrical dimensions. Dimensions have been considered to follow Gaussian distributions of mean value equal to the nominal value and standard deviation equal to one third of the fabrication tolerance. Additional software has been created in MATLAB [111] to automate this analysis for a high number of random dimension sets.

The full analysis of each horn takes around 40 minutes. A 4-CPU computer has been used in order to run 4 analyses in parallel at any time. The total simulation time has been over one month. Two analyses have been performed, one with fabrication tolerance for small corrugation features equal to 5 μm , and another one with tolerance equal to 10 μm . The frequency chosen for the analysis is 868 GHz, ALMA band 10 center frequency. In the case of 5- μm tolerance, 2512 corrugated horns with random dimensions within the expected tolerances were simulated. In the case of 10- μm tolerance, 2067 horns were simulated. The quasi-optical analysis results in terms of mean and standard deviation for both cases are presented in table 5.2. Co-polar E-fields in the horn aperture plane (XY plane) are linearly polarized along the x axis.

Table 5.2. Results of Monte Carlo analysis of ALMA band 10 corrugated horns

	Design	Tolerance 5 μm		Tolerance 10 μm	
		Mean	Std Dev	Mean	Std Dev
Gaussicity (%)	98.70	99.55	0.16	99.40	0.36
Waist size along x (mm)	0.806	0.826	0.033	0.835	0.062
Waist size along y (mm)	0.802	0.821	0.027	0.826	0.049
Distance from waist to horn aperture (mm)	13.280	14.207	0.433	14.210	0.844
Cross-polar level (dB)	-47.23	-34.50	4.12	-29.67	3.80

Some of the results are unexpected and difficult to explain by theory. The average Gaussicity of non-ideal horns is higher than that of a horn with design dimensions. In addition, the waist size is larger for non-ideal horns and it increases with tolerance. The position of the waist with respect to the horn aperture is the same for non-ideal cases and it is almost 1 mm deeper in the horn than in the ideal case. The cross-polarization level with respect to the co-polar maximum is also noticeably worse than for the ideal case and it is worse for larger tolerances. Histograms of the parameters under analysis are presented in figure 5.2. A careful analysis of those histograms reveals that the changes in the position of the horn waist are very large for larger tolerances. In the case of 5 μm tolerances, the calculated focus position roughly spreads over a 2.5 mm range, whereas for 10 μm tolerances, this becomes almost 5 mm. In the case of the cross-polarization level, the results using tolerances reveal values closer to measurements and the histograms show that values with cross-polarization as high as -20 dB (-24 dB) are possible for 10 μm (5 μm) tolerances. Values of cross-polarization level as good as the ideal case are also found, but the percentage of occurrence is very low. As a conclusion, the waist and cross-polarization of THz corrugated horns depend very much on the ability to accurately manufacture the corrugations, and not only on the design.

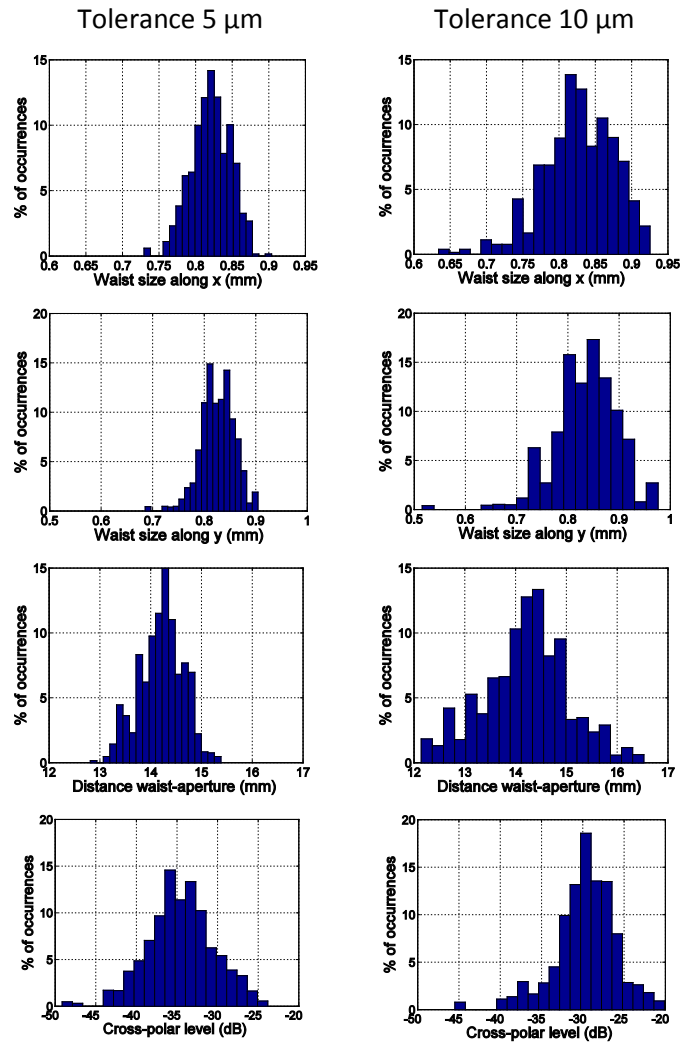


Figure 5.2. Histograms of the Monte Carlo analysis of ALMA band 10 corrugated horns

5.2.2. Optics tolerance analysis

The ALMA band 10 receiver detects two orthogonal linear polarizations in the 787-950 GHz frequency range. The optics design of the ALMA band 10 receiver was thoroughly described in chapter 4. However, for the sake of understanding, a photo of a real assembly is presented in figure 5.3. Two ellipsoidal mirrors, M1 and M2, are used to focus the radiation coming from the ALMA Cassegrain antenna secondary, located 5.883 m above band 10 focus. The focused radiation is then divided into two linear polarizations, P0 and P1, by means of a wire grid and each polarization is then received by one corrugated horn.

Two different kinds of tolerances have been considered for the statistical analysis of ALMA band 10 optics: fabrication and assembly tolerances. Each component presents some fabrication tolerances which must be considered. In addition, assembly tolerances in position and angle alignment must be taken into account. The considered design values and tolerances are presented in table 5.3 at room temperature. The mechanical design has been carefully performed to minimize

these tolerances by manufacturing all mirrors in the same aluminum block and by using alignment pins for the corrugated horns and wire grid box. The statistics of the analysis variables are considered to follow Gaussian distributions of mean value equal to the nominal design value and standard deviation equal to one third of the total tolerance. GRASP has been used for Physical Optics simulations. A large number of simulations with different geometrical values have been run on GRASP and results have been analyzed using fundamental Gaussian beam techniques and far-field transformation to calculate illumination efficiencies at the secondary reflector of the ALMA Cassegrain antennas. The feed inputs for the Physical-Optics model are the results of the corrugated horn simulations considering fabrication tolerances previously obtained using CHAMP. PO co-polar E-fields are aligned along the x axis and P1 co-polar E-fields are along the y axis.

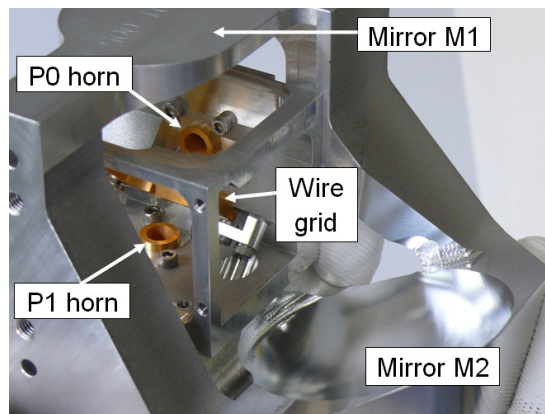


Figure 5.3. Corrugated horns assembled on mirror block

Table 5.3. Tolerances for Monte Carlo analysis of corrugated horns

	Nominal Value	Manufacturing Tolerance	Assembly Tolerance
P0 Corrugated Horn Position	(0,-15,15) mm	20 μ m	40 μ m
P0 Horn Pointing Angle in Azimuth	90°		1 mrad
P0 Horn Pointing Angle in Elevation	0°		1 mrad
P1 Corrugated Horn Position	(0,0,0) mm	20 μ m	40 μ m
P1 Horn Pointing Angle in Azimuth	0°		1 mrad
P1 Horn Pointing Angle in Elevation	0°		1 mrad
Grid Pointing Angle in Azimuth	45°		1 mrad
Grid Pointing Angle in Elevation	0°		1 mrad
M1 mirror Position	(0,0,45) mm	20 μ m	40 μ m
M1 mirror Pointing Angle in Azimuth	22.5°		0.8 mrad
M1 mirror Pointing Angle in Elevation	0°		0.8 mrad
M1 mirror Input Radius of Curvature	58.6 mm	20 μ m	
M1 mirror Output Radius of Curvature	35.9 mm	20 μ m	
M2 mirror Position	(56.6, 0, -11.6) mm	20 μ m	40 μ m
M2 mirror Pointing Angle in Azimuth	22.987°		0.8 mrad
M2 mirror Pointing Angle in Elevation	0°		0.8 mrad
M2 mirror Input Radius of Curvature	44.4 mm	20 μ m	
M2 mirror Output Radius of Curvature	185.1 mm	20 μ m	

Three different Monte Carlo simulations have been performed: a) with nominal-dimensions corrugated horns, b) with corrugated horns with 5- μm corrugation tolerance, c) with corrugated horns with 10- μm corrugation tolerance. The first case is useful to understand the effect of tolerances in electrical performance with independence of the tolerances in corrugated horns. The second and third cases should yield results quite close to real ALMA band 10 optics.

During the initial measurement characterization of ALMA band 10 corrugated horns, the wire grid is not usually used, in order to measure the cross-polarization of the horn itself and not to modify it by means of the grid. In order to recreate this situation in these Monte Carlo simulations, the effect of the wire grid has not been considered on polarization P1. Therefore, the results of cross-polarization for P1 represent the cross-polarization due to horn and mirrors only, whereas the results of cross-polarization for P0 represent the cross-polarization of real ALMA band 10 optics taking into account the effects of the wire grid. The effects of not considering the wire grid for P1 on P1 co-polarization pattern are assumed to be minimal.

5.2.2.1. With nominal-dimensions corrugated horns

A total of 3500 simulations have been performed with corrugated horns with design dimensions and optics with tolerances indicated in table 5.3. The results of Gaussian Beam fitting, cross-polarization, beam squint and efficiency analysis are reported in table 5.4. The focus offset in table 5.4 refers to the difference in focus position for quasi-optical and Physical-Optics analyses. The results obtained for the nominal ALMA band 10 design are included for comparison. Gaussicity is determined only by the corrugated horn and therefore, it is the same as for design dimensions. The final waist average size is the same as for the design and the standard deviation is very small. The position of the optical focus is slightly further than for the design and standard deviation is not large. Pointing angle averages are similar to ideal, with a 0.072 degrees standard deviation. Cross-polarization and edge-taper average values do not change much. Final efficiencies are degraded only 0.1% in average. Beam squint is also degraded, with an average of 2.60% and standard deviation of 1.31%.

Table 5.4. Results of Monte carlo analysis (3500 sim.) for nominal corrugated horns

	Design		P0		P1	
	P0	P1	Mean	Std Dev	Mean	Std Dev
Gaussicity (%)	98.15	98.17	98.15	0.00	98.15	0.00
Waist size in x (mm)	2.067	2.055	2.068	0.007	2.055	0.006
Waist size in y (mm)	2.055	2.065	2.055	0.007	2.065	0.007
Focus offset (mm)	0.690	0.645	0.715	0.359	0.672	0.362
Pointing Angle Azimuth (deg)	0.974	0.975	0.972	0.072	0.974	0.072
Pointing Angle Elevation (deg)	0.009	0.000	0.005	0.072	0.000	0.069
Near-Field Xs-pol (dB)	-36.21	-35.65	-36.14	0.12	-35.56	0.08
Edge Taper (dB)	10.15	10.11	10.19	0.11	10.14	0.11
Taper Efficiency (%)	91.01	91.06	90.93	0.16	90.98	0.16
Spillover Efficiency (%)	95.59	95.57	95.54	0.14	95.53	0.14
Aperture Efficiency (%)	86.97	87.00	86.87	0.13	86.91	0.12
Beam Squint (% FWHM)	0.85	0.85	2.60	1.31	2.60	1.31

5.2.2.2. Corrugated horns with 5- μm corrugation tolerance

A total of 2532 simulations have been performed with corrugated horns with the tolerances indicated in table 5.1 and small-feature tolerance of 5 μm ; and mirrors with the tolerances indicated in table 5.3. The results of Gaussian Beam fitting, cross-polarization, beam squint and efficiency analysis are reported in table 5.5. The results obtained for the nominal ALMA band 10 design are included for comparison.

Table 5.5. Results of Monte Carlo analysis (2532 sim.) for corrugated horns with 5 μm tolerance

	Design		P0		P1	
	P0	P1	Mean	Std Dev	Mean	Std Dev
Gaussicity (%)	98.15	98.17	98.04	0.47	98.04	0.48
Waist size in x (mm)	2.067	2.055	2.074	0.053	2.058	0.041
Waist size in y (mm)	2.055	2.065	2.057	0.041	2.070	0.053
Focus offset (mm)	0.690	0.645	0.996	2.543	0.855	2.561
Pointing Angle Azimuth (deg)	0.974	0.975	0.973	0.072	0.974	0.072
Pointing Angle Elevation (deg)	0.009	0.000	0.007	0.073	0.000	0.071
Near-Field Xs-pol (dB)	-36.21	-35.65	-36.12	0.19	-34.50	1.58
Edge Taper (dB)	10.15	10.11	10.29	0.88	10.22	0.88
Taper Efficiency (%)	91.01	91.06	90.77	1.51	90.82	1.52
Spillover Efficiency (%)	95.59	95.57	95.53	0.66	95.51	0.66
Aperture Efficiency (%)	86.97	87.00	86.70	0.97	86.74	0.98
Beam Squint (% FWHM)	0.85	0.85	2.61	1.36	2.61	1.36

Average Gaussicity is slightly degraded, even though the average Gaussicity of horns is larger as presented in table 5.2, and the standard deviation is larger (0.5%). The average waist size is just slightly larger, but the standard deviation gets quite large (around 0.05 mm). The average position of the waist is slightly further away from the optics than for the design case. The standard deviation of the position of the waist is very large, around 2.5 mm. The pointing angle analysis does not change with respect to the case of nominal horns. Therefore, corrugated horns do not have an influence on the pointing angles. Cross-polarization for P0 (with wire grid) is almost the same as for nominal horns. Cross-polarization for P1 (without wire grid) degrades and the standard deviation is large (1.58 dB). Comparing this to the results in table 5.2, the average cross-polarization for this case is similar to that of the corrugated horns alone. However, the standard deviation is much smaller than reported in table 5.2. Edge Taper is slightly lower in average. Final efficiencies do not degrade much in average and standard deviation is 1 %. Beam squint is the same as for nominal horns as reported in table 5.4.

5.2.2.3. Corrugated horns with 10- μm corrugation tolerance

A total of 2560 simulations have been performed with corrugated horns with the tolerances indicated in table 5.1 and small-feature tolerance of 10 μm ; and mirrors with the tolerances indicated in table 5.3. The results of Gaussian Beam fitting, cross-polarization, beam squint and efficiency analysis are reported in table 5.6. The results obtained for the nominal ALMA band 10 design are included for comparison.

Table 5.6. Results of Monte Carlo analysis (2560 sim.) for corrugated horns with 10 μm tolerance

	Design		P0		P1	
	P0	P1	Mean	Std Dev	Mean	Std Dev
Gaussicity (%)	98.15	98.17	97.68	1.12	97.78	0.97
Waist size in x (mm)	2.067	2.055	2.076	0.102	2.066	0.078
Waist size in y (mm)	2.055	2.065	2.061	0.081	2.076	0.102
Focus offset (mm)	0.690	0.645	0.353	4.991	0.299	5.000
Pointing Angle Azimuth (deg)	0.974	0.975	0.971	0.073	0.973	0.073
Pointing Angle Elevation (deg)	0.009	0.000	0.006	0.073	0.001	0.069
Near-Field Xs-pol (dB)	-36.21	-35.65	-36.15	0.30	-32.49	2.54
Edge Taper (dB)	10.15	10.11	10.39	1.65	10.39	1.59
Taper Efficiency (%)	91.01	91.06	90.56	2.86	90.48	2.83
Spillover Efficiency (%)	95.59	95.57	95.42	1.24	95.44	1.20
Aperture Efficiency (%)	86.97	87.00	86.38	1.88	86.32	1.90
Beam Squint (% FWHM)	0.85	0.85	2.63	1.31	2.63	1.31

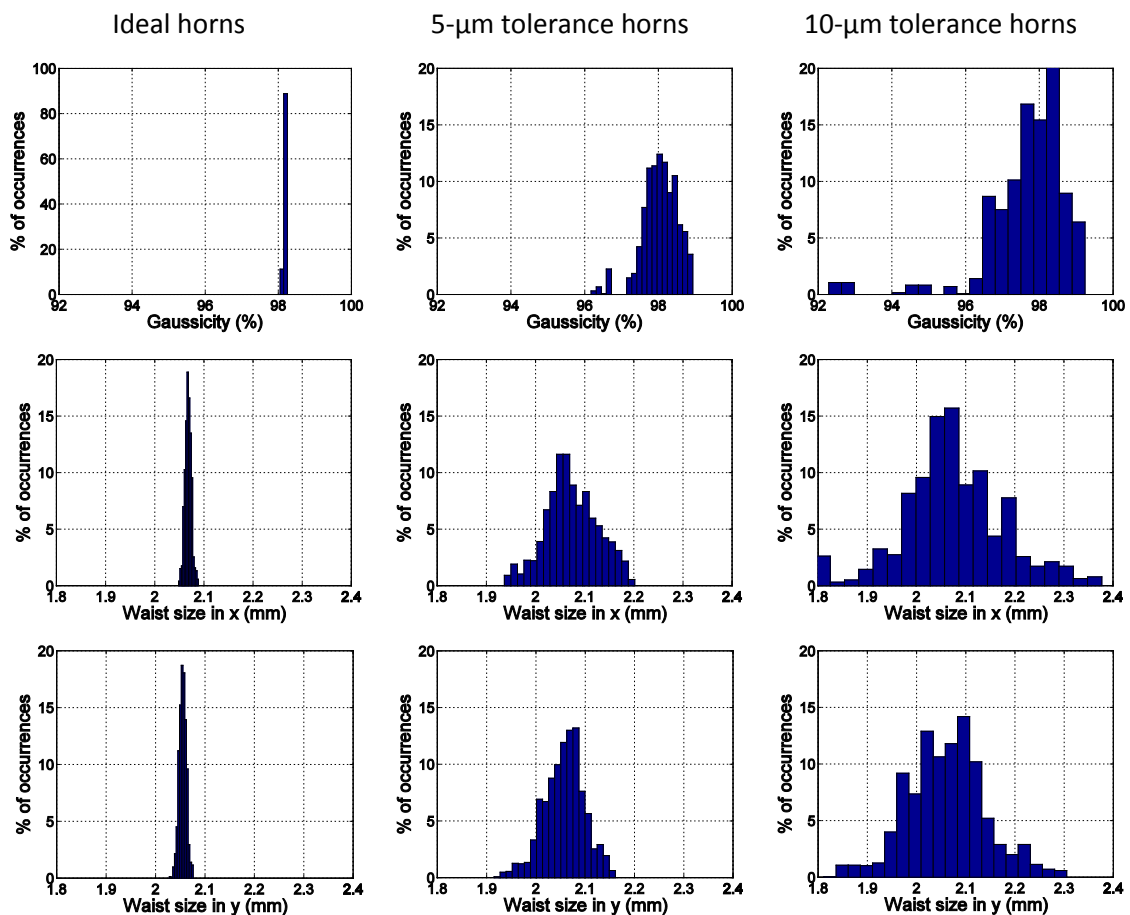
The results of the Monte Carlo analysis of optics using horns with 10- μm small-feature tolerance are qualitatively similar to those with optics using horns with 5- μm small-feature tolerance. The difference is mainly the larger values of standard deviation on the parameters which depend on horn tolerance. For example, the focus offset has now a standard deviation of 5 mm, compared to 2.5 mm for 5- μm tolerance. Some other average values which are worth pointing out are the Gaussicity, near-field cross-polarization and aperture efficiency. Gaussicity degrades noticeably for 10- μm tolerance (more than 0.4 %). Table 5.2 indicates that Gaussicity for 10- μm tolerance horns is very high. However, when the effect of the non-ideal optics is included, the final Gaussicity degrades due to reflections in the mirrors. Near-field cross-polarization also degrades to -32.5 dB with 2.5 dB standard deviation in the case the wire grid is not considered. However, the corresponding value in table 5.2 was -29.7 dB with 3.8 dB standard deviation. This means the effect of the optics improves the average slightly and decreases the standard deviation. In the case the wire grid is considered, the influence of the tolerance of horns is negligible. Finally, the degradation in terms of average aperture efficiency is 0.6 - 0.7 % (double than with 5- μm tolerance) with a standard deviation of around 2 %.

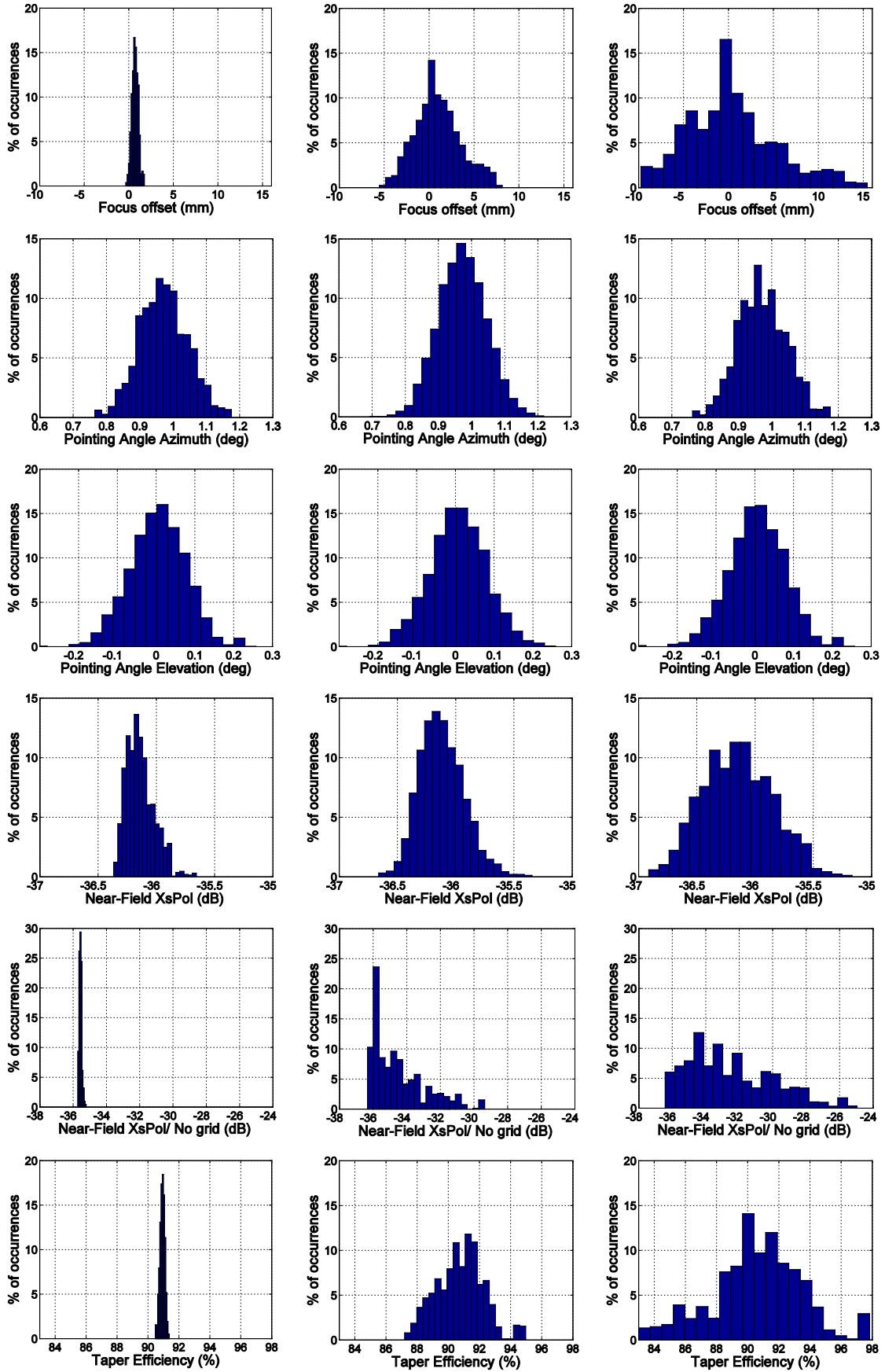
5.2.2.4. Histograms

A selection of interesting histograms of the three Monte Carlo analysis performed are presented and compared in figure 5.4 for polarization P0 (if not indicated otherwise). These histograms are useful to visually appreciate the variation of results and what the worst cases are for the performed simulations. For example, the worst case of aperture efficiency for both polarizations is around 81%, still within ALMA specifications (>80%). The worst case for cross-polarization level in the near-field is better than -35 dB for P0 (using wire grid) and better than -25 dB for P1 (not using wire grid). As expected, the use of a polarizing wire grid improves the final optical system cross-polarization, compared to the corrugated horns performance. Beam squint is also less than 9 % in all cases (ALMA specification < 10 %) and depends only on the parameters of the optics, not on the horns. These

results show that for the expected fabrication tolerances, ALMA band 10 optics is compliant with ALMA requirements. Irregular errors in mirror surfaces and horns, parallelism of the different wires in the wire grid and other defaults are difficult to model and have not been included in this analysis. Therefore, an extra slight degradation of performance is to be expected in real optics.

Some other histograms which deserve more comments are the focus offset, waist size and efficiencies. The focus offset variation is large for non-ideal horns. The position of the focus considering optics tolerances only is within 2 mm, whereas if horn tolerances are included, that value increases to around 13 mm for 5 μm tolerances, and 25 mm for 10 μm tolerances. Therefore, the spread of the focus position depends mostly on the tolerance of the horn corrugations. The effect of the increase of tolerances is an increase of the range of possible values for the focus offset. The previous comments also apply to the waist size. The spread of values of the waist size is the main reason of illumination efficiency degradation when non-ideal horns are considered. For ideal horns, the taper and spill-over efficiency values are within a 1 % range. This value dispersion is due to the pointing angle variation. When the different horn waist sizes and positions are considered, the effect is a much larger spread of results. In the case horn corrugation tolerances are considered, the aperture efficiency changes around 5 % and 10 %, for 5 and 10 μm tolerances, respectively. These results highlight again the need for very accurate fabrication of corrugations.





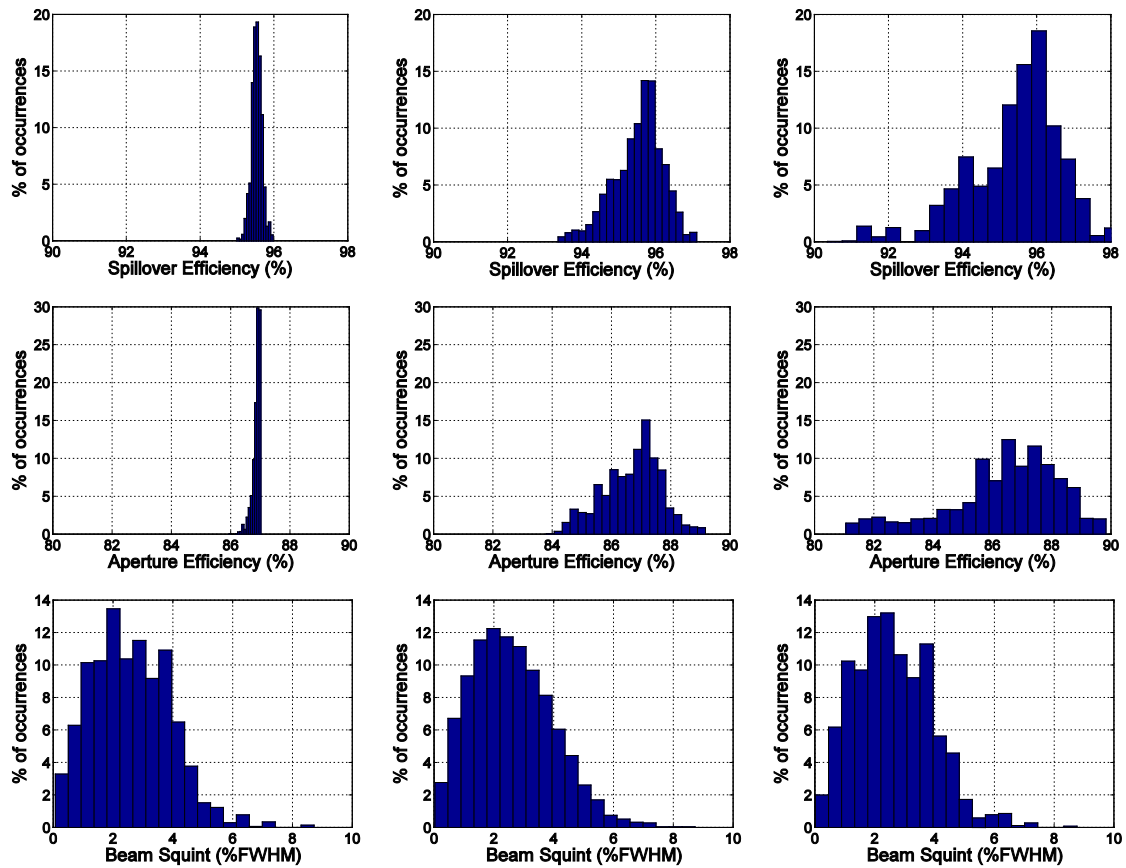


Figure 5.4. Selection of histograms of Monte Carlo analysis results

5.2.2.5. Analysis of results

Finally, as a summary of results of the Monte Carlo analysis of optics, the dependence of each parameter on the horns/optics tolerance is analyzed:

- Gaussicity: it depends on the horn exclusively. Higher horn small-feature tolerance means lower average Gaussicity.
- Waist size: it depends on the horn. Optics with ideal horns yield results close to ideal with low standard deviation. Standard deviation for 10- μm horn tolerance is double than for 5- μm horn tolerance. Standard deviation along one plane is larger than along the perpendicular one. This means the beam symmetry can be easily lost.
- Focus offset: it depends on both optics and horns. The standard deviation is huge and it varies greatly with the horn tolerance. Offsets of more than 15 mm are possible for the considered tolerances.
- Pointing angles: they depend on the optics only. The average is close to simulations with design dimensions.
- Cross-polarization:
 - with wire grid: the degradation due to the optics tolerances is small. The horn tolerance does not affect the average cross-polarization level but affects the standard deviation of results.

- without wire grid: the degradation of cross-polarization is large due to the degradation of horn cross-polarization. Worse horn tolerances increase the average and the dispersion of results.
- Edge Taper: the change due to optics tolerances is minimal. Main changes are due to horns alone. Larger horn tolerances mean larger average Edge Taper and standard deviation.
- Efficiencies: optics tolerances alone do not change efficiencies much overall. Horn tolerance degrades efficiency more significantly. Taper efficiency is more sensitive than spillover efficiency.
- Beam squint: it depends only on the optics and the average is around 2.6 % for all three cases.

5.2.3. Measurement results

All corrugated horns and mirror blocks for use in ALMA band 10 receivers are characterized at room temperature. Since the number of horns and mirror blocks needed for all the band 10 receivers is very large, this is an excellent opportunity to validate the previous Monte Carlo analysis results from a measurement point of view.

Up to 35 different corrugated horns have been manufactured and characterized at room temperature with similar ellipsoidal mirror blocks. Some of these horns are shown in figure 5.5. The measurement system is the one presented in chapter 4 for the characterization of horns and optics at room temperature in the frequency range from 832 to 896 GHz. Near-field measurements near the optical system focal point of the horns mounted on optics blocks have been fitted with fundamental Gaussian beams to obtain the values of waist radius and pointing angles for each particular optical system. These data have been used to calculate the average values and standard deviation for each parameter. The results of this statistical analysis are presented in table 5.7. The data obtained from the previous Monte Carlo analyses are also included for comparison.

Values extracted from measurements compare well with Monte Carlo analysis results. Standard deviations are slightly lower than those from simulations. Cross-polarization is slightly higher for measurements, but within the ranges presented in previous histograms. Its standard deviation is between the values of the two Monte Carlo analyses performed. The histogram of measured cross-polarization levels is presented in figure 5.6. The large dispersion of the data and the peak at around -32 dB are the most remarkable features.



Figure 5.5. 14 similar corrugated horns at sub-mm frequencies

Table 5.7. Results of Gaussian beam fitting on measurements of ALMA band 10 optics

	Measurements		Simulation 5 μm tol		Simulation 10 μm tol	
	Mean	Std dev	Mean	Std dev	Mean	Std dev
Gaussicity (%)	98.13	0.16	98.04	0.48	97.78	0.97
Waist size in x (mm)	2.077	0.042	2.058	0.041	2.066	0.078
Waist size in y (mm)	2.093	0.031	2.070	0.053	2.076	0.102
Angle Azimuth (deg)	0.918	0.036	0.974	0.072	0.973	0.073
Angle Elevation (deg)	0.096	0.045	0.000	0.071	0.001	0.069
Near-Field Cross-pol (dB)	-30.36	2.20	-34.50	1.58	-32.49	2.54

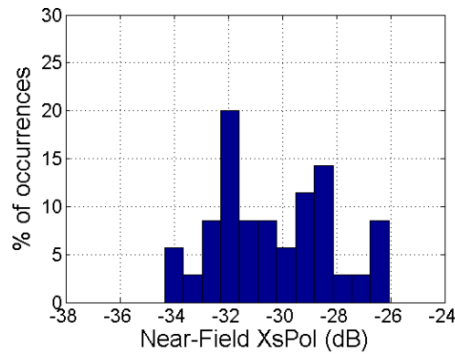


Figure 5.6. Histogram of measured cross-polarization

At this point, it is interesting to try to calculate the average small-feature tolerance for the characterized corrugated horns using the simulation results. From the analysis in section 5.2.2, the variables which depend mostly on horn tolerances are the Gaussicity average value and standard deviation and the waist size and cross-polarization standard deviations. The average cross-polarization also depends mostly on horns, but it also depends on other fabrication errors difficult to quantify. Values of these parameters for the simulated and measured cases are presented in table 5.8. The interpolated dependence of the parameters under study on horn tolerance is shown in figures 5.7 and 5.8. Values of tolerances can be directly read from each of these curves. Results of estimated tolerances using these figures are in the last column of table 5.8.

Table 5.8. Parameters affected by horn tolerance

	Ideal	5 μm	10 μm	Measured	Tol (μm)
Average Gaussicity (%)	98.15	98.04	97.78	98.13	1
Gaussicity Std Dev (%)	0.00	0.48	0.97	0.16	1.5
Waist in x Std Dev (mm)	0.006	0.041	0.078	0.042	4.5
Waist in y Std Dev (mm)	0.007	0.053	0.102	0.031	2.5
XsPol Std Dev (dB)	0.08	1.58	2.54	2.20	8

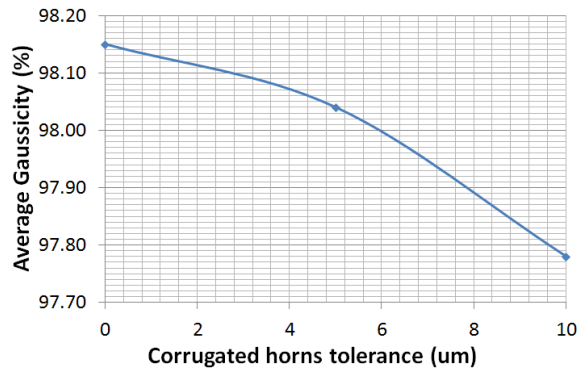


Figure 5.7. Dependence of average Gaussicity on tolerance

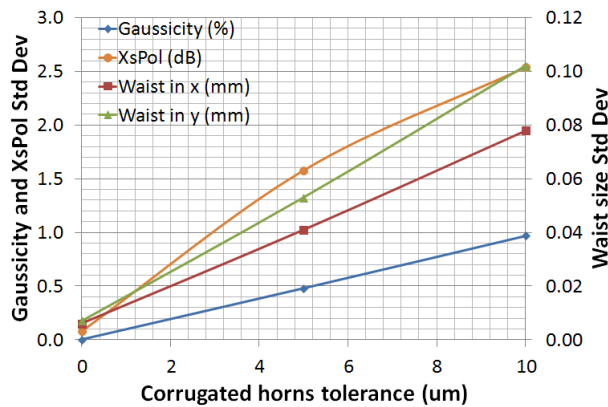


Figure 5.8. Dependence of standard deviations on tolerance

The estimated tolerance is quite different depending on the curve used. The value derived from cross-polar values is quite high. This is probably due to the extra cross-polarization due to fabrication defaults difficult to quantify in this analysis. As a conclusion, the corrugated horn fabrication tolerance must be between 1.5 and 4.5 μm .

5.2.4. Statistics of the first 60 ALMA band 10 cartridges

A total of 60 ALMA band 10 receivers have already been produced and tested. Therefore, it is possible to calculate interesting statistics from their measurement results. Table 5.9 shows the average values and standard deviations of measured efficiencies for the all the fabricated ALMA band 10 production receivers. Average values compare well with the calculated values in section 5.2.2. Additionally, standard deviations are about half the value of the calculations for standard tolerances in the optics and 5 micron tolerances in corrugated horn small features. This means that the fabrication and assembly tolerances actually achieved in the receivers are better than the maximum values of tolerances allowed. It is interesting to observe that the approximate proportion of the standard deviations (aperture : taper : spillover efficiencies) in these measurements is 1: 1.25 : 0.75, whereas it was 1: 1.5: 0.7 for the values calculated in table 5.5. This is quite similar considering all tolerances and manufacturing errors cannot be modeled.

Table 5.9. Average values (out of parenthesis) and standard deviation (within parenthesis) of the measured tolerances for all ALMA band 10 production cartridges up to date

	Aperture eff. (%)	Taper eff. (%)	Spillover eff. (%)	Polarization eff. (%)
P0 804 GHz	86.16 (0.59)	91.29 (0.78)	94.70 (0.40)	99.88 (0.03)
P1 804 GHz	86.13 (0.58)	91.49 (0.73)	94.46 (0.41)	99.87 (0.04)
P0 879 GHz	86.19 (0.60)	91.59 (0.68)	94.43 (0.34)	99.88 (0.03)
P1 879 GHz	86.20 (0.59)	91.72 (0.70)	94.31 (0.37)	99.89 (0.04)
P0 943 GHz	85.95 (0.61)	91.14 (0.65)	94.68 (0.44)	99.87 (0.05)
P1 943 GHz	85.94 (0.70)	91.13 (0.83)	94.65 (0.32)	99.87 (0.04)

5.3. 900-GHz HEB Receiver Tolerance Analysis

In chapter 4, it was shown that the measured beam patterns of the HEB mixer receiver developed by Prof. Yamamoto's group at the University of Tokyo did not match simulation results. Instead, beam patterns were quite distorted, with the consequent degradation of the science capabilities of the receiver. Therefore, it is critical to understand if those distorted patterns are a consequence of a design very dependent on tolerances or just a consequence of a defective component. Using a similar approach to that for ALMA band 10 optics, an analysis of the effect of fabrication and assembly errors on performance has been carried out for the optics of this receiver. The analysis has been carried out at the design frequency of 900 GHz. MATLAB has been used to create the PO simulation input files using random dimensions, positions and orientations for all optical components. The generated models have been analyzed using the PO software GRASP. Then, co-polarization patterns have been fitted by fundamental Gaussian beams for easier comparison, and cross-polarization levels have been calculated. In the calculation of cross-polarization levels, no wire grids have been considered in order to have a more clear understanding of how the cross-polarization depends on the horn and the ellipsoidal mirror. The effects of truncation in IR filters and cryostat window have not been considered this time in order to speed up lengthy simulations. Fabrication and assembly errors for each simulation have been obtained independently using Gaussian statistics with mean the design value and with different standard deviations σ , considering that the tolerance is equal to 3σ . More than 1000 simulations have been run with different sets of random values for errors. At first, the same standard deviations as for the ALMA band 10 analysis were used. This is 20 microns fabrication tolerance, 20 microns assembly tolerance in each dimension and 1 mrad for orientation tolerance (model 1). The results of this simulation did not show any important degradation in the co-polarization pattern. Therefore, two more analyses were performed. The second analysis consisted of increasing all tolerances by a factor 2 (model 2). The third analysis consisted of using the same tolerances as for the first and adding some errors in the diagonal horn (model 3). Specifically, the diagonal horn modes TE_{10} and TE_{01} were chosen to have slightly different amplitudes and phases. The differences were $3\sigma = 5\%$ for amplitude and $3\sigma = 10$ degrees for phase. Results of mean values and standard deviations of the Monte Carlo analyses of models 1-3 are presented in table 5.10.

Table 5.10. Results of mean values (out of parentheses) and standard deviations (between parentheses) of fundamental Gaussian beam fitting and cross-polarization results for models 1 to 3 at 900 GHz

	Ideal	Model 1 (nominal tolerance)	Model 2 (tolerance x2)	Model 3 (horn modes)
Gaussicity (%)	94.603	94.603 (0.014)	94.585 (0.033)	94.586 (0.022)
Waist size in x (mm)	3.330	3.331 (0.009)	3.331 (0.016)	3.330 (0.009)
Waist size in y (mm)	3.337	3.337(0.009)	3.337 (0.016)	3.337 (0.009)
Distance to focus (mm)	136.754	136.759 (0.122)	136.777 (0.200)	136.764 (0.124)
Offset in x (mm)	0.088	0.077 (0.346)	0.074 (0.692)	0.089 (0.340)
Offset in y (mm)	0.000	0.008 (0.222)	0.010 (0.384)	-0.004 (0.225)
Tilt in x (deg)	0.034	0.032 (0.069)	0.032 (0.137)	0.034 (0.068)
Tilt in y (deg)	0.000	0.002 (0.044)	0.002 (0.075)	-0.001 (0.044)
Cross-polarization (dB)	-13.22	-13.22 (0.04)	-12.90 (0.24)	-12.91 (0.24)

Results of the previous Monte Carlo analyses show small deviations of the Gaussian beam parameters around the average values. The effect of doubling the tolerances is just an increase of the standard deviation (about double). The effect of considering some differences in the horn modes is just a slight degradation of Gaussicity and cross-polarization. None of the patterns calculated in the analyses of models 1-3 showed any significant degradation in terms of average values or spread of results. Average values were very close to ideal and standard deviation values were small. Therefore, this means that tolerances alone cannot explain why the measurements presented in chapter 4 are different from PO simulations. Additionally, this indicates that some of the optical components in the receiver under study are defective. In other words, either the diagonal horn or the ellipsoidal mirror has not been properly fabricated.

To study this, two extra Monte Carlo analyses (models 4 and 5) have been performed using nominal dimensions for all components except for the component under study. In model 4, the diagonal horn dimensions have been changed, allowing non-square apertures, using a Gaussian distribution with standard deviation equal to 1% of average values. In model 5, the ellipsoidal mirror surface has been considered non-ellipsoidal. The mirror surface has been described as a second-order polynomial whose parameters do not necessarily describe an ellipsoidal surface. Each parameter has been modeled as a Gaussian variable with a 1 % standard deviation. The mean values and standard deviations for Gaussian beam fitting and cross-polarization levels of Monte Carlo analysis results are presented in table 5.11 for models 4 and 5.

Results of the Monte Carlo analyses of models 4 and 5 indicate that the effects of a faulty mirror impact more on total performance than those of a faulty horn, for a 1% error in dimensions. Most importantly, in model 5, the consequences on the average final Gaussian beam are a decrease of Gaussicity, change of waist dimensions, beam defocus, offset increase in the x dimension and cross-polarization degradation. Another key result is the large standard deviations of Gaussicity, waist sizes and waist positions in the case of model 5. The standard deviation of 2% in Gaussicity means that values below 90% are possible. The waist size standard deviation shows that variations in the

order of mm are possible. In the case of the waist position, the standard deviation is around 52 mm, which means that the position of the focus strongly relies on the mirror. In other words, model 5 results prove that if the ellipsoidal mirror is defective, it cannot focus the beam properly in terms of Gaussicity, waist sizes, symmetry and waist position. These degradations perfectly fit the degradations found in the measured beams. In addition to this, all beam patterns generated in the Monte Carlo analyses of models 1-5 have been stored. An inspection of these patterns shows that, in the case of the analyses of models 1-4, there were not any distorted patterns, whereas in the case of the analysis of model 5, there were many distorted patterns. Actually, some of these resembled the measured patterns in chapter 4, as shown in figure 5.9, even if the effects of truncation in the cryostat mirror were not considered.

Table 5.11. Results of mean values (out of parentheses) and standard deviations (between parentheses) of fundamental Gaussian beam fitting and cross-polarization results when some component is defective at 900 GHz

	Ideal	Model 4 (Diagonal Horn)	Model 5 (Ellipsoidal Mirror)
Gaussicity (%)	94.603	94.597 (0.016)	93.437 (2.061)
Waist size in x (mm)	3.330	3.333 (0.024)	3.677 (1.487)
Waist size in y (mm)	3.337	3.339 (0.023)	3.781 (1.489)
Distance to focus (mm)	136.754	136.741 (0.863)	175.838 (52.110)
Offset in x (mm)	0.088	0.088 (0.005)	0.162 (0.340)
Offset in y (mm)	0.000	0.000 (0.001)	0.000 (0.000)
Tilt in x (deg)	0.034	0.034 (0.001)	0.047 (0.069)
Tilt in y (deg)	0.000	0.000 (0.001)	0.000 (0.000)
Cross-polarization (dB)	-13.22	-13.19 (0.05)	-12.08 (2.49)

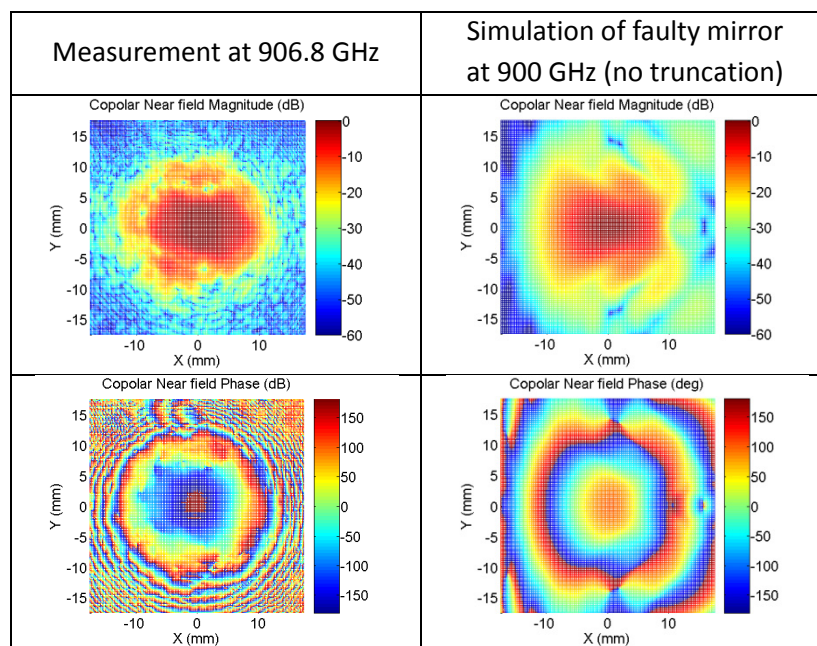


Figure 5.9. Comparison of measured patterns and simulations with a slightly non-ellipsoidal mirror

Monte Carlo analyses generate much data from individual PO simulations, which can be used to generate histograms of the Gaussian beam parameters. These histograms provide more insight about the kind of distribution which parameters follow when errors follow specific distributions, such as Gaussian in the case of models 1-5. Figure 5.10 presents the histograms for Gaussicity, waist size, focus offset and cross-polarization for models 2 and 5. It thus provides a comparison between a case in which errors are due to usual tolerances and a case in which there is a faulty component. Notice that horizontal scales are very different. Histograms for model 5 show a great dispersion of the data and distributions which are not Gaussian. In the case of model 2, histograms show distributions with approximately Gaussian shapes, except in the case of cross-polarization. Moreover, the data spreads for model 2 are at least one order of magnitude less than in the case of model 5.

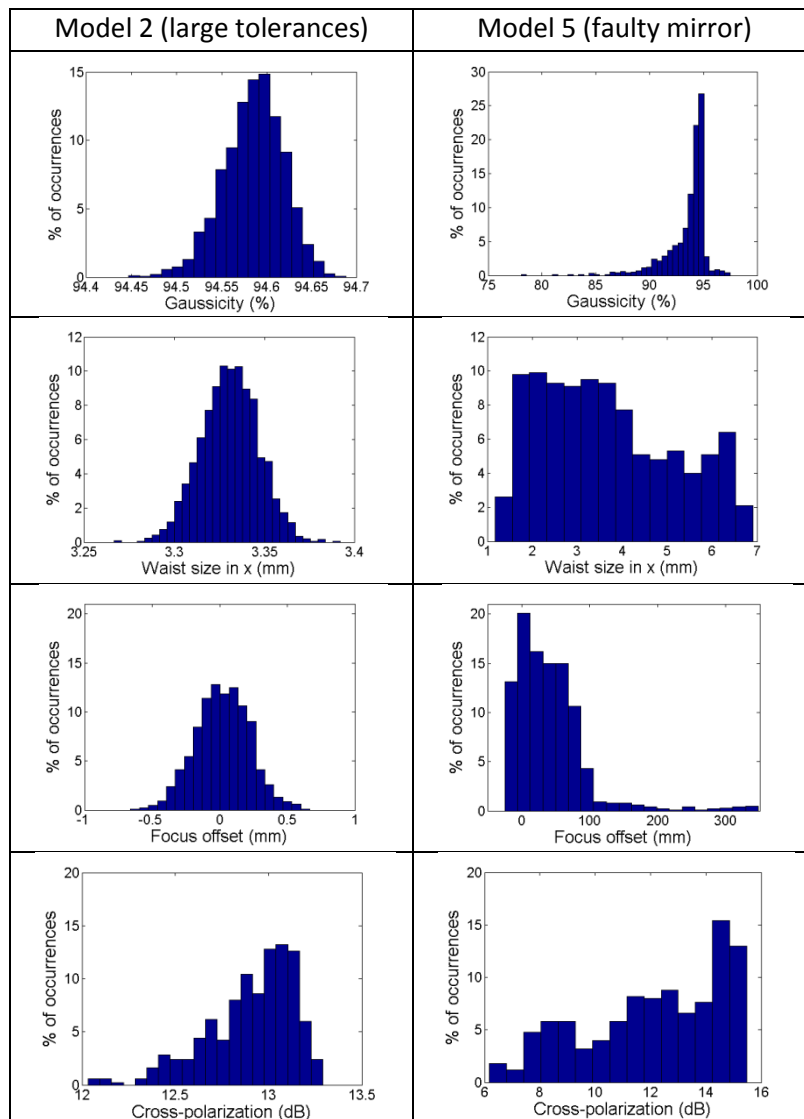


Figure 5.10. Histograms of Gaussicity, waist size, focus offset and cross-polarization for models 2 and 5 at 900 GHz

Finally, the conclusions of the Monte Carlo analysis have been tested by checking the beam performance of the ellipsoidal mirror and by measuring its surface by laser. Firstly, the mirror was

disassembled from the receiver and placed on a XYZ stage in front of a probe horn. A room-temperature receiver based on Schottky diodes and manufactured by VDI [88] with diagonal horn input has been used to detect the radiation coming from the probe horn and reflected in the ellipsoidal mirror. A photograph of the measurement setup is shown in figure 5.11. Since the diagonal horn dimensions used in this receiver are different from the HEB mixer block diagonal horn dimensions, new quasi-optical analyses and GRASP simulations have been performed to compare the measured data to the expected radiation patterns. The position of the XYZ stage has been adjusted to provide the best possible beam focus. Results of the measurements at the waist position and the calculated far fields are compared to GRASP simulations in figure 5.12. Results show that even though high beam Gaussicity can be achieved (around 97%), the phase distribution in the near field is much distorted. This translates in distorted beams in the far field, such as those measured for the whole receiver and shown in chapter 4.

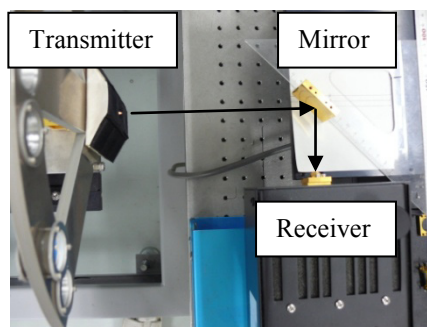
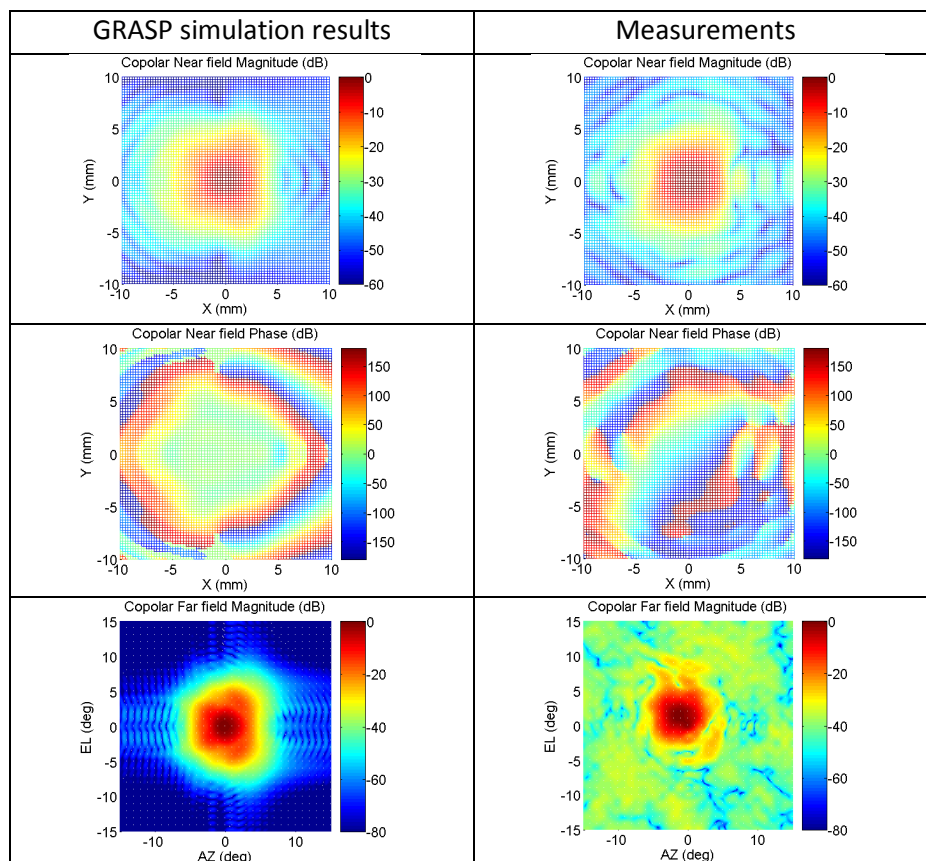


Figure 5.11. Measurement setup for the room-temperature characterization of the ellipsoidal mirror



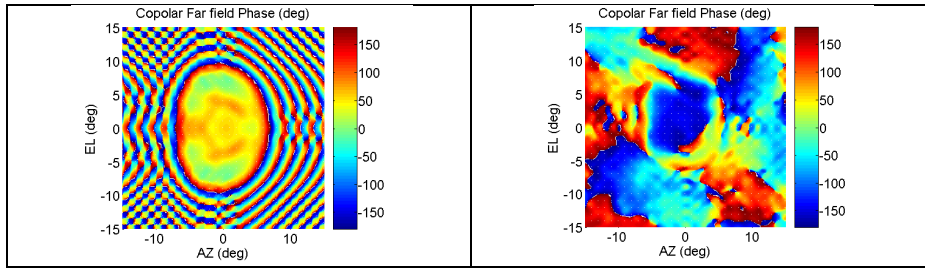


Figure 5.12. Comparison of GRASP simulations and room-temperature measurement results

The final check on the mirror has been a 3D laser measurement performed at NAOJ. Figure 5.13 shows the measurement setup. The comparison of the measured mirror surface with the theoretical ellipsoidal surface shows large surface errors in the entire mirror surface. In addition, there is a strange large error structure near the mirror center, which further distorts the reflected beam. Results of the 3D laser measurement are presented in figure 5.14.

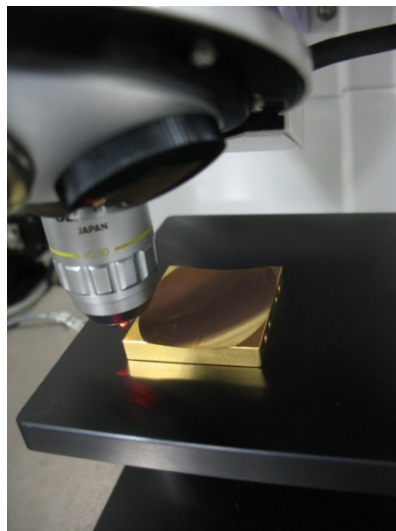


Figure 5.13. Measurement setup of the 3D laser measurement of the ellipsoidal mirror surface

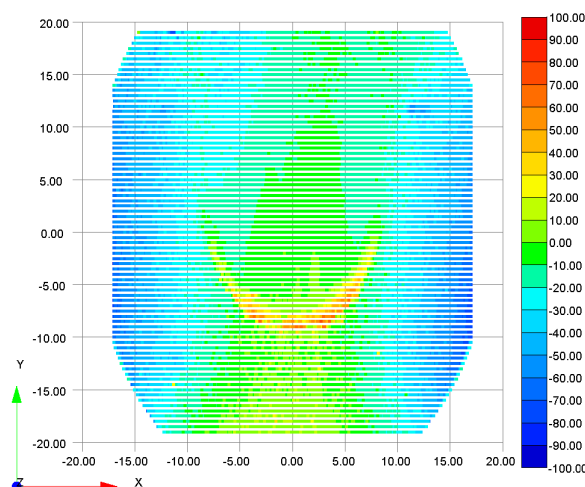


Figure 5.14. 3D laser measurement results of the ellipsoidal mirror surface. Values plotted are the difference in microns between the measured surface and the theoretical ellipsoidal surface

In conclusion, the ellipsoidal mirror is of poor quality and it is distorting the receiver beam patterns. The combination of simulations and measurements has proved to be a useful and powerful tool to trace problems in a quasi-optical system. The ellipsoidal mirror will be replaced in the future in order to improve the receiver optical efficiency and enhance astronomical observation capabilities.

Chapter 6

Effect of Infrared Filters on ALMA Band 10 Optics

6.1. Introduction

ALMA band 10 tertiary optics is located in the 4K stage of the ALMA cryostat and the RF signal has to go through one quartz window and two infrared (IR) filters in the optical path between the secondary mirror of the telescope antenna and the corrugated horns in the receivers. The optical efficiency measured at room temperature is very similar to the simulated performance using GRASP. However, when the standard optics design was used at cryogenic temperatures in the real receiver for the first time, performance in terms of aperture efficiency was degraded with respect to measurements at room-temperature without filters and window. This means worse astronomical observation capabilities. This degradation was unexpected and the cause was unknown. An example of a good beam at room temperature compared with a distorted beam measured at cryogenic temperature at 804 GHz is presented in figure 6.1.

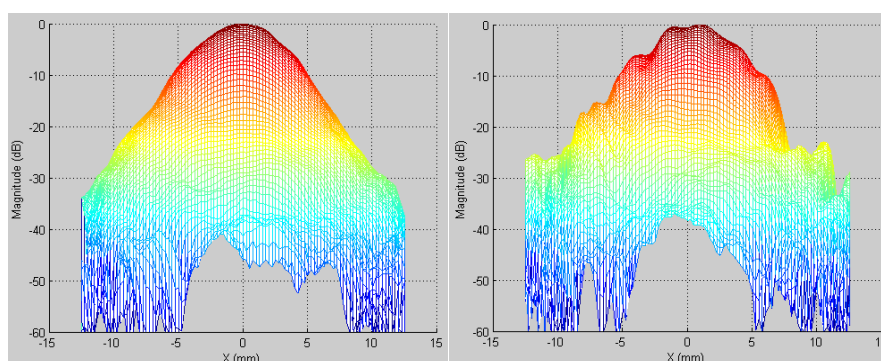


Figure 6.1. Beam at 804 GHz measured at room temperature without IR filters and cryostat window (left) and measured at cryogenic temperature in the test cryostat (right)

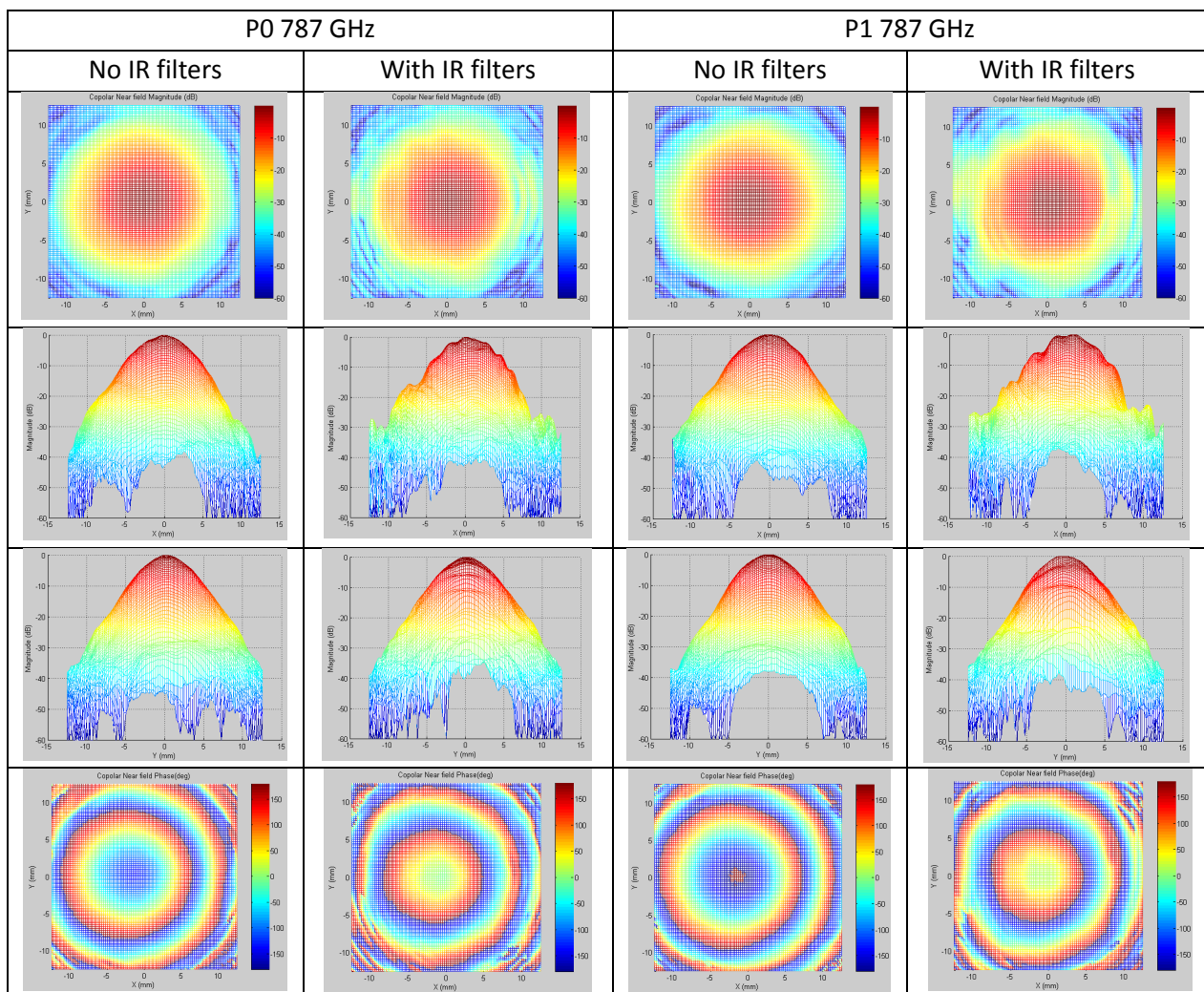
Careful investigation into the problem showed a potential risk of reflections in the IR filters. Circuitual simulations using the results derived from Terahertz Time Domain Spectroscopy (THz-TDS)

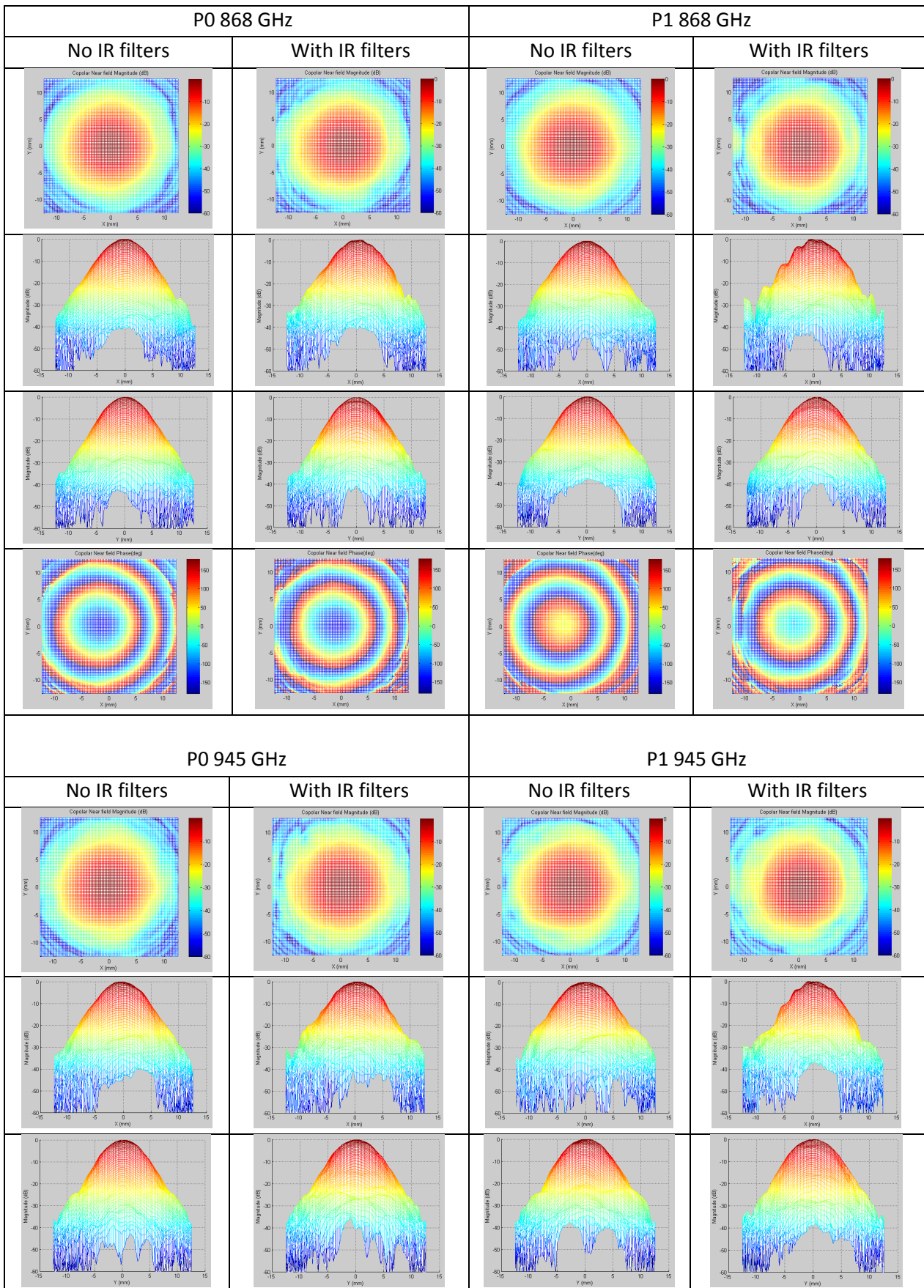
measurements [112] showed that the reflectivity of the filters dielectric could be non-negligible at the lower frequencies of ALMA band 10, which were the frequencies with greater beam degradation at cryogenic operation.

Once the cause of the problem was identified, appropriate modifications of the optics components were performed to avoid multiple reflections in filters and in the plane of the corrugated horn aperture. These changes worked and aperture efficiency was improved back to the levels measured at room temperature.

6.2. ALMA Band 10 Optical Performance using IR Filters in the Cryostat

The beam patterns of the ALMA band 10 receiver when the IR filters are placed in the cryostat inner shields are distorted with respect to the beam patterns measured at cryogenic temperature without IR filters. The comparison between the co-polar and cross-polarization patterns in the two cases for the ALMA band 10 prototype model are presented in figures 6.2 and 6.3.





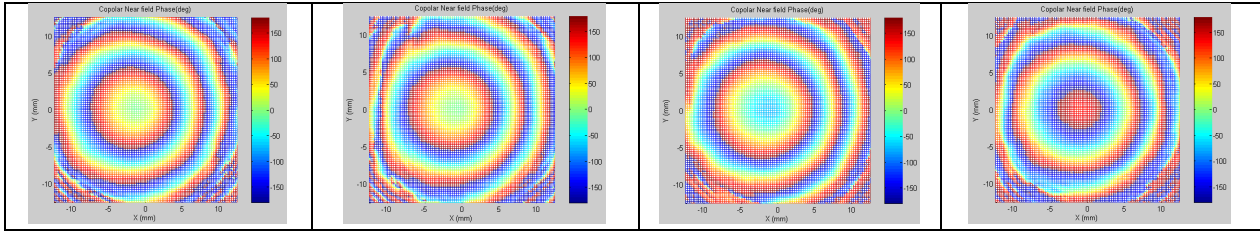


Figure 6.2. Near-field co-polarization patterns (magnitude and phase) with and without filters

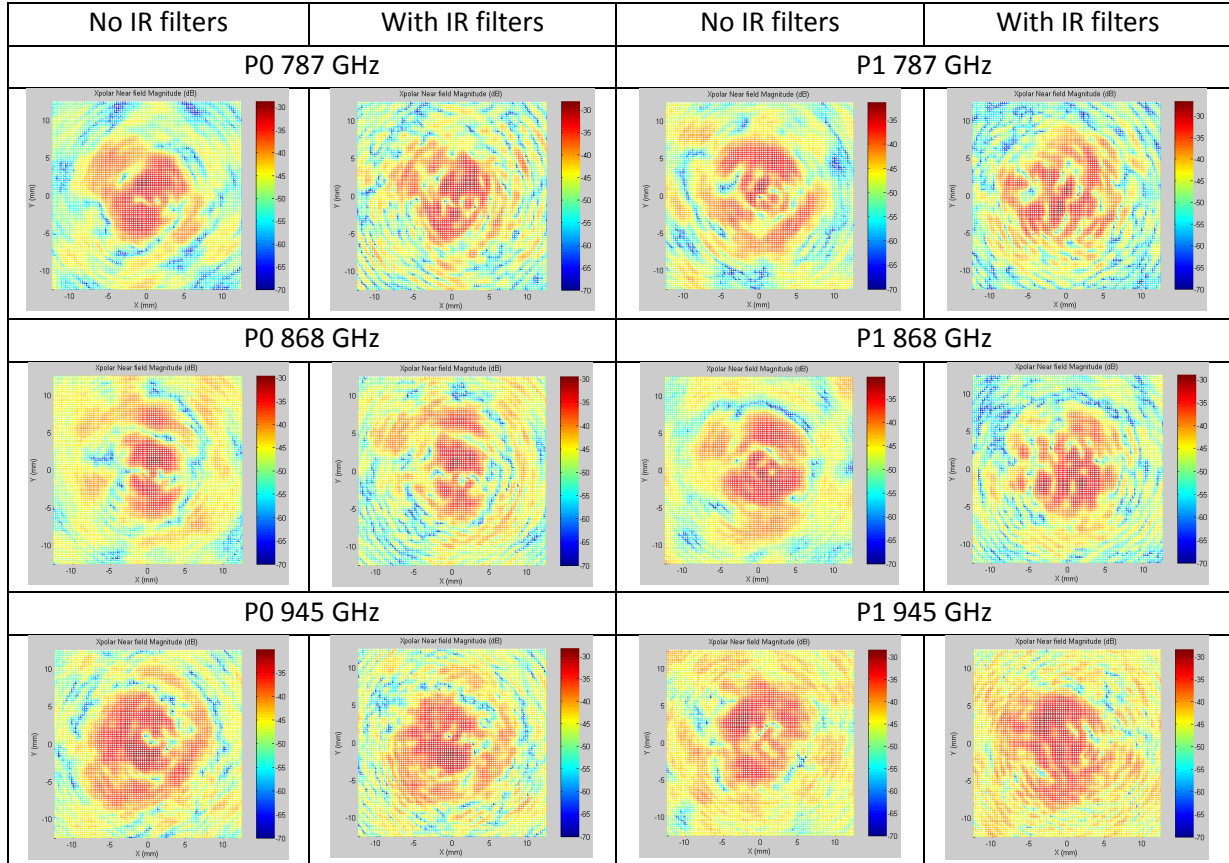


Figure 6.3. Near-field cross-polarization patterns (magnitude) with and without filters

The previous measurements have been fitted by fundamental Gaussian beams and cross-polarization levels have been calculated. Results are reported in table 6.1. Patterns measured with IR filters show lower Gaussianity, increased cross-polarization and decreased efficiencies. The degradation in total aperture efficiency is as large as almost 1% at 787 GHz. The effect of filters at 868 and 945 GHz is less than at 787 GHz. Parameters such as offsets, tilt angles or beam squint are not reliable in the case of the measurements with IR filters, due to the distorted shape of the beams. These parameters are calculated by fitting the measurements to theoretical functions. Since the beam shape is distorted in the case with IR filters, it is difficult to find a meaningful fit and the optimization performed when fitting the beam will just be that one which provides the least error, which is not necessarily the best one. Hence, the parameters of the optimized theoretical beam are not as meaningful as in the case of beams without distortion.

Table 6.1. Gaussian beam fitting, efficiencies, cross-polarization and beam squint analyses with (w/) and without (w/o) IR filters

RF Frequency (GHz)	787 GHz				868 GHz				945 GHz			
	P0		P1		P0		P1		P0		P1	
	w/o	w/	w/o	w/	w/o	w/	w/o	w/	w/o	w/	w/o	w/
Gaussianity, [%]	97.759	97.193	98.280	96.930	98.099	98.029	98.416	97.741	97.827	97.865	97.255	97.625
w0x, [mm]	2.254	2.325	2.245	2.226	2.034	2.028	2.037	2.033	1.843	1.843	1.818	1.896
w0y, [mm]	2.232	2.242	2.312	2.289	2.046	2.051	2.066	2.016	1.862	1.880	1.837	1.825
z_from_w0xy, [mm]	83.473	84.140	84.349	85.193	81.814	81.867	84.161	83.206	81.415	84.104	84.010	82.064
XOffset, [mm]	0.199	-0.351	0.206	-0.275	0.217	-0.225	0.174	-0.286	0.305	-0.268	0.123	-0.254
YOffset, [mm]	-0.191	-0.065	-0.015	0.056	-0.112	-0.011	0.023	0.049	-0.132	-0.052	-0.034	0.033
XTilt, [deg]	0.945	0.980	0.893	0.922	0.937	0.916	0.938	0.923	0.871	0.942	0.984	0.905
YTilt, [deg]	-0.038	0.010	-0.074	-0.070	-0.071	-0.031	-0.110	-0.115	-0.036	-0.018	-0.055	-0.019
Xpol level (dB)	29.22	28.05	31.17	26.83	29.57	28.92	30.44	28.93	30.21	28.35	28.37	28.06
Edge taper (dB)	-9.89	-10.82	-10.38	-10.72	-9.54	-9.65	-10.05	-9.54	-9.05	-9.39	-8.66	-10.10
Taper eff (%)	92.16	91.11	91.04	91.33	91.85	91.56	91.14	92.04	92.67	92.20	93.46	92.31
Spillover eff (%)	94.68	94.21	94.13	93.65	94.06	93.94	94.31	93.69	93.80	93.67	93.16	93.71
Polariz eff on sec (%)	99.84	99.86	99.89	99.86	99.87	99.88	99.87	99.87	99.85	99.83	99.83	99.78
Defocus Eff (%)	100.00	100.00	100.00	100.00	99.99	99.99	99.99	99.99	99.98	99.99	99.98	99.99
Aperture eff (%)	86.35	85.40	85.92	85.18	86.09	85.69	85.75	85.97	86.69	86.11	86.70	86.12
Beam Squint (%)	4.01	0.44	4.01	0.44	2.34	2.63	2.34	2.63	2.37	2.88	2.37	2.88

6.3. Reasons for Degraded Optics Performance

ALMA band 10 IR filters are composed of thin dielectric layers of Mupor and Gore-Tex. Cryostat windows are made of quartz with Teflon anti-reflection coatings. Characterization of these materials using THz-TDS can provide accurate values of transmittance and absorption at a broad bandwidth.

THz-TDS is a well-known spectroscopic technique which consists of irradiating very short pulses, in the order of 100 fs, on a sample of the material under analysis and then, analyzing the shape of the received pulses after going through the material sample. A sample of the originally irradiated pulse, which is delayed by delay lines, is sent to the receiver at the same time as the information pulse arrives in order to “gate” the response of the THz detector. The schematic of a typical THz-TDS system is presented in figure 6.4. The received pulse is Fourier transformed to get spectral information over a wide bandwidth. The use of very short pulses and high time-resolution detectors makes this system extremely wideband. However, the frequency resolution is worse than for other spectroscopic techniques. Typical bandwidths are around 2-5 THz with a spectral resolution of around 50 GHz [113]. The advantage of THz-TDS with respect to other spectroscopic techniques is it can provide not only amplitude but also phase information of the pulse through the sample. This allows the characterization of transmittance and absorption of materials.

Mupor of different thicknesses have been characterized by THz-TDS at room temperature in vacuum using the facilities at NICT/Koganei. Real and imaginary parts of dielectric constant have been calculated from power transmittance and phase shift measurements. The filter located at the 15 K stage, shown in figure 6.5 (left), is composed of a single layer of PM131D Mupor. The measured complex refractive index was $n = 1.222 + j0.0012$. The filter located at the 110 K stage, shown in figure 6.5 (right), is composed of a layer of Gore-Tex plus one layer of PM21MD Mupor. The measured complex refractive index for this Mupor layer was $n = 1.242 + j0.0045$.

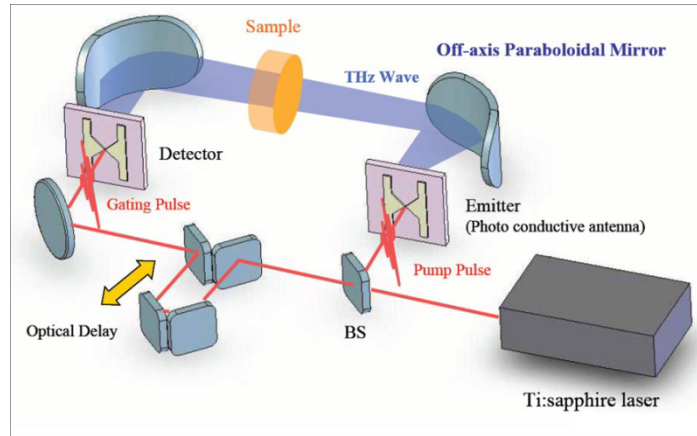


Figure 6.4. Schematic of a typical THz-TDS system
 (SOURCE: RIKEN, http://www.riken.jp/lab-www/THz-img/English/annual_gas.htm)

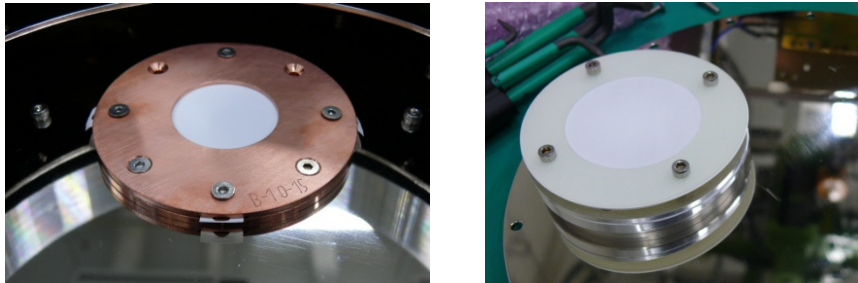


Figure 6.5. 15K (left) and 110 K (right) IR filters mounted on cryostat shields

These results were obtained by fitting THz-TDS power transmittance and phase shift data with the theoretical results for different complex refractive indexes (n , k). The best fitting results are presented in figure 6.6 for the 15 K filter, and in figure 6.7 for the 110 K filter.

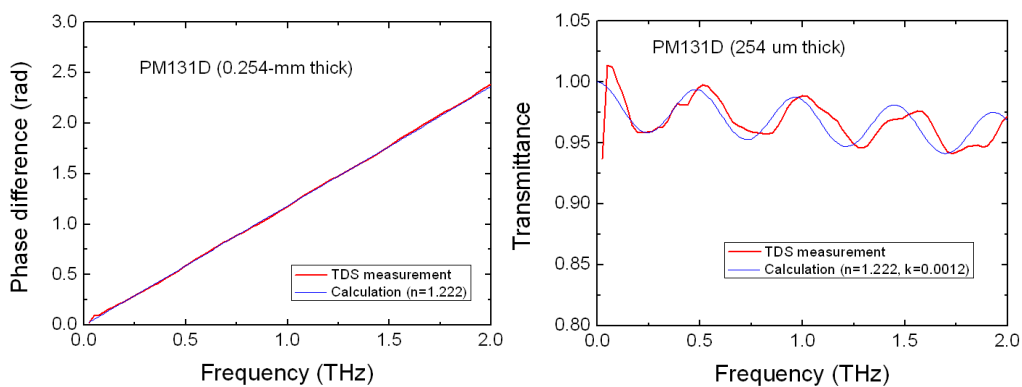


Figure 6.6. Phase shift and transmittance comparison for THz-TDS measurement and calculated result for $n=1.222$, $k=0.0012$ for PM131D Mupor

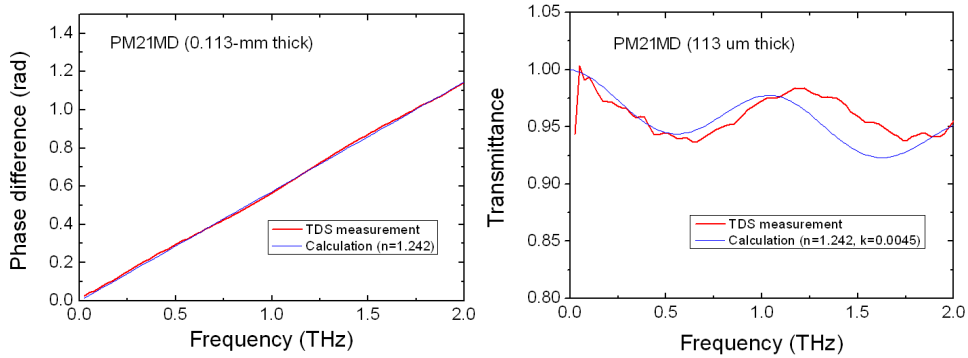


Figure 6.7. Phase shift and transmittance comparison for THz-TDS measurement and calculated result for $n=1.242$, $k=0.0045$ for PM21MD Mupor

A simple transmission line equivalent model [114] has been used to calculate the transmitted and reflected power for dielectric layers of the measured thickness and complex refractive index. The refractive index n has been used to calculate the equivalent transmission line dielectric constant and the extinction coefficient k has been used to estimate the loss in dB/m. Models with the exact values used for simulation are presented in figure 6.8.

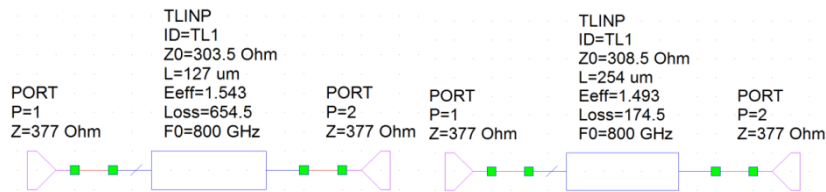


Figure 6.8. Equivalent waveguide circuits to calculate transmittance and reflectivity of Mupor dielectric layers. The upper circuit is for PM21MD Mupor and the lower circuit is for PM131D Mupor

Results, in figure 6.9, show that power transmission is lower at the lower frequencies of ALMA band 10 for both Mupor layers. Results of reflectivity in figure 6.10 show that this translates in a large reflectivity at those frequencies. The maximum of the reflected beam in the 15 K filter is only 15 dB less than the incident beam maximum.

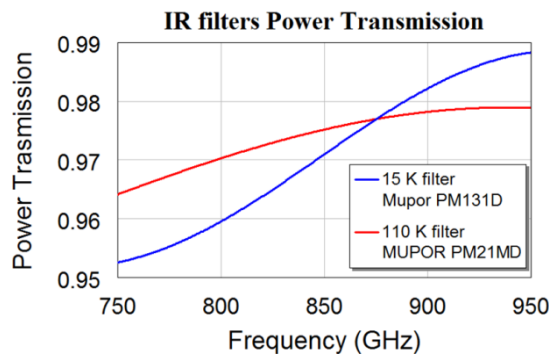


Figure 6.9. Simulated power transmission for Mupor materials used in ALMA band 10 IR filters

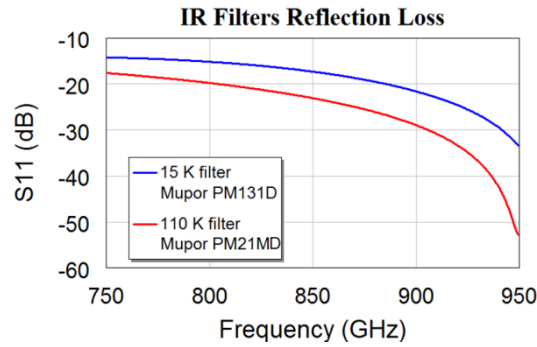


Figure 6.10. Simulated reflection loss for Mupor materials used in ALMA band 10 IR filters

Simple ray tracing simulations in figure 6.11 show that the reflected energy in all IR filters and cryostat window will hit the area around the corrugated horn rim. With the current optics design, this reflected beam will be reflected again around the horn rim and it will interfere with the main beam. This explains the distorted beams when IR filters are used. The simplest solution to avoid this interference is to prevent this reflection around the horn rim and, if possible, to absorb this energy so it does not bounce uncontrolled in the 4 K stage of the cryostat.

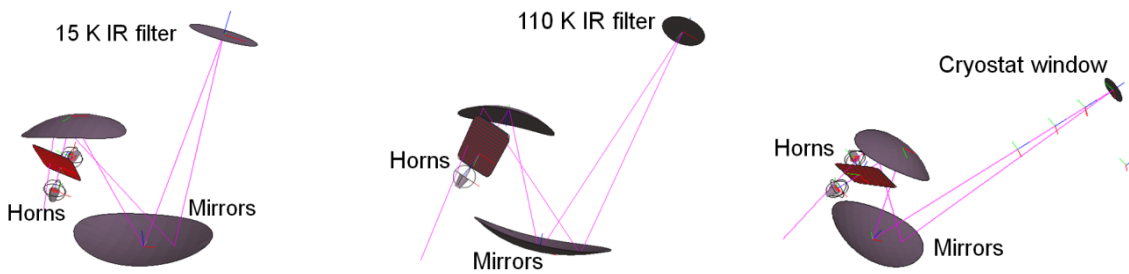


Figure 6.11. Ray tracing shows that reflected energy will be reflected in the mirrors and hit near the corrugated horn rim

6.4. Proposed Solution

Two slight modifications in ALMA band 10 optics have been proposed to avoid mirror-like reflections around the horn rim. Firstly, corrugated horn rims have been chamfered at 45 degrees so that energy hitting the rim will be dispersed in a different direction. Secondly, THz absorbent paint has been applied around the horn rim in order to absorb the energy hitting around the rim. The modification of the corrugated horn rim is shown in figure 6.12. The rim chamfered at 45 degrees is clearly visible in the horn on the right. The right-hand side photo in figure 6.13 shows how the absorbent paint has been applied around the horn rim. Currently, instead of painting directly, a small aluminum plate previously painted with absorbent paint is assembled on the wire grid box. The used absorbent paint is composed of SiC grains (350 μm diameter), stycast epoxy 2850FT and curing agent catalyst 9 [96].



Figure 6.12. Original ALMA band 10 corrugated horn (left) and new 45-degree chamfered horn (right)

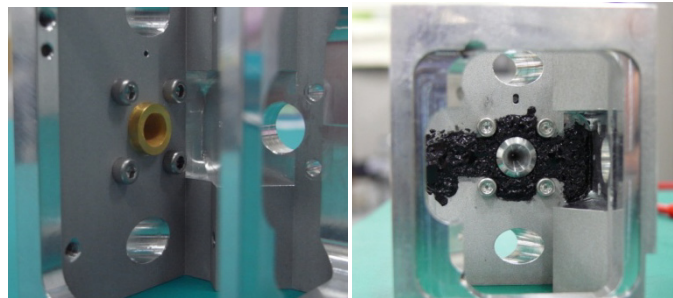


Figure 6.13. Old and new design corrugated horns mounted on wire grid box Without (left) and with (right) absorbent paint around horn rim

6.5. Validation through Measurements

Room-temperature measurements using a Schottky-diode receiver and prototype IR filters at the same position as in the ALMA cryostat have been performed. The room-temperature measurement setup used for this experiment is the same as presented in chapter 4 for room-temperature characterization, but mounting ALMA band 10 optics on a support structure which can also hold the IR filters and cryostat window at appropriate positions. A photograph of this support structure is presented in figure 6.14. Notice that IR filters and cryostat window can be easily mounted on or removed from the support structure. This allows comparison of beams with different filters/window combinations or without any of them.

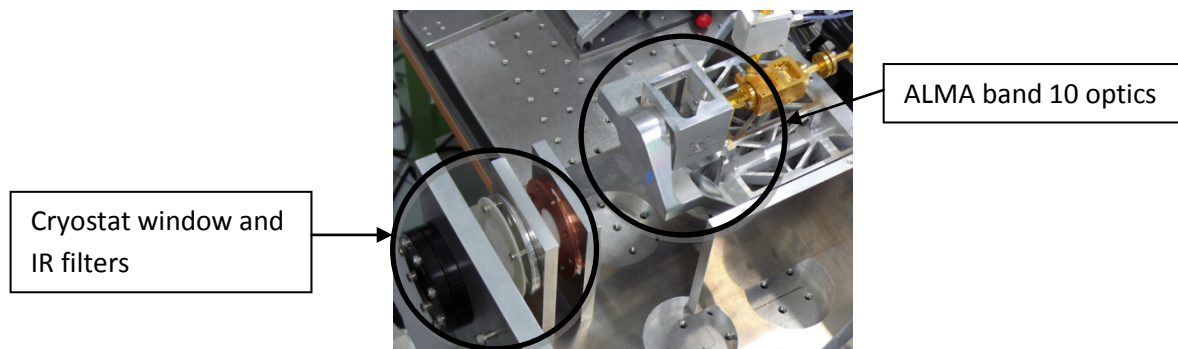


Figure 6.14. Measurement setup at room temperature to characterize beam performance with and without IR filters and cryostat window

Some interesting results are shown in figure 6.15. For these measurements, the cryostat window has been removed in order not to truncate the reflected beams. The left-hand side beam patterns are those of the original design. The predicted reflected beam is easily visible not far from the main beam. This reflected beam will be diffracted in the cryostat window aperture and interfere with the main beam creating the interference pattern which can be seen in the beam pattern on the right in figure 6.1. In other cases, for different optics components or cooling cycles in real cryogenic operation, the beam could be reflected in a different angle and the final reflection could be within the main beam. The right-hand side beam patterns are those of the modified optics design. The reflected beam is greatly absorbed and only some residual reflected energy is left.

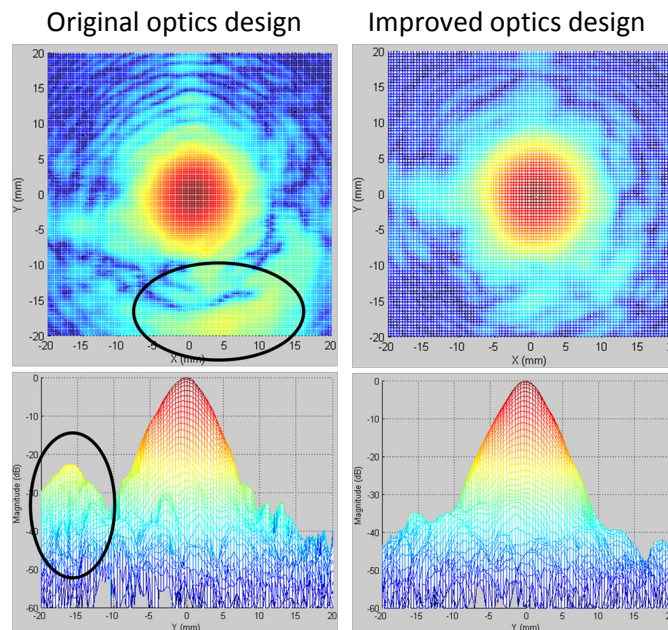


Figure 6.15. Room-temperature beam measurement results at 832 GHz for original and improved optics design with infrared filters in both cases. The reflected beam clearly appears on the left in the case of the original optics design

A comparison between the measured beam patterns after the cryostat window has been put in place is presented in figure 6.16. The improved optics design presents a ripple-free main beam and no large side lobes, as opposed to the beam measured for the original optics design.

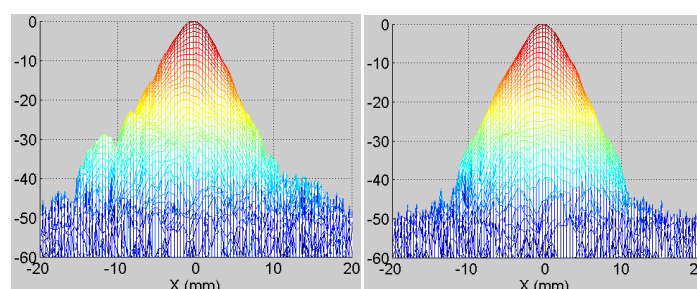
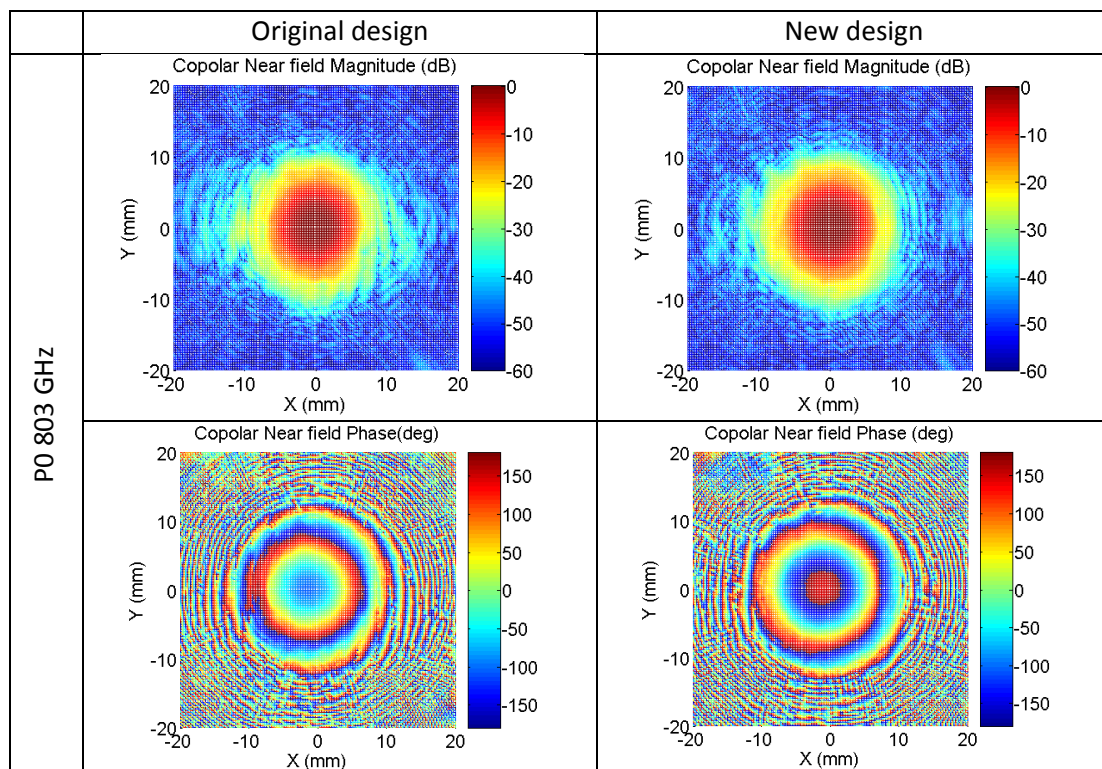
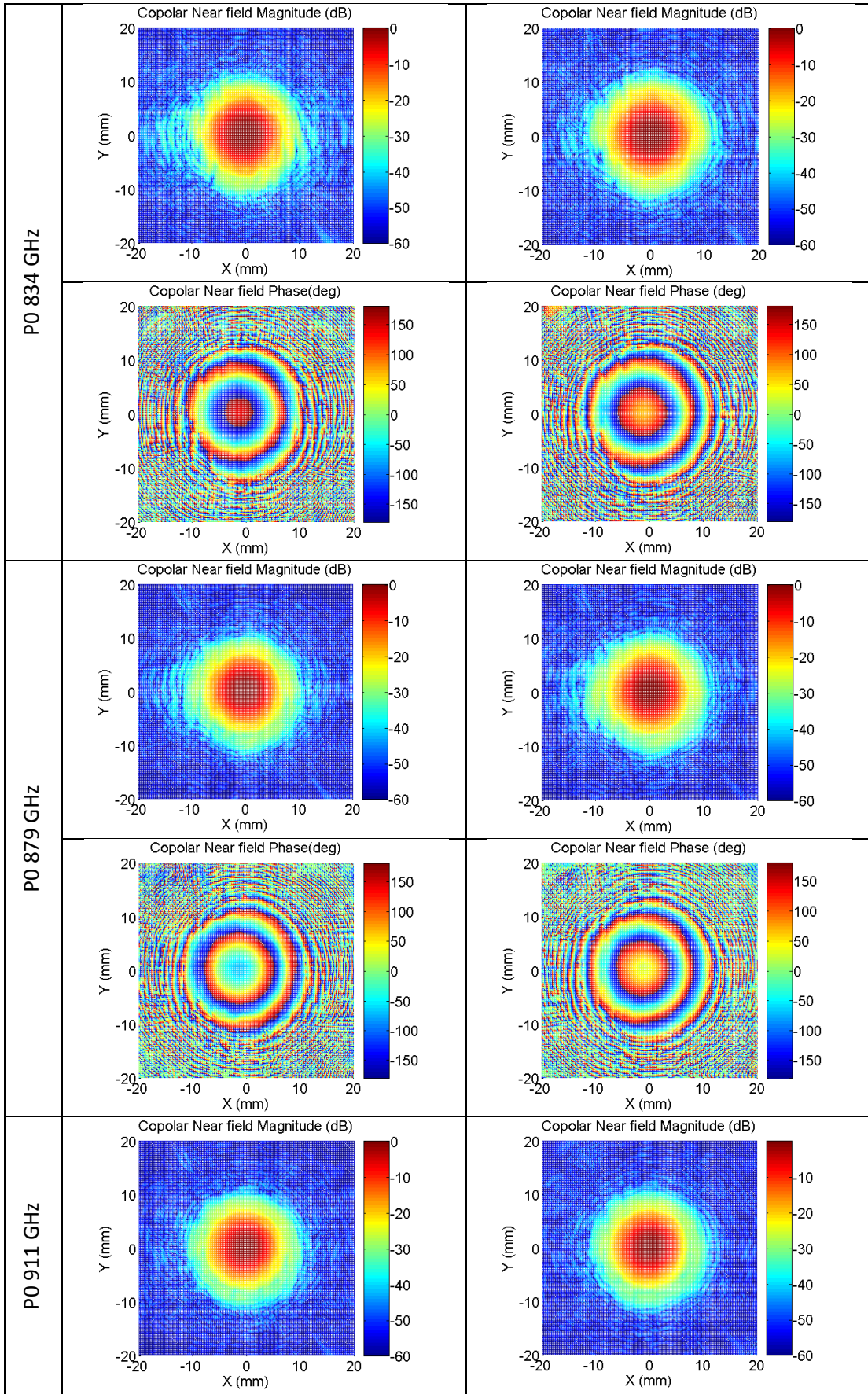


Figure 6.16. Beam measured at room temperature with IR filters and cryostat window for the original optics (left) and for the improved optics (right) at 832 GHz

One of the first ALMA band 10 cartridges has been characterized using the original and the improved optics designs. The beam results in amplitude and phase when the original optics is used is compared to the case when chamfered-rim horns and absorbent paint are used in figures 6.17 and 6.18 for polarizations P0 and P1, respectively. In the case of the original optics, the amplitude pattern has lots of ripples and the phase pattern shows a clear interference pattern. In the case of the new design, the beam shape is greatly improved and no interference signs apart from those of slight truncation at the cryostat window can be seen in the magnitude or phase beam patterns. The improvement is very clear at lower frequencies and polarization P1. Cross-polarization measurements have also been performed in order to confirm no unexpected cross-polarization degradation occurred due to chamfering the horns or due to the new absorbers. Results showed no changes in cross-polarization patterns and levels. Cross-polarization patterns are presented in figure 6.19.

Efficiencies at the secondary of the Cassegrain antenna have been computed in order to quantitatively compare both cases. The efficiency analyses at 804, 834, 879, 911 and 943 GHz are presented in table 6.2 for both polarizations. Improvements are significant when the new optics is used. The improvement is especially remarkable at lower frequencies, when the reflection in the IR filters is more important. In this case, improvements greater than 1% and, even up to 2%, were achieved. Results in table 6.2 show a slight degradation of aperture efficiency at 879 GHz for P1 and at 911 GHz for P0. At these frequencies, the influence of reflections in the original design was not critical. Therefore, measurement errors and different cartridge alignments can explain this slight degradation for beams which are similar.





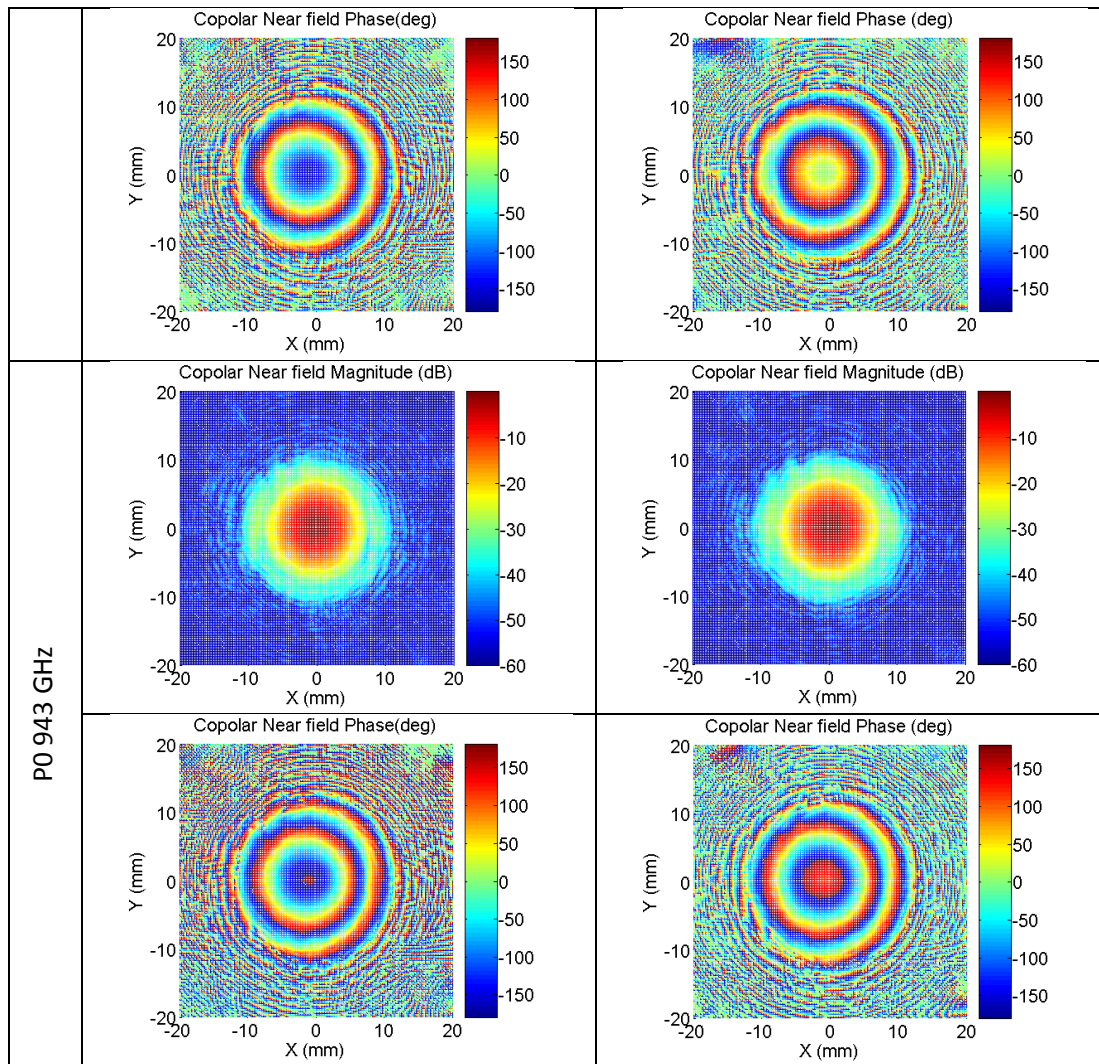
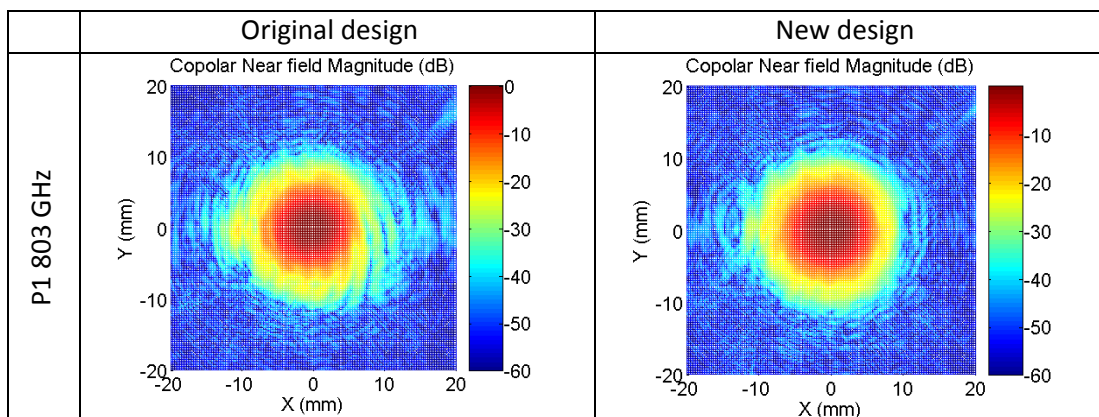
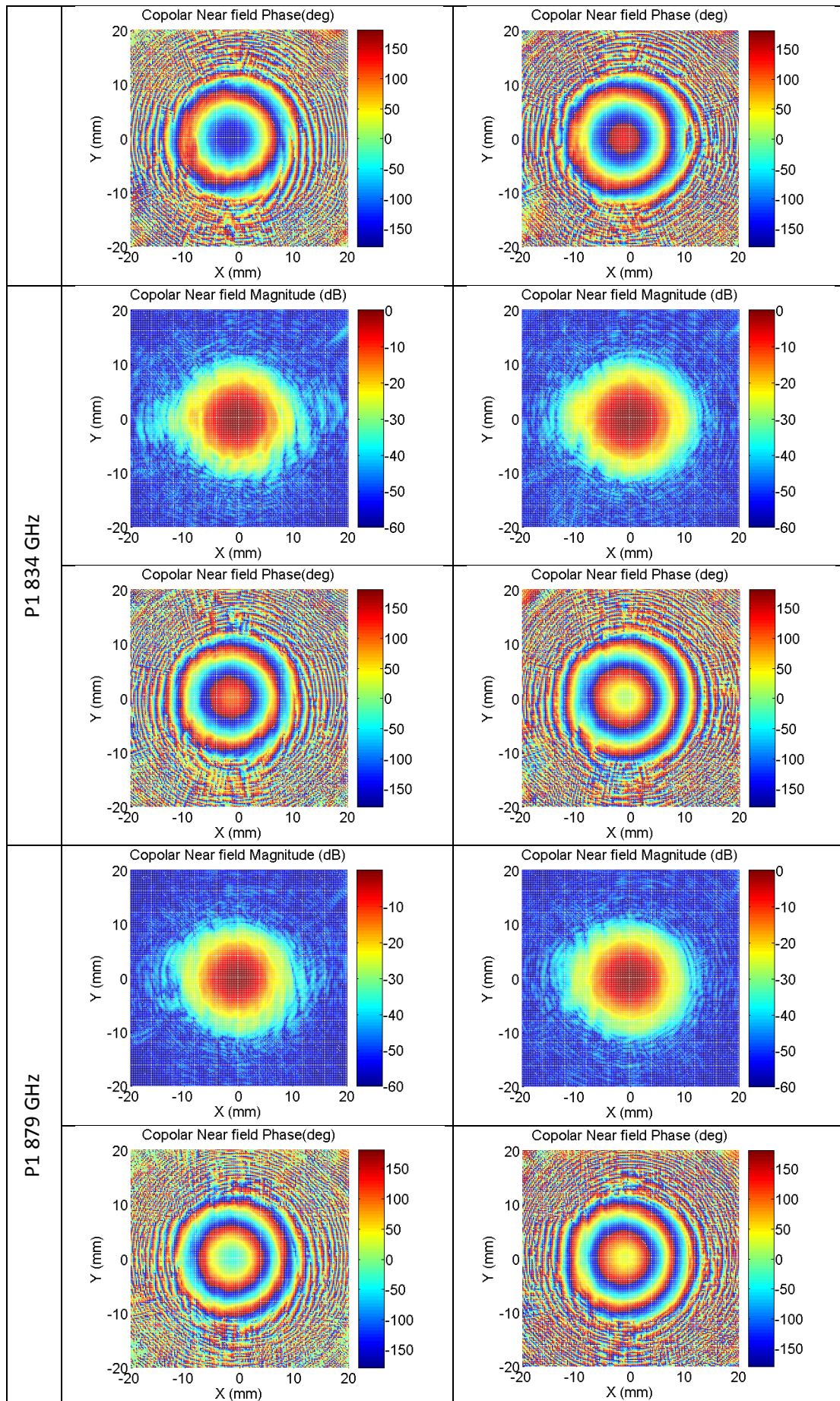


Figure 6.17. Comparison of co-polarization patterns measured for polarization P0 of cartridge #6 using the original and the improved ALMA band 10 optics design





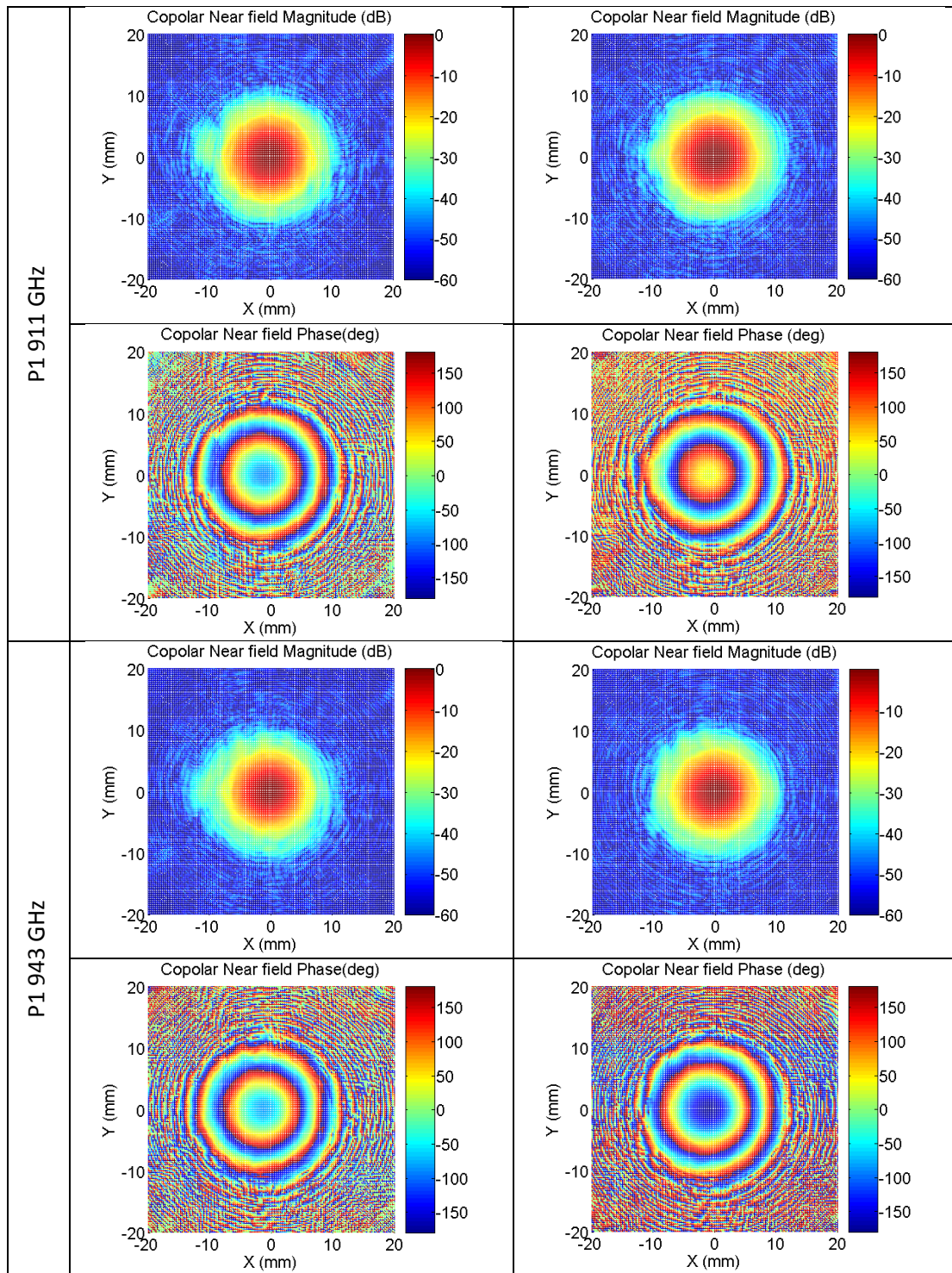
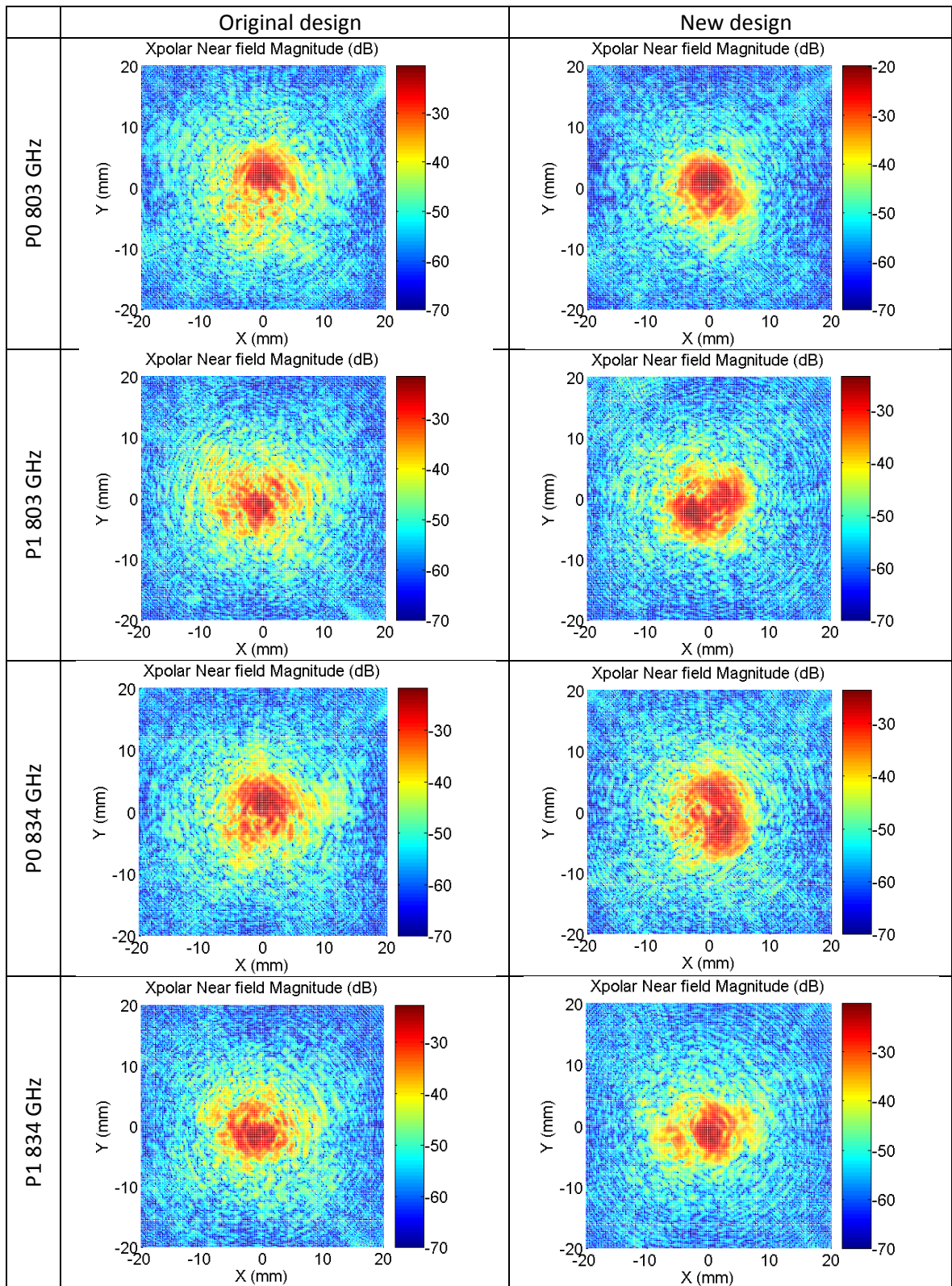
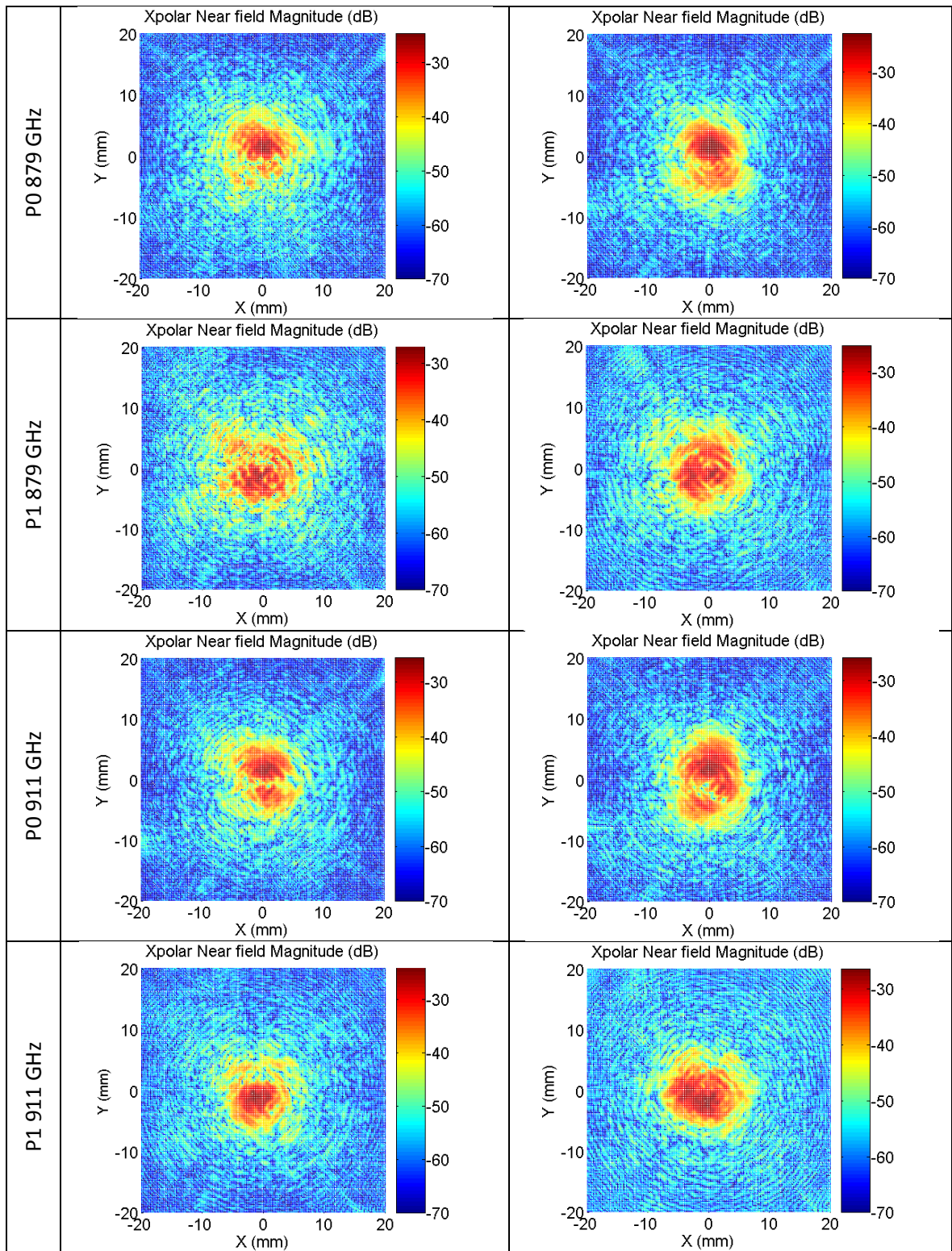


Figure 6.18. Comparison of co-polarization patterns measured for polarization P1 of cartridge #6 using the original and the improved ALMA band 10 optics design





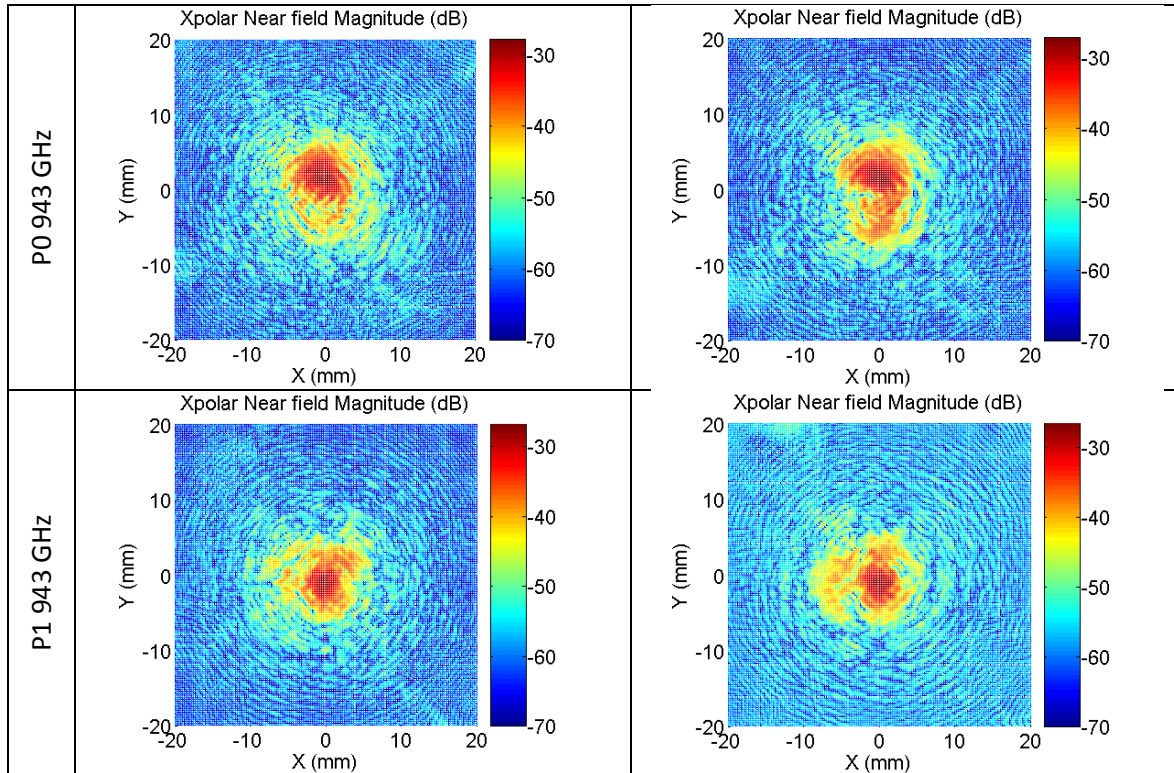


Figure 6.19. Comparison of cross-polarization patterns measured for cartridge #6 using the original and the improved ALMA band 10 optics design

Table 6.2. Efficiency analysis for ALMA band 10 cartridge #6 when the original (No abs.) and improved (Abs.) optics are used

f	pol	Taper eff. (%)		Spillover eff. (%)		Polarization eff. on sec. (%)		Defocus eff. (%)		Aperture eff. (%)	
		No abs.	Abs.	No abs.	Abs.	No abs.	Abs.	No abs.	Abs.	No abs.	Abs.
804	0	87.55	90.10	93.22	92.12	99.71	99.57	99.963	99.986	81.05	82.39
804	1	89.58	91.79	92.70	91.49	99.78	99.73	99.963	99.986	82.46	83.57
834	0	88.60	90.12	93.13	92.66	99.68	99.75	100.000	100.000	82.01	83.17
834	1	89.52	92.51	92.16	91.20	99.77	99.69	100.000	100.000	82.05	83.99
879	0	88.28	90.10	94.39	93.44	99.83	99.69	100.000	100.000	83.03	83.77
879	1	90.83	91.54	93.03	92.20	99.87	99.82	100.000	100.000	84.23	84.16
911	0	90.21	89.95	94.03	93.75	99.83	99.79	100.000	100.000	84.48	84.06
911	1	91.05	91.38	93.64	93.44	99.79	99.78	100.000	100.000	84.93	85.13
943	0	91.09	91.42	94.69	94.62	99.84	99.83	99.999	100.000	85.89	86.18
943	1	89.97	91.51	94.52	93.66	99.85	99.84	99.999	100.000	84.72	85.37

Chapter 7

Study on Cross-Polarization Performance

7.1. Introduction

One of ALMA main capabilities is astronomical polarization observations or the ability to measure simultaneously the intensity of light in orthogonal linear polarizations from an astronomical source. Polarization observations are important to study magnetic fields or scattering in molecular clouds [115]-[117]. In order to be able to perform these observations, ALMA receiver cross-polarization performance must be very good. For example, the better it is, the weaker the measurable magnetic fields are. The cross-polarization specification in an astronomical telescope is usually related to the total integrated cross-polar on the secondary with respect to the total integrated co-polar. In some other cases, it could be specified as the maximum value of cross-polar with respect to the maximum of the co-polar pattern. In the case of ALMA, the original cross-polarization specification for all the receivers in the different frequency bands was -23 dB for the integrated cross-polar on the secondary. However, that specification has proven too stringent for receivers in some bands.

ALMA band 4 [118] is currently under production at NAOJ. ALMA band 4 uses common optics for both orthogonal linear polarizations and then, an orthomode transducer (OMT) is used to separate polarizations after detection in a dual mode corrugated horn. The tertiary optics is composed of an ellipsoidal mirror and a flat mirror and is located out of the ALMA cryostat, at room temperature. ALMA band 4 optics is shown in figure 7.1. In spite of band 4 optics simplicity, the -23 dB cross-polarization requirement has been found difficult to meet. Even if individual optical components offered good performance, the total system cross-polarization was out of specifications for some cartridges.

At the time when this problem was found, there were no appropriate answers to why this happens. Most ways to tackle this problem in other bands (band 3, 6...) have been from a pure engineering point of view, without trying to look for the real physical causes of cross-polarization degradation. Band 3 proposed a modification of the ALMA requirement such that a percentage of already manufactured components could be useable. In the case of band 6, the cross-polarization levels of the components in the RF path were used to calculate the worst-case and the RMS values of the total receiver cross-polarization.

In the case of ALMA band 4, a complete explanation of the physics behind this low cross-polarization performance has been sought. Efforts have been two-fold. Firstly, the physical reasons why the addition of cross-polarization contributions from different optical components is very harmful in the case of band 4 were explained using higher-order Gaussian modes and tracking how the different contributions are combined. This was used to relax ALMA band 4 specification to a more realistic cross-polarization performance target for the current receiver architecture. Secondly, different electromagnetic analyses were performed in order to explain the non-understood frequency behavior of the system cross-polarization. These analyses have been a combination of theoretical studies and numerical simulations.

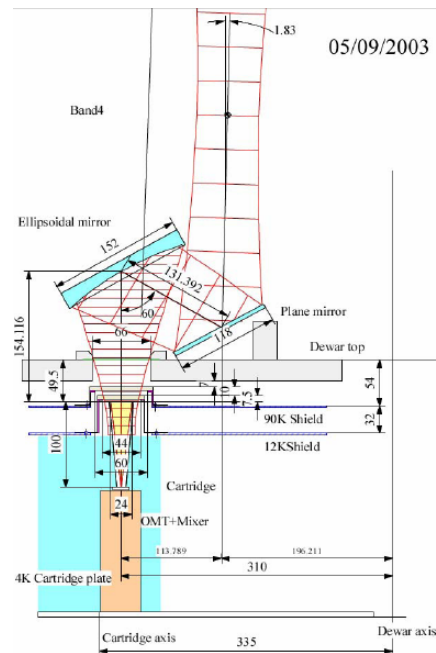


Figure 7.1. ALMA band 4 optics

7.2. Cross-Polarization in Optical Components

Some optical components can add an extra cross-polarization component into an electric field when the field goes through or is reflected in them. The additional cross-polarization is generated from the incident co-polarization components. The combination of all the cross-polarization contributions in an optical system will determine the total system cross-polarization.

7.2.1. Cross-polarization in metallic mirrors

The cross-polarization generated at non-flat mirrors is due to the reflection of an extended beam on a non-flat surface and it increases with the angular offset of the incident beam with respect to the mirror axis. In the case of a plain mirror, there is no cross-polarization component added to the fields. The created cross-polar component would be minimized by a beam incident along one of the

symmetry axes of the mirror surface, which is not usually practical. In the case of an ellipsoidal mirror, the cross-polarization (XsP) level after reflection with respect to the maximum of the reflected co-polarized (CoP) field is given by equation (7.1),

$$\frac{XsP_{\max}}{CoP_{\max}} = \frac{1}{\sqrt{2e}} \frac{w_m}{f} \tan \alpha_i \quad (7.1)$$

where w_m is the beam size at the mirror, f is the mirror focal length and α_i is the semi-bend angle provided by the mirror.

The generated cross-polar beam pattern can be properly described as a first approximation by a single higher-order Gaussian mode E_{10}/E_{01} if the incident co-polar beam pattern is a fundamental Gaussian mode. The phase difference between the generated cross-polarization and the original co-polarization is 180 degrees (minus sign for the XsP/CoP ratio) [119].

7.2.2. Cross-polarization in dielectric surfaces

The cross-polarization generated in dielectric surfaces is due to the misalignment of the incident beam with respect to the main optical axes of the dielectric surface. The difference of Fresnel transmission coefficients and/or refraction indexes for orthogonal main optical axes propagation creates cross-polarization.

For a co-polar beam polarization which differs an angle α from the orientation of one of the dielectric main optical axes, the transmitted beam can be expressed as stated in equation (7.2) in the general case of birefringence.

$$\vec{E}_{TX} = T_1 \cos \alpha \hat{e}_1 + T_2 \sin \alpha e^{j\delta\phi} \hat{e}_2 \quad (7.2)$$

where T_1 and T_2 are the Fresnel coefficients for parallel and orthogonal incidence (or vice versa), $\delta\phi$ is the phase difference of optical path for the main optical axes of the dielectric due to birefringence and e_1, e_2 are the unitary vectors in the direction of the main optical axes.

The transmitted field expressed in equation (7.2) can be converted into co-polar and cross-polar components according to the orientation of the original co-polar field. This is done in equations (7.3) and (7.4).

$$E_{CoP} = T_1 \cos^2 \alpha + T_2 \sin^2 \alpha e^{j\delta\phi} = T_1 - \sin^2 \alpha (T_1 - T_2 e^{j\delta\phi}) \quad (7.3)$$

$$E_{XsP} = \sin \alpha \cos \alpha (T_1 - T_2 e^{j\delta\phi}) \quad (7.4)$$

In the case of ALMA filters and windows, the dielectric materials are aligned in the filters so that cross-polarization generation is minimized. Therefore, the polarization alignment with respect to the optical axes of the dielectrics are supposed to be pretty good and the angle α must be close to 0 degrees. In that case, some approximations can be done in order to simplify equations (7.3) and (7.4).

Results ignoring second order contributions in α are used to express the relationship between CoP and XsP components in equation (7.5).

$$\frac{XsP}{CoP_{max}} \cong \alpha \left(1 - \frac{T_1}{T_2} e^{j\delta\phi} \right) \quad (7.5)$$

The angle α is minimized for the whole incident beam by carefully choosing the orientation of the filters and window. The difference between T_1 and T_2 can be minimized by choosing dielectrics with low dielectric constant or minimizing the incident angle θ as deduced from equations (7.6)-(7.7). The phase difference $\delta\phi$ depends on the birefringence of the material and other geometrical considerations. Stacked layers of difference dielectrics or grooved dielectrics can also be birefringent even for non-birefringent materials [120].

$$T_{\perp} = \frac{2 \cos \theta}{\cos \theta + \frac{n_1}{n_0} \sqrt{1 - \left(\frac{n_0}{n_1} \sin \theta\right)^2}} \quad (7.6)$$

$$T_{\parallel} = \frac{2 \frac{n_0}{n_1} \cos \theta}{\cos \theta + \frac{n_0}{n_1} \sqrt{1 - \left(\frac{n_0}{n_1} \sin \theta\right)^2}} \quad (7.7)$$

The phase term due to birefringence is frequency dependent as shown by equation (7.8).

$$\delta\phi = \frac{2\pi}{\lambda} d \left(\frac{1}{\cos \beta_2} - \frac{1}{\cos \beta_1} \right) \quad (7.8)$$

where β_1 and β_2 are the refracted angles into the dielectric and d is the dielectric thickness.

Notice that for a single dielectric layer, there will only be a clear dependence on frequency in the case of birefringence. If the material and the complete dielectric structure are not birefringent, the complex exponential term in equation (7.4) will be equal to 1 and there will not be any strong frequency dependence, since T_1 and T_2 do not depend directly on frequency.

The cross-polarization pattern generated by dielectric layers can be approximated in first-order by a single Gaussian mode E_{10} or E_{01} if the incident co-polar beam pattern is a fundamental Gaussian mode [121].

In order to calculate the phase difference between the original co-polar and the generated cross-polar in the case of non-birefringent structures, the equations and method proposed in [121] are useful. In the case of a simple dielectric layer of non-birefringent material, it is easy to see that the ratio XsP/CoP will be proportional to the amount $(T_{\parallel} - T_{\perp})$ which is always negative as can be derived after some algebra using equations (7.6) and (7.7). This means that in the case no extra phase shift is introduced by birefringence, the original CoP and the generated XsP are 180 degrees out of phase. The proof for this follows:

$$T_{\parallel} - T_{\perp} = \frac{2n_2 \cos \theta}{n_1 \cos \theta + n_2 \cos \beta} - \frac{2n_2 \cos \theta}{n_2 \cos \theta + n_1 \cos \beta} = \frac{2n_2 \cos \theta (n_2 - n_1) (\cos \theta - \cos \beta)}{(n_1 \cos \theta + n_2 \cos \beta) (n_2 \cos \theta + n_1 \cos \beta)} \quad (7.9)$$

where θ is the incident angle, β is the refracted angle and n_1, n_2 are the refraction indexes of the two media. In the case of incidence from air/vacuum into a dielectric,

$$\begin{aligned} n_2 - n_1 &> 0 \\ \cos \theta - \cos \beta &< 0 \end{aligned}$$

And since the denominator is always positive for angles below 90 degrees, the amount $(T_{\parallel}-T_{\perp})$ in (7.9) will be negative.

7.2.3. Cross-polarization in horns

The cross-polarization generated in horns in reception is exactly the same as in transmission, in virtue of the reciprocity theorem [76]. The fields radiated by a horn, can be calculated as the Fourier transform of the currents in the horn aperture. In the case the horn rim is finite, the equivalent currents in the horn aperture are both magnetic and electric, \mathbf{M}_s and \mathbf{J}_s , and the electric field \mathbf{E} is calculated as stated in (7.10), using the expression for the electric and magnetic vector potentials, \mathbf{A} and \mathbf{F} , in (7.11)-(7.12).

$$\vec{\mathbf{E}} = -j\omega\vec{\mathbf{A}} - j\frac{1}{\omega\mu\epsilon}\nabla(\nabla\cdot\vec{\mathbf{A}}) - \frac{1}{\epsilon}\nabla\times\vec{\mathbf{F}} \quad (7.10)$$

$$\vec{\mathbf{A}} = \frac{\mu}{4\pi}\iint_S \vec{\mathbf{J}}_s \frac{e^{-jkR}}{R} ds' \approx \frac{\mu e^{-jkr}}{4\pi r} \iint_S \vec{\mathbf{J}}_s e^{jkr' \cos \psi} ds' \quad (7.11)$$

$$\vec{\mathbf{F}} = \frac{\epsilon}{4\pi}\iint_S \vec{\mathbf{M}}_s \frac{e^{-jkR}}{R} ds' \approx \frac{\epsilon e^{-jkr}}{4\pi r} \iint_S \vec{\mathbf{M}}_s e^{jkr' \cos \psi} ds' \quad (7.12)$$

where \mathbf{r} and \mathbf{r}' are the position vectors of the observation points and the sources, respectively, R is the magnitude of the vector $\mathbf{R}=\mathbf{r}-\mathbf{r}'$, and ψ is the angle between \mathbf{r} and \mathbf{r}' . The integrations in (7.11)-(7.12) are performed over the surface with sources, S , whose differential is ds' .

The equivalent currents \mathbf{M}_s and \mathbf{J}_s can be calculated from the electric and magnetic fields in the aperture, \mathbf{E}_{ap} and \mathbf{H}_{ap} , as stated in (7.13)-(7.14).

$$\vec{\mathbf{J}}_s = \hat{\mathbf{n}} \times \vec{\mathbf{H}}_{ap} \quad (7.13)$$

$$\vec{\mathbf{M}}_s = -\hat{\mathbf{n}} \times \vec{\mathbf{E}}_{ap} \quad (7.14)$$

where $\hat{\mathbf{n}}$ is the unitary vector perpendicular to the aperture and pointing out of the horn.

The horn will transform the waveguide modes in the horn input to some fields in the aperture which will determine the co-polar and cross-polar radiation patterns. Therefore, the value of cross-polarization will be determined in first stance by the horn design. Aperture fields are very sensitive to small fabrication defaults and small errors will change the radiated fields and usually increase cross-polarization.

In the case of a horn which radiates a co-polar beam which can be approximated by a fundamental Gaussian beam, as in the case of a corrugated horn, the cross-polarization can be modeled as an E_{11} Gaussian mode.

7.2.4. Cross-polarization in OMTs

An OMT (orthomode transducer) is a waveguide component used to separate a signal in two orthogonal polarization signals. An OMT has an input, which is normally a square or a circular waveguide which can support both input orthogonal polarizations, and two outputs, one for each orthogonal polarization. In the case of the OMT, cross-polarization is generated when the energy from one polarization is converted into the orthogonal polarization and transmitted to the wrong output port. This is measured by the Isolation parameter of the OMT. The cross-polarization created by an OMT is just co-polarization which goes out of the wrong output port. Therefore, it can be modeled as a fundamental Gaussian beam in the radiated fields.

7.3. Cross-Polarization of a Quasi-Optical System

A quasi-optical system is composed of several elements, some of which generate cross-polarization. Examples of such elements are ellipsoidal mirrors, horns and/or dielectric layers. The total cross-polarization of a quasi-optical system, XsP_{sys} , is the addition of the different cross-polarization components generated in elements in the RF path. These components are complex quantities which can be expressed in terms of magnitude, $|XsP_i|$, and phase, θ_i . Their addition will thus depend both on their magnitude and phase as stated in (7.15). Notice that only the magnitude of the system cross-polarization is of interest to specify the performance of quasi-optical systems.

$$|XsP_{sys}| = |\sum_i |XsP_i| e^{-j\theta_i}| \quad (7.15)$$

Depending on the phase of the different components, the magnitudes can add constructively and increase system cross-polarization, or destructively and improve it. A first approach to the problem which avoids the direct estimation of the phases is provided by the worst-case or the RMS (root mean square) values. In the case of the worst-case values, all components are considered to add in phase, which renders the cross-polarization value stated in (7.16). In the case of the RMS value, all components are supposed to be in quadrature, which renders the RMS cross-polarization value stated in (7.17).

$$|XsP_{sys}| = \sum_i |XsP_i| \quad (7.16)$$

$$|XsP_{sys}| = \sqrt{\sum_i |XsP_i|^2} \quad (7.17)$$

These values (7.16)-(7.17) have been used by some ALMA groups in the past to estimate the achievable cross-polarization performance of a receiver. However, the worst-case and RMS value

approaches are just estimations and do not consider the physics of cross-polarization generation and propagation. If the phases θ_i were known for a given receiver, an appropriate addition could be performed, as in (7.15).

The different cross-polarization components generate from the same incident co-polarization beam. Therefore, the initial phase of the cross-polarization will be related to the phase of the co-polar beam at the position at which cross-polarization is generated. Afterwards, cross-polarization components will propagate following a different phase law with respect to the co-polar beam. If generation and propagation phases are computed appropriately, the exact addition in (7.15) is possible. In the case the co-polarization beam can be approximated by a Gaussian beam, and the approximations used in quasi-optics are applicable, the different cross-polarization components can be approximated by higher-order Gaussian modes. The exact equation for higher order modes is given in (7.18).

$$E_{mn} = \sqrt{\frac{1}{\pi w^2 2^{m+n-1} m! n!}} H_m\left(\frac{\sqrt{2}x}{w}\right) H_n\left(\frac{\sqrt{2}y}{w}\right) \cdot \exp\left(-\frac{x^2+y^2}{w^2} - jkz - \frac{j\pi(x^2+y^2)}{\lambda R} + j(m+n+1) \operatorname{atan}\frac{\lambda z}{\pi w_0^2}\right) \quad (7.18)$$

where w is the beam radius, w_0 is the waist size, R is the radius of curvature, H are Hermite polynomials and m, n are the order in x and y , respectively.

Therefore, cross-polarization patterns will be an interference pattern of different cross-polarization contributions added with different phases. If only Gaussian modes are considered, the phase differences between the fundamental Gaussian mode which represents the co-polarization field and the higher-order modes which represent the cross-polarization from different components are well defined. This phase difference increases with distance and follows an arc tangent function, as stated in (7.18).

Normally, the shape of the cross-polarization pattern does not follow a single Gaussian mode. It is normally quite complex and depends very much on fabrication and alignment tolerances and defaults. However, for this simple analysis, only single-mode cross-polarization patterns will be considered. As described in previous sections, the cross-polarization patterns of ellipsoidal mirrors and dielectric layers can be modeled as an E_{10} mode, the pattern of horns as an E_{11} mode and the pattern of OMTs as an E_{00} mode. The phase difference between the co-polar E_{00} mode and the cross-polar E_{10} and E_{11} modes is given by ϕ_0 and $2\phi_0$, respectively, where ϕ_0 is $\operatorname{atan}(\lambda z / \pi w_0^2)$, z is the distance from the waist and w_0 is the waist size. The computation of the exact phases is quite tricky and requires careful investigation into the beams propagation. Mode E_{00} phase will follow the function $\phi_0 = \operatorname{atan}(\lambda z / \pi w_h)$ between the horn waist w_h and the first ellipsoidal mirror in the system (if any). The mirror will make the beam contract towards a different waist with different waist size. The phase will therefore also change. The phase at the mirror will be the value of the former function with z equal to the distance between the horn waist and the mirror. From the mirror, the phase function will have a $\phi_0 = \operatorname{atan}(\lambda z / \pi w_0)$ dependence, with w_0 , the size of the final waist, and z , negative between the mirror and the waist and positive from the waist. Formally, this ϕ_0 function can be expressed as (7.19):

$$E_{00} \text{ phase: } \begin{cases} \tan^{-1}\left(\frac{\lambda z}{\pi w_h}\right) & 0 \leq z \leq z_M \\ \tan^{-1}\left(\frac{\lambda z_M}{\pi w_h}\right) + \tan^{-1}\left(\frac{\lambda d_{MW}}{\pi w_0}\right) + \tan^{-1}\left(\frac{\lambda(z-z_M-d_{MW})}{\pi w_0}\right) & z_M \leq z \end{cases} \quad (7.19)$$

where z_M is the distance from the mirror to the horn waist and d_{MW} is the distance from the mirror to the final system waist. The same procedure applies in the case that there are several ellipsoidal mirrors.

E_{10} modes will be generated at cryostat IR filters, cryostat window and ellipsoidal mirrors and their differential phase will propagate following a $2\phi_0$ function. The initial phase will depend on the value of the E_{00} phase at the generation point and the effect of mirrors on E_{10} phase will be similar to the effect on E_{00} phase.

E_{11} and E_{00} modes generated at horns and OMTs will propagate following $3\phi_0$ and ϕ_0 functions, respectively. The effect of mirrors is similar as in the cases above.

Since different Gaussian modes have different amplitude patterns, cross-polarization contributions have maximums in different angular directions in the far field. This means that maximum cross-polarization values do not add together in the same direction. However, in the case integrated cross-polarization on the secondary is considered, this performance value can change significantly depending on the number of cross-polarization maxima which hit or miss the secondary mirror.

Some additional comments must be made with respect to the original phase difference between the original co-polar field and the generated cross-polarization in each component. Cross-polar modes E_{00} and E_{11} will only be generated by one component in the system, OMT and horn respectively, whereas E_{10} modes will be generated by several components: filters, window and ellipsoidal mirrors. The different lobes in the cross-polar pattern of E_{10} and E_{11} modes have a 180 degrees phase difference. Therefore, a difference of 180 degrees between different E_{00} , E_{10} and E_{11} modes, when these are added, will not make any difference in terms of maximum or integrated cross-polarization at antenna level. The only difference will be a rotation/symmetry of the cross-polar field patterns. Therefore, is not important if the initial phase of E_{00} and E_{11} modes is 0 or 180 degrees with respect to the original co-polar fields. On the other hand, the initial phase of E_{10} components will be critical when several cross-polar components of the same mode are added together. In the case of E_{10} created by ellipsoidal mirrors or non-birefringent structures, the modes will be 180 degrees out of phase with the original co-polarization beam from which they originated. In the case of birefringent structures, the same phase difference can be used as an estimate, since the phase difference for the two main axes refracted paths should not be large for not too thick dielectrics, such as the usual IR filters and windows.

In order to estimate the total system cross-polarization, all modes have to be added with the right waist size and phase in an appropriate position. Two interesting places where this addition of different cross-polar fields can be calculated are the final waist position and the far field. Notice that the phase difference between modes will be different in these two cases and, therefore, different

maximum values of cross-polarization and different cross-polar patterns are expected in these two cases or at any other distance z .

7.4. ALMA Band 10 Optics Cross-Polarization

As already explained in chapter 4, ALMA band 10 optics is composed of two corrugated horns, one for each orthogonal polarization, a polarizing wire grid which separates between polarizations, and two ellipsoidal mirrors which redirect the beam and match it to the secondary. Figure 7.2 shows a schematic of ALMA band 10 optics.

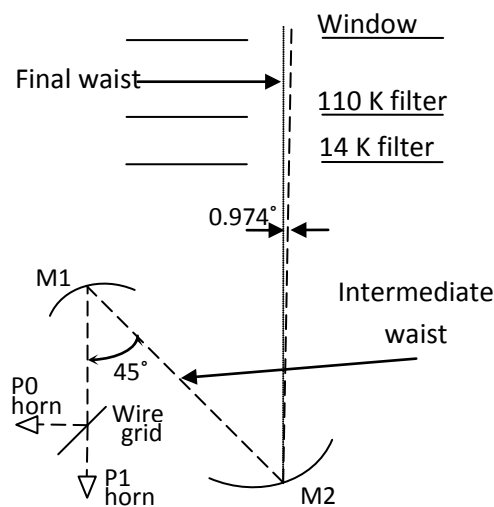


Figure 7.2. ALMA band 10 optics schematic

The analysis of ALMA band 10 optics in terms of cross-polarization performance is slightly more complex than the analysis of band 4 optics, which will be presented in 7.5, due to the extra waist between ellipsoidal mirrors. However, the Gaussian model introduced in 7.3 can be applied in a straightforward manner. Moreover, since a wire grid is used to separate orthogonal polarizations, the cross-polar contributions of horns will be almost suppressed by it and can be neglected as a first approximation. Therefore, the only elements to take into account are the two ellipsoidal mirrors and the IR filters and window. The cross-polarization generated at mirrors can be calculated using equation (7.1). At 864 GHz, the first mirror will add -24 dB and the second one, -26 dB. These values are very high, but compensate each other as it will be shown. According to ALMA requirements, IR filters and window cross-polarization must be less than -30 dB.

In order to assess realistic values of expected cross-polarization, the contribution of each component has been modeled by a single Gaussian mode and phase differences between modes have been considered. Some software has been developed using MATLAB in order to compute the total integrated cross-polarization from the system cross-polarization pattern. For a given set of cross-polarization levels for different components, the co-polar waist size and theoretical phase differences between co-polar and cross-polar fields are calculated. Then, these values are used to

create theoretical cross-polarization patterns for each component and to add them with the appropriate phase difference. All phases are normalized with respect to the co-polar phase at the waist. The resulting cross-polar field pattern represents an estimate of the cross-polarization pattern in the waist position. The resulting near-field cross-polar and co-polar fields are then transformed into far fields and the results are integrated over the surface of the secondary mirror. This calculation yields an estimate of the integrated cross-polar level, which is the actual ALMA requirement.

Figure 7.3 shows the evolution of the phase of the fundamental mode with respect to distance from the horn waist. Horns are behind a wire grid and their cross-polar contribution will be negligible. The contributions of both ellipsoidal mirrors are in almost opposition of phase and will approximately compensate each other. Filters and window have a waist between them, which means the phase will change quickly with distance in that area. This means that the phase difference for different contributions will be as large as possible for the given distance. All this makes this design robust in terms of total receiver cross-polarization.

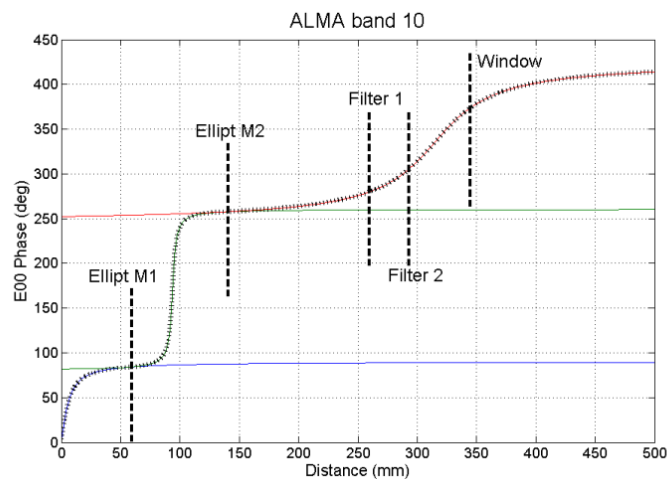


Figure 7.3. Evolution of E_{00} mode phase in ALMA band 10 optics

The phase difference between different contributions in the far field can be estimated and results are stated in table 7.1. The contribution of mirrors is almost in opposition of phase and the contribution of filters and window are close to quadrature. Filter 1 and 2 are physically quite close, but the phase difference between them is more than 20 degrees.

Table 7.1. Far-field phase of different cross-polarization components normalized to the phase of the cross-polarization at the window

Mirror 1	E10	287.8 deg
Mirror 2	E10	114.3 deg
Filter 1	E10	91.9 deg
Filter 2	E10	67.8 deg
Window	E10	0 deg

The estimated integrated cross-polar levels for several combinations of IR filters and window cross-polarization levels are presented in table 7.2. Actual measurements are usually around -28 dB, and in some cases, a little bit worse. Therefore, the simulated results are coherent with measurement results. This also shows that theoretical cross-polarization values are well within the -23 dB ALMA specification. Notice also that the results provided by RMS and worst-case analysis are meaningless in this study case.

Table 7.2. Maximum far-field cross-polarization (in dB) for ALMA band 10 using different models

Mirror 1	-24	-24	-24
Mirror 2	-26	-26	-26
Filter 1	-30	-34	-50
Filter 2	-30	-34	-50
Window	-30	-30	-50
RMS combination	-20.2	-20.8	-21.9
WC combination	-15.1	-15.7	-18.4
Gaussian model	-24.2	-27.1	-36.8

There are two reasons why ALMA band 10 optics works so well in terms of cross-polarization:

1. There is an intermediate waist between the two ellipsoidal mirrors in the tertiary optics. This translates in a phase difference of 173.4 degrees for their cross-polar contributions, which means that the second mirror cross-polarization component will compensate the first mirror component. The estimated cross-polarization of the two mirror system is -36.8 dB. Measurements at room temperature show measurement results better than -34 dB even with the extra corrugated horn cross-polar leaking through the wire grid. In turn, this means the receiver cross-polarization will be basically fixed by the IR filters and cryostat window.
2. The final optics waist is located between the two filters and the window. The arc tangent function which determines the phase difference between contributions varies more quickly near the waist. That means that even though the two filters are quite close, the phase difference between their cross-polarization components is more than 20 degrees. In addition, the difference between the window cross-polar and the first filter cross-polar is around 90 degrees, which means they combine as an RMS combination. All this translates into a low final contribution from IR filters and window.

7.5. ALMA Band 4 Optics Cross-Polarization

7.5.1. Analysis of the total system cross-polarization

ALMA band 4 optics (125-163 GHz) are composed of one OMT for separation of two orthogonal linear polarizations, a dual-mode corrugated horn and two mirrors, one ellipsoidal and one flat, which refocus and redirect the beam from the secondary into the horn. There are two IR filters and

one cryostat window between the horn and the ellipsoidal mirror. A schematic of the optics is presented in figure 7.4.

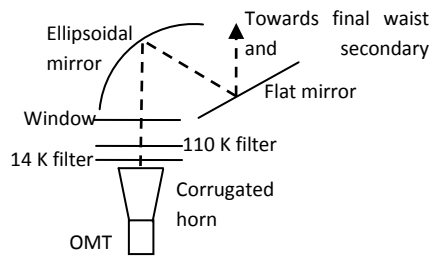


Figure 7.4. ALMA band 4 optics schematic

In the case of ALMA band 4, the horn is not behind a wire grid as in the case of ALMA band 10. Actually, since the polarization separation is performed by an OMT, there are two new cross-polarization components to be added to the components generated by the mirror, cryostat window and IR filters. As already mentioned in the introduction, ALMA band 4 did not usually comply with the -23 dB ALMA cross-polarization specification. Therefore, the cross-polarization performance of individual components was carefully measured in the laboratory.

OMT cross-polarization (or isolation between OMT output ports for orthogonal polarizations) can be characterized at these frequencies by commercially available vector analyzers. The results for up to 53 components are shown in figure 7.5. A statistical analysis of the previous results shows that the percentage of cases which is better than -25 dB is 86.8%, better than -28 dB is 66%, better than -30 dB is 41.5%, better than -32 dB is 34%, better than -35 dB is 22.6% and better than -40 dB is 5.7%. Besides that, the performance at lower frequencies is worse than at upper frequencies.

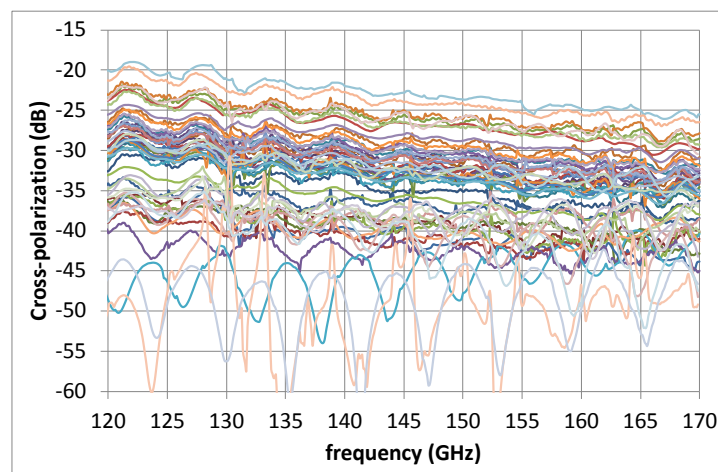


Figure 7.5. Cross-polarization performance of ALMA band 4 OMTs

Band 4 prototype corrugated horn cross-polarization level worsens for increasing frequencies and it was lower than -30 dB at all frequencies. Actually, it was lower than -36 dB in most of the band. However, the horn is fabricated in two pieces: the horn itself and the transition from circular to

rectangular waveguide with some of the initial corrugations. The latter piece is just inserted into the larger piece by pressure. In the case the electrical connection between the two parts is not good, due to the existence of an air gap between them, cross-polarization has been reported to increase to even more than -20 dB. Recently, 5 different ALMA band 4 horns have been measured at 7 different frequencies across the band with the cross-polarization performance reported in table 7.3. The worse case value for each horn has been highlighted in yellow. Amongst the characterized horns, only serial number #59 shows a better than -30 dB performance at all frequencies; two horns (#26, #37) present values around -27, -29 dB; and the other two horns (#36, #48) present quite high levels at some frequencies. These data show the technical difficulty of manufacturing high quality band 4 corrugated horns with better than -30 dB cross-polarization performance at all frequencies.

Table 7.3. Measured cross-polarization for 5 different corrugated horns (values in dB)

Serial #	127 GHz		131 GHz		135 GHz		143 GHz		151 GHz		155 GHz		161 GHz	
	P0	P1												
26	-34.8	-37.1	-30.9	-29.8	-36.9	-36.5	-31.5	-30.0	-34.7	-36.2	-30.0	-28.6	-32.6	-30.2
36	-38.2	-34.7	-31.4	-30.6	-36.8	-36.9	-26.5	-31.6	-31.1	-31.5	-24.2	-29.1	-28.4	-28.5
37	-35.5	-43.5	-34.6	-34.4	-42.5	-41.0	-27.5	-34.9	-35.4	-39.6	-28.6	-27.0	-30.7	-30.9
48	-22.2	-27.1	-30.0	-32.7	-29.2	-33.8	-37.7	-34.9	-30.7	-31.4	-29.4	-27.4	-31.1	-31.8
59	-41.8	-41.1	-33.6	-32	-40.8	-39.9	-38.5	-39.9	-38.8	-39.4	-31	-31.3	-32	-34.3

Additional experiments have been performed connecting an OMT with worst-case performance of -27 dB (around 131 GHz) and horn #36. Results are reported in table 7.4. The horn cross-polar pattern follows an E_{11} Gaussian mode, which presents 4 maxima, and the OMT cross-polarization can be represented by a fundamental Gaussian beam mode. Therefore, their maxima will be located at different angular locations. As a result, even though both contributions are in phase, they do not add their maxima in phase, and the measured maxima are not as high as those provided by worst-case analysis. Actually, results are pretty close to an RMS combination.

Table 7.4. Analysis of the combination of a corrugated horn and one OMT (values in dB)

	127 GHz	131 GHz	135 GHz	143 GHz	151 GHz	155 GHz	161 GHz
Only horn 36	-34.7	-30.6	-36.9	-31.6	-31.5	-29.1	-28.5
OMT	-27.8	-28.7	-28.9	-30.0	-30.4	-31.3	-32.3
Horn 36 + OMT	-27.7	-25.9	-29.0	-26.9	-26.7	-25.4	-27.7
R.m.s. combination	-26.9	-26.5	-28.3	-27.7	-27.9	-27.1	-27.0
Worst-case comb.	-24.5	-23.6	-26.0	-24.7	-24.9	-24.1	-24.2

The ellipsoidal mirror used to refocus the beam has a focal distance of 150.474 mm and a semi-bend angle of 30 degrees. The size of the beam at the mirror is 23.59 mm at 144 GHz. Therefore, using equation (7.1), the theoretical cross-polarization due to the mirror is -28.2 dB at 144 GHz. The frequency dependence of this cross-polarization contribution is small.

The first IR filter (at 15K shield) is located 7.5 mm away from the horn aperture and is a 0.85 mm thick layer of Goretex tilted 2.2 degrees with respect to the optical beam. The second filter (at 110K shield) is located at around 15 mm from the horn aperture and it is composed of molded PFA with anti-reflecting coating using triangular grooves, as shown in figure 7.6. It is tilted 3.2 degrees. The cryostat window is made of HDPE Fineline resin grade with the antireflection coating geometry

shown in figure 7.7 and tilted 1.2 degrees. The characterization of window and filters has been performed for beam incidence normal to the filters as indicated in [122]. These measurements show that both filters and window were compliant with the ALMA requirement of -30 dB for these components.

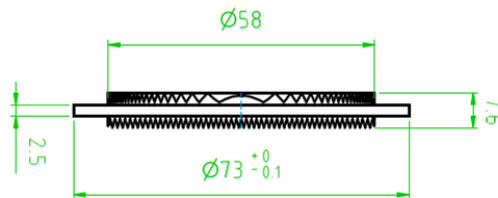


Figure 7.6. Band 4 110K IR filter

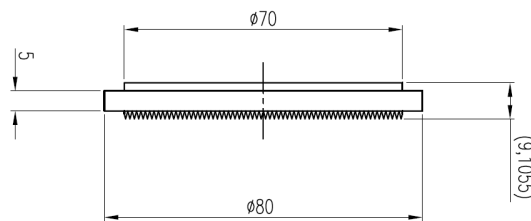


Figure 7.7. Band 4 Cryostat window

The core structure of ALMA band 4 optics: OMT + corrugated horn + mirrors, has been characterized at room temperature and cross-polarization levels have been measured for all the horns above and for a very good OMT (worst-case XsP = -35 dB). The same measurements have been performed with IR filters and cryostat window and results have been compared. Figure 7.8 shows the frequency behavior of the integrated cross-polarization level at the secondary mirror. The current ALMA specification indicates that this value must be better than -23 dB at all band 4 frequencies. The performance degradation that occurs when window and filters are included in the system is clear. Except for the optics which use corrugated horn #48 (high XsP at 127 GHz as indicated in table 7.3), all the other ALMA band 4 optics are well within specifications. The insertion of window and filters makes that the complete system integrated cross-polarization is out of specifications, especially at frequencies at the band edges. It is important to point out the unusual high cross-polarization degradation which affects the optics performance at 131 GHz. At some points, in the center of the band, it looks like the insertion of window and filters slightly improves the cross-polarization. However, this slight improvement must be due to measurement errors.

The results of measurements without window and IR filters have been used to calculate expected RMS and worst-case values of cross-polarization when window and filters with XsP level of -30 dB are included. These results are plotted against the real measurements of integrated cross-polarization in figure 7.9. The results at central frequencies show that cross-polarization level is better than the RMS combination. However, as it will be shown later, and since almost all cross-polarization individual components are almost in phase, this can be understood as the filters and

window having better performance than -30 dB. In the case of the edges of the band, the performance is degraded to values worse than the RMS combination. Finally, the system integrated cross-polarization at 131 GHz is dramatically degraded by window and filters. In the case of polarization P0, the measurement results are worse than worst-case combination of cross-polarization fields. This phenomenon will be explained in detail later in this chapter and it is due to an extra degradation of the horn cross-polarization due to dielectric loading from the IR filters.

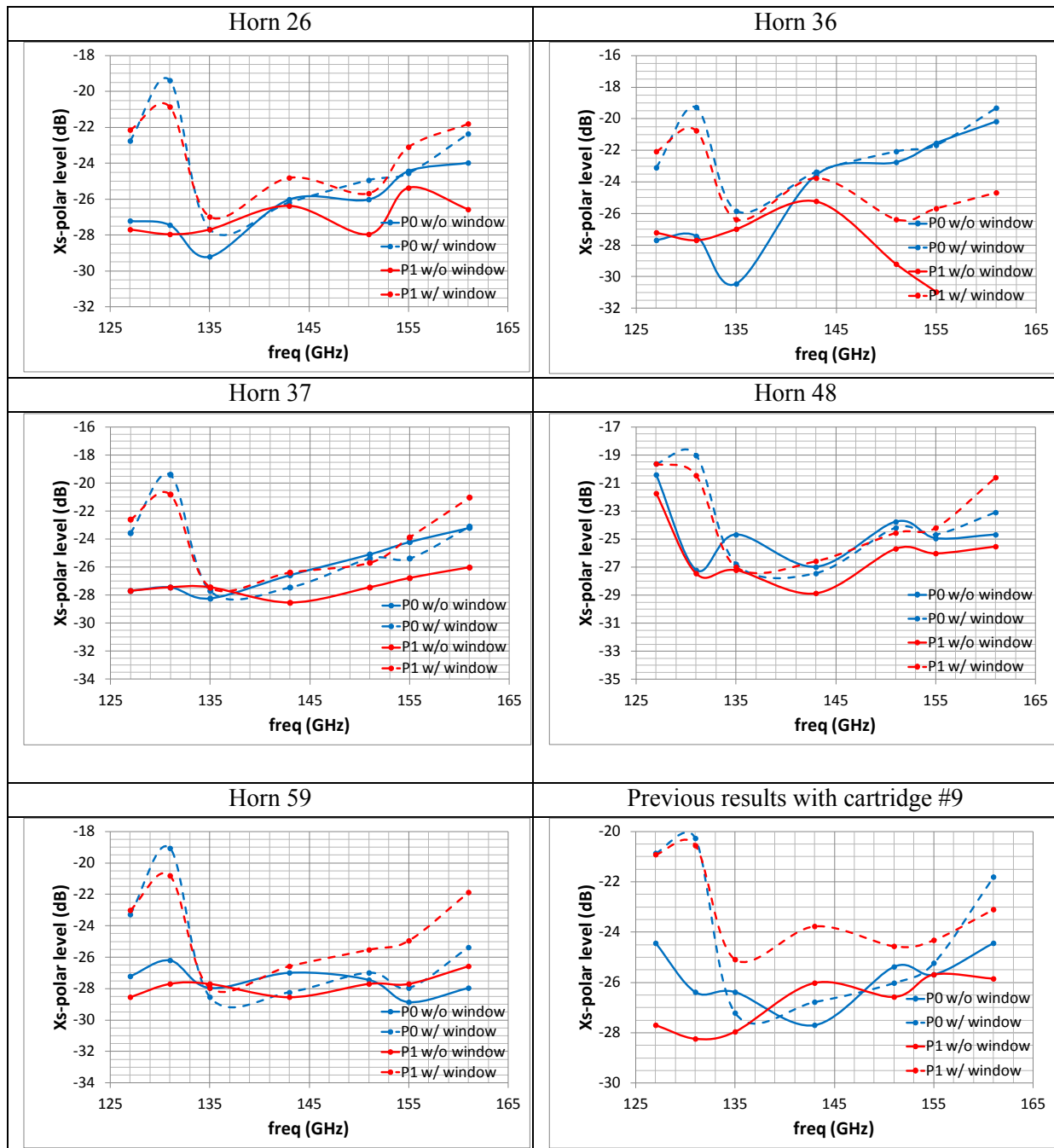


Figure 7.8. Integrated cross-polarization measurement with and without IR filters and windows

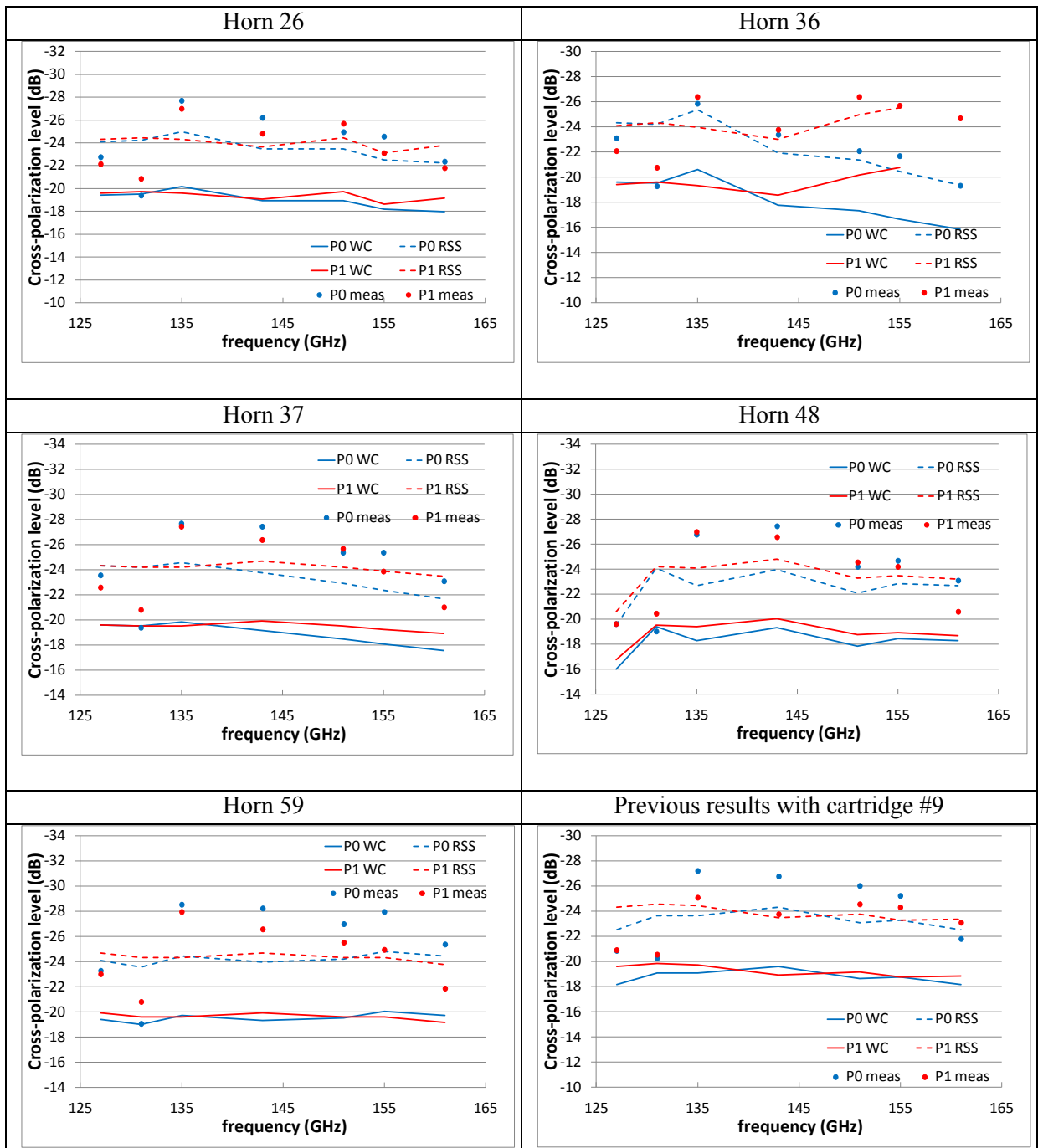


Figure 7.9. RMS and worst-case levels compared with measured integrated cross-polarization level

After analyzing the expected cross-polarization of each ALMA band 4 component in detail, it is time to check how the different contributions will combine using the method introduced in section 7.3. In the case of band 4, there are fewer components than in the analysis for band 10 and it is possible to write down a not-too-long formula for the cross-polar pattern at the waist using the cross-polar patterns of all individual components of band 4 optics. This formula is stated in equation (7.20), where all sub-indexes can be easily understood.

$$\begin{aligned}
X_{SP}(x,y) = & X_{SP_{OMT}}(x,y) + X_{SP_H}(x,y)e^{2j\left(\tan^{-1}\left(\frac{\lambda z_M}{\pi w_h}\right) + \tan^{-1}\left(\frac{\lambda d_{MW}}{\pi w_0}\right)\right)} \\
& + e^{j\tan^{-1}\left(\frac{\lambda d_{MW}}{\pi w_0}\right)} \left\{ X_{SP_M}(x,y) + e^{j\tan^{-1}\left(\frac{\lambda z_M}{\pi w_h}\right)} \right. \\
& \cdot \left. \left[X_{SP_{F1}}(x,y)e^{-j\tan^{-1}\left(\frac{\lambda z_{F1}}{\pi w_h}\right)} + X_{SP_{F2}}(x,y)e^{-j\tan^{-1}\left(\frac{\lambda z_{F2}}{\pi w_h}\right)} + X_{SP_w}(x,y)e^{-j\tan^{-1}\left(\frac{\lambda z_w}{\pi w_h}\right)} \right] \right\}
\end{aligned}
\tag{7.20}$$

Using (7.20), the phase difference for each contribution at 144 GHz at the waist position can be calculated. Results are presented in table 7.5. Almost all the contributions of components which can be modeled with an E₁₀ mode are almost in phase. This is not good in terms of system performance, since they will add almost as a worst-case combination.

Table 7.5. Phase of different cross-polarization components at band 4 waist position

OMT	E00	0 deg
Horn	E11	268.2 deg
Filter 1	E10	87.9 deg
Filter 2	E10	82.9 deg
Window	E10	72.1 deg
Mirror	E10	58.2 deg

The evolution of the phase of the co-polarization fields with respect to distance to the horn waist is presented in figure 7.10. This figure indicates the phase with which different cross-polar components generate. Notice that the phases in filters and window are very close and cross-polar components will add almost in phase. This means that if levels are the same for all these components, total cross-polarization will degrade 9.5 dB by inserting them in the optical path. Therefore, even if their individual cross-polarization performance is better than for example -36 dB, their total cross-polarization contribution will be around -26.5 dB.

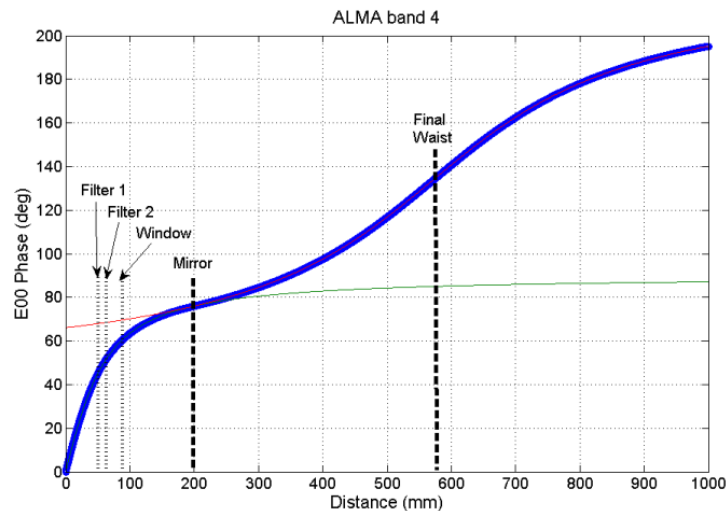


Figure 7.10. Evolution of E₀₀ mode phase in ALMA band 4 optics

The current cross-polarization specification and achievable performance for each component is given in table 7.6. The current filter cross-polarization specification states that the combination of

both filters must produce less than -30 dB. Since the cross-polar radiation of both components adds almost in phase, each filter must add less than -36 dB.

Table 7.6. Cross-polarization specifications and good values for different components

Component	Cross-polarization specification (dB)	Good cross-polarization (dB)
OMT	-25 dB	-28 dB
Corrugated horn	-27 dB	-30 dB
Filters	-30 dB (-36 dB each)	-32 dB (-38 dB each)
Window	-30 dB	-40 dB
Warm Optics	-28 dB	-28 dB

A first simulation of the integrated cross-polar level has been done with the specification values in table 7.6. The resulting integrated cross-polar level is -18.0 dB and maximum cross-polar levels in the near and far field are -18.1 dB and -17.3 dB, respectively. The values for RMS and worst-case combinations are -13.8 and -20.6, respectively. Cross-polar patterns are presented in figure 7.11. In the case that the good performances in table 7.6 are considered, -20.1 dB can be achieved, with maximum cross-polarization in the near and far field regions of -20.0 dB and -19.6 dB, respectively. The values for RMS and worst-case combinations are -16.3 and -22.8 dB, respectively. Notice that the -23 dB ALMA requirement is not realistically achievable even for good performance components. The frequency dependence due to the change in waist size is minimal. Therefore, the existing frequency dependence is due to the change of each cross-polarization contribution with frequency.

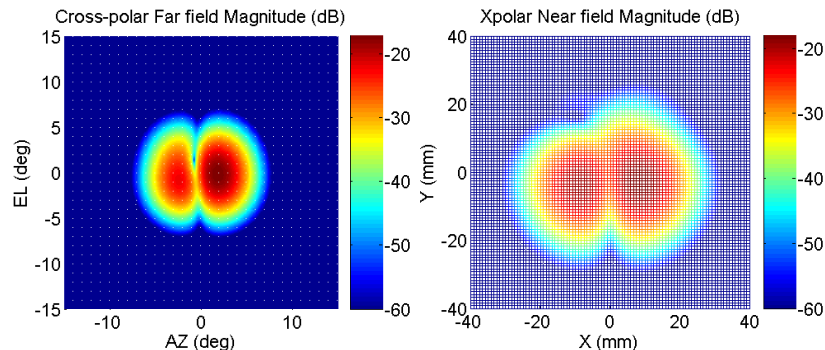


Figure 7.11. Calculated far- and near-field cross-polarization patterns at 144 GHz for ALMA band 4 optics

Since many optical components have been individually characterized during this study, the results of the Gaussian model can be compared to measurements in order to check the accuracy/validity of the model. Firstly, the model has been applied to the combination OMT + horn + mirror. The values used for the cross-polarization of each component are those measured for each component previously. In the case of the ellipsoidal mirror, the theoretical value of -28.2 dB has been used. The results of the calculations using RMS / worst-case combinations and the Gaussian model are presented in table 7.7. The Gaussian model generally gets the results closest to measurements. Differences are within possible measurement errors.

Table 7.7. Integrated cross-polarization estimation for the combination of several contributions
(all values in dB)

	H59 144GHz	H59 131GHz	H48 127GHz	H36 144GHz
OMT	-40.0	-36.0	-36.0	-36.0
horn	-38.0	-32.0	-22.2	-26.5
warm optics	-28.2	-28.2	-28.2	-28.2
RMS	-27.5	-25.8	-21.1	-23.8
WC	-24.2	-22.0	-17.6	-19.8
Model	-27.1	-26.1	-20.8	-23.6
Measurement	-27.0	-26.2	-20.4	-23.4

The values of cross-polarization introduced by the IR filters and cryostat window have not been measured for the components available in the ALMA band 4 laboratory. However, it can be seen that filters cross-polarization equal to -36 dB and window cross-polarization equal to -40 dB produce acceptable matches between the model and the measurement results in several cases. Table 7.8 summarizes the results of the model and RMS / worst-case combinations at 131 GHz.

Table 7.8. Estimation of cross-polarization in filters / window at 131 GHz using the Gaussian model
(all values in dB)

	Polarization P0			Polarization P1		
	H26 131GHz	H37 131GHz	H48 131GHz	H26 131GHz	H37 131GHz	H48 131GHz
OMT	-36.0	-36.0	-36.0	-36.0	-36.0	-36.0
horn	-34.8	-35.5	-22.2	-29.8	-34.4	-23.7
15K filter	-36.0	-36.0	-36.0	-36.0	-36.0	-36.0
110K filter	-36.0	-36.0	-36.0	-36.0	-36.0	-36.0
window	-40.0	-40.0	-40.0	-40.0	-40.0	-40.0
warm optics	-28.2	-28.2	-28.2	-28.2	-28.2	-28.2
RSS	-25.7	-25.8	-20.8	-25.0	-26.1	-21.8
WC	-18.8	-18.9	-15.2	-18.9	-20.0	-15.8
model	-21.3	-21.3	-18.7	-20.8	-21.2	-19.3
measurement	-19.4	-19.4	-19.0	-20.9	-20.8	-20.5

In summary, there are two reasons why ALMA band 4 cross-polarization level is high:

1. All optical components are pretty close to each other and the phase with which cross-polarization components are generated is very similar. This results in almost-in-phase cross-polar E-field combinations of the cross-polarization contributions of the IR filters, the cryostat window and the ellipsoidal mirror in the warm optics.
2. The warm optics is composed of only one ellipsoidal mirror which generates cross-polarization. Its maximum value of cross-polarization is around -28 dB and this contribution is not compensated by any other component, as opposed to band 10 optics. This means that even if the IR filters and window are very good in terms of cross-polarization, the total system cross-polarization cannot be better than -28 dB. Even in the case of good filters and

windows, the -23 dB ALMA specification cannot be achieved for current production components at all frequencies.

7.5.2. Research on the frequency dependence of system cross-polarization

After the -23 dB ALMA requirement was proved to be too stringent for ALMA band 4 current optics design, this requirement was relaxed to -20 dB (-19 dB at the edges of the band). This new specification continues to be challenging but it can be met by many of current components according to the Gaussian model introduced in 7.3. After this change of specifications, the ALMA band 4 team was requested to measure cross-polarization every 1 GHz in the entire band for 5 different receivers. This means a tremendous amount of work and it is rarely done in normal circumstances. This measurement campaign showed that all the receivers show cross-polarization peaks at certain frequencies which depend on the operation temperature and IR filters configuration. These cross-polarization peaks are often non-compliant even with the new ALMA specification and appear even if all components in the RF path show excellent performance. Figure 7.12 shows the results of these measurements for polarizations P0 and P1. Such level of detail in the measurements allows a clear observation of the cross-polarization frequency behavior and its repeatability for different receivers. Moreover, the measurements in figure 7.12 show that the frequency dependence is different for orthogonal linear polarizations P0 and P1, and that peaks are at approximately the same frequencies for a given polarization and for all measured cartridges. In order to properly understand this frequency behavior, all components in the RF path which could introduce some frequency dependences as those found in experiments have been analyzed with full-wave electromagnetic simulations using HFSS [104]. These components are the OMT and the IR filters. The square waveguide connection between the corrugated horn and the OMT has also been studied.

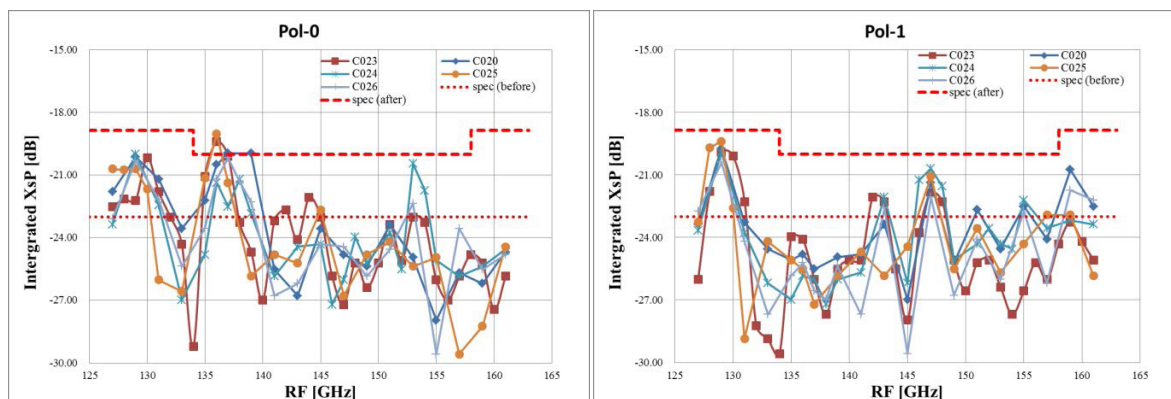


Figure 7.12. Cross-polarization behavior with respect to frequency for orthogonal linear polarizations P0 and P1 for 5 different ALMA band 4 cartridges

7.5.2.1. Connection between horn and OMT

The connection between the corrugated horn and the OMT is done by means of a 1.65 mm square waveguide. This waveguide is overmoded at band 4 frequencies and there are four propagative modes in most of the band, as shown in table 7.9. Figure 7.13 presents the field distribution for each of these four propagative modes. The connection between the horn and the OMT will not always be ideal. The difference in the size of the two waveguides and the assembly misalignment are factors to consider. Full-wave electromagnetic simulations with HFSS have been performed in order to understand what the effect of these defaults is on cross-polarization. The HFSS schematic is shown in figure 7.14.

Table 7.9. Cut-off frequency of modes in a 1.65 mm square waveguide [123]

Modes (number)	Cut-off frequency (GHz)
TE ₁₀ , TE ₀₁ (1, 2)	90.846
TE ₁₁ , TM ₁₁ (3, 4)	128.476
TE ₂₀ , TE ₀₂	181.692

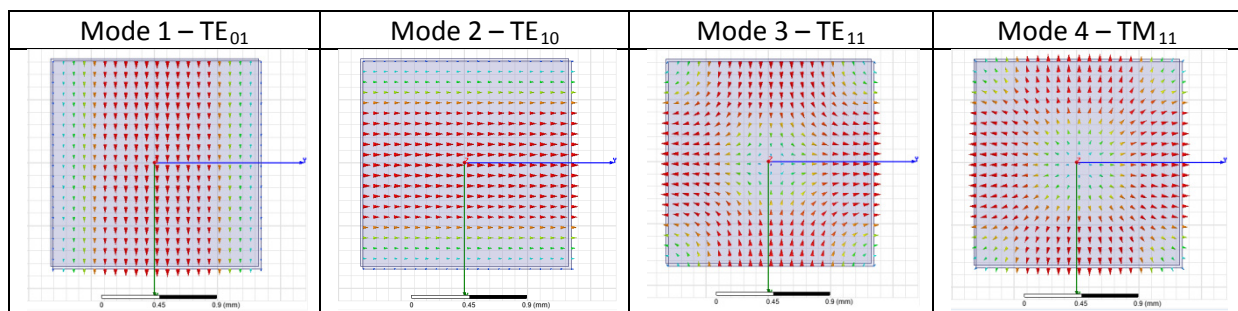


Figure 7.13. Electric field distribution for the propagative modes in ALMA band 4 square waveguide

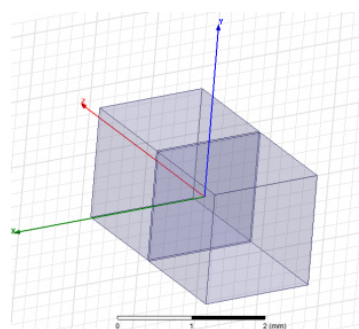


Figure 7.14. HFSS schematic for the analysis of overmoded square waveguide connections

Results of isolation (similar to OMT cross-polarization level) between orthogonal waveguide modes are presented in figure 7.15. S-parameters notation is as follows: S(output port : mode number, input port : mode number), where the mode number is between parenthesis in table 7.9. Figure 7.15 shows the following cases: no misalignment between waveguides (0x0 μm), misalignments in x and y ranging from 10 to 30 μm (10x10 μm , 20x20 μm and 30 μm), misalignment

in only one axis (0x10 μm , 0x20 μm , 20x0 μm) and two waveguides with the same axes but with a size difference of 20 μm . Moreover, the case of 20x20 μm has been simulated with a shrink and an expansion of 1% of all dimensions to see what the effect of changing the waveguide size is.

Results show that there is a resonance in isolation between modes TE_{10} and TE_{01} , $S(2:2, 1:1)$, in the cases of misalignments in both axes. Misalignments in only one axis do not generate significant resonances. The frequency of the resonance is exactly the same as the cut-off frequency of modes TE_{11} and TM_{11} . The peak magnitude of the resonance increases when misalignments increase. Peak values are much higher than the average isolation values. The change in waveguide dimensions changes the position of the resonance, since the cut-off frequency of higher order modes also changes. A change in waveguide size in the horn - OMT connection does not seem to have significant effects on isolation.

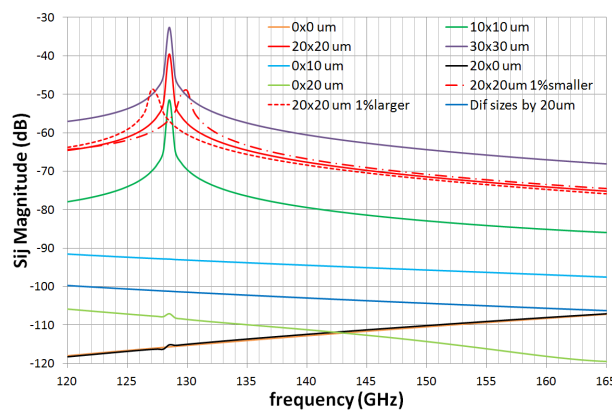


Figure 7.15. Isolation between fundamental modes $S(2:2,1:1)$ due to horn and OMT misalignments

In order to explain these results, it is necessary to look into more S-parameters. Figure 7.16 shows all coupling S-parameters for the cases of misalignment in only one axis (in x: 20x0 μm , and in y: 0x20 μm). The first thing to notice is that only one of the modes TE_{10} , TE_{01} converts into TE_{11} and TM_{11} depending on the axis in which the misalignment occurs. Mode TE_{10} will convert into TE_{11} and TM_{11} when the shift is in y; and mode TE_{01} will convert into TE_{11} and TM_{11} when the shift is in x. The isolation between TE_{10} and TE_{01} is very high in all cases (more than 100 dB). However, the conversion into higher-order modes is very high, especially at the cut-off frequency of these modes. In the case of 20 μm misalignments, the peak of this mode conversion is around -20 dB. This is the key to explaining the degradation of cross-polarization in the case of misalignments in both axes. Energy of modes TE_{10} , TE_{01} converts into modes TE_{11} and TM_{11} and then, if the shift in the other axis also exists, modes TE_{11} and TM_{11} are converting back into TE_{10} and TE_{01} . In this process, energy from mode TE_{10} will end up as mode TE_{01} and vice versa. Numerically, in the case of 20 μm shifts, notice that a double mode conversion with a peak value of -20 dB would degrade isolation between modes TE_{10} and TE_{01} to -40 dB, which is exactly the value simulated with HFSS for the case of 20 x 20 μm . The conversion between modes TE_{10} and TE_{01} happens via mode TM_{11} . The conversion from modes TE_{10} and TE_{01} into TE_{11} decreases at the resonance frequency. Figure 7.17 shows all mode conversion parameters for the case of misalignments in both axes. The peak magnitude value of $S(2:2,1:1)$ is half the value in dB of the peak of the magnitude of $S(2:4,1:1)$ (or 2)).

In conclusion, the misalignment between horn and OMT square waveguides can potentially generate a cross-polarization peak at around 128 GHz. Modes TE_{10} and TE_{01} convert into each other by means of an intermediate conversion into mode TM_{11} . It is necessary to have misalignments in both axes to have this sharp increase in cross-polarization. This cross-polarization peak can be removed by properly aligning the horn and the OMT.

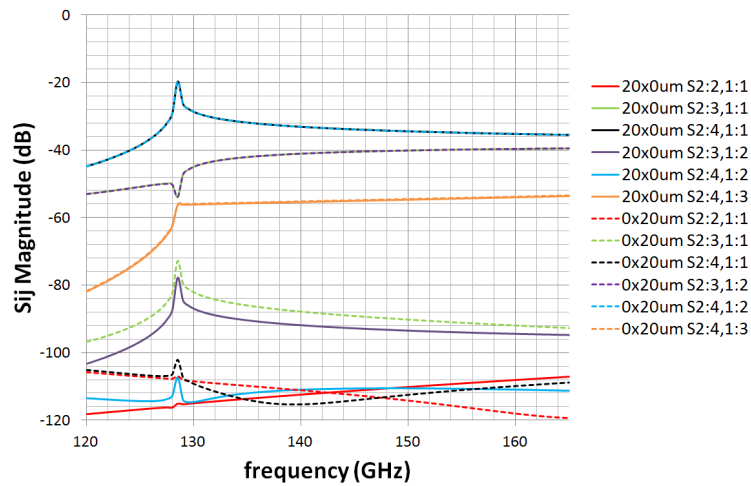


Figure 7.16. Coupling between different modes due to waveguide misalignment in one axis

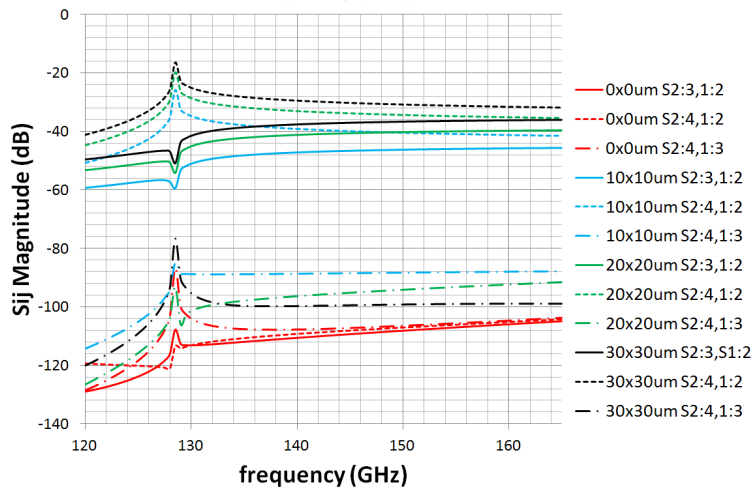
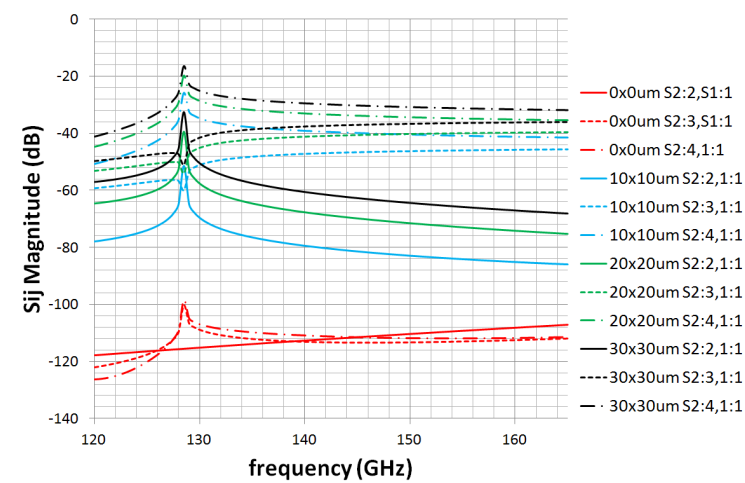


Figure 7.17. Coupling between different modes due to waveguide misalignment in two axes

7.5.2.2. OMT analysis

Firstly, the ideal OMT has been simulated with HFSS. Then, the misalignment between horn and OMT has been included in the simulations. Finally, the assembly error between the two metal blocks which compose the OMT has been considered together with the input misalignment, as presented in figure 7.18.

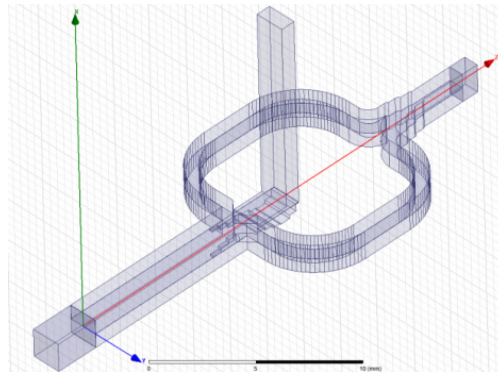


Figure 7.18. OMT schematic including assembly errors and misalignments

The results of introducing the input waveguide misalignment and the OMT assembly error are shown in figures 7.19 and 7.20. The return loss (RL) for mode 1 (Pol 0) does not change much. RL for mode 2 (P1) changes but does not show much degradation. There is a resonance at 136.5 GHz which appears when the assembly error gets large. However, this resonance does not show up in isolation curves. Somehow, this indicates there is some strange mode excited at around that frequency. Isolation also degrades at all frequencies with increasing assembly errors. When the error is small (2 μm), the main feature in isolation curves is the resonance at 128.5 GHz due to the input waveguide misalignment. The ripples in that curve are related to the distance between the simulation input port and the misalignment plane. For increasing errors, the isolation degrades, the ripples disappear and the resonance is masked by the low isolation values.

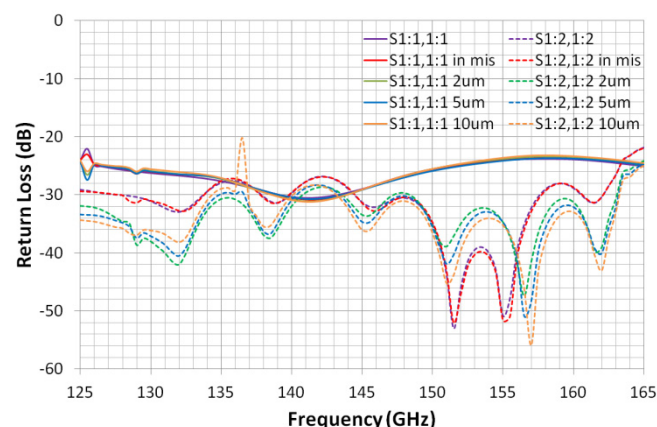


Figure 7.19. OMT Return Loss considering assembly errors and misalignments

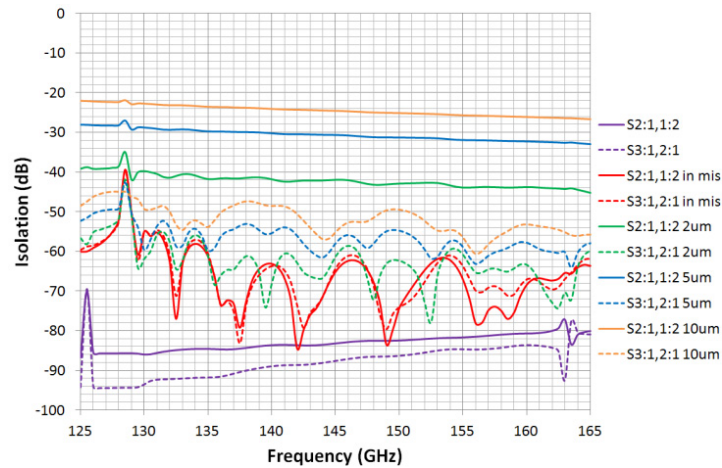


Figure 7.20. OMT Isolation considering assembly errors and misalignments

Measurement results presented in figure 7.5 are similar to HFSS simulations in figure 7.20. Ripples are large when isolation is good and small when the isolation is bad. The improvement of isolation with frequency is also similar to simulations. The values of isolation compared to simulations can provide an estimate of the actual assembly errors. Most OMTs show isolations which correspond to a simulated 5 μm assembly error. OMTs with very bad isolation (less than 25 dB) should be reassembled in order to improve their performance. These measurements were done by network analyzer and using a rectangular to square transition in the input. This transition and a good assembly are the reasons why there are no resonances at 128.5 GHz due to the square waveguide misalignment.

In short, assembly errors do not change RL much, but degrade the isolation to an almost constant value at all frequencies. There seems to be no resonances in the isolation. There are two resonances in RL at 125.5 GHz for P0 and at 136.5 GHz for P1. An improvement in isolation can be achieved by reducing the assembly error.

7.5.2.3. Infrared filters analysis

HFSS has been used to simulate the transmission of electromagnetic waves through ALMA band 4 IR filters. Simulations have been set up using Floquet modes and Master-Slave conditions to reproduce periodic conditions and avoid the simulation of huge dielectric structures. Floquet modes are a decomposition of plane waves in different components. Each particular structure can propagate a number of Floquet modes while the higher order modes are evanescent. The first two Floquet modes correspond to fields aligned along x and y or what we call polarizations P0 and P1. In order to use Master-Slave conditions, the tilt of the IR filter can be simulated by tilting the incident electric fields. This can be easily done in the setup of the Master-Slave boundary conditions. However, if both filters are included in the simulation, the same tilt angle must be chosen for both of them. The effective change in the 15K filter thickness by considering a 3.2 degree tilt is only 0.09%. This is a minor change from the real situation but it is worth to keep it in mind. Using this simulation setup, modal parameters of the dielectric structure can be calculated: reflection loss and coupling between polarizations, Y-parameters... This setup can be used to calculate the generation of cross-

polarization due to the IR filters alone. The schematics of the HFSS simulations of individual filters are presented in figure 7.21.

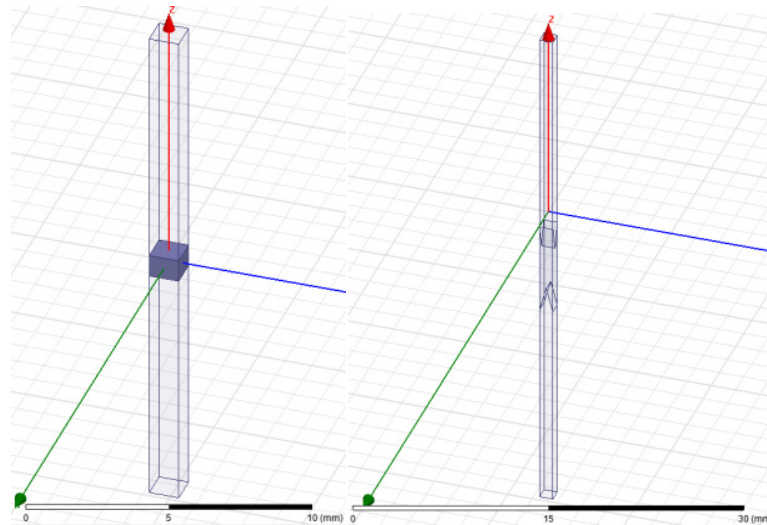


Figure 7.21. HFSS schematics of individual IR filters

Observation of the 110K filter under the microscope shows that the actual triangles in the filter anti-reflection layer are not perfect. There is truncation of the triangle tip in all triangle rows and, additionally, many of these triangles are tilted. These two effects have also been simulated in HFSS as shown in figure 7.22.

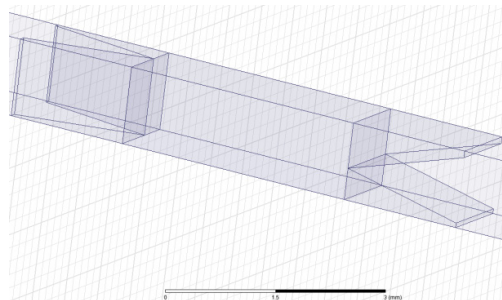


Figure 7.22. IR filter anti-reflection layer imperfections as simulated in HFSS

Results of cross-polarization coupling between orthogonal linear polarizations are presented in figure 7.23. They show no significant cross-polarization generation due to the IR filters. Cross-polarization degrades with tilted teeth and this is probably the main mechanism why measurements are around -35/-40 dB for actual filters. Ideal filters would add negligible cross-polarization. The effect of dielectric teeth truncation is negligible. Actually, performance seems to improve but it is only because there is less dielectric left in the optical path after truncation.

Reflection loss results are presented in figure 7.24 for the sake of completeness. Ideal filters show reflection loss better than -25 dB at ALMA band 4 frequencies. However, fabrication defaults in the

110K filter, especially teeth truncation, degrade the reflection loss and make it different for orthogonal linear polarizations PO and P1.

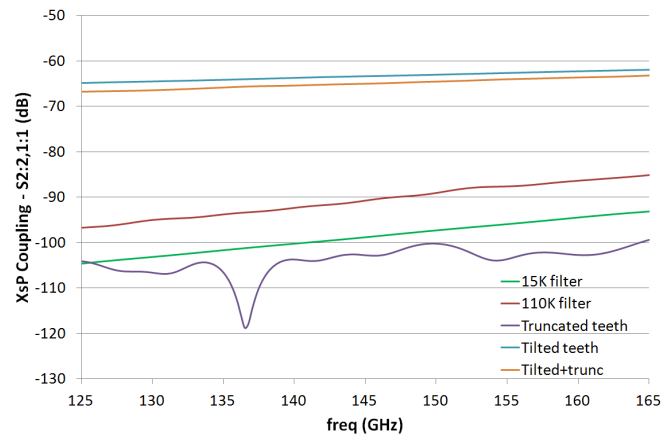


Figure 7.23. Simulation results of cross-polarization coupling between linear orthogonal polarizations due to IR filters

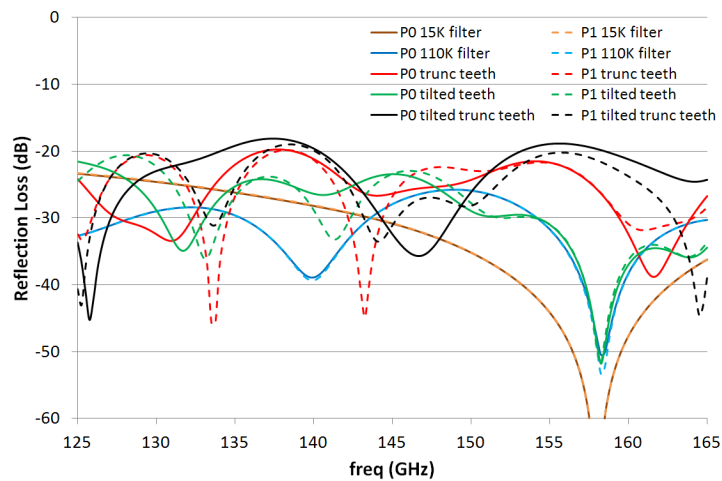


Figure 7.24. Simulation results of Reflection Loss at the IR filters, including common fabrication defaults

After analyzing each filter on its own, a HFSS model with both filters was prepared as shown in figure 7.25. The exact distance between filters in the real laboratory measurement setup is difficult to determine. Different ALMA band 4 documents have values slightly different for the distances, due to the tilt angle of the IR filter support structure. In addition, the tilts of both IR filters will be the same in the model, even if they are actually 2.2 and 3.2 degrees for the 15K and 110K IR filters, respectively. This will be a possible source of disagreement with measurements which must be considered. Furthermore, the actual beam will be a Gaussian beam with incidence in different angles from the main pointing angle, and not a plane wave as simulated with HFSS. All these effects will have a bigger impact on PO, which is the polarization tilted with respect to the IR filters plane. However, these simulations are good enough approximations to reality and worth analyzing. Cross-

polarization coupling and reflection loss have been calculated using HFSS for the combination of the two filters at different distances and are shown in figures 7.26-7.27.

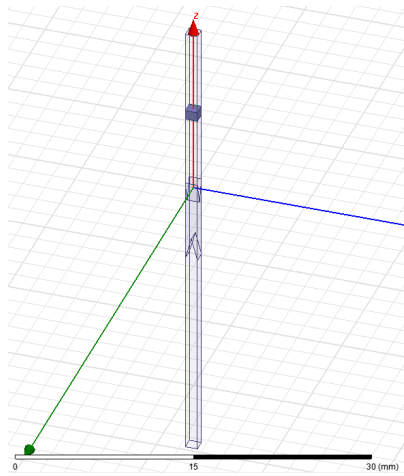


Figure 7.25. HFSS schematics for the simulation of the two IR filters together

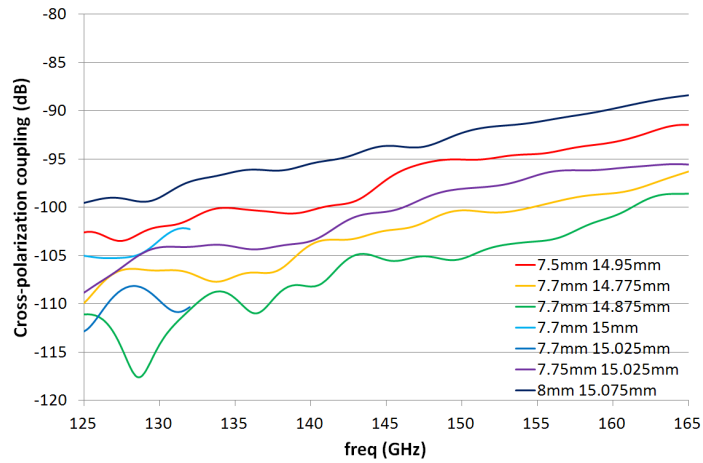


Figure 7.26. Simulation results of cross-polarization coupling between linear orthogonal polarizations due to IR filters. Distances are from horn aperture to 15K filter and to 110K filter, respectively

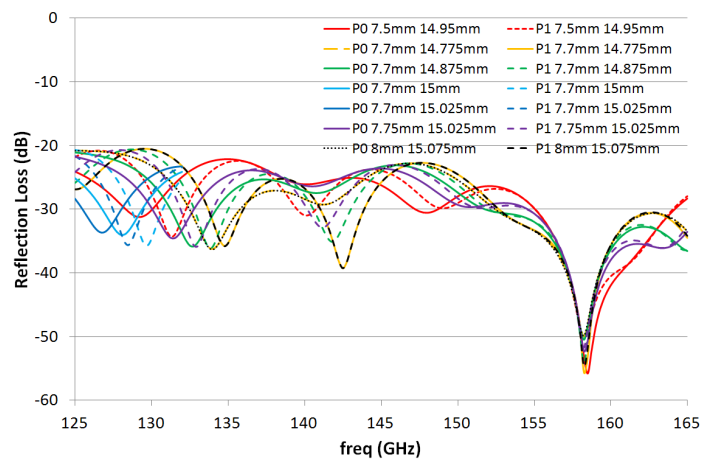


Figure 7.27. Simulation results of Reflection Loss at the IR filters. Distances are from horn aperture to 15K filter and to 110K filter, respectively

Cross-polarization values are really low and cannot explain the degradation in measurements. Reflection losses are very similar to those obtained with individual IR filters. Values of input admittance vary very much for small changes in distances, even in the order of tenths of mm, as just shown in figure 7.27. This is due to changes of input admittance/impedance at the simulation wave port due to the different distances between dielectric layers.

7.5.3. Influence of IR filters on the corrugated horn

Room temperature cross-polarization measurements with different combinations of IR filters and cryostat window in the optical path have proved the influence of the 110 K filter in the generation of cross-polarization peaks, as shown in figure 7.8. More detailed results, with different combinations of IR filters and window are presented in figure 7.28 for both polarizations, P0 and P1. When the window is removed, the decrease in cross-polarization is minimal in both polarizations. However, when the 110 K filter is removed, it improves dramatically at those frequencies at which it was high.

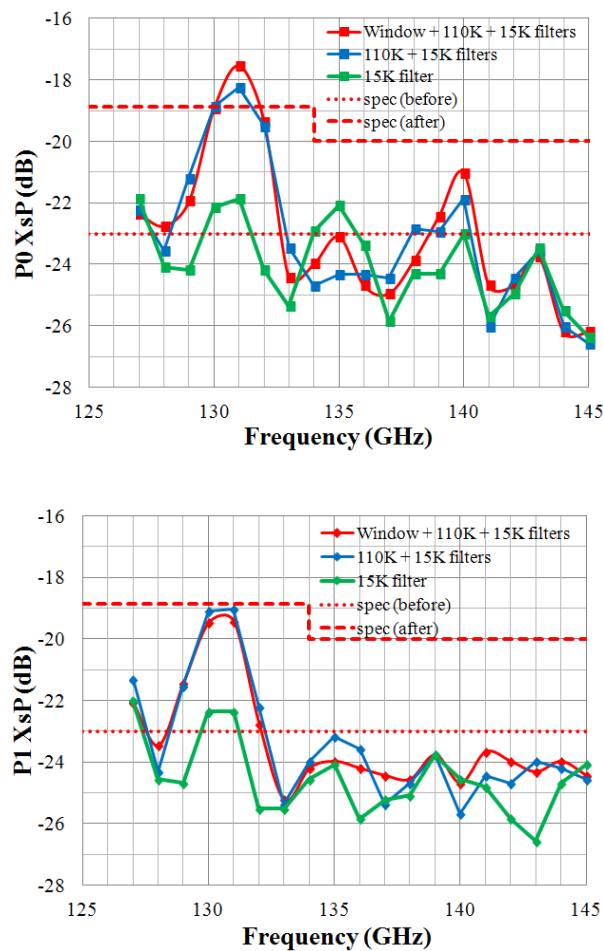


Figure 7.28 . ALMA band 4 cross-polarization measurement results with different combinations of IR filters and cryostat window

Even though the influence of IR filters on the generation of the cross-polarization peak is clear, it was shown in section 7.5.2.3 that the IR filters alone do not generate high cross-polarization at any frequency. A probable explanation of the strong dependence of cross-polarization performance on IR filters is that the co-polar and cross-polar radiation patterns of the antenna are modified by the presence of the dielectric structure just on top of the aperture. The effective impedance that the aperture sees is not that of free space, but that of the combination of dielectric layers followed by free space. In other words, the IR filters are loading the horn aperture and effectively changing the horn performance. This will be analyzed theoretically in the analyses which follow.

7.5.3.1. Electromagnetic fields in terms of input admittance

Using Maxwell equations, the curls of the electric and magnetic fields can be expressed as:

$$\nabla \times \vec{E} = -\vec{M} - j\omega\mu\vec{H} \quad (7.21)$$

$$\nabla \times \vec{H} = \vec{J} + j\omega\varepsilon\vec{E} \quad (7.22)$$

where \mathbf{J} and \mathbf{M} are the electric and magnetic currents, respectively. Taking the curl on both sides of (7.21) and using the result in (7.22), the wave equation for \mathbf{E} (7.23) can be obtained:

$$\nabla^2 \vec{E} + \omega^2 \mu \varepsilon \vec{E} = j\omega\mu \vec{J} + \nabla \times \vec{M} \quad (7.23)$$

After some manipulations in the spectral domain and using dyadic notation and spectral Green functions [124], (7.23) can be expressed in a more compact fashion as stated in (7.24):

$$\vec{E}(\mathbf{k}_x, \mathbf{k}_y, k_z) = G_J(\mathbf{k}_x, \mathbf{k}_y, k_z) \cdot \vec{J}(\mathbf{k}_x, \mathbf{k}_y, k_z) + G_M(\mathbf{k}_x, \mathbf{k}_y, k_z) \cdot \vec{M}(\mathbf{k}_x, \mathbf{k}_y, k_z) \quad (7.24)$$

where G_J and G_M are the dyadic Green Functions in k -space for electric and magnetic currents, respectively.

In the case of a horn with its aperture in the $z=0$ plane, currents will be entirely contained in this plane. Therefore, if the k_z dimension is transformed back to z , the previous expression can be written as (7.25). The dependence of G_J and G_M on z and the indication that currents are at $z=0$ will be omitted hereon in order to simplify notation.

$$\vec{E}(\mathbf{k}_x, \mathbf{k}_y, z) = G_J(\mathbf{k}_x, \mathbf{k}_y, z) \cdot \vec{J}(\mathbf{k}_x, \mathbf{k}_y, 0) + G_M(\mathbf{k}_x, \mathbf{k}_y, z) \cdot \vec{M}(\mathbf{k}_x, \mathbf{k}_y, 0) \quad (7.25)$$

The spatial components of the E-field can be expressed using inverse Fourier transforms as:

$$E_x(x, y, z) = \frac{e^{-jk_z z}}{(2\pi)^2} \iint_{-\infty}^{+\infty} [G_{J_{xx}} J_x(\mathbf{k}_x, \mathbf{k}_y) + G_{M_{xy}} M_y(\mathbf{k}_x, \mathbf{k}_y) + G_{J_{xy}} J_y(\mathbf{k}_x, \mathbf{k}_y) + G_{M_{xx}} M_x(\mathbf{k}_x, \mathbf{k}_y)] e^{-jk_x x} e^{-jk_y y} dk_x dk_y \quad (7.26)$$

$$E_y(x, y, z) = \frac{e^{-jk_z z}}{(2\pi)^2} \iint_{-\infty}^{+\infty} [G_{J_{yy}} J_y(\mathbf{k}_x, \mathbf{k}_y) + G_{M_{yx}} M_x(\mathbf{k}_x, \mathbf{k}_y) + G_{J_{yx}} J_x(\mathbf{k}_x, \mathbf{k}_y) + G_{M_{yy}} M_y(\mathbf{k}_x, \mathbf{k}_y)] e^{-jk_x x} e^{-jk_y y} dk_x dk_y \quad (7.27)$$

where the different components of the spectral Green Function dyadics, G_J and G_M , multiply the different components of the currents in the horn aperture. The two components in the first line of each equation are co-polarization and the two components in the second line are cross-polarization.

On the other hand, these spectral Green function components can be written using TE and TM voltages of an equivalent transmission line scenario with electric or magnetic generators indicated in the superscripts of V_{TE}/V_{TM} as j and m, respectively [125], as stated in the group of equations (7.28):

$$\begin{aligned}
G_{J_{xx}} &= -\frac{k_x^2 V_{TM}^j + k_y^2 V_{TE}^j}{k_x^2 + k_y^2} \\
G_{J_{xy}} &= \frac{k_x k_y}{k_x^2 + k_y^2} (V_{TE}^j - V_{TM}^j) = G_{J_{yx}} \\
G_{J_{yy}} &= -\frac{k_y^2 V_{TM}^j + k_x^2 V_{TE}^j}{k_x^2 + k_y^2} \\
G_{M_{xx}} &= \frac{k_x k_y}{k_x^2 + k_y^2} (V_{TM}^m - V_{TE}^m) = -G_{M_{yy}} \\
G_{M_{xy}} &= -\frac{k_x^2 V_{TM}^m + k_y^2 V_{TE}^m}{k_x^2 + k_y^2} \\
G_{M_{yx}} &= \frac{k_y^2 V_{TM}^m + k_x^2 V_{TE}^m}{k_x^2 + k_y^2}
\end{aligned} \tag{7.28}$$

Using the equivalent transmission line circuits and considering the input admittance Y_{in} , the different voltages can be expressed as:

$$V_{TE, TM}^m = \frac{2Y_0}{Y_0 + Y_{in, TE, TM}} \tag{7.29}$$

$$V_{TE, TM}^j = \frac{2}{Y_0 + Y_{in, TE, TM}} \tag{7.30}$$

Using (7.29)-(7.30), the E-field components can be finally expressed as (7.31)-(7.34):

$$\begin{aligned}
E_{x, CoP} &= \\
&\frac{2e^{-jk_z z}}{(2\pi)^2} \iint_{-\infty}^{+\infty} -\frac{1}{k_x^2 + k_y^2} \left(\frac{k_x^2}{Y_0 + Y_{in, TE}} + \frac{k_y^2}{Y_0 + Y_{in, TM}} \right) (J_x(k_x, k_y) + Y_0 M_y(k_x, k_y)) e^{-jk_x x} e^{-jk_y y} dk_x dk_y
\end{aligned} \tag{7.31}$$

$$\begin{aligned}
E_{x, XSP} &= \\
&\frac{2e^{-jk_z z}}{(2\pi)^2} \iint_{-\infty}^{+\infty} \frac{k_x k_y}{k_x^2 + k_y^2} \frac{Y_{in, TM} - Y_{in, TE}}{(Y_0 + Y_{in, TM})(Y_0 + Y_{in, TE})} (J_y(k_x, k_y) + Y_0 M_x(k_x, k_y)) e^{-jk_x x} e^{-jk_y y} dk_x dk_y
\end{aligned} \tag{7.32}$$

$$\begin{aligned}
E_{y, CoP} &= \\
&\frac{2e^{-jk_z z}}{(2\pi)^2} \iint_{-\infty}^{+\infty} -\frac{1}{k_x^2 + k_y^2} \left(\frac{k_x^2}{Y_0 + Y_{in, TM}} + \frac{k_y^2}{Y_0 + Y_{in, TE}} \right) (J_y(k_x, k_y) - Y_0 M_x(k_x, k_y)) e^{-jk_x x} e^{-jk_y y} dk_x dk_y
\end{aligned} \tag{7.33}$$

$$\begin{aligned}
E_{y, XSP} &= \\
&\frac{2e^{-jk_z z}}{(2\pi)^2} \iint_{-\infty}^{+\infty} \frac{k_x k_y}{k_x^2 + k_y^2} \frac{Y_{in, TM} - Y_{in, TE}}{(Y_0 + Y_{in, TM})(Y_0 + Y_{in, TE})} (J_x(k_x, k_y) + Y_0 M_y(k_x, k_y)) e^{-jk_x x} e^{-jk_y y} dk_x dk_y
\end{aligned} \tag{7.34}$$

It is clear from (7.32) and (7.34) that cross-polarization can be calculated from the Fourier transforms of the electric and magnetic currents in the aperture and from the input admittance of the RF path seen from the horn aperture. The cross-polarization for both orthogonal linear polarizations depends on the same coefficient which multiplies the currents. This coefficient is in general a complex number and so are currents. This makes the interpretation of this formula difficult. The formulas for co-polarization, (7.31) and (7.33), indicate that the beams change when the input admittance differs from Y_0 and those changes depend on frequency via k_x and k_y .

The previous formulas for cross-polarization have been derived considering that the dielectrics can be well modeled by a transmission line equivalent circuit. However, this is just an approximation in this case due to the tilt of the filters with respect to the RF path. Moreover, the 15 K filter is tilted 2.2 degrees whereas the 110 K filter is tilted 3.2 degrees. This makes that reflections between components will be getting further and further away from the optical axis with each reflection, and even first-order reflections will be tilted. This will make standing waves difficult, whereas the transmission line equivalent circuit assumes the existence of standing waves.

The coefficients depending on input admittances which multiply the aperture currents do not depend on k_x and k_y and can be brought out of the integrals in (7.32) and (7.33). Finally, since the object of this study is the cross-polarization magnitude, it is appropriate to take the magnitude of the complex expressions. This yields the next two expressions (7.35)-(7.36) for the magnitude of cross-polarization:

$$|E_{x \text{ XSP}}| = \frac{2}{(2\pi)^2} \left| \frac{Y_{\text{in TM}} - Y_{\text{in TE}}}{(Y_0 + Y_{\text{in TM}})(Y_0 + Y_{\text{in TE}})} \right| \left| \iint_{-\infty}^{+\infty} \frac{k_x k_y}{k_x^2 + k_y^2} \left(J_y(k_x, k_y) + Y_0 M_x(k_x, k_y) \right) e^{-jk_x x} e^{-jk_y y} dk_x dk_y \right| \quad (7.35)$$

$$|E_{y \text{ XSP}}| = \frac{2}{(2\pi)^2} \left| \frac{Y_{\text{in TM}} - Y_{\text{in TE}}}{(Y_0 + Y_{\text{in TM}})(Y_0 + Y_{\text{in TE}})} \right| \left| \iint_{-\infty}^{+\infty} \frac{k_x k_y}{k_x^2 + k_y^2} \left(J_x(k_x, k_y) + Y_0 M_y(k_x, k_y) \right) e^{-jk_x x} e^{-jk_y y} dk_x dk_y \right| \quad (7.36)$$

The cross-polarization magnitude expression is very similar for different polarizations. There is a coefficient depending on admittances which multiplies an integral depending on aperture currents. Since the admittance coefficient is common in (7.35) and (7.36), the different cross-polarization frequency behavior for different polarizations must be explained by the difference of currents integrals in (7.35) and (7.36). The integrals are difficult to compute without the appropriate software and therefore, the exact frequency dependence for each polarization cannot be calculated at the moment. However, the admittance term can be readily calculated using HFSS and provides some interesting conclusions. Results of HFSS simulations including both IR filters are presented in figure 7.29 for the cases of dielectric constants and thickness representing room-temperature and cryogenic conditions. As expected, curves are very similar and shifted to higher frequencies in the case of cryogenic conditions (smaller dimensions). Several simulations with different horn-to-filter distances and with slightly different dielectric constants have been performed, and results show minimal differences as presented in figure 7.30 for distances at room temperature.

Figure 7.29 shows that at most frequencies, the coefficient multiplying the integrals in (7.35)-(7.36) is greater than 0 dB and, therefore it amplifies the cross-polarization associated to the integral. However, at frequencies higher than 155 GHz, it is usually negative (in dB) and, therefore, it attenuates the cross-polarization. It also presents a zero around 136-137 GHz, which causes attenuation. This agrees with measurement results, which show generally low cross-polarization at higher frequencies and in the range 131-134 GHz for both polarizations. The position of this zero differs, but this small difference can be explained by the strong dependence of the position of the zero on the 110 K filter thickness, as shown in figure 7.31. Results of simulations with different thickness of the 15 K / 110 K filters show that the position of the zero depends only on the thickness of the 110 K filter, as shown in figure 7.32. Concretely, a change of only 0.1-0.2 mm in thickness makes the zero shifts to the range 131-134 GHz, as measured for band 4 cartridges.

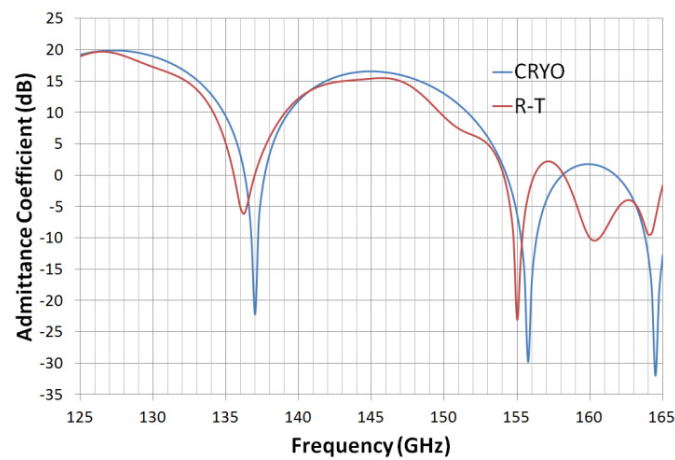


Figure 7.29. Admittance coefficient at room-temperature and cryogenic conditions

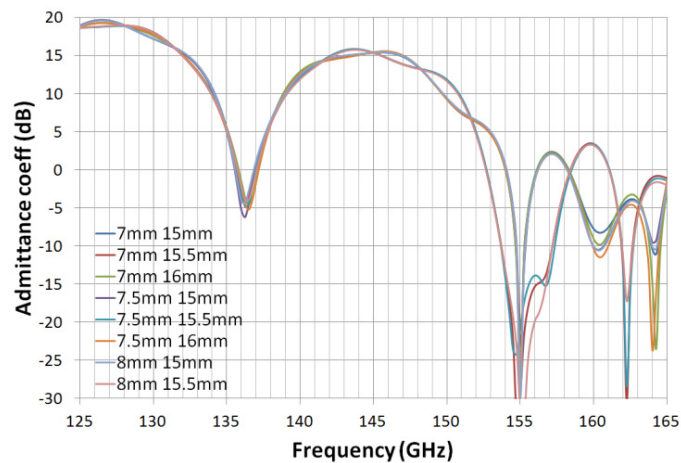


Figure 7.30. Admittance coefficient for different values of the distances from horn to filters at room temperature

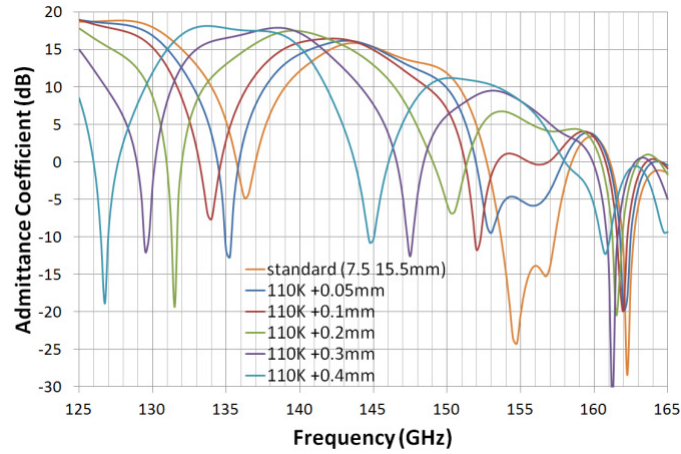


Figure 7.31. Admittance coefficients for small changes of the 110 K filter thickness

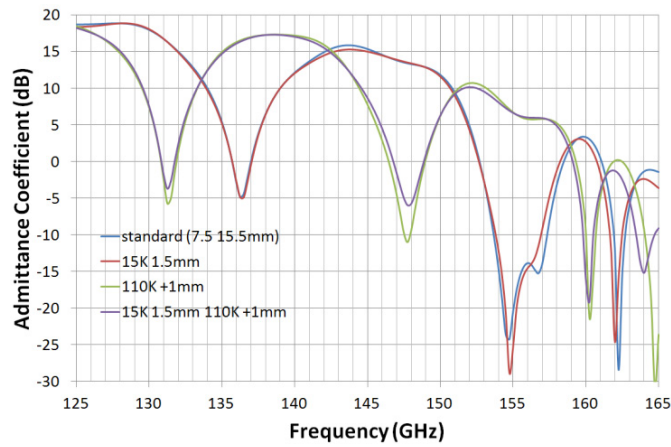


Figure 7.32. Admittance coefficients when the thickness of IR filters changes

7.5.3.2. Changes in input admittance

The corrugated horn aperture input admittance is a key parameter to understand how the two infrared filters affect the horn radiated fields [126]. For the horn alone, the input admittance can be expressed as the parallel of some admittance which depends on the horn and the free space admittance Y_0 . When the IR filters are used, there will be an extra admittance related to the IR filters in parallel with the previous two. This change in admittance can be calculated using HFSS, by calculating the input admittance of the IR filters dielectric structure and subtracting Y_0 . Additionally, a theoretical expression for the change due to dielectrics can be derived from the expression of admittance, as it will be shown.

The input admittance can be calculated as indicated in (7.37):

$$Y_{in} = \frac{2}{|V|^2} P^* = \frac{2}{|V|^2} \{ \text{Re}(P) - j \text{Im}(P) \}, \quad (7.37)$$

where V is the aperture voltage reference and P is the Poynting vector, which can be calculated from the fields in the aperture AP, E_{AP} and H_{AP} , as stated in (7.38) in the spectral domain (k_x, k_y) :

$$P = \frac{1}{8\pi^2} \int_{-\infty}^{+\infty} \int_{-\infty}^{+\infty} (\vec{\mathcal{E}}_{AP} \times \vec{\mathcal{H}}_{AP}^*) \cdot \hat{z} \, dk_x dk_y, \quad (7.38)$$

where $\vec{\mathcal{E}}_{AP}$ and $\vec{\mathcal{H}}_{AP}$ are the Fourier transforms of E_{AP} and H_{AP} , and can be expressed as:

$$\vec{\mathcal{E}}(k_x, k_y, z) = \vec{f}(k_x, k_y) e^{-jk_z z} = f_x \hat{x} + f_y \hat{y} + f_z \hat{z} \quad (7.39)$$

$$\text{with } k_z = \begin{cases} \sqrt{k^2 - k_x^2 - k_y^2} & \text{for } k^2 \geq k_x^2 + k_y^2 \quad (\text{Propagative waves}) \\ \sqrt{k_x^2 + k_y^2 - k^2} & \text{for } k^2 < k_x^2 + k_y^2 \quad (\text{Evanescent waves}) \end{cases}$$

and where f_x and f_y represent co-polar and cross-polar components or vice versa.

The z -component of f can be calculated from the other two components as follows:

$$f_z = -\frac{f_x k_x + f_y k_y}{k_z} \quad (7.40)$$

The electric field can be recovered from (7.39) using the inverse transformation in (7.41):

$$\vec{E}(x, y, z) = \frac{1}{4\pi^2} \int_{-\infty}^{+\infty} \int_{-\infty}^{+\infty} \vec{\mathcal{E}}(k_x, k_y, z) e^{-j(k_x x + k_y y)} \, dk_x dk_y, \quad (7.41)$$

The spectral fields in the aperture ($z=0$) can be easily expressed in terms of components of f as:

$$\vec{\mathcal{E}}_{AP} = \vec{\mathcal{E}}(k_x, k_y, 0) = f_x \hat{x} + f_y \hat{y} \quad (7.42)$$

$$\vec{\mathcal{H}}_{AP} = \vec{\mathcal{H}}(k_x, k_y, 0) = -\frac{1}{k\eta} (\vec{f} \times \vec{k}) = \frac{1}{k\eta} [\hat{x}(f_z k_y - f_y k_z) + \hat{y}(f_x k_z - f_z k_x) + \hat{z}(f_y k_x - f_x k_y)] \quad (7.43)$$

Using (7.42) and (7.43), the product $(\vec{\mathcal{E}}_{AP} \times \vec{\mathcal{H}}_{AP}^*) \cdot \hat{z}$ can be expressed as:

$$(\vec{\mathcal{E}}_{AP} \times \vec{\mathcal{H}}_{AP}^*) \cdot \hat{z} = \frac{1}{k\eta k_z^2} \left[|f_x|^2 (k_z^{*2} + k_x^2) + |f_y|^2 (k_z^{*2} + k_y^2) + 2k_x k_y \text{Re}(f_x f_y^*) \right] \quad (7.44)$$

Using (7.44) in (7.38) and after some manipulations, the input admittance can be expressed as:

$$Y_{in} = \frac{1}{4\pi^2 |V|^2 k\eta} \left\{ \iint_{k_x^2 + k_y^2 \leq k^2} \frac{1}{\sqrt{k^2 - k_x^2 - k_y^2}} \cdot \left[(k^2 - k_y^2) |f_x|^2 + (k^2 - k_x^2) |f_y|^2 + 2k_x k_y \text{Re}(f_x f_y^*) \right] dk_x dk_y + \right.$$

$$j \iint_{k_x^2 + k_y^2 > k^2} \frac{1}{\sqrt{k_x^2 + k_y^2 - k^2}} \cdot \left[(k^2 - k_y^2) |f_x|^2 + (k^2 - k_x^2) |f_y|^2 + 2k_x k_y \text{Re}(f_x f_y^*) \right] dk_x dk_y \} \quad (7.45)$$

The real part of the admittance corresponds to the region of radiated fields and the imaginary part corresponds to the region of evanescent reactive fields. The expression in both integrals is the same for the real and imaginary parts. The only difference between them is the integration region. From this point on, only the expression for the real part of the admittance will be provided.

When dielectrics are put in front of the horn, Y_{in} will change by some value ΔY_{in} which can be expressed as the difference of the input admittance of the dielectric structure and the free space admittance. The change ΔY_{in} can be calculated from (7.45), considering the initial fields f_{x0} , f_{y0} change by an amount Δf_x , Δf_y . These changes also mean changes in co-polar and cross-polar electric fields.

Let's consider that the original f_{x0} becomes f_x after the IR filters are put close to the horn and the same for f_y . Then,

$$f_x(k_x, k_y) = f_{x0}(k_x, k_y) + \Delta f_x(k_x, k_y) \quad (7.46)$$

$$f_y(k_x, k_y) = f_{y0}(k_x, k_y) + \Delta f_y(k_x, k_y) \quad (7.47)$$

The change in admittance can be calculated by introducing (7.46)-(7.47) in (7.45) and grouping all the terms which correspond to the original admittance. Doing this for the real part of the admittance, (7.48) is obtained.

$$\begin{aligned} \Delta \text{Re}(Y_{in}) &= \frac{1}{4\pi^2 |V|^2 k \eta} \cdot \\ &\iint_{k_x^2 + k_y^2 \leq k^2} \frac{1}{\sqrt{k^2 - k_x^2 - k_y^2}} \left[(k^2 - k_y^2) (|\Delta f_x|^2 + 2\text{Re}(f_{x0}^* \Delta f_x)) + (k^2 - k_x^2) (|\Delta f_y|^2 + 2\text{Re}(f_{y0}^* \Delta f_y)) \right. \\ &\left. + 2k_x k_y \left(\text{Re}(f_{x0}^* \Delta f_y) + \text{Re}(f_{y0}^* \Delta f_x) + \text{Re}(\Delta f_x \Delta f_y^*) \right) \right] dk_x dk_y \end{aligned} \quad (7.48)$$

By design, one of the field components f_x or f_y will be much larger than the other, since one represents co-polarization and the other cross-polarization. Additionally, the variations in co-polarization can be considered much smaller than the maximum of the co-polarization. Using these approximations, expressions for the change in input admittance (7.49)-(7.50) can be derived for the case $f_x \gg f_y$.

$$\Delta \text{Re}(Y_{in}) \approx \frac{1}{2\pi^2 |V|^2 k \eta} \iint_{k_x^2 + k_y^2 \leq k^2} \frac{1}{\sqrt{k^2 - k_x^2 - k_y^2}} \text{Re} \{ [(k^2 - k_y^2) \Delta f_x + k_x k_y \Delta f_y] \cdot f_{x0}^* \} dk_x dk_y \quad (7.49)$$

$$\Delta \text{Im}(Y_{in}) \approx \frac{1}{2\pi^2 |V|^2 k \eta} \iint_{k_x^2 + k_y^2 > k^2} \frac{1}{\sqrt{k^2 - k_x^2 - k_y^2}} \text{Re} \{ [(k^2 - k_y^2) \Delta f_x + k_x k_y \Delta f_y] \cdot f_{x0}^* \} dk_x dk_y \quad (7.50)$$

For the other polarization (P0 or P1), $f_x \ll f_y$,

$$\Delta \text{Re}(Y_{in}) \approx \frac{1}{2\pi^2 |V|^2 k \eta} \iint_{k_x^2 + k_y^2 \leq k^2} \frac{1}{\sqrt{k^2 - k_x^2 - k_y^2}} \text{Re}\{[(k^2 - k_x^2)\Delta f_y + k_x k_y \Delta f_x] \cdot f_{y0}^*\} dk_x dk_y \quad (7.51)$$

$$\Delta \text{Im}(Y_{in}) \approx \frac{1}{2\pi^2 |V|^2 k \eta} \iint_{k_x^2 + k_y^2 > k^2} \frac{1}{\sqrt{k^2 - k_x^2 - k_y^2}} \text{Re}\{[(k^2 - k_x^2)\Delta f_y + k_x k_y \Delta f_x] \cdot f_{y0}^*\} dk_x dk_y \quad (7.52)$$

Equations (7.49)-(7.52) indicate that changes in input admittance are due to changes in the fields radiated by the horn or vice versa. These two magnitudes are thus related. However, it is not easy to get a clearer relationship between them from (7.49)-(7.52). Experimental results clearly indicate that changes in co-polar and cross-polar patterns occur for the band 4 receiver when IR filters are used. Co-polar beams become slightly wider and the cross-polar level is normally degraded. Co-polar and cross-polar patterns were measured at room temperature using only the 15K filter. Results of Edge taper of the co-polar pattern and integrated cross-polarization are shown in figure 7.33. Intuitively, large changes in input admittance will create wider beams and degrade cross-polarization.

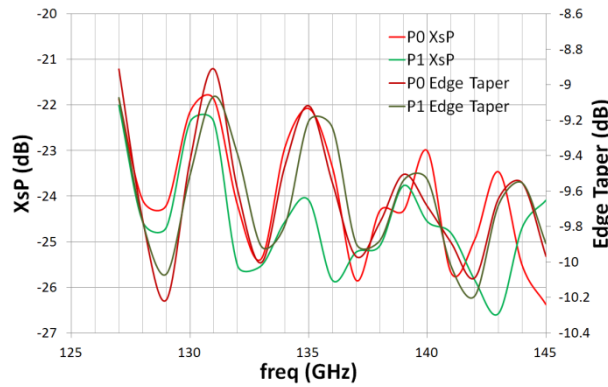


Figure 7.33. Variation of co-polarization (Edge Taper) and cross-polarization when the 15K filter is used

The values of Y_{in} of the IR filters structure have been calculated using HFSS. HFSS can calculate the Y-parameters at the simulation wave ports. If that wave port is coincident with the horn aperture, then, Y_{in} can be calculated from the simulated Y-parameters Y_{ij} as indicated in (7.53):

$$Y_{in} = Y_{11} - \frac{Y_{12}Y_{21}}{Y_{22} + Y_0}, \quad (7.53)$$

where Y_0 is the admittance of free space $1/(120\pi)$ Siemens.

Results depend very much on the exact distances between elements. Figure 7.34 shows that small variations in distances, even in the order of tenths of mm, result in large variations of Y_{in} . Because of this, presumably, the approximations introduced in the HFSS model will be more critical

in this case. Firstly, the plane at which Y_{in} is calculated is parallel to the 110 K filter and not to the horn aperture. The difference is only 3 degrees. Secondly, both filters are modeled with the same tilt angle, whereas, there is a tilt difference of 1 degree between them. Finally, the Floquet port input is a plane wave and not a Gaussian beam. The errors due to these approximations should be more visible in the polarization with parallel incidence on filters, P0.

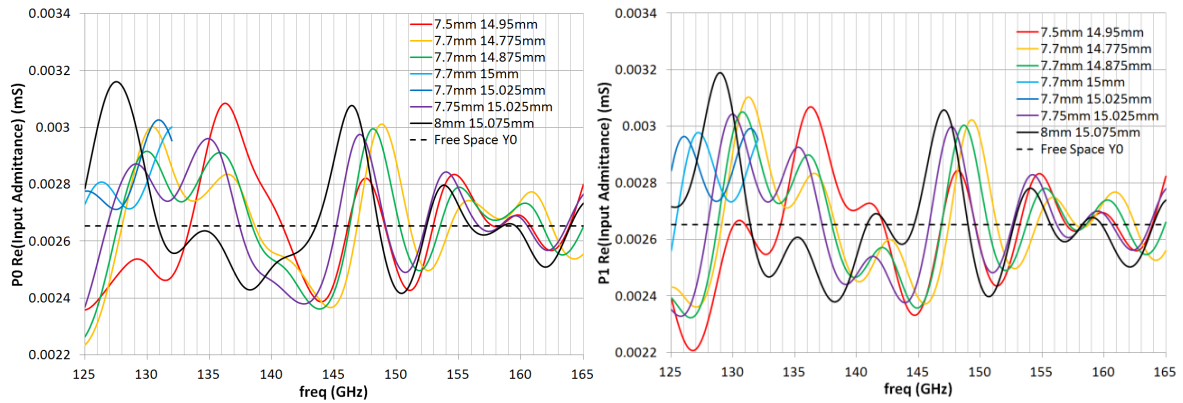


Figure 7.34. Real part of Y_{in} associated to IR filters for polarizations P0 and P1. Distances in the legend are from horn to 15K filter and to 110K filter, respectively

After many simulations, a set of distances around the nominal distances which provides good fitting to measurements at room and at cryogenic temperature were found. The fittings are shown in figure 7.35 and 7.36. Notice that the match for P1 is better than for P0 as expected. There could be other good fittings with different sets of distances, but these matches are good and in the range of possible distances. Actually, it was found that Y_{in} was almost periodic with changes in distances; e.g. a change of 1.1 mm in the horn-to-filters distance yielded very similar values of Y_{in} . This periodicity is shown in figure 7.37.

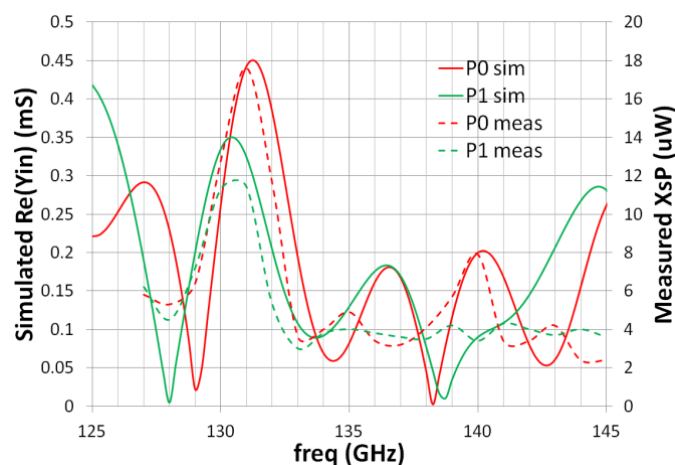


Figure 7.35. Comparison of input admittance simulation results and cross-polarization measurements at room-temperature

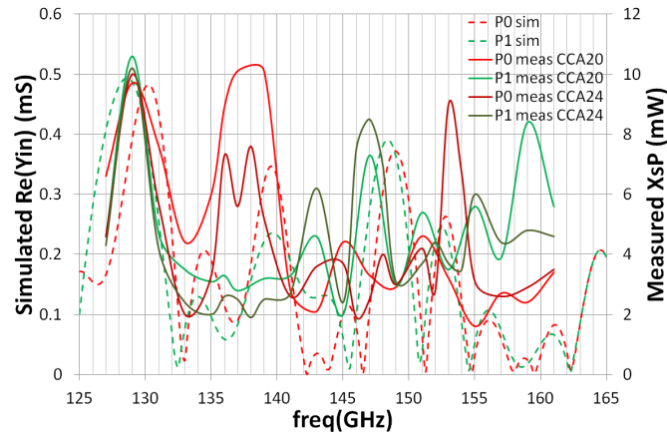


Figure 7.36. Comparison of input admittance simulation results and cross-polarization measurements at cryogenic temperature of ALMA band 4 cartridges

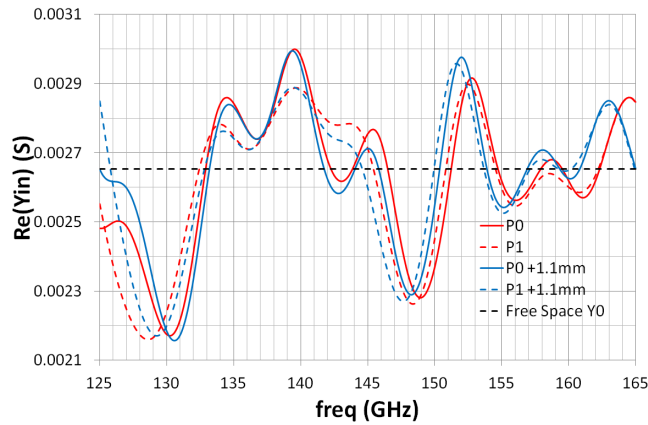


Figure 7.37. Quasi-periodic behavior of $\text{Re}(\text{input admittance})$ with respect to horn-IR filters distance

Finally, the comparison of measured cross-polarization and simulated ΔY_{in} also helps to explain some other test results. For example, it was found that when the 110K filter was heated up to 180 K, the P0 cross-polarization peak moved to lower frequencies and the P1 cross-polarization peak frequency slightly increased, as shown in figure 7.38. Similar results were observable when a 3 mm insert was used to change the position of the 110K filter. Since results are very similar for both experiments, it is thought that the cross-polarization dependence on temperature is due to an actual change in distances between horn and filter and to the thermal expansion of the filter itself when temperatures change. The temperature experiment is difficult to simulate with HFSS, since thermal expansion coefficients at low temperatures are not well-known for these materials. Besides, the dielectric constants also change with temperature [127]. However, the experiment with the 3 mm insert can be modeled in a quite straightforward fashion, just changing one distance in the model. HFSS simulations yielded results qualitatively similar to measurements, as presented in figure 7.39.

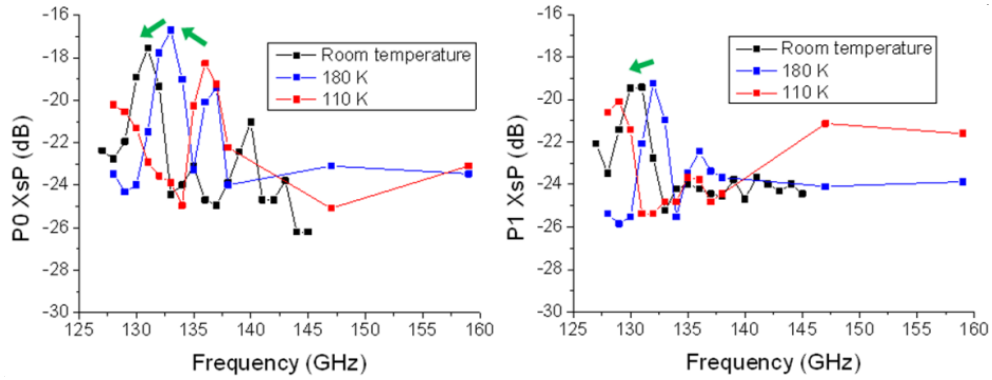


Figure 7.38. Measured cross-polarization when the temperature of the 110K IR filter changes

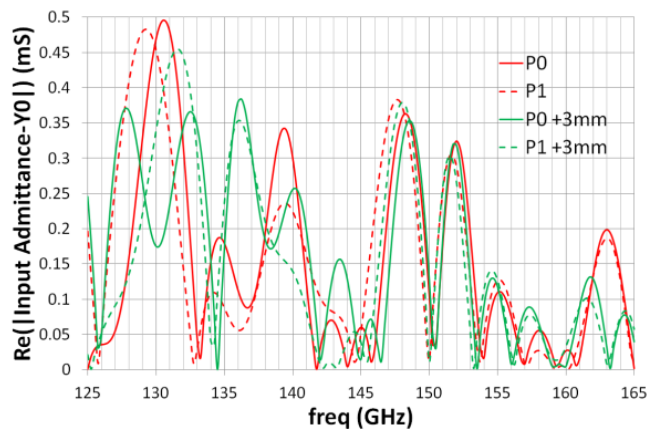


Figure 7.39. $\text{Re}(\Delta Y_{in} - Y_0)$ when the 110K filter is 3mm further from the horn aperture

7.5.3.3. Conclusions of this analysis

All components which contribute to the ALMA Band 4 receiver cross-polarization have been analyzed in order to find out the origin of the strong cross-polarization peaks measured for production cartridges. Waveguide transitions, OMT and IR filters alone do not present any strong frequency dependence which explains these peaks. However, it has been shown theoretically that the IR filters can effectively affect the corrugated horn input admittance and therefore, change the radiated fields. On the one hand, a relationship has been found between the real part of the input admittance of the IR filters structure at the horn aperture plane and the radiated cross-polarization. The frequency behavior of the real part of the input admittance properly matches cross-polarization measurements and explains the results of several experiments. On the other hand, it has been proven that the influence of IR filters at higher ALMA band 4 frequencies is some attenuation of the cross-polarization, which explains the generally good levels of XsP at 155-165 GHz. In conclusion, the dielectric loading of the corrugated horn by the IR filters properly explains the measured XsP degradations at certain frequencies. The degradation of the cross-polarization performance at certain frequencies may jeopardize astronomical polarization observations at those frequencies. It is therefore very important to understand properly the physics behind this degradation.

Chapter 8

Summary and Conclusions

8.1. Summary

The quality of astronomical observations at Terahertz frequencies depends greatly on the performance of the receivers in the radio telescope. Slight performance degradations due to unwanted effects will translate into worse observations than expected. This may mean less sensitivity, more time required to get a result or even image distortion. Therefore, it is important to tune all the elements of the receiver for maximum performance. This thesis has studied the different optical systems in an astronomical receiver. Along the different chapters, different analysis methods have been applied to optics used to bring the astronomical signals from the secondary mirror of the telescope to the detectors or for pumping the local oscillator signal into heterodyne detectors. THz astronomy has seen a great development in recent years, which has been pushed forward by the development of the ALMA telescope, among others. The implementation of the ALMA telescope has been the first time that state-of-the-art THz superconducting receivers have been mass-produced. Hundreds of feed horns, ellipsoidal mirrors, dielectric IR filters and ultra-sensitive detectors have been manufactured in order to implement the cartridges which will populate the cryostats in the secondary focus of the ALMA antennas. In terms of optics, this kind of mass-production of advanced technology has exposed for the first time some critical issues involving the repeatability of performance for different implementations of the same optical design or some other problems which surface on when receivers are operated within the confined environment of a cryostat, with IR filters and a window. Usual astronomical receivers are fabricated once or a few times at most. Therefore, if problems derived from tolerances or from practical operation arise, a solution which mitigates the problem is looked for and careful investigations are not necessary. However, these issues become critical when around 80 similar implementations of a design have to be manufactured in a time frame of a few years. In this case, usual engineering solutions must be combined with more careful studies based on physics.

The achievements described in this thesis can be summarized in the following points:

- Introduction of design method for LO power injection
- Novel quasi-optical attenuators
- Tolerance analysis method using Physical Optics and Monte Carlo techniques
- Effect of IR filter reflections on optical performance and ways to mitigate this effect

- Novel method to estimate total quasi-optical receiver cross-polarization performance
- Physical causes of degraded cross-polarization performance unveiled for ALMA band 4

In terms of LO power injection, quasi-optics provide a good alternative to classic waveguide power transmission schemes at frequencies approaching 1 THz. In this thesis, new design equations have been derived for a proposed horn to horn power transmission system. This system has been implemented in the injection of the LO signal in the SIS mixers of the ALMA band 10 receiver. This solution overcomes all of the problems of a previous design based on waveguide technology and provides stable operation of the detectors in the receiver. This improvement in stability means more stable and better astronomical observations. Additionally, a new kind of quasi-optical attenuator has been used in that quasi-optical LO injection system to carefully control the SIS mixer pumping current while the LO chain of multipliers are operated at their maximum output power, which guarantees minimum noise. These attenuators are very simple, easy to fabricate and light. By using them, the sensibility of the receiver can be improved at the same time that the LO pumping is guaranteed. In other words, the use of the quasi-optical LO injection and these attenuators make it possible that the LO pumping of detectors does not have a negative impact on astronomical observations.

The core of the thesis deals with the analysis of tolerances in astronomical receiver optical systems, the physical investigation of the effects of IR attenuators on optical performance and the physical analysis of cross-polarization performance. These topics have been applied to two ALMA receivers using SIS mixers, band 4 and 10, and to a HEB mixer receiver designed at University of Tokyo for the ASTE telescope. The new analysis methods and investigations developed have allowed increasing and better understanding the performance of these receivers. In the case of ALMA, this translates into improved performance of one of the largest and most demanded telescopes ever built. An increase in optical performance may translate into shorter observation times for the same results, allowing a better use of the ALMA telescope, or into more accurate measurements, which improves the science capabilities of ALMA. In the case performance could not be improved, these analyses have been useful to understand the capabilities and limitations of the astronomical receivers.

Chapter 5 described a new method to quantify the effect of tolerances on final performance. Usually, tolerance analyses of THz optics are based on ray tracing, which is not physically rigorous and does not yield good approximations at these frequencies. The use of ray tracing is an influence of optics design in the visible and near-infrared spectrum. Telescopes working in this spectral region are well-modeled by ray tracing and such a tolerance analysis is meaningful. However, in the case of THz receivers, it is necessary to consider the effects of the size of optical elements as well as the effects of diffraction. Therefore, the combination of Physical Optics and Geometrical Theory of Diffraction is a suitable combination of analysis techniques in the THz range. Using these methods, beam patterns can be calculated for specific dimensions and angle error values and the effect of tolerances on efficiency and other performances can be readily quantified. Monte Carlo methods provide an appropriate way to get the geometrical dimensions and angles of the models including tolerances and to obtain meaningful statistics when the number of simulated cases is high. Using these combinations of analysis methods, expected performances and standard deviations were obtained for the ALMA band 10 receivers. In chapter 5, it was shown that the standard deviation of

efficiencies would actually depend on tolerances. It was also shown that average values can be different from design values in certain cases. Finally, it was confirmed that the average values and standard deviations calculated with this analysis are pretty close to the statistics derived of the measurements of the 60 ALMA band 10 receivers manufactured and tested up to date.

The tolerance analysis presented in chapter 5 and the careful analysis and measurement characterization in chapter 4 were also useful to determine that there was a faulty component in the optics of the HEB receiver. A careful analysis considering several causes for the extra deviations in performance showed that the ellipsoidal mirror was probably the culprit of the unexpected degradation. Room temperature beam measurements of the mirror alone and 3D laser measurement of the mirror surface confirmed the mirror has clear fabrication errors. The replacement of this mirror will eventually improve the efficiency of the whole receiver with the consequent improvement in science capabilities.

Chapter 6 presented the effect of the IR filters on the optical performance of the ALMA band 10 receiver. When this effect was discovered, the cause of the efficiency and beam shape degradation was completely unknown. A careful measurement campaign and the physical analysis of the situation allowed finding the cause. Once the cause of the distortion was understood, it was straightforward to come up with a solution which improved the measured aperture efficiency of all production cartridges from that moment on. The solution using chamfered corrugated horns and absorber paint around the horn aperture was introduced in all ALMA band 10 production cartridges (from serial number 7 on), whereas the pre-production cartridges (from serial number 1 to 6) use the original optics design. [100] reports on the performance of the first 6 ALMA band 10 cartridges. The comparison of average aperture efficiencies of the first 6 receivers (pre-production models) is compared to the average values for the last 54 receivers (production models) in table 8.2. The final aperture efficiency improvement is clear. As explained in chapter 6, the influence of the optics change has more impact at lower frequencies and at polarization P1. The improvement of aperture efficiency achieved for polarization P1 at 804 GHz is 2.61 % in average.

Table 8.2. Summary of the improvement in aperture efficiency derived of using the optics modification introduced in chapter 6

	P0 804 GHz	P1 804 GHz	P0 879 GHz	P1 879 GHz	P0 943 GHz	P1 943 GHz
Pre-production	84.26 %	83.52 %	84.13 %	84.63 %	85.63 %	85.69 %
Production	86.16 %	86.13 %	86.19 %	86.20 %	85.95 %	85.94 %
Improvement	1.90 %	2.61 %	2.06 %	1.57 %	0.32 %	0.25 %

Chapter 7 focuses on the study of cross-polarization in quasi-optical systems in astronomical THz receivers. A novel method to quantify total system cross-polarization has been introduced. This method is based on the use of Gaussian beam theory and tries to compute the phase with which the cross-polarization contributions of the different components add together towards a total system cross-polarization. To the knowledge of the author, this is the only method in literature which aims at calculating the total system cross-polarization on physical grounds. Other methods are usually based on root mean squares or worst-case additions and do not consider the physics involved. The proposed method has been applied to the ALMA band 4 and band 10 receivers. In the case of the

band 4 receiver, it has been used to prove that the current receiver optics design cannot achieve the stringent -23 dB ALMA requirement even with very good components. It has also been used to propose a new physically-meaningful requirement. In the case of the band 10 receiver, the method has provided some insight into why this design is very robust in terms of cross-polarization. These examples indicate some guidelines to follow in order to design receivers which are good in terms of cross-polarization performance:

- A pair of ellipsoidal mirrors with a waist between them is better than a single mirror
- Wire grids are better than OMTs if both options are possible
- If possible, locate components (including IR filters) in a way that cross-polarization contributions add as much out-of-phase as possible

The calculated expected cross-polarization for ALMA band 10 using this model is -27.1 dB (table 7.2) for just-compliant IR filters and window cross-polarization values. Table 5.9 shows that the measured average polarization efficiency for the last 54 band 10 receivers is 99.88 %, which means an average -29.2 dB cross-polarization level. This shows that actual IR filters and window are a bit better in terms of cross-polar than their requirement value, as expected.

The last part of chapter 7 constitutes an attempt at identifying the cause of the frequency-dependent degradation of ALMA band 4 cross-polarization performance. This analysis combines the results derived from electromagnetic theory with the data calculated in full-wave electromagnetic simulations to explain the physics behind this degradation. Figure 8.1 shows the results of the measurements of 43 ALMA band 4 cartridges. Figure 8.1 clearly shows the repeatability of the cross-polarization degradation for all 43 receivers.

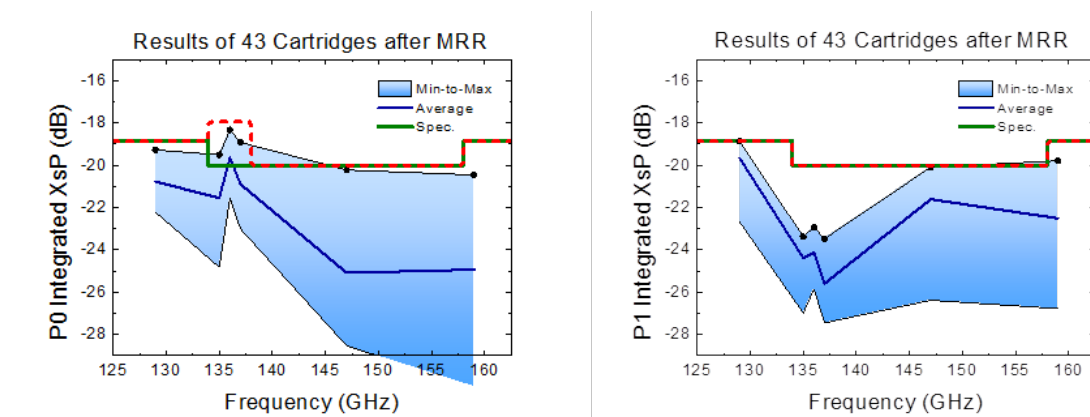


Figure 8.1. Summary of the measured cross-polarization performance of the last 43 ALMA band 4 receivers

All components which contribute to ALMA Band 4 receiver cross-polarization have been analyzed in order to find out the origin of the strong cross-polarization peaks measured for production cartridges. Waveguide transitions, OMT and IR filters alone do not present any strong frequency dependence which explains these peaks. However, it has been shown theoretically that the IR filters can effectively affect the corrugated horn input admittance and therefore, change the radiated fields. On the one hand, a relationship has been found between the real part of the input admittance of the

IR filters structure at the horn aperture plane and the radiated cross-polarization component magnitude. The frequency behavior of the real part of the input admittance properly matches cross-polarization measurements and explains the results of several experiments. On the other hand, it has been proven that the influence of IR filters at higher ALMA band 4 frequencies is some attenuation of the cross-polarization, which explains the generally good levels at 155-165 GHz. In conclusion, the dielectric loading of the corrugated horn by the IR filters properly explains the measured cross-polarization degradations.

8.2. Conclusions

As receivers achieve performance close to physical limits, new subtle performance degradations appear. The effects of tolerances and infrared filters should not be neglected in this context. Additionally, as astronomers request polarization observations, cross-polarization performance should be a key aspect to take into account during the design phase of a receiver. Good engineering practices do not suffice in many of these cases and careful physical analyses must be performed. This approach has allowed the improvement of the performance of the ALMA band 10 receiver and to better understand the performance limits of the ALMA band 4 receiver. The application of the proposed tolerance analysis has allowed determining a defective component in the HEB mixer receiver for ASTE.

The methods developed in this thesis are of interest for any astronomical receiver in the THz range, especially for those to be operated within a cryostat. They can also be useful for any quasi-optical system to be used in any other applications.

The unexpected cross-polar degradation found for the ALMA band 4 receiver can potentially occur for any superconducting receiver, especially at the low THz range or at cm wavelengths, when the size of optics is large and IR filters and cryostat window are invariably very close to the receiver horn aperture. In these cases, IR filters should be considered during the feed horn design in order to model their effects from the first stages of the optics design.

In conclusion, the research results in this thesis have proved useful to characterize and improve the optics performance of state-of-the-art superconducting receivers used for the ALMA and ASTE telescopes, with the consequent potential improvements in future astronomical observations.

Acknowledgments

Special thanks are due to the ALMA band 10 (and 4) group leader Professor Yoshinori Uzawa and my thesis supervisor Professor Satoshi Yamamoto. Firstly, I would like to thank Uzawa-san for all his kind support during the last four years of work in ALMA, for providing a pleasant working environment for all the band 10 team and ultimately, for hiring me for such an exciting job. I would specially like to thank Yamamoto-sensei for all his support during the last months of this work in spite of his busy schedule and for making possible a fruitful collaboration between our research groups. I would also like to thank him for suggesting me to contact Uzawa-san for job inquiries back in September 2009. The research work in this thesis basically started at that moment.

I am very grateful to all of the band 10 team members. The final 4 years of the ALMA band 10 receiver design and production have been great thanks to all the nice people which compose the team. It has been a pleasure to work hard with all of them. Special thanks to Mr. Yasunori Fujii for managing the laboratory and scheduling the testing of the ALMA band 10 cartridges and for teaching me lots of useful things in the laboratory. Thanks to Ms. Keiko Kaneko, for taking care of the mechanical design of the receiver and for the hard work together to understand the connection between mechanical and electrical measurements; and for taking many beam pattern measurements when I was absent. Thanks to Dr. Matthias Kroug and Mr. Akihira Miyachi for providing wonderful SIS devices and for nice conversations about any imaginable topic; to Mr. Takao Yokoshima for taking care of the calibration of instruments; to Mr. Koichi Kuroiwa for help in the LO injection measurements and for lots of interesting conversations; and to Dr. Takafumi Kojima, for many interesting physical and technical discussions.

I am also grateful to Mr. Tatsuya Soma and Dr. Tatsuya Shiino for our fruitful collaboration and for their help with the HEB receiver beam measurements. In special, I would like to thank Soma-san for stimulating conversations about antenna theory, astrophysics and HEB physics, and for supplying me with a lot of data related to the HEB receiver.

I would also like to thank the ALMA band 4 group at NAOJ, specially Mr. Koichi Kubo and Ms. Miki Karatsu, for taking care of all the cross-polarization measurements of the band 4 receiver; and Mr. Saigo Saito at NICT for letting us use their THz-TDS systems for material characterization.

I would like to thank many people for interesting discussions about optics, superconductivity or physics in general. These include Dr. Masahiro Sugimoto, Mr. Yasuhiro Fujimoto, Dr. Norikazu Mizuno, Prof. Hiroshi Matsuo, Prof. Yutaro Sekimoto, Prof. Satoru Iguchi... among many.

Finally, I am grateful to the members of my dissertation committee.

Last but not least, I would like to thank my parents and brothers in Spain for taking care of me for so many years and providing the environment and resources necessary for my education and well-being. Gracias. I would like to thank my wife, Naoko, and my son, Yuuhi, for their help and for making my life meaningful and interesting every single day.

Appendix A

Probe horn compensation

One of the key elements in any antenna / optics characterization near-field test bench is the probe horn with which the near field patterns of the optics under test are measured. Ideally, a probe horn with an isotropic radiation pattern and no cross-polarization would be required to guarantee the probe horn has no effects on the measurement results. However, this is not possible and horn antennas or open waveguides are preferred at THz frequencies. A WG-1.2 open rectangular waveguide is used in the ALMA Band 10 measurement setup. An open waveguide has a pretty wide radiation pattern, but far from isotropic. Besides, since the radiating aperture dimension is twice larger in one direction than in the other in the XY plane, the radiation pattern will be twice narrower in that direction. In addition, cross-polarization levels will be low but not negligible.

The actual measurements obtained using non-ideal probe antennas are the convolution of the radiation patterns of the probe antenna and the optics under test. If the cross-polarization is also considered, this relation gets more complex.

ALMA Band 10 probe horn has been characterized in order to account for the non-ideality of the probe horn and to correct performed measurements.

A.1. Probe horn measurement set-up

When the far field co-polar CoP and cross-polar XsP radiation patterns of an antenna (AUT) are measured, the actual measured patterns are given by equations (A.1) and (A.2). It is important to insist in the fact that these radiation patterns must be in the far field. Far fields must be calculated from near fields through Fourier transform application.

$$\text{Measured CoP} = \text{AUT CoP} \cdot \text{Probe CoP} + \text{AUT XsP} \cdot \text{Probe XsP} \quad (\text{A.1})$$

$$\text{Measured XsP} = \text{AUT XsP} \cdot \text{Probe CoP} + \text{AUT CoP} \cdot \text{Probe XsP} \quad (\text{A.2})$$

(A.1) and (A.2) will be used for the correction of measurements, but are also useful for probe horn characterization. If both antennas are the same, (A.1) and (A.2) get simpler, as stated in (A.3) and (A.4). That is the reason why probe horns are normally manufactured and sold in pairs with the same characteristics.

$$\text{Measured CoP} = \text{Probe CoP}^2 + \text{Probe Xs}^2 \quad (\text{A.3})$$

$$\text{Measured XsP} = 2 \cdot \text{Probe XsP} \cdot \text{Probe CoP} \quad (\text{A.4})$$

From (A.3) and (A.4), it is possible to calculate the Probe CoP and XsP radiation patterns as:

$$\text{ProbeCoP} = \frac{1}{\sqrt{2}} \sqrt{\text{MeasuredCoP} + \sqrt{\text{MeasuredCoP}^2 - \text{MeasuredXsP}^2}} \approx \sqrt{\text{MeasuredCoP}} \quad (\text{A.5})$$

$$\text{Probe XsP} = \frac{\text{Measured XsP}}{2 \text{ Probe CoP}} \quad (\text{A.6})$$

The approximation in (A.5) is justified because of the great difference of around 30 dB between the measured CoP and XsP patterns. If not applied, the exact equation (A.5) becomes difficult to evaluate using software due to problems with phase wrapping.

The probe horn far field starts very close to the aperture due to the small dimensions of the waveguide. The distance at which far fields are well established is given by (A.7).

$$\text{distance} = 2 \frac{\text{Largest dimension of aperture}^2}{\lambda} \quad (\text{A.7})$$

At a frequency of 864 GHz, far fields created by a 0.305 mm x 0.152 mm open waveguide start at 0.67 mm from the aperture. That distance is really short and for practical reasons, probe fields must be measured in the far field directly. Far field coordinates must be Azimuth and Elevation, whereas fields can only be sampled in an XY plane in front of the antenna in the ALMA band 10 setup. Therefore, it is necessary to perform a coordinate transformation which will affect the value of the measurements. The situation is depicted in figure A.1. Notice that the antenna under test has a wide beam. Therefore, the measurement plane must be pretty near the antenna if the dimensions of the measurement plane are to be small enough to be sampled finely in a reasonable time.

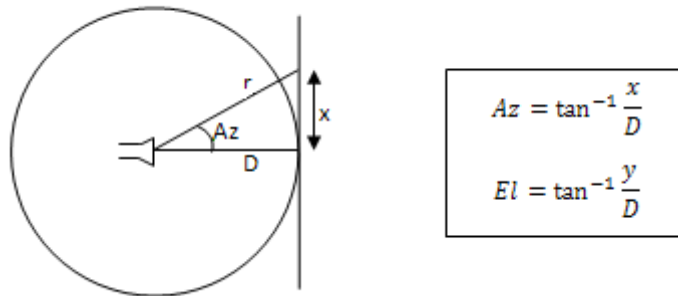


Figure A.1. Geometry of the probe horn far field measurement

For a point (x,y) in the XY plane, the distance r to the measurement plane will be given by $r = \sqrt{D^2 + x^2 + y^2}$, whereas in a far field measurement, this distance should be constant and equal to D. The propagation equation of a far field spherical wave is given by (A.8).

$$\vec{E} = \vec{E}_0 \frac{e^{-j\vec{k} \cdot \vec{r}}}{r} \quad (\text{A.8})$$

In the case under study, r changes at each point of the measurement XY plane. Since we are interested in the fields over a sphere and not over a plane, the amplitude and phase correction in equation (A.9) can be performed on the measured field values.

$$\vec{E}_{on\ sphere} = \sqrt{1 + \frac{x^2+y^2}{D^2}} e^{j\frac{2\pi f}{c}(\sqrt{D^2+x^2+y^2}-D)} \vec{E}_{measured} \quad (A.9)$$

The coordinate transformation (x,y) to (Az, El) can be performed using the equations in figure A.1.

On the other hand, the standing wave compensation procedure must be changed for these measurements. In Band 10 optics measurements, two XY planes at a distance $\lambda/4$ are sampled and measured values are combined to eliminate the contribution of the standing wave. However, in this case, since distance D must be short, the distance between two parallel XY planes will be seen differently under different angles. This situation is depicted in figure A.2.

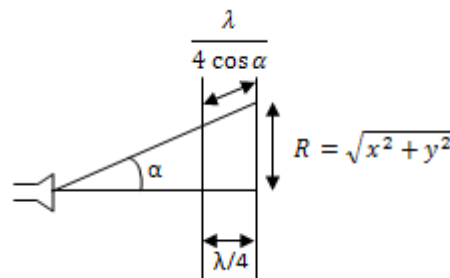


Figure A.2. Geometry of the standing wave correction procedure

In general, in the presence of a standing wave, the relationship between two measurements taken a distance d apart is:

$$V(z) = V^+ e^{-jkz} (1 + \rho e^{2jkz}) \quad (A.10)$$

$$V(z+d) = V^+ e^{-jkz} e^{-jkd} (1 + \rho e^{2jk(z+d)}) \quad (A.11)$$

Using the first measurement as the phase reference, z can be equaled to 0. If the second measurement is taken in a parallel plane at a distance d from the first plane, the distance between measurements is $d/\cos(\alpha)$. Then,

$$V_1 = V^+ (1 + \rho) \quad (A.12)$$

$$V_2 = V^+ e^{-j\frac{kd}{\cos\alpha}} (1 + \rho e^{j\frac{2kd}{\cos\alpha}}) \quad (A.13)$$

After some algebraic work, and for $|\alpha| < 90^\circ$, equation (A.14) provides the way to calculate the voltage without standing wave, V^+ .

$$V^+ = j \frac{V_2 - V_1 e^{j\theta}}{2 \sin \theta} \quad \text{with } \theta = \frac{2\pi}{\lambda} d \sqrt{1 + \frac{x^2+y^2}{D^2}} \quad (A.14)$$

Equation (A.14) shows some problems when the $\sin(\theta)$ in the denominator approaches 0. That means when the variable θ takes values $n\pi$. Those values correspond to circles of radii $R = D\sqrt{\left(\frac{n\lambda}{2d}\right)^2 - 1}$.

The first circle radius can be increased by increasing D or decreasing d . As explained before, D must be as small as possible to obtain most of the radiation pattern information in a small enough area in the measurement plane. If D is increased, the area to be mapped increases and so does the time required to measure it. Therefore, it is recommended to reduce the distance d . It is important to notice at this point that according to (A.14), there is no advantage in taking $d = \lambda/4$. In conclusion, it is better to take a value of d as small as possible. This time, $d = \lambda/12$ was used, which yields an increase in the critical radius of a little bit less than 3. Measurements were taken at $D = 8\text{mm}$ from the probe horn. Figure A.3 shows the distortion circles which appear in the manipulated data if D and d are not chosen properly.

In ALMA band 10 optics measurements, the distance D is very large with respect to the measurement plane dimensions. This makes the variable θ is approximately 90 degrees for $d = \lambda/4$ and equation (A.14) becomes the usual equation used for standing wave compensation.

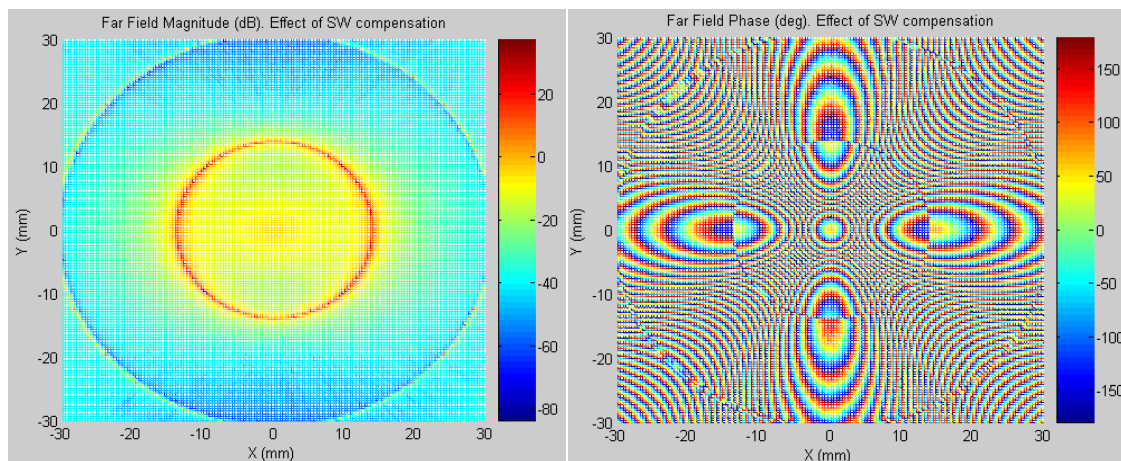


Figure A.3. Possible distortion in the standing wave free measurements due to equation (A.14)

In short, the probe horn characterization process can be summarized in the following steps:

- Measurements at a distance $D = 8\text{ mm}$ and $d = \lambda/12$ away.
- Use of equation (A.14) to remove the standing wave contribution
- Correction of the measurement coordinate system using equation (A.9)
- Use of equations (A.5) and (A.6) to isolate individual probe antennas contributions

A.2. Measurement results

The available probe horns were characterized at frequencies 842.4, 864 and 892.8 GHz and the measurements were processed as explained in the previous section. Example measurements before applying (A.9) are shown in figure A.4.

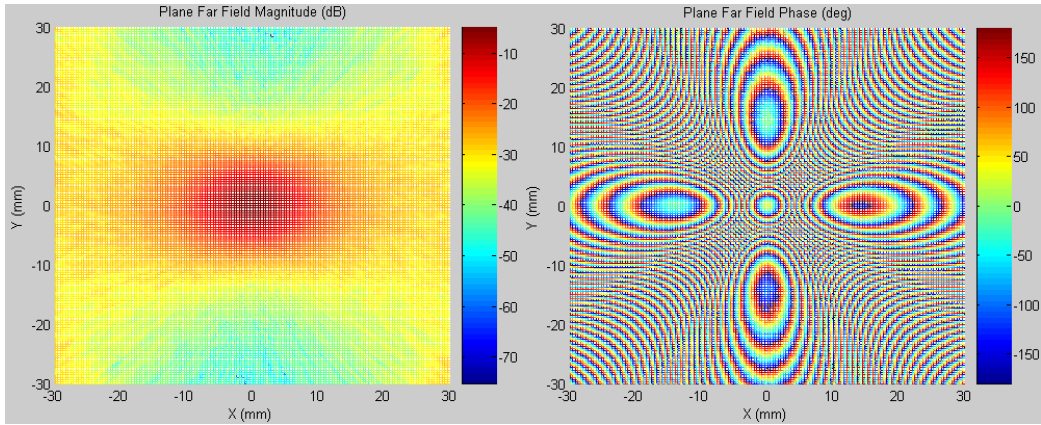


Figure A.4. Far field co-polar radiation pattern of probe horn at 864 GHz measured on an XY plane

In order to compare the results with theory, GRASP simulations were performed to calculate the radiation pattern under the same conditions of the measurements. The theoretical result of the measurement in figure A.4 is presented in figure A.5. The similarity is remarkable. Notice however, that the measurement in figure A.4 accounts for the contribution of two horns and the square root of all values must be taken. This will be done later in this Appendix. Cross-polarization measurements and theoretical results using GRASP are shown in figures A.6 and A.7.

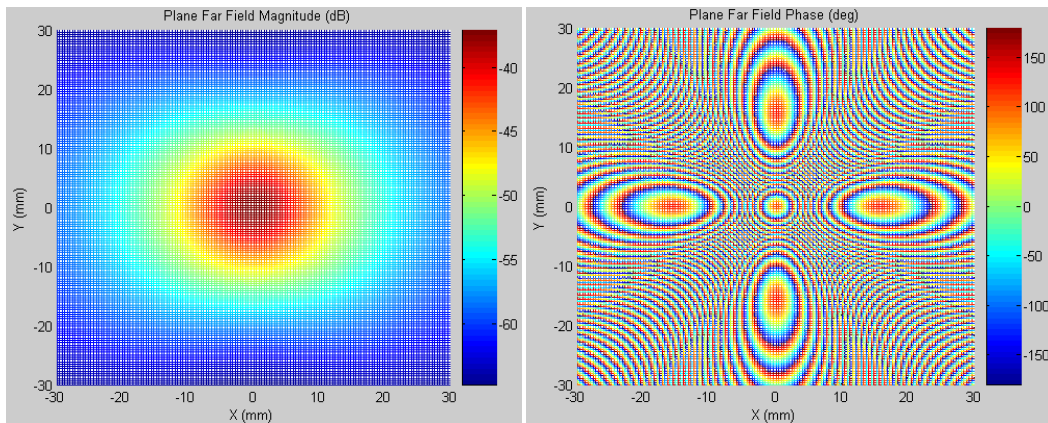


Figure A.5. Far field co-polar radiation pattern of probe horn at 864 GHz on an XY plane calculated with GRASP

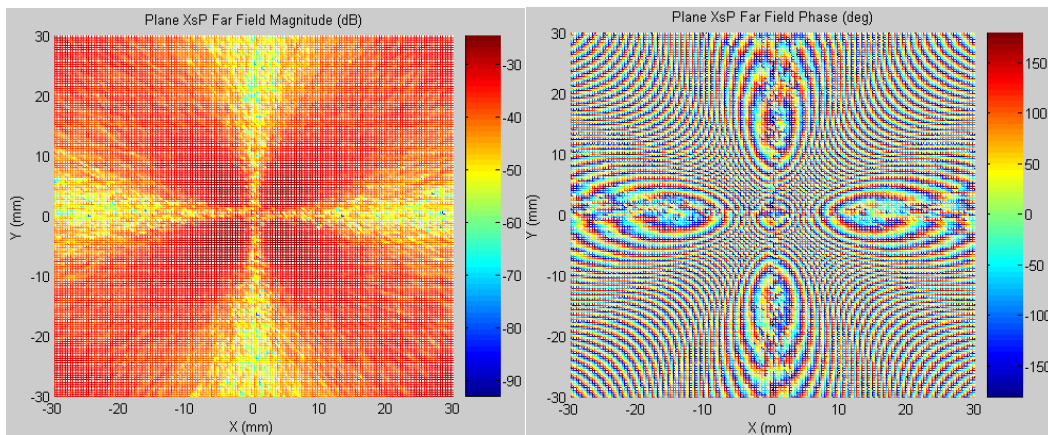


Figure A.6. Far field cross-polar radiation pattern of probe horn at 864 GHz measured on an XY plane

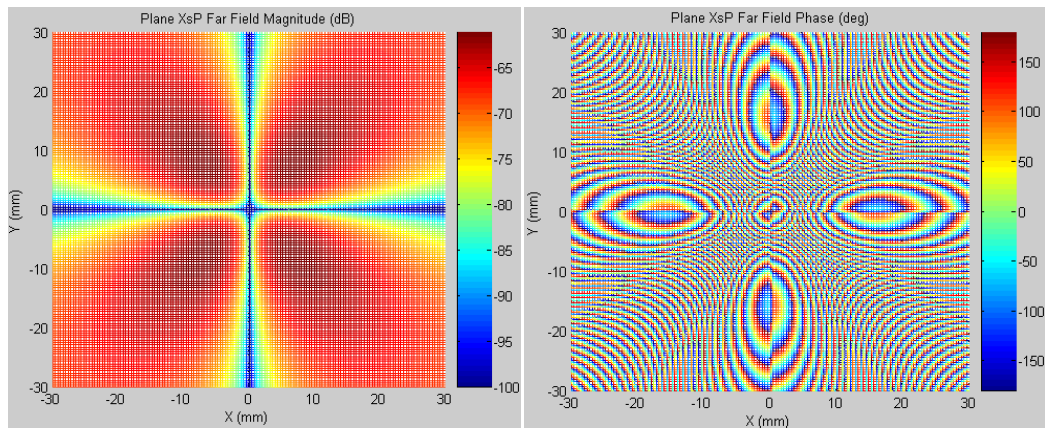


Figure A.7. Far field cross-polar radiation pattern of probe horn at 864 GHz on a XY plane calculated with GRASP

The next step in the process is the correction of the measurements and change of coordinates to have the radiation patterns expressed in terms of Azimuth and Elevation coordinates. This is done using equation (A.9). The theoretical patterns calculated with GRASP are shown in figure A.8 at 892.8 GHz. The phase is constant in the co-polarization pattern and constant with sign changes in each space quadrant in the cross-polarization pattern.

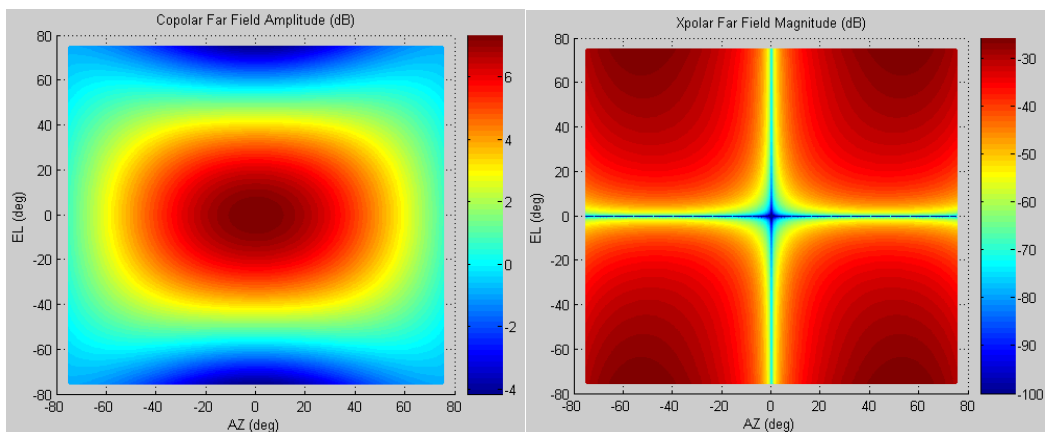


Figure A.8. Theoretical radiation patterns at 892.8 GHz calculated using GRASP

In the coordinate correction process, the value of the variable D is very important and difficult to measure in practice. However, this final step in the process provides a way of accurately calculating the value of D . Since the phase must be constant in the co-polar pattern, D can be optimized to get a phase as constant as possible. Figure A.9 shows the results if $D = 9$ mm and figure A.10 shows the final result when $D = 8$ mm.

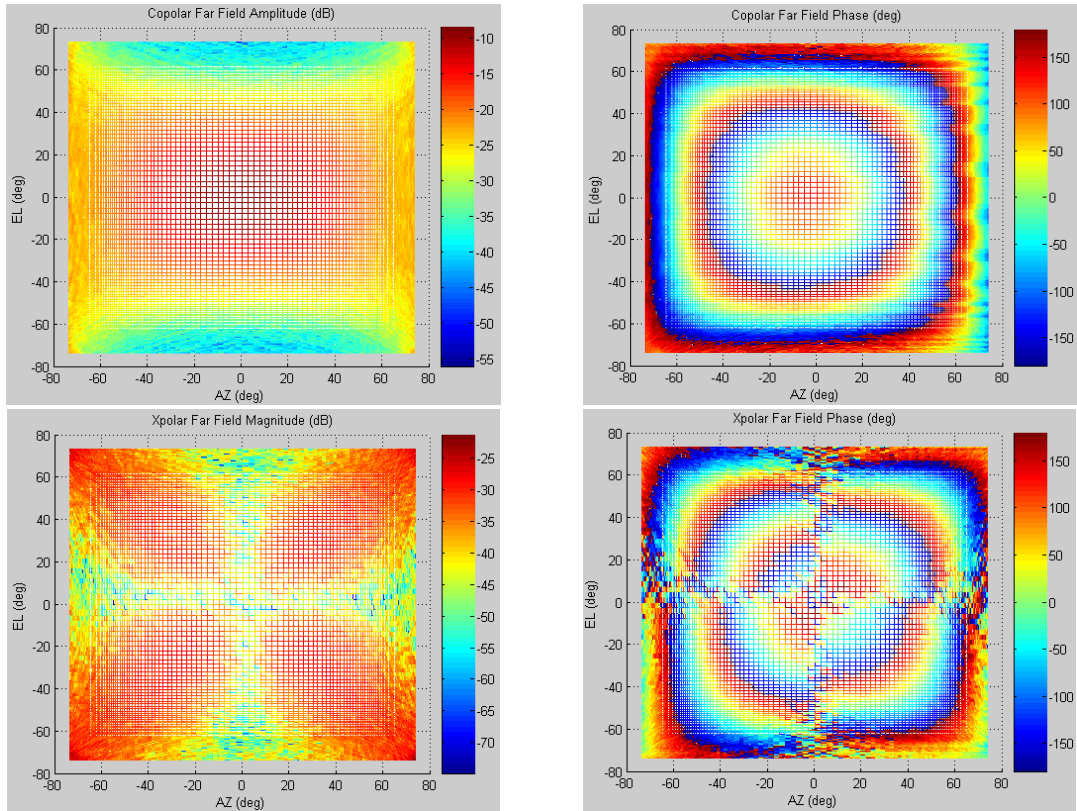


Figure A.9. Far field radiation patterns considering $D = 9$ mm

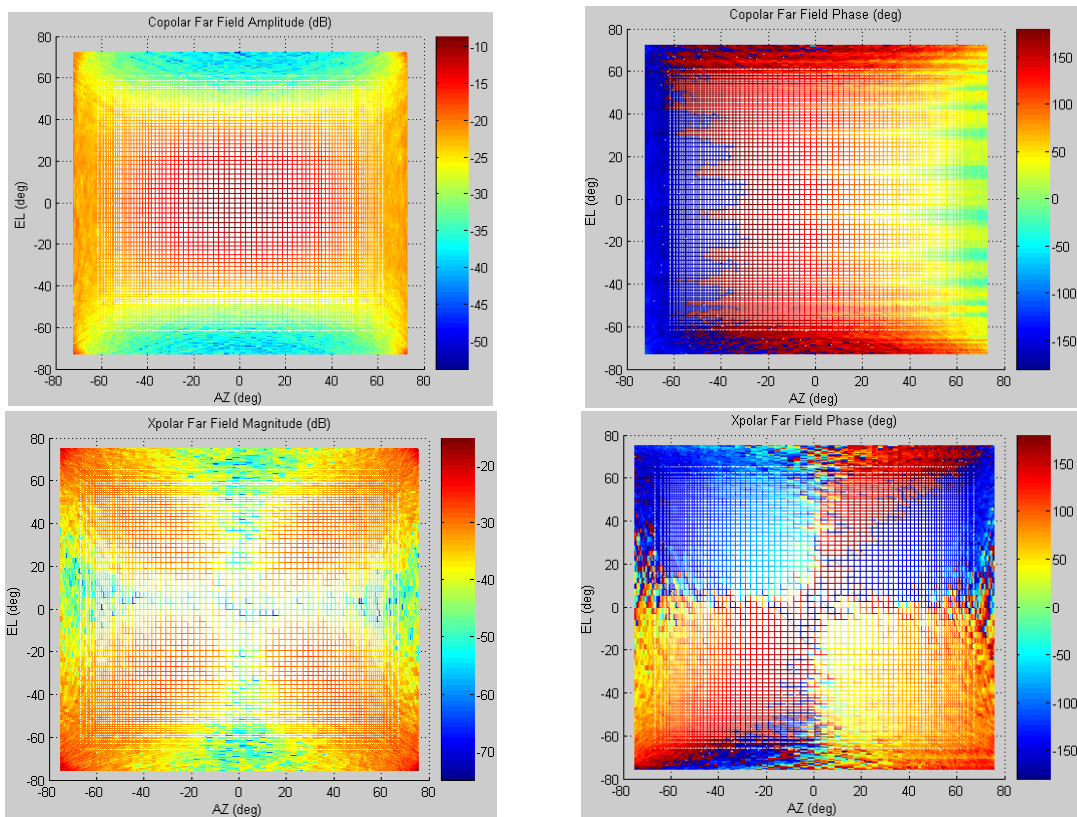


Figure A.10. Far field radiation patterns considering $D = 8$ mm

As it can be seen in figure A.10, the phase is constant for $D = 8\text{mm}$ except for alignment errors. $D = 8\text{mm}$ provides optimal results for the measurements performed.

Finally, the contribution of both probe horns involved in these measurements must be separated using equations (A.5) and (A.6). The results of applying equations (A.5) and (A.6) have been presented together with GRASP simulations in figures A.11 and A.12.

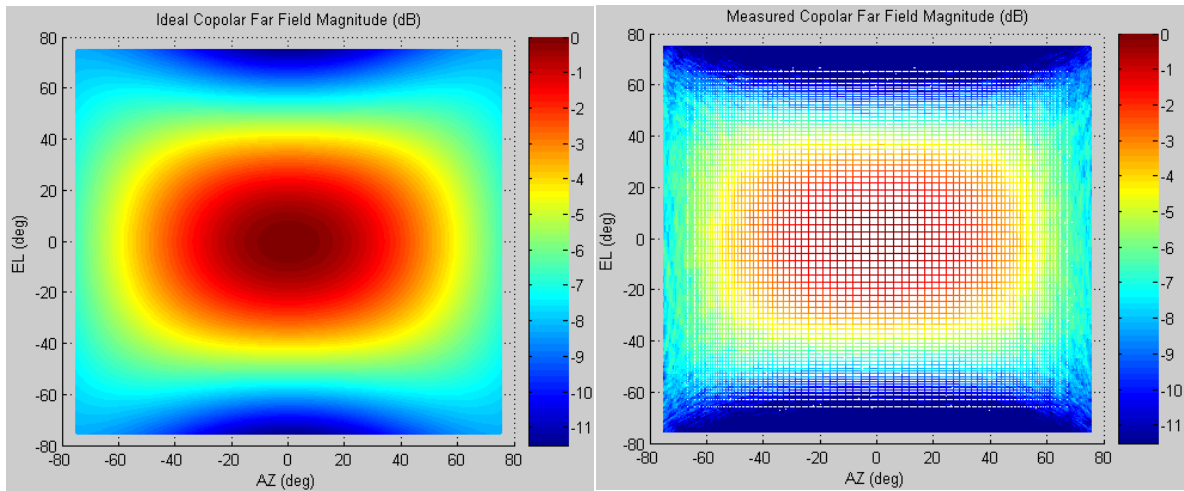


Figure A.11. Co-polar far-field radiation pattern of ALMA Band 10 probe horn. GRASP simulation on the left, measurement on the right

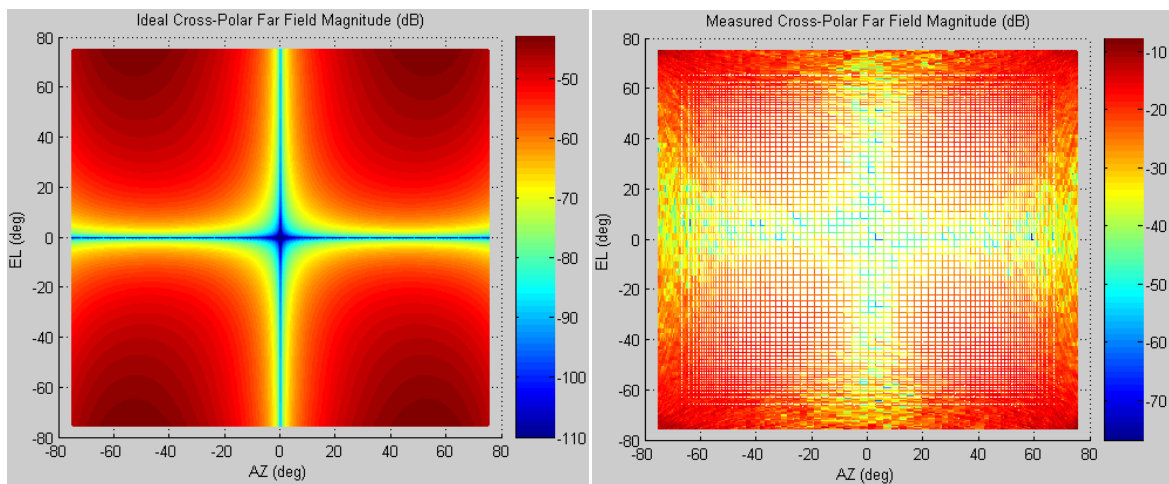


Figure A.12. Cross-polar far-field radiation pattern of ALMA Band 10 probe horn. GRASP simulation on the left, measurement on the right. Scales are different

Theoretical and measured co-polar far field patterns are strikingly similar. Some markers were used on 3D plots to see how similar measurements are. This is shown in figure A.13. The same was done for cross-polarization patterns in figure A.14.

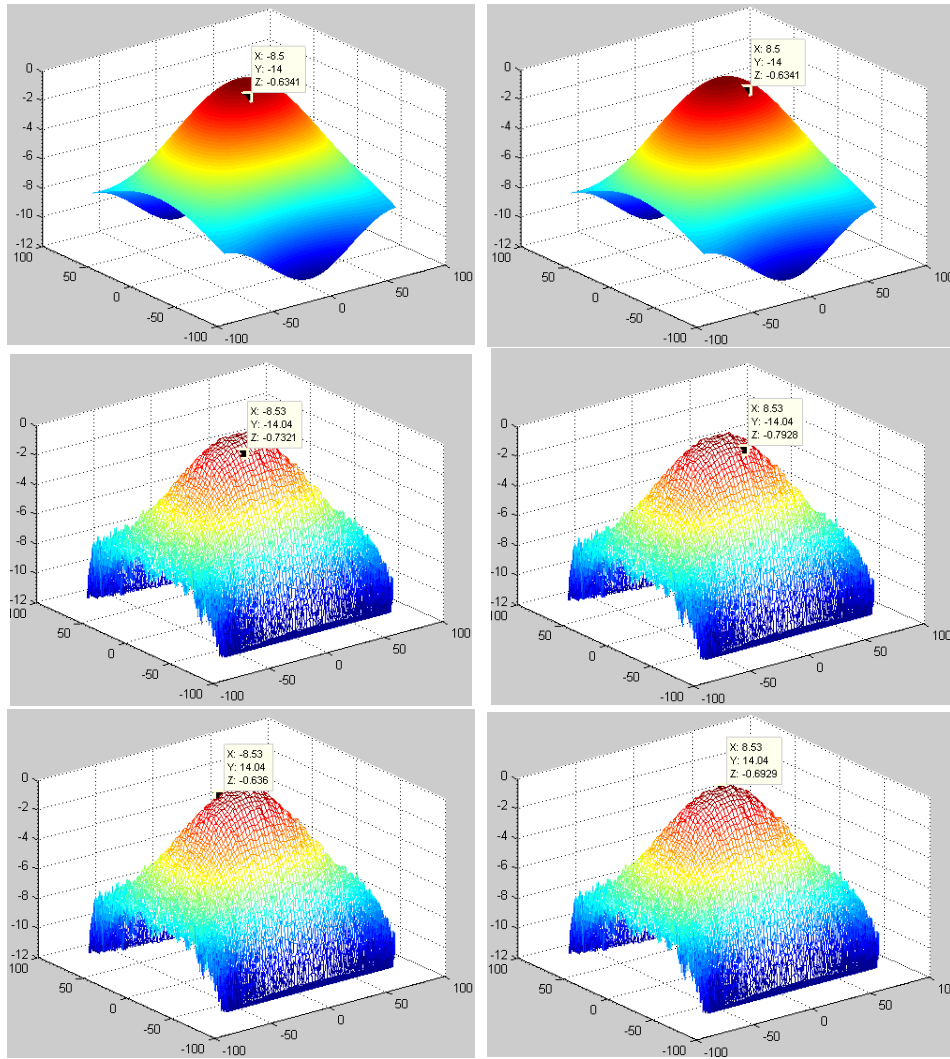


Figure A.13. Co-polar patterns. First row, GRASP simulation. Then, markers on measurement plots

In the co-polarization patterns, ideal and measured shapes and values are really similar. The differences could be explained just because of noise, alignment errors, measurement tolerances, etc. In the cross-polarization measurements, the shape looks very similar but the peak values in the angular region of interest are more realistic for the measured patterns. It is important to notice that, in both cases, these patterns are very noisy. The resemblance of measured and simulated patterns in the angular region of interest for measurement probe compensation suggests the use of ideal simulated patterns instead of the measured ones. Like this, noise-free patterns at all frequencies are readily available at any desired angle sampling accuracy. Besides, some frequencies cannot be measured at room temperature due to bandwidth limitations of the used room temperature mixers.

Therefore, ideal GRASP simulations have been used to correct the measurement data throughout this thesis. In the case of the cross-polar pattern, it must be modified so the cross-polar value at the edge of the measurement $(AZ, EL) = (15, 15^\circ)$ is around the measured value at those points, e.g. markers in figure A.14.

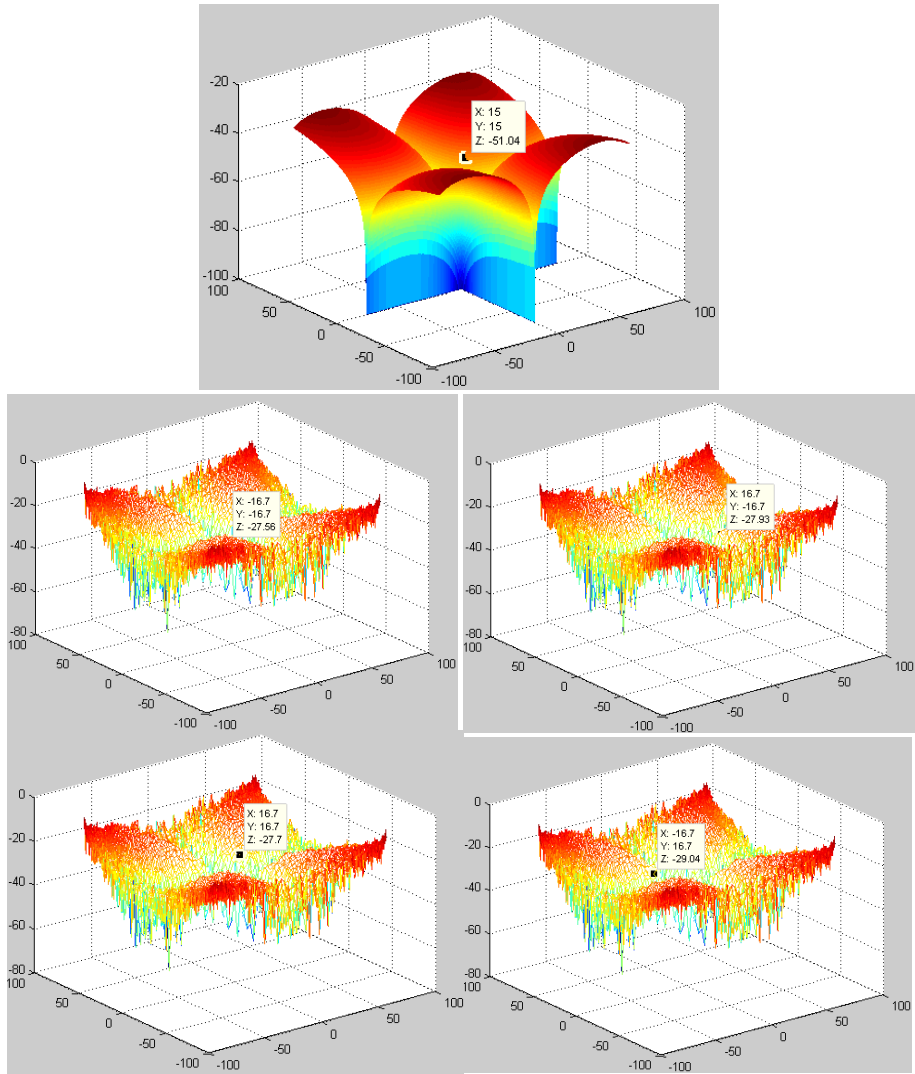


Figure A.14. Cross-polar patterns. First row, GRASP simulation. Then, markers on measurement plots

Appendix B

Joint Paper

Optics characterization of a 900-GHz HEB receiver for the ASTE telescope: design, measurement and tolerance analysis

A. Gonzalez^{1,*}, T. Soma², T. Shiino², K. Kaneko¹, Y. Uzawa¹ and S. Yamamoto²

¹National Astronomical Observatory of Japan, Mitaka, Tokyo, 181-8588, Japan

²University of Tokyo, Department of Physics, Graduate School of Science, Bunkyo, Tokyo, 113-0033, Japan

*Corresponding author: Alvaro.Gonzalez@nao.ac.jp

Abstract

The optics of a 900-GHz HEB receiver for the ASTE telescope have been analyzed by quasi-optical analysis and Physical Optics simulations in combination with beam pattern measurements. The disagreement between simulations and measurements has motivated an extensive campaign of Monte Carlo analyses to find out the cause of such a difference in results. Monte Carlo analyses have considered fabrication and assembly tolerances in all components in the RF chain, as well as some non-expected fabrication errors. This strategy has allowed determining the faulty component. In short, the use of all available analyses techniques together with measurements has allowed singling out an underperforming element in an astronomical receiver. The change of this component will improve the optical efficiency and ease astronomical observations. These ideas can be of interest for any quasi-optical receiver at THz frequencies.

Keywords: Astronomical receivers, Quasi-optical systems, Physical optics simulations, Near-field beam-pattern measurements, Monte Carlo methods

1. Introduction

The Atacama Submillimeter Telescope Experiment (ASTE) 10m-aperture telescope is located in Pampa la Bola, Chile, at 4860 m over sea level, and very near the Atacama Large Millimeter-submillimeter Array (ALMA) site [1]. This telescope was initially conceived as a test bench for antenna and receiver technology at (sub-) millimeter wavelengths, and as a first step towards the Japanese ALMA antenna. Actually, the 10m reflector antenna was a pre-prototype of the Japanese ALMA 12m antenna [2], and the first qualification model of the ALMA band 8 receiver [3] was tested in the ASTE telescope. Therefore, the cartridge size and cryostat requirements for ASTE are similar to those for ALMA. On the other hand, several receivers implemented by different universities and institutes have been used in ASTE for astronomical observations [4-5]. In the last years, a Hot Electron Bolometer (HEB) dual-band receiver working at 900 GHz and at 1.3 THz showing good noise performance has been developed at University of Tokyo and successfully used for observations with ASTE [6]. The HEB mixers are fabricated and noise tested at University of Tokyo. However, the receiver beam patterns cannot be measured in-house. Since the lower frequency band of this receiver is very close to that of ALMA band 10 (787-950 GHz) [7] and ASTE and ALMA cryostat and cartridge sizes are similar, the beam patterns could recently be measured in the ALMA band 10 laboratory at NAOJ. At the same time, the quasi-

optical design was validated using Physical Optics (PO) simulations. However, measurement results significantly differed from simulation results. Several Monte Carlo tolerance analyses [8] using Physical Optics have been performed considering manufacture and assembly tolerances in order to identify the causes of the degraded optical performance of this receiver. Quasi-optical and PO simulations in combination with laboratory measurements have been found useful to identify what component is degrading the overall optics performance.

2. Optics design

The sub-mm wavelength receiver developed at University of Tokyo uses HEB mixers [6] to detect radiation in the atmospheric windows around 900 and 1300 GHz [9]. Due to the large difference in frequency, each band is detected by different HEB mixers located in different mixer blocks with integrated diagonal horns. The input signal is separated in the two frequency bands by means of a wire grid located just after the cryostat window, which reflects the lower band and is transparent for the upper band. Fig.1 shows the 4K stage of the receiver, with some modifications to have a clear view of the optics. In this paper, only the 900 GHz optics is of interest and its schematic is presented in Fig. 2. This optics uses a single ellipsoidal mirror to match the beam coming from the secondary mirror of the ASTE antenna to the required beam size in the diagonal horn attached to the HEB mixer block. The local oscillator (LO) signal is generated outside of the cryostat and then, radiated by a diagonal horn and focused by an ellipsoidal mirror attached to this horn. This LO beam enters the cryostat through a side window and it is then reflected in a couple of flat mirrors in the receiver. Finally, the LO signal is coupled to the RF signal by means of a wire grid, located before the ellipsoidal mirror in the RF path, and both of them are received by the diagonal horn in the HEB mixer block. That mirror is not present in Fig. 1, because the vertical plate on which it sits has been removed for a clear view of the optics. The polarization of the LO and RF beams is the same after the wire grid coupling. The LO signal provides the pumping current for the HEB mixer and must therefore be as stable as possible.

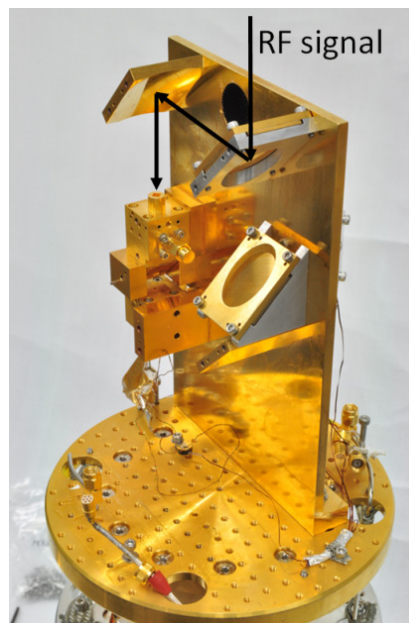


Fig. 1. 4K stage of the HEB dual-frequency receiver, modified for a clear view of the optics

In the case of the ALMA band 10 test cryostat, there are no windows for LO injection on the side of the cryostat and the LO must be injected from the RF cryostat window. Fortunately, the total distance of the LO optical path is long enough to allow the LO signal to be coupled to the RF signal and to be input together from the cryostat window. For the beam measurements at NAOJ, the optics was slightly modified to account for this need. The RF/LO coupling wire grid was removed from the receiver and used out of the cryostat. The modified optics for the measurement campaign is presented in Fig. 3. The RF signal optical path is the same in both situations, which means the quasi-optical analysis [10] and Physical Optics (PO) simulations with GRASP [11] are the same in both cases.

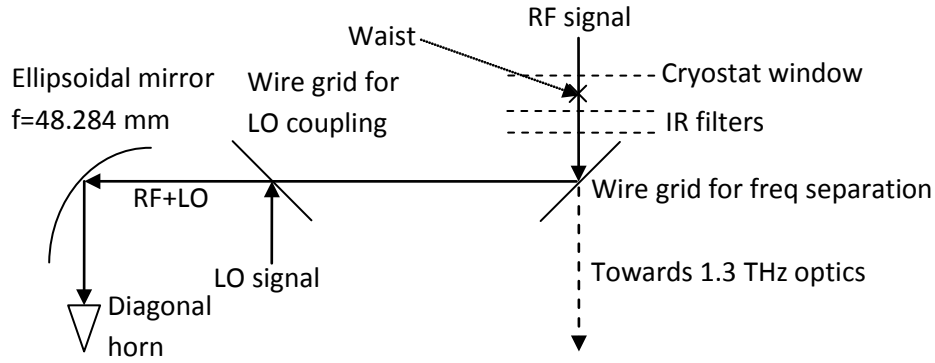


Fig. 2. 900-GHz ASTE receiver optics

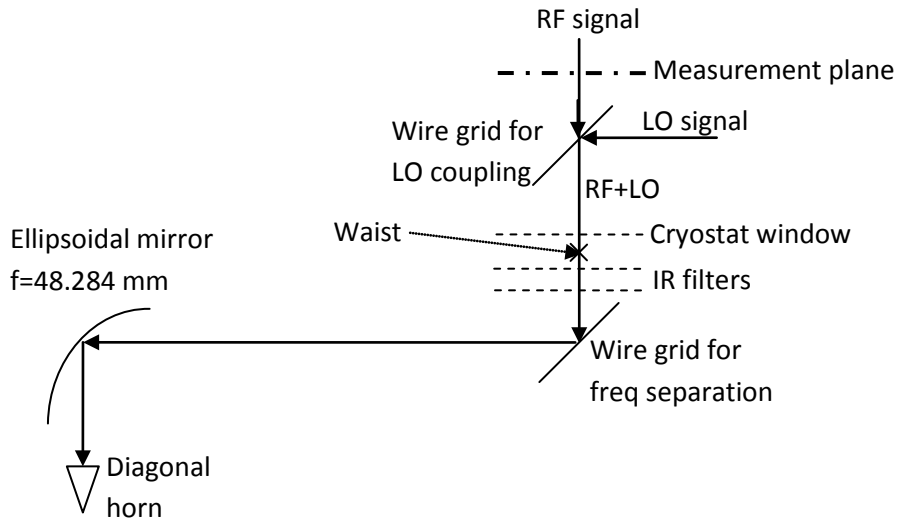


Fig. 3. Modification of 900-GHz ASTE receiver optics for beam pattern measurements

The receiver optics has been analyzed using Fundamental Gaussian beam analysis [10] in order to obtain the sizes and radii of curvature of the ideal beams at different frequencies. The results, together with design dimensions, are presented in Table I.

TABLE 1. Quasi-optical analysis of ASTE 900-GHz optics (all distances in mm)

	Design	881.3 GHz	906.8 GHz	925 GHz	944 GHz
Horn side aperture	3.5				
Horn slant angle (°)	7.64°				
Horn waist radius		1.000	0.984	0.973	0.961
Distance from waist to horn aperture		10.456	10.717	10.897	11.080
Distance from horn to ellipsoidal mirror	48.699				
Beam size at ellipsoidal mirror		6.483	6.431	6.396	6.361
Beam input radius of curvature at ellipsoidal mirror		60.597	60.840	61.006	61.175
Ellipsoidal mirror focal length	48.284				
Beam output radius of curvature at ellipsoidal mirror		-237.621	-233.959	-231.525	-229.131
Final waist radius		3.385	3.290	3.225	3.160
Distance ellipsoidal mirror-waist		172.848	172.735	172.660	172.586
Distance ellipsoidal mirror-cryostat window	186.649				
Beam size at window		3.414	3.320	3.256	3.192

3. Physical optics analysis

The optics under study has been analysed by the Physical Optics (PO) software GRASP [11]. The beam truncation in the infrared filters and cryostat window has also been considered. Electric fields have been calculated at the theoretical beam waist location at 900 GHz (172.767 mm from ellipsoidal mirror) and at a plane at a distance of 165 mm from that waist position, which is close to the measurement plane in the performed experiments. Cross-polarization patterns have also been calculated. For the study of cross-polarization, two situations have been considered to model the frequency separation wire grid in the RF path: a perfect wire grid and a flat mirror. The actual cross-polarization of the receiver must be between those two values, depending on the quality of the wire grid. The schematic of the simulation setup in GRASP is shown in Fig. 4.

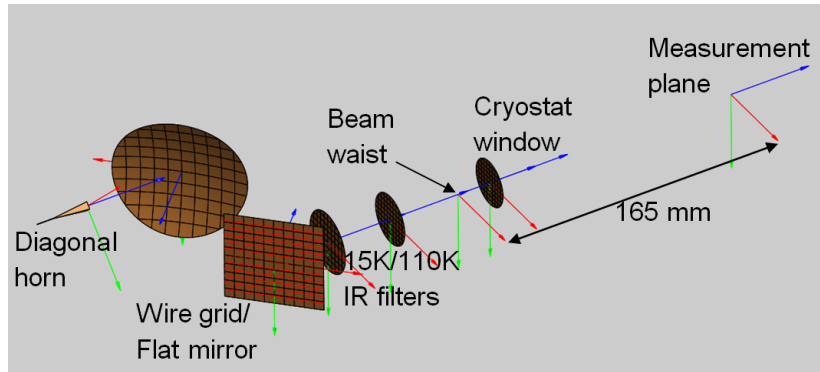
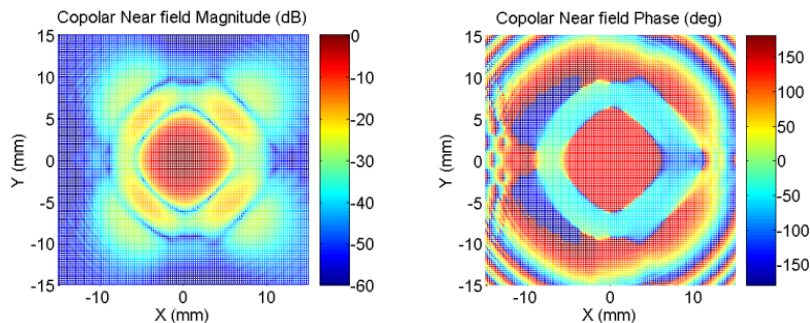


Fig. 4. Schematic of the GRASP simulation of the optics

The results of the calculations have been fitted by fundamental Gaussian beams in order to compare with the ideal quasi-optical design. Results of the fundamental Gaussian beam fitting and cross-polarization at the two planes under consideration are shown in Table II. These results are in good agreement with the quasi-optical analysis results in Table I. As expected, the shapes of the beams are similar at all frequencies. As an example, the beams at 906.8 GHz at the waist position and in the measurement plane are presented in Fig. 5 and 6 respectively.

TABLE II. Gaussian beam fitting of PO results

	At waist, 172.767 mm from mirror				At meas. plane, 165 mm from waist			
Frequency (GHz)	881.3	906.8	925.0	944.0	881.3	906.8	925.0	944.0
Gaussicity (%)	94.529	94.476	94.442	94.410	94.164	94.132	94.115	94.097
Waist size in x (mm)	3.388	3.293	3.229	3.164	3.388	3.293	3.229	3.164
Waist size in y (mm)	3.382	3.286	3.221	3.156	3.382	3.286	3.221	3.156
Defocus (mm)	2.561	2.536	2.519	2.502	162.384	162.409	162.426	126.443
Offset in x (mm)	0.000	0.000	0.000	0.000	0.000	0.000	0.000	0.000
Offset in y (mm)	0.005	0.009	0.012	0.014	0.103	0.111	0.116	0.121
Tilt in x (deg)	0.000	0.000	0.000	0.000	0.000	0.000	0.000	0.000
Tilt in y (deg)	0.034	0.035	0.036	0.037	0.034	0.035	0.036	0.037
Cross-Pol wire grid (dB)	-35.22	-35.15	-35.10	-35.05	-34.86	-34.69	-34.57	-34.43
Cross-Pol flat mirror (dB)	-15.02	-15.06	-15.11	-15.17	-12.74	-12.62	-12.54	-12.46



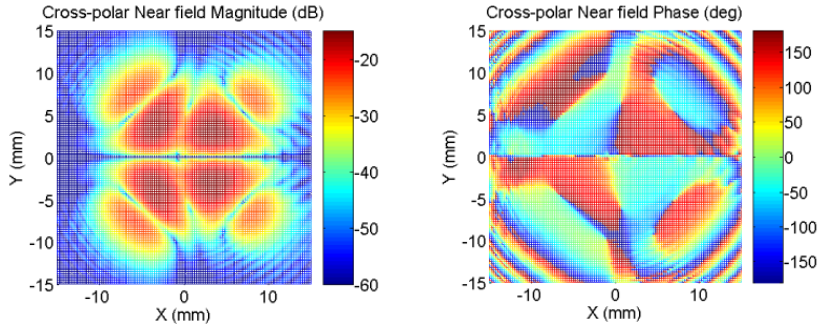


Fig. 5. Physical optics results at the waist plane at 906.7 GHz

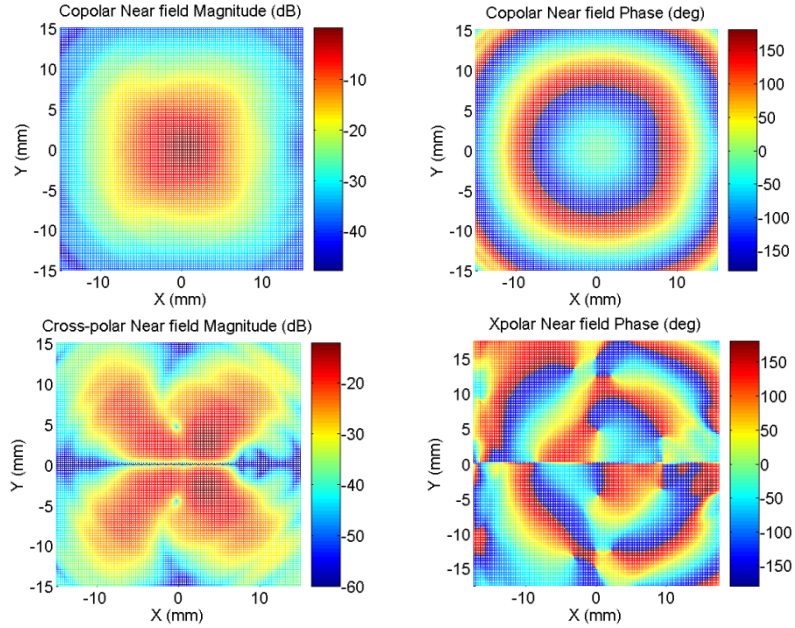


Fig. 6. Physical optics results at 165mm from waist plane at 906.7 GHz

4. Measurement results

The corrugated horn and the HEB mixer waveguide block are built together and cannot be separated. Consequently, room temperature measurements are not possible and the ASTE receiver optics must be cooled down to 4 K for its characterization using the HEB mixer to down-convert the RF signal. Mechanical 3D measurements of the cartridge were performed to guarantee that it was compatible in terms of size with the ALMA band 10 test cryostat. After size compatibility was confirmed, new cryostat beam ports and shields at the 110 K and 15 K stages were manufactured and installed in the ALMA band 10 cryostat. These parts were necessary to provide a way out of the cryostat for the beam. These are different from the parts used for ALMA band 10, because the optical path positions of both receivers are different with respect to the cryostat axis and beams emerge from different positions [12]. ALMA band 10 Infrared filters [13] were used at the 15 and 110 K shields and a 12 micron thick Kapton film was used as cryostat window. As explained before, the coupling of the LO and RF signals was initially done by means of a wire grid. The wire grid frame was mounted on the cryostat window and it was carefully designed in order to not truncate the beam. The wires in the grid were tilted 12 degrees in order to couple both signals with the same polarization. The LO source was attached to the measurement system support structure and carefully positioned by position screws in order to provide appropriate pumping of the HEB mixer. Later on, in order to measure cross-polarization patterns, the wire grid for RF-LO coupling was changed by an 8.5 micron thick Kapton film. Both coupling methods are presented in Fig. 7. A main concern at this point was if the injected LO signal would be stable enough for the HEB mixer, since the cryostat vibrates with a 1Hz frequency. The first measurements proved that the HEB bias point was acceptably stable.

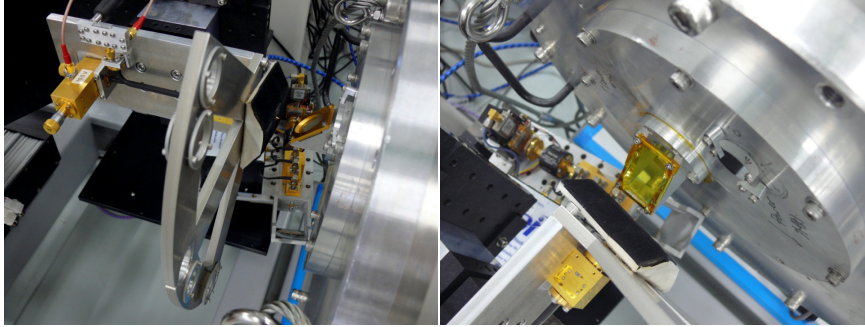


Fig. 7. Coupling of the signals coming from the RF source (up) and the LO source (down) using a wire grid (photograph on the left) and a thin Kapton film (photograph on the right)

The measurement system block diagram is presented in Fig. 8. It is based on the ALMA band 10 room temperature measurement setup [12] with some important modifications to adapt it to the IF frequencies of the HEB mixer, which are around 1 GHz instead of in the 4-12 GHz frequency range for ALMA band 10. Using this setup, amplitude and phase of the signal can be measured. By changing the position of the RF probe horn using a XYZ θ stage, the near field patterns can be measured as explained in [7]. The alignment between the XYZ θ stage and the test cryostat was done using a theodolite and small alignment mirrors on the RF probe support structure and on the cryostat.

Measurements of co- and cross-polarization beam patterns of the receiver were performed at 4 different frequencies within the RF bandwidth of the receiver. Three of the chosen frequencies are of interest for astronomy (881.3, 906.8 and 944 GHz), whereas the other one (925 GHz) was chosen to provide a good sampling of the RF bandwidth. Co-polarization patterns using wire grid and Kapton film coupling were similar. Cross-polarization patterns using Kapton film coupling could be measured properly and cross-polarization levels with respect to the maximum value of co-polarization could be calculated except at 906.8 GHz. At this frequency, the measured reference co-polarization pattern saturated and was unusable as a reference. Results of Gaussian beam fitting of the measured beams and cross-polarization levels are presented in Table III. Contrary to expectations, measured patterns are quite different from simulations. Measurements have a lower Gaussicity than expected, which is mainly due to a quite flat beam in the boresight direction. In addition, the beams are asymmetric and waist sizes are quite different from the design values at all frequencies. Beams are also tilted, with angles of almost 0.5 degrees in the X coordinate, which is the most sensitive to tolerances. Finally, the distance between the focal plane and the measurement plane changes much and has strong frequency dependence.

With respect to polarization purity, it is necessary to indicate that measured levels are higher than for the actual receiver at nominal operation. The Kapton film used to couple the RF and LO signals introduces a significant amount of cross-polarization, whereas at nominal operation, the LO coupling is done by a wire grid without cross-polarization generation. The theoretical cross-polarization of the ellipsoidal mirror and the diagonal horn are -24.9 dB and -10.2 dB respectively using quasi-optical theory [10], and the previous PO analysis showed that possible values of total cross-polarization (without IR filters and Kapton films) are between -34.7 and -12.7 dB at 900 GHz. The measured values of cross-polarization are however quite high, between -11 and -19 dB, which is probably due to some component being faulty and a strong cross-polarization component from Kapton films.

TABLE III. Results of fundamental Gaussian beam fitting and cross-polarization levels

Frequency (GHz)	881.3	906.8	925	944
Gaussicity (%)	90.418	89.471	90.574	88.495
Waist size in x (mm)	2.755	2.650	2.591	2.405
Waist size in y (mm)	3.072	3.149	3.093	2.815
Distance to focus (mm)	145.329	142.338	123.360	134.742
Tilt in x (deg)	0.497	0.458	0.469	0.450
Tilt in y (deg)	-0.084	-0.105	-0.104	-0.120
Cross-Polarization (dB)	-13.05		-18.91	-11.24

Far-field patterns can be easily calculated from the measured data using Fourier transformation. As an example, the far-field patterns at 925 GHz are presented in Fig. 10.

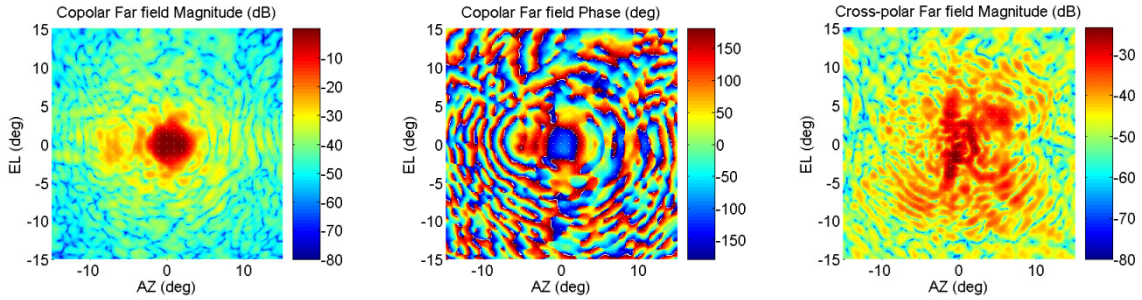


Fig. 10. Far-field patterns at RF freq = 925 GHz

5. Fabrication and assembly error analysis

Using a similar approach to that for ALMA band 10 optics [14], an analysis of the effect of fabrication and assembly errors on performance has been carried out at the design frequency of 900 GHz. MATLAB [15] has been used to create the PO simulation input files using random dimensions, positions and orientations for all optical components. The generated models have been analyzed using the PO software GRASP. Then, co-polarization patterns have been fitted by fundamental Gaussian beams for easier comparison, and cross-polarization levels have been calculated. In the calculation of cross-polarization levels, no wire grids have been considered in order to have a more clear understanding of how the cross-polarization depends on the horn and the ellipsoidal mirror. The effects of truncation in IR filters and cryostat window have not been considered this time in order to speed up lengthy simulations. Fabrication and assembly errors for each simulation have been obtained independently using Gaussian statistics with mean the design value and with different standard deviations σ , considering that the tolerance is equal to 3σ . More than 1000 simulations have been run with different sets of random values for errors. At first, the same standard deviations as for ALMA band 10 analysis were used. This is 20 microns fabrication tolerance, 20 microns assembly tolerance in each dimension and 1 mrad for orientation tolerance (model 1). The results of this simulation did not show any important degradation in the co-polarization pattern. Therefore, two more analyses were performed. The second analysis consisted of increasing all tolerances by a factor 2 (model 2). The third analysis consisted of using the same tolerances as for the first and adding some errors in the diagonal horn (model 3). Specifically, the diagonal horn modes TE_{10} and TE_{01} were chosen to have slightly different amplitudes and phases. The differences were $3\sigma = 5\%$ for amplitude and $3\sigma = 10$ degrees for phase. Results of mean values and standard deviations of the Monte Carlo analyses of models 1-3 are presented in Table IV.

Results of the previous Monte Carlo analyses show small deviations of the Gaussian beam parameters around the average values. The effect of doubling the tolerances is just an increase of the standard deviation (about double). The effect of considering some differences in the horn modes is just a slight degradation of Gaussicity and cross-polarization. None of the patterns calculated in the analyses of models 1-3 showed any significant degradation in terms of average values or spread of results. Average values were very close to ideal and standard deviation values were small. Therefore, this means that tolerances alone cannot explain why measurements are

different from PO simulations. Additionally, this indicates that some of the optical components in the receiver under study are faulty. In other words, either the diagonal horn or the ellipsoidal mirror has not been properly fabricated.

TABLE IV. Results of mean values (out of parentheses) and standard deviations (between parentheses) of fundamental Gaussian beam fitting and cross-polarization results for models 1 to 3 at 900 GHz

	Ideal	Model 1 (nominal tolerance)	Model 2 (tolerance x2)	Model 3 (horn modes)
Gaussicity (%)	94.603	94.603 (0.014)	94.585 (0.033)	94.586 (0.022)
Waist size in x (mm)	3.330	3.331 (0.009)	3.331 (0.016)	3.330 (0.009)
Waist size in y (mm)	3.337	3.337(0.009)	3.337 (0.016)	3.337 (0.009)
Distance to focus (mm)	136.754	136.759 (0.122)	136.777 (0.200)	136.764 (0.124)
Offset in x (mm)	0.088	0.077 (0.346)	0.074 (0.692)	0.089 (0.340)
Offset in y (mm)	0.000	0.008 (0.222)	0.010 (0.384)	-0.004 (0.225)
Tilt in x (deg)	0.034	0.032 (0.069)	0.032 (0.137)	0.034 (0.068)
Tilt in y (deg)	0.000	0.002 (0.044)	0.002 (0.075)	-0.001 (0.044)
Cross-polarization (dB)	-13.22	-13.22 (0.04)	-12.90 (0.24)	-12.91 (0.24)

To study this, two extra Monte Carlo analyses (models 4 and 5) have been performed using nominal dimensions for all components except for the component under study. In model 4, the diagonal horn dimensions have been changed, allowing non-square apertures, using a Gaussian distribution with standard deviation equal to 1% of average values. In model 5, the ellipsoidal mirror surface has been considered non-ellipsoidal. The mirror surface has been described as a second-order polynomial whose parameters do not necessarily describe an ellipsoidal surface. Each parameter has been modelled as a Gaussian variable with a 1% standard deviation. The mean values and standard deviations for Gaussian beam fitting and cross-polarization levels of Monte Carlo analysis results are presented in Table V for models 4 and 5.

TABLE V. Results of mean values (out of parentheses) and standard deviations (between parentheses) of fundamental Gaussian beam fitting and cross-polarization results when some component is faulty at 900 GHz

	Ideal	Model 4 (Diagonal Horn)	Model 5 (Ellipsoidal Mirror)
Gaussicity (%)	94.603	94.597 (0.016)	93.437 (2.061)
Waist size in x (mm)	3.330	3.333 (0.024)	3.677 (1.487)
Waist size in y (mm)	3.337	3.339 (0.023)	3.781 (1.489)
Distance to focus (mm)	136.754	136.741 (0.863)	175.838 (52.110)
Offset in x (mm)	0.088	0.088 (0.005)	0.162 (0.340)
Offset in y (mm)	0.000	0.000 (0.001)	0.000 (0.000)
Tilt in x (deg)	0.034	0.034 (0.001)	0.047 (0.069)
Tilt in y (deg)	0.000	0.000 (0.001)	0.000 (0.000)
Cross-polarization (dB)	-13.22	-13.19 (0.05)	-12.08 (2.49)

Results of the Monte Carlo analyses of models 4 and 5 indicate that the effects of a faulty mirror impact more on total performance than those of a faulty horn, for a 1% error in dimensions. Most importantly, in model 5, the consequences on the average final Gaussian beam are a decrease of Gaussicity, change of waist dimensions, beam defocus, offset increase in the x dimension and cross-polarization degradation. Another key result is the large standard deviations of Gaussicity, waist sizes and waist positions in the case of model 5. The standard deviation of 2% in Gaussicity means that values below 90% are possible. The waist size standard deviation shows that variations in the order of mm are possible. In the case of the waist position, the standard deviation is around 52 mm, which means that the position of the focus strongly relies on the mirror. In other words, model 5 results prove that if the ellipsoidal mirror is faulty, it cannot focus the beam properly in terms of Gaussicity, waist sizes, symmetry and waist position. These degradations perfectly fit the degradations found in the measured beams. Additionally, all beam patterns generated in the Monte Carlo analyses of models 1-5 have

been stored. An inspection of these patterns shows that, in the case of the analyses of models 1-4, there were not any distorted patterns, whereas in the case of the analysis of model 5, there were many distorted patterns. Actually, some of these resembled the measured patterns, as shown in Fig. 11, even if the effects of truncation in the cryostat mirror were not considered.

Monte Carlo analyses generate much data from individual PO simulations, which can be used to generate histograms of the Gaussian beam parameters. These histograms provide more insight about the kind of distribution which parameters follow when errors follow specific distributions, such as Gaussian in the case of models 1-5. Fig. 12 presents the histograms for Gaussicity, waist size, focus offset and cross-polarization for models 2 and 5. It thus provides a comparison between a case in which errors are due to usual tolerances and a case in which there is a faulty component. Notice that horizontal scales are very different. Histograms for model 5 show a great dispersion of the data and distributions which are not Gaussian. In the case of model 2, histograms show distributions with approximately Gaussian shapes, except in the case of cross-polarization. Moreover, the data spreads for model 2 are at least one order of magnitude less than in the case of model 5.

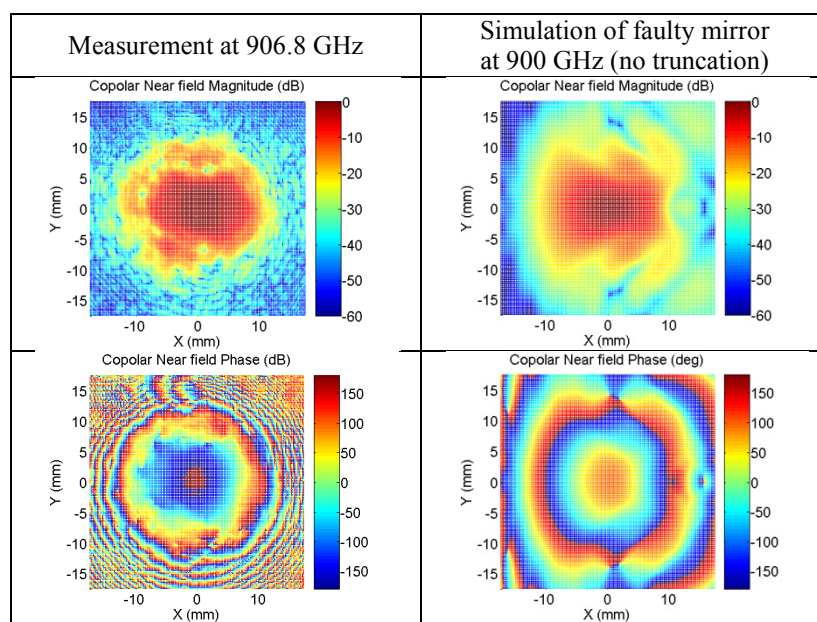
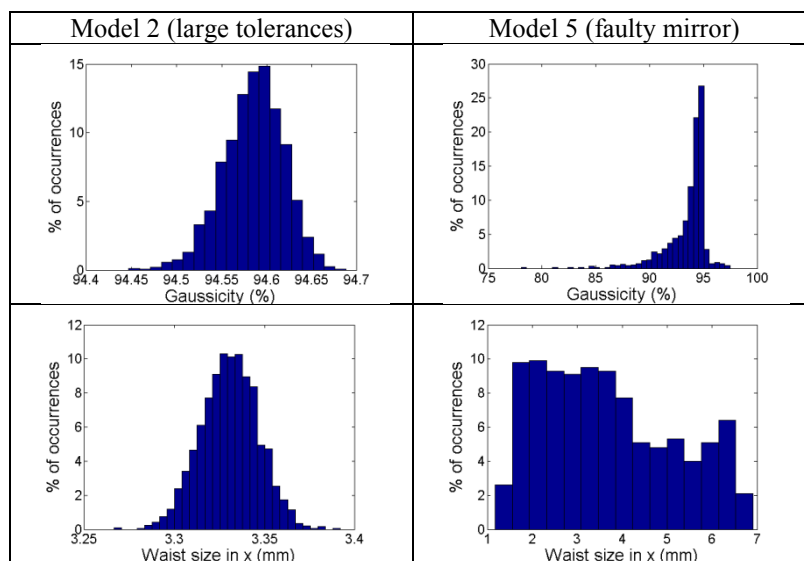


Fig. 11. Comparison of measured patterns and simulations with a slightly non-ellipsoidal mirror



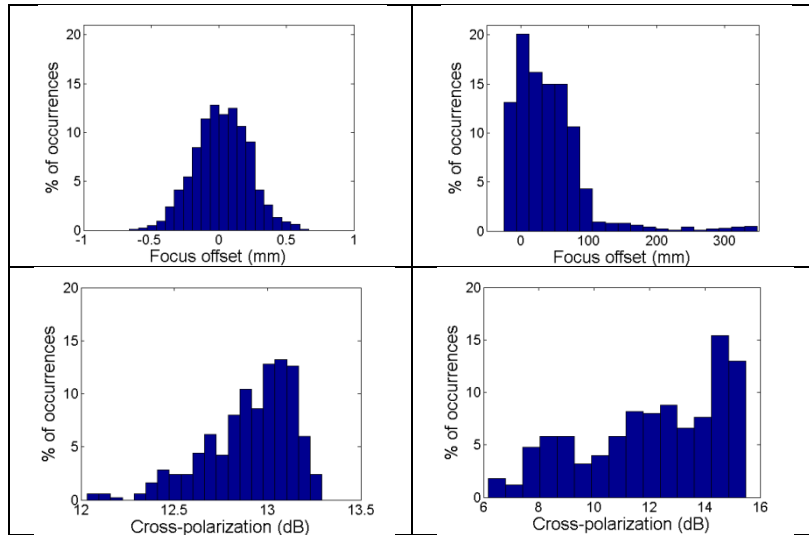


Fig. 12. Histograms of Gaussicity, waist size, focus offset and cross-polarization for models 2 and 5 at 900 GHz

Finally, the conclusions of the Monte Carlo analysis were tested by checking the beam performance and 3D measurement of the ellipsoidal mirror. Firstly, the mirror was disassembled from the receiver and placed on a XYZ stage in front of a probe horn. A room-temperature receiver based on Schottky diodes and manufactured by VDI [16] with diagonal horn input has been used to detect the radiation coming from the probe horn and reflected in the ellipsoidal mirror. A photograph of the measurement setup is shown in Fig. 13. Since the diagonal horn dimensions used in this receiver are different from the HEB mixer block diagonal horn, new quasi-optical analyses and GRASP simulations have been performed to compare the measured data to the expected radiation patterns. The XYZ stage has been adjusted to provide the best possible beam focus. Results of the measurements at the waist position and the calculated far fields are compared to GRASP simulations in Fig. 14. Results show that even though high beam Gaussicity can be achieved (around 97%), the phase distribution in the near field is much distorted. This translates in distorted beams in the far field, such as those measured for the whole receiver and shown in Fig. 9 and 10.

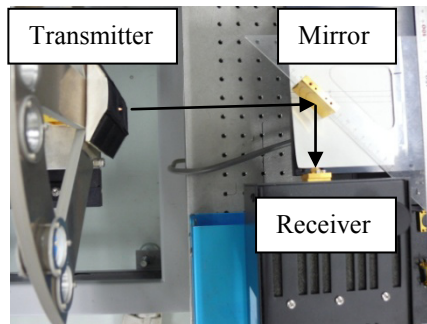
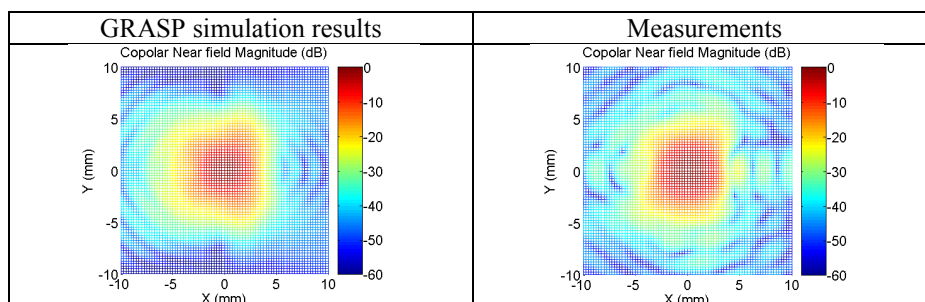


Fig. 13. Measurement setup for the room-temperature characterization of the ellipsoidal mirror



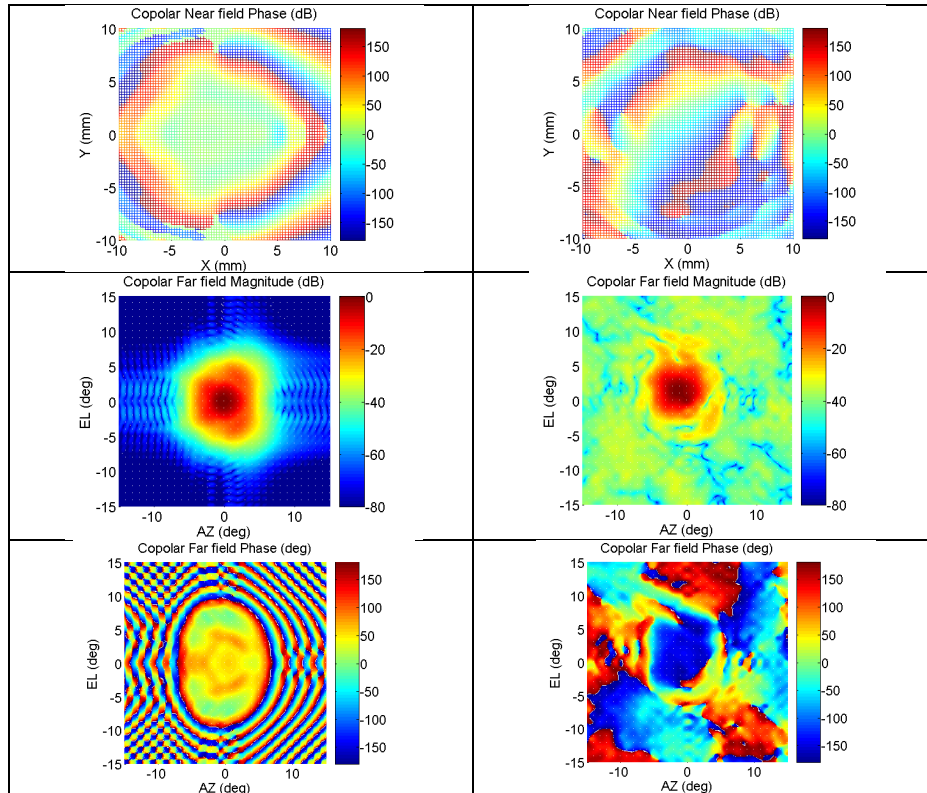


Fig. 14. Comparison of GRASP simulations and room-temperature measurement results

The final check on the mirror has been a 3D laser measurement performed at NAOJ. Fig. 15 shows the measurement setup. The comparison of the measured mirror surface to the theoretical ellipsoidal surface shows large surface errors in the entire mirror surface. In addition, there is a strange large error structure near the mirror center, which further distorts the reflected beam. Results of the 3D laser measurement are presented in Fig. 16.

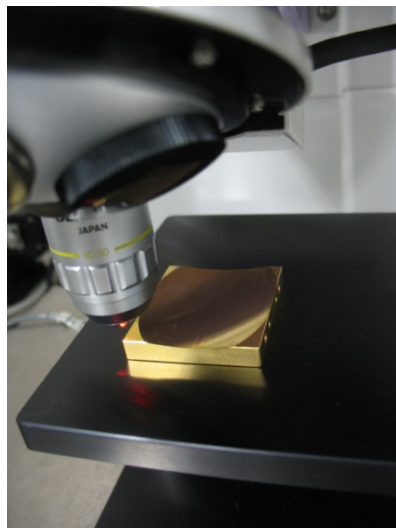


Fig. 15. Setup of the 3D laser measurement of the ellipsoidal mirror surface

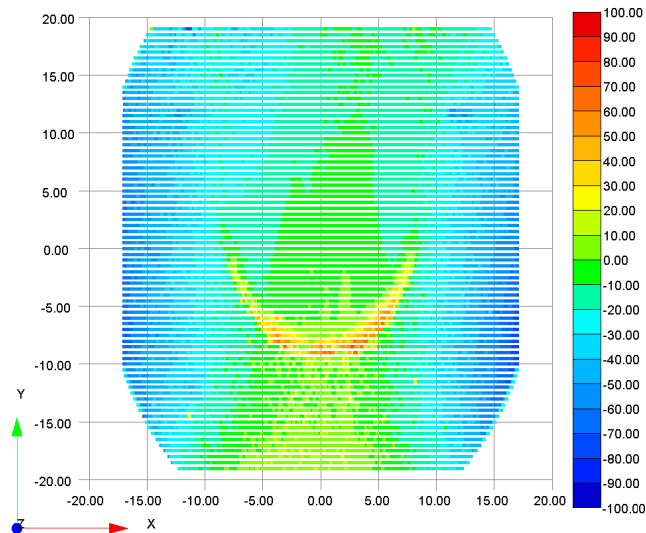


Fig. 16. 3D laser measurement results of the ellipsoidal mirror surface

In conclusion, the ellipsoidal mirror is of poor quality and it is distorting the receiver beam patterns. The combination of simulations and measurements has proved to be a useful and powerful tool to trace problems in a quasi-optical system. The ellipsoidal mirror will be replaced in the future in order to improve the receiver optical efficiency.

6. Conclusions

The optical performance of a 900-GHz HEB receiver designed at University of Tokyo to be used in the ASTE telescope has been analyzed using quasi-optical techniques and PO simulations. Measurements have been performed at the ALMA band 10 laboratory and results clearly differ from simulations. Five different Monte Carlo analyses have been performed in order to try to find out what the reason for such differences is. The statistical analyses showed that usual tolerances cannot explain such beam pattern distortions and probably, those are due to a defective ellipsoidal mirror. This conclusion of the statistical analysis has been confirmed by room-temperature beam measurements and 3D characterization of the mirror. This paper shows how a proper use of all available simulation and measurement techniques can help assess the expected optical performance and identify faulty components in a quasi-optical design. It also highlights the importance of Monte Carlo analyses to gain more insight in how fabrication and assembly imperfections affect beam patterns. These ideas can be of interest for any quasi-optical receiver at THz frequencies.

References

- [1] K. Kohno, "The Atacama Submillimeter Telescope Experiment", The Cool Universe: Observing Cosmic Dawn, ASP Conference Series, Vol. 344, 2005
- [2] M. Ishiguro and the LMSA Working Group, "Japanese Large Millimeter and Submillimeter Array", Proc. of SPIE 3357, pp. 244-253, 1998
- [3] N. Satou, Y. Sekimoto, Y. Iizuka, T. Ito, W. L. Shan, T. Kamba, K. Kumagai, M. Kamikura, Y. Tomimura, Y. Serizawa, et al., "A Submillimeter Cartridge-Type Receiver: ALMA Band 8 (385-500 GHz) Qualification Model", Publications of the Astronomical Society of Japan, 60:1199, 2008
- [4] H. Inoue, K. Muraoka, T. Sakai, A. Endo, K. Kohno, S. Asayama, T. Noguchi, and H. Ogawa, "350 GHz Sideband Separating Receiver for ASTE", Proceedings of the 19th International Symposium on Space Terahertz Technology, pp 28-30, 2008
- [5] G.W. Wilson, J.E. Austermann, T.A. Perera, K.S. Scott, P.A.R. Ade, J.J. Bock, J. Glenn, S.R. Golwala, S. Kim, Y. Kand, et al., "The AzTEC mm-wavelength camera", Monthly Notices of the Royal Astronomical Society, Vol. 386, Issue 2, pp. 807-818, 2008
- [6] T. Shiino, "Development of a low noise HEB mixer receiver for spectroscopic observations in the THz band", Doctoral Thesis, University of Tokyo, Japan, Dec. 2012

- [7] Y. Fujii, A. Gonzalez, M. Kroug, K. Kaneko, A. Miyachi, T. Yokoshima, K. Kuroiwa, H. Ogawa, K. Makise, Z. Wang, and Y. Uzawa, "The First Six ALMA Band 10 Receivers", IEEE Transactions on Terahertz Science and Technology, Vol. 3, No. 1, Jan. 2013
- [8] J.M. Hammersly and D.C. Handscomb, "Monte Carlo Methods", Wiley, New York, 1964
- [9] S. Matsushita, H. Matsuo, J.R. Pardo, S.J.E. Radford, "FTS Measurements of Submillimeter-Wave Atmospheric Opacity at Pampa la Bola II : Supra-Terahertz Windows and Model Fitting", Publications of the Astronomical Society of Japan, v.51, p.603, 1999
- [10] P. F. Goldsmith, "Quasioptical Systems", IEEE Press, New Jersey, 1998
- [11] TICRA GRASP Software Description, [Online]. Available: <http://www.ticra.com/products/software/grasp>
- [12] A. Gonzalez, Y. Uzawa, Y. Fujii, and K. Kaneko, "ALMA Band 10 Tertiary Optics", Infrared Physics & Technology, Vol. 54, pp. 488-496, 2011
- [13] A. Gonzalez, Y. Uzawa, K. Kaneko, S. Saito, and Y. Fujii, "Improvements in ALMA Band 10 Optics: Influence of IR filters and Solutions", IEEE Transactions on Terahertz Science and Technology, Vol. 3, No. 1, Jan. 2013
- [14] A. Gonzalez, Y. Uzawa, "Tolerance Analysis of ALMA Band 10 Corrugated Horns and Optics", IEEE Transactions on Antennas and Propagation, Vol. 60, No. 7, July 2012
- [15] MATLAB [On-line]. Available: <http://www.mathworks.com/products/matlab/>
- [16] Virginia Diodes Inc. (VDI), Available: <http://vadiodes.com/>

Bibliography

- [1] J.C. Maxwell, "A Treatise on Electricity and Magnetism", Dover, 1954
- [2] K. Rohlfs, T.L. Wilson, "Tools of Radio Astronomy", 3rd ed., Chapter 1, Springer, 2000
- [3] A.A. Oliner, "Historical Perspectives on Microwave Field Theory", IEEE Transactions on Microwave Theory and Techniques, vol. MTT-32, pp. 1022-1045, Sept. 1984
- [4] K. Yamada, G. Winnewisser, "Interstellar Molecules. Their Laboratory and Interstellar Habitat", Springer Tracts in Modern Physics, Vol. 241, Chapter 2, 2011
- [5] M. Harwit, "Astrophysical Concepts", 4th ed., Appendix A, Springer, 2006
- [6] Penzias, A.A.; R. W. Wilson (July 1965). "A Measurement Of Excess Antenna Temperature At 4080 Mc/s". *Astrophysical Journal*, vol. 142, p.419-421
- [7] R. Giacconi, "Nobel Lecture: The dawn of x-ray astronomy", *Reviews of Modern Physics*, Vol. 75, pp. 995-1010, July 2003
- [8] [On-line]. Available: http://imagine.gsfc.nasa.gov/docs/science/know_l1/history_gamma.html
- [9] TG. Phillips, J. Keene, "Submillimeter Astronomy", *Proceedings of the IEEE*, Vol. 80, No. 11, pp. 1662-1678, Nov. 1992
- [10] C. Kulesa, "Terahertz Spectroscopy for Astronomy: From Comets to Cosmology," *IEEE Transactions on Terahertz Science and Technology*, vol.1, no.1, pp.232-240, Sept. 2011
- [11] J.E Dickens et al., "Searches for new interstellar molecules, including a tentative detection of aziridine and a possible detection of propenal", *Spectrochimica Acta Part A: Molecular and Biomolecular Spectroscopy*, Vol. 57, Issue 4, March 2001, pp. 643-660
- [12] S. Dodelson, "Modern Cosmology", chapter 1.2, Elsevier, 2003
- [13] A. Li, B. T. Draine, "Infrared Emission from Interstellar Dust. II. The Diffuse Interstellar Medium", *Astrophysical Journal*, Vol. 554, No. 2, pp. 778-802, June 2001
- [14] R.E. Hills, A.J. Beasley, "The Atacama Large Millimeter/submillimeter Array", *Proc. SPIE 7012, Ground-based and Airborne Telescopes II, 70120N*, August 27th, 2008
- [15] K. Tatematsu et al., "Atomic Carbon Is a Temperature Probe in Dark Clouds", *Astrophysical Journal*, Vol. 526, pp. 295-306, Nov. 1999

- [16] T. Hunter, A. Wooten, "ALMA: Science at Band 10 and Beyond", Alma in the Coming Decade, NRAO, March 2011, On-line: https://science.nrao.edu/facilities/alma/alma2011/ALMA-CDP/19-Hunter/ALMA_band10_science.pdf
- [17] J.R. Pardo et al., "Deuterium Enhancement in Water toward Orion IRc2 Deduced from HDO Lines above 800 GHz", *Astrophysical Journal*, Vol. 562, pp. 799-803, Dec. 2001
- [18] Falgarone et al., "Strong CH⁺ J=1–0 emission and absorption in DR21", *Astronomy and Astrophysics*, Vol. 518, L118, July-Aug 2010
- [19] J. Zmuidzinas, P.L. Richards, "Superconducting Detectors and Mixers for Millimeter and Submillimeter Astrophysics", *Proceedings of the IEEE*, Vol. 92, No. 10, Oct. 2004
- [20] P.L. Richards, T.M. Shen, R.E. Harris, F.L. Lloyd, "Quasiparticle heterodyne mixing in SIS tunnel junctions", *Applied Physics Letters*, Vol. 34, No. 5, pp. 345-347, Mar. 1979
- [21] E. Gershenzon, G. Gol'tsman, Y. Gousev, A. Elantev, A. Semenov, "Electromagnetic-radiation mixer based on electron heating in resistive state of superconductive Nb and YbaCuO films", *IEEE Transactions on Magnetism*, vol. 27, pp. 1317-1320, Mar. 1991
- [22] P.K. Day, H. LeDuc, B. Mazin, A. Vayonakis, J. Zmuidzinas, "A broadband superconducting detector suitable for use in large arrays", *Nature* 425, 817-821, Oct. 2003
- [23] K. Irwin, "An application of electrothermal feedback for high-resolution cryogenic particle-detection", *Applied Physics Letters*, vol. 66, no. 15, pp. 1998-2000, 1995
- [24] Y. Yang, A. Shutler, D. Grischkowsky, "Measurement of the transmission of the atmosphere from 0.2 to 2 THz", *Optics Express*, vol. 19, no. 9, pp. 8830-8838, Apr. 2011
- [25] S.J.E. Radford, B.J. Butler, S. Sakamoto, K. Kohno, "ALMA Memo 384. Atmospheric Transparency at Chajnantor and Pampa La Bola", ALMA Memo Series, Aug. 2001. On-line: <http://legacy.nrao.edu/alma/memos/html-memos/alma384/memo384.pdf>
- [26] J.S. Lawrence, "Infrared and Submillimeter Atmospheric Characteristics of High Antarctic Plateau Sites", *Publications of the Astronomical Society of the Pacific*, vol. 116, pp. 482-492, May 2004
- [27] ESA Herschel, On-line: <http://sci.esa.int/herschel/>
- [28] P. Roelfsema et al., "The SAFARI imaging spectrometer for the SPICA space observatory", *Proceedings of the SPIE*, Volume 8442, article id. 84420R,15
- [29] T. Nakagawa, H. Matsuhara, Y. Kawakatsu, "The next-generation infrared space telescope SPICA", *Proceedings of the SPIE*, Volume 8442, id 84420O, Aug. 2012
- [30] W.S. Holland et al., "SCUBA-2: The 10000 pixel bolometer camera on the James Clerk Maxwell Telescope", submitted for publication, <http://arxiv.org/abs/1301.3650>
- [31] A. Kosowsky, "The Atacama Cosmology Telescope", *New Astronomy Reviews*, vol. 47, 11–12: 939, 2003

- [32] J. E. Carlstrom et al., "The 10 Meter South Pole Telescope", Publications of the Astronomical Society of the Pacific, 123:568-581, 2011
- [33] S.R. Golwala et al., "Status of MUSIC, the Multiwavelength Sub/millimeter Inductance Camera", SPIE Conference Series 8452, 2012
- [34] A-MKID camera, On-line: http://www.cosmonanoscience.tudelft.nl/?page_id=511
- [35] A. Monfardini et al., "A Dual-band Millimeter-wave Kinetic Inductance Camera for the IRAM 30 m Telescope", The Astrophysical Journal Supplement, Volume 194, Issue 2, article id. 24, June 2011
- [36] A. R. Thompson, J.M. Moran, G.W. Swenson, "Interferometry and Synthesis in Radio Astronomy", Wiley, 1986
- [37] ALMA, On-line: www.almaobservatory.org
- [38] Maas, "Noise in Linear and Nonlinear Circuits", Artech House, 2005
- [39] T. van Duzer, C.W. Turner, "Principles of Superconductive Devices and Circuits", 2nd ed., Prentice Hall, 1999
- [40] J. R. Tucker, "Quantum limited detection in tunnel junction mixers," IEEE Journal of Quantum Electronics, vol.15, no.11, pp.1234-1258, Nov. 1979
- [41] T. de Graauw et al., "The Herschel-Heterodyne Instrument for the Far-Infrared (HIFI)", Astronomy and Astrophysics, Volume 518, id.L6, 7, July 2010
- [42] P.L. Yagoubov et al., "TELIS – development of a new balloon borne THz/submm heterodyne limb sounder", 14th International Symposium Space Terahertz Technology, Tucson, AZ, USA, April 22-24, 2003, On-line: <http://www.cplire.ru/html/lab234/pubs/2003-11.pdf>
- [43] SOFIA, On-line: http://www.nasa.gov/mission_pages/SOFIA/
- [44] On-line: <http://www.apex-telescope.org/sites/chajnantor/atmosphere/transpwv/>
- [45] On-line: <http://almascience.nao.ac.jp/about-almata/atmosphere-model>
- [46] A. Wooten, T.A. Richard, "The Atacama Large Millimeter/Submillimeter Array", Proceedings of the IEEE, Vol. 97, Issue 8, p.1463-1471, Aug. 2009
- [47] Y. Uzawa, Y. Fujii, A. Gonzalez et al., "Development and testing of Band 10 receivers for the ALMA project", Physica C: Superconductivity, Available online 16 April 2013, <http://dx.doi.org/10.1016/j.physc.2013.04.008>
- [48] J. Wagg, T. Wiklind, C.L. Carilli, et al., "[C II] Line Emission in Massive Star-forming Galaxies at $z = 4.7$ ", 2012, Astrophysical Journal Letters, 752, L30.
- [49] J. D. Vieira, D. P. Marrone, S. C. Chapman et al., "Dusty starburst galaxies in the early Universe as revealed by gravitational lensing", 2013 Nature 495, 344

- [50] S. Casassus, G. van der Plas, S. Perez M. et al. "Flows of gas through a protoplanetary gap", 2013, *Nature*, 493, 191
- [51] M. Maercker, S. Mohamed, W.H.T. Vlemmings, S. Ramstedt et al., "Unexpectedly large mass loss during the thermal pulse cycle of the red giant star R Sculptoris", 2012, *Nature* 490, 232
- [52] K. Kohno, "The Atacama Submillimeter Telescope Experiment", *The Cool Universe: Observing Cosmic Dawn*, ASP Conference Series, Vol. 344, 2005
- [53] M. Ishiguro and the LMSA Working Group, "Japanese Large Millimeter and Submillimeter Array", *Proc. of SPIE* 3357, pp. 244-253, 1998
- [54] N. Satou, Y. Sekimoto, Y. Iizuka, T. Ito, W. L. Shan, T. Kamba, K. Kumagai, M. Kamikura, Y. Tomimura, Y. Serizawa, et al., "A Submillimeter Cartridge-Type Receiver: ALMA Band 8 (385-500 GHz) Qualification Model", *Publications of the Astronomical Society of Japan*, 60:1199, 2008
- [55] G.W. Wilson, J.E. Austermann, T.A. Perera, K.S. Scott, P.A.R. Ade, J.J. Bock, J. Glenn, S.R. Golwala, S. Kim, Y. Kand, et al., "The AzTEC mm-wavelength camera", *Monthly Notices of the Royal Astronomical Society*, Vol. 386, Issue 2, pp. 807-818, 2008
- [56] H. Inoue, K. Muraoka, T. Sakai, A. Endo, K. Kohno, S. Asayama, T. Noguchi, and H. Ogawa, "350 GHz Sideband Separating Receiver for ASTE", *Proceedings of the 19th International Symposium on Space Terahertz Technology*, pp 28-30, 2008
- [57] T. Shiino, "Development of a low noise HEB mixer receiver for spectroscopic observations in the THz band", *Doctoral Thesis, University of Tokyo, Japan*, Dec. 2012
- [58] A. Gonzalez, Y. Uzawa, Y. Fujii, and K. Kaneko, "ALMA Band 10 Tertiary Optics", *Infrared Physics & Technology*, Vol. 54, pp. 488-496, 2011
- [59] A. Gonzalez, Y. Uzawa, Y. Fujii, K. Kaneko, K. Kuroiwa, "A horn-to-horn power transmission system at terahertz frequencies", *IEEE Transaction on Terahertz Science and Technology*, vol. 1, no. 2, pp. 416-424, Nov. 2011
- [60] J. Zmuidzinas, H.G. LeDuc, "Quasi-optical slot antenna SIS mixers," *IEEE Transactions on Microwave Theory and Techniques*, vol.40, no.9, pp.1797-1804, Sept. 1992
- [61] Y. Uzawa, Z. Wang, A. Kawakami, "Quasi-optical NbN/AlN/NbN mixers in submillimeter wave band", *IEEE Transactions on Applied Superconductivity*, vol.7, no.2, pp.2574-2577, June 1997
- [62] P.F. Goldsmith, "Quasioptical Systems", *IEEE Press*, 1998
- [63] A. Gonzalez, Y. Uzawa, "Tolerance Analysis of ALMA Band 10 Corrugated Horns and Optics", *IEEE Transactions on Antennas and Propagation*, Vol. 60, No. 7, July 2012
- [64] A. Gonzalez, T. Soma, T. Shiino, Y. Uzawa, S. Yamamoto, "Optics characterization of a 900-GHz HEB receiver for the ASTE telescope: design, measurement and tolerance analysis", submitted for publication to *Infrared Physics and Technology*

- [65] A. Gonzalez, Y. Uzawa, K. Kaneko, S. Saito, and Y. Fujii, "Improvements in ALMA Band 10 Optics: Influence of IR filters and Solutions", IEEE Transactions on Terahertz Science and Technology, Vol. 3, No. 1, Jan. 2013
- [66] A. Gonzalez, Y. Uzawa, "Cross-polarization in quasi-optical receivers: ALMA band 4 and 10," 37th International Conference on Infrared, Millimeter, and Terahertz Waves (IRMMW-THz), 2012 , 23-28 Sept. 2012
- [67] A. Gonzalez, Y. Uzawa, "Investigation on ALMA band 4 frequency-dependent cross-polarization", submitted for publication to IEEE Transactions on Terahertz Science and Technology
- [68] E. Hecht, "Optics", 4th ed., chapter 6.2.1, Addison-Wesley, 2002
- [69] J. Volakis, "Antenna Engineering Handbook", 4th ed., Chapter 15, Mc Graw Hill, 2007
- [70] C.A. Balanis, "Antenna Theory", 3rd ed., p.899, Wiley, 2005
- [71] C.A. Balanis, "Advanced Engineering Electromagnetics", Chapter 12, Wiley, 1989
- [72] TICRA GRASP. On-line: <http://www.ticra.com/products/software/grasp>
- [73] C.A. Balanis, "Advanced Engineering Electromagnetics", Chapter 13, Wiley, 1989
- [74] J.B. Keller, "Geometrical theory of diffraction", Journal of the Optical Society of America, vol. 52, no. 2, pp.116-130, Feb. 1962
- [75] G. Evans, "Antenna Measurement Techniques", Artech House, 1990
- [76] C.A. Balanis, "Antenna Theory", 3rd ed., p.148-150, Wiley, 2005
- [77] D. Slater, "Near-Field Antenna Measurements", Chapter 3, D. Slater, Artech House, 1991
- [78] R.G. Lyons, "Understanding Digital Signal Processing", 2nd ed., pp. 74-82, Prentice Hall, 2004
- [79] P.F. Goldsmith, "Quasioptical Systems", pp.133-138, IEEE Press, 1998
- [80] J.W.M. Baars, "Characteristics of a reflector antenna", ALMA memo 456, 2003, On-line: <http://legacy.nrao.edu/alma/memos/html-memos/alma456/memo456.pdf>
- [81] P.F. Goldsmith, "Quasi-optical Techniques", Proceedings of the IEEE, Nov. 1992, Vol. 80, Issue 11, pp. 1729-1747
- [82] J.A. Murphy, M. McCabe and S. Withington, "Gaussian Beam Mode Analysis of the Coupling of Power between Horn Antennas", International Journal of Infrared and Millimeter Waves, Vol.18, No.2, 1997
- [83] N. Erickson, "A 200-350 GHz Heterodyne Receiver", IEEE Transactions on Microwave Theory and Techniques, Vol. MTT-29, No. 6, June 1981

- [84] W. Jellema, A. Baryshev, D. Paveliev, J. Hesler, W. Wild, and S. Withington, "Development Status of a 420-1980 GHz Vector Network Analyzer for Time-Domain Reflectometry and Imaging Applications", 15th IRMMW-THz Conference, Cardiff, Sept. 2007
- [85] H.B.G. Casimir and J. Ubbink, "The Skin Effect in Superconductors", Philips Technical Review, Vol. 28, p.366-381
- [86] G. A. Ediss, "Measurements and Simulations of Overmoded Waveguide Components at 70–118 GHz, 220–330 GHz and 610–720 GHz," proceedings of 14th Int. Symp. on Space THz Tech., 138–147, 2003, Available: ALMA Memo 467 at <http://www.mma.nrao.edu>
- [87] F.J. Tischer, "Excess Conduction Losses at Millimeter Wavelengths", IEEE Transactions on Microwave Theory and Techniques, Vol. MTT-24, NO.11, Nov. 1976
- [88] Virginia Diodes Inc. (VDI), on-line: <http://vadiodes.com/>
- [89] Y. Fujii et al., "Performance of the ALMA Band 10 SIS Receiver Prototype Model", IEEE Transactions on Applied Superconductivity, Issue 99, Dec. 2010
- [90] J.A. Murphy, M. McCabe and S. Withington, "Gaussian Beam Mode Analysis of the Coupling of Power between Horn Antennas", International Journal of Infrared and Millimeter Waves, Vol.18, No.2, 1997
- [91] J.F. Johansson, N.D. Whyborn, "The diagonal horn as a sub-millimeter wave antenna," IEEE Transactions on Microwave Theory and Techniques, vol.40, no.5, pp.795-800, May 1992
- [92] Erickson Instruments PM-4 millimeter-submillimeter power meter. Available: <http://www.virginiadiodes.com/Erickson/PM4%20Manual.pdf>
- [93] D. M. Pozar, "Microwave Engineering", 3rd ed., John Wiley & Sons, 2005, p.59
- [94] P.K. Tien and J.P. Gordon, "Multiphoton process observed in the interaction of microwave fields with the tunnelling between superconductor films", Phys. Rev., vol.129, pp. 647-651, 1963
- [95] "AM Noise in Front End Local Oscillators", ALMA document, FEND-40.10.00.00-093-B-REP, 2009-07-06
- [96] "ALMA Band 9 Cartridge SiC-Stycast Absorbing Coating Manufacturing Procedure", ALMA document, S-00003-0, 2006-02-21
- [97] Y. Umul, "Modified theory of physical optics", Optics Express, Vol. 12, Issue 20, pp. 4959-4972, 2004
- [98] S. Matsushita, H. Matsuo, J.R. Pardo, S.J.E. Radford, "FTS Measurements of Submillimeter-Wave Atmospheric Opacity at Pampa la Bola II : Supra-Terahertz Windows and Model Fitting", Publications of the Astronomical Society of Japan, v.51, p.603, 1999
- [99] Kapton properties, on-line: http://www2.dupont.com/Kapton/en_US/assets/downloads/pdf/summaryofprop.pdf

- [100] Y. Fujii, A. Gonzalez, M. Kroug, K. Kaneko, A. Miyachi, T. Yokoshima, K. Kuroiwa, H. Ogawa, K. Makise, Z. Wang, and Y. Uzawa, "The First Six ALMA Band 10 Receivers", IEEE Transactions on Terahertz Science and Technology, Vol. 3, No. 1, Jan. 2013
- [101] M.C. Carter et al., "ALMA front-end optics", Proceeding SPIE, vol. 5489, 2004, pp. 1074-1084
- [102] P. Goldsmith, et al., "Analysis of the optical design for the SAFIR telescope", Proceedings SPIE 6265, Space Telescopes and Instrumentation I: Optical, Infrared, and Millimeter, 62654A, June 2006
- [103] TICRA CHAMP Corrugated Horn Analysis by Modal Processing. On-line:
<http://www.ticra.com/products/software/champ>
- [104] Ansys HFSS. On-line:
<http://www.ansys.com/Products/Simulation+Technology/Electromagnetics/Signal+Integrity+&+Power+Integrity/ANSYS+HFSS>
- [105] C.-Y.E. Tong, D.V. Meledin, D.P. Marrone, S.N. Paine, H. Gibson, R. Blundell, Near field vector beam measurements at 1 THz, IEEE Microwave and Wireless Components Letters 13 (2003) 235–236
- [106] B. Lazareff, "Alignment Tolerances for ALMA Optics", ALMA memo 395, Oct. 2001, On-line:
<http://legacy.nrao.edu/alma/memos/html-memos/abstracts/abs395.html>
- [107] M. Candotti, Y. Uzawa, S. V. Shitov, Y. Fujii, K. Kaneko, "ALMA band 10 optics tolerance analysis", Proceeding of the ISSTT, 2008, pp. 521-527, On-line:
<http://www.nrao.edu/meetings/isstt/papers/2008/2008521527.pdf>
- [108] Hammersly, J.M., and D.C. Handscomb, "Monte Carlo Methods", John Wiley & Sons, 1964
- [109] J.W. Lamb, "Optimized optical layout for MMA 12-m antennas", Available: ALMA Memo 246 at <http://www.mma.nrao.edu>
- [110] M. Sugimoto et al., "Design of the central cone for the subreflector of the ACA 7-m antenna", Available: ALMA Memo 574 at <http://www.mma.nrao.edu>
- [111] MATLAB [On-line]. Available: <http://www.mathworks.com/products/matlab/>
- [112] K.P. Cheung, D.H. Auston, "A novel technique for measuring far-infrared absorption and dispersion", Infrared Physics, Vol. 26, Issue 1, Jan. 1986, pp. 23-27
- [113] B. Ferguson and X.-C. Zhang, "Materials for terahertz science and technology", Rev. Article Nature Materials, vol. 1, p. 26, 2002
- [114] C.A. Balanis, "Advanced Engineering Electromagnetics", chapter 5.5, Wiley, 1989

- [115] S. V. Berdyugina, and S. K. Solanki, "The molecular Zeeman effect and diagnostics of solar and stellar magnetic fields. I. Theoretical spectral patterns in the Zeeman regime", *Astronomy and Astrophysics*, vol. 385, pp. 701-715, 2002
- [116] S. V. Berdyugina, S. K. Solanki, C. Frutiger, "The molecular Zeeman effect and diagnostics of solar and stellar magnetic fields. II. Synthetic Stokes profiles in the Zeeman regime", *Astronomy and Astrophysics*, vol. 412, pp. 513-527, 2003
- [117] S. Sengupta, and M.S. Marley, "Multiple Scattering Polarization of Substellar-mass Objects: T Dwarfs", *The Astrophysical Journal*, vol. 707, pp. 716-726, 2009
- [118] S. Asayama, S. Kawashima, H. Iwashita, et al., "Design and Development of ALMA Band 4 Cartridge Receiver", 19th International Symposium on Space Terahertz Technology, Groningen, the Netherlands, 2008. On-line:
<http://www.nrao.edu/meetings/isstt/papers/2008/2008244249.pdf>
- [119] M.J. Gans and R. A. Semplak, "Some Far-Field Studies of an Offset Launcher", *The Bell System Technical Journal*, Vol. 54, No. 7, Sept. 1975
- [120] D.G. Bodnar, H.L. Bassett, "Analysis of an Anisotropic Dielectric Radome", *IEEE Transactions on Antennas and Propagation*, Nov. 1975, pp. 841-846
- [121] A. Kohazi-Kis, "Cross-polarization effects of light beams at interfaces of isotropic media", *Optics Communications* 253, 2005, pp 28-37
- [122] ALMA document, FEND-40.03.01.04-064-A-REP-20091001, "ALMA Front End Molded Window and IR-Filter Verification Cross-Polarization and RF Loss Test Report"
- [123] D. M. Pozar, "Microwave Engineering", 3rd ed., John Wiley & Sons, 2005, p.112-113
- [124] C-T. Tai, "Dyadic Green Functions in Electromagnetic Theory", IEEE Press, 1994
- [125] Nuria Llombart, "Development of Integrated Printed Array Antennas Using EBG Substrates", PhD thesis, Universidad Politecnica de Valencia, Valencia, Spain, 2006
- [126] C.A. Balanis, "Antenna Theory", 3rd edition, Wiley Interscience, 2005, section 12.9.5, pp. 713-721
- [127] T. Shimizu and Y. Kobayashi, "Millimeter wave measurements of temperature dependence of complex permittivity of dielectric plates by a cavity resonance method with coaxial excitation", Technical Report of IEICE, ED2000-188, MW2000-145 (2000-11)